

Master Thesis: Dust reverberation mapping of AGN in the local universe

LYNGE R. B. LAURITSEN

University of Copenhagen

August 2018

Acknowledgements:

To my loving parents that have helped and supported me throughout

and

my grandfather for nurturing a budging interest in natural sciences from an early age

Abstract

The exact value of the Hubble constant has been disputed since its inception. As precision astrophotometry evolved, so did the ability to accurately determine distances and luminosities of celestial objects, and thus the quality of the Hubble constant estimate, based on local universe measurements, improved. In the last decade, however, it has become increasingly clear, through sound horizon measurements from the Planck Collaboration, that a discrepancy exists between local universe estimate and those at the sound horizon for the Hubble constant. This project is a steppingstone, in an attempt to use the various AGNs as an improved distance ladder for Hubble constant measurements, through the use of reverberation mapping. This paper will utilise data from the Rapid Eye-Mount telescope at the La Silla Observatory site in Chile, observed in the JHKgriz filters to produce light curves for a number of AGNs in the local universe. Further, it has been attempted to create an algorithm for a photometric reverberation mapping analysis using the hot dust continuum of local AGNs based on the obtained light curves without prior knowledge of the AGN driving function. The latter attempt was ultimately unsuccessful, however the various considerations in taken in this algorithm will be discussed further.

Contents

1	Introduction	1
1.1	AGN and Cosmology	1
1.1.1	Measuring the Hubble Constant in the local universe	3
1.1.2	The Hubble constant and reverberation mapping	5
1.2	Active Galactic Nuclei	6
1.2.1	Observing and identifying the AGN	6
1.2.2	AGN morphology	6
1.2.2.1	Seyfert Galaxies	7
1.2.2.2	Quasars	8
1.2.2.3	Radio Galaxies	8
1.2.3	Stellar radiation	9
1.2.4	AGN structure	9
1.2.4.1	The Driving Engine	11
1.2.4.1.1	The Black Hole:	11
1.2.4.1.2	The Accretion Disk:	12
1.2.4.2	Broad-Line Region	13
1.2.4.3	Reverberation Mapping	18
1.2.4.4	Narrow-Line Region	19
1.2.4.5	Dust Torus	21
1.2.4.6	Unification Theory	23
2	Absolute Flux and Absolute Magnitude	25
2.1	Earth Atmosphere and associated uncertainties	25
2.1.0.0.1	Water Vapour:	26
2.1.0.0.2	Ozone:	27
2.1.0.0.3	CO_2 :	27
2.2	Magnitudes and Fluxes:	28
2.2.1	Apparent magnitude:	28
2.2.2	Absolute magnitude:	29
2.2.3	Flux:	30
2.2.4	Error in Fluxes	32
3	Defining a Light Curve	36
3.1	Kelly manipulations	36
3.2	Power Spectral Density	39

3.3	Structure Function	40
4	Reducing the Data	42
4.1	The REM Telescope	43
4.2	Finding the AGN	44
4.2.1	Astrometry of the AGN	44
4.2.2	Aperture Choice	46
4.3	The Light Curve Algorithm	48
4.3.1	The use of SEXtractor	48
4.3.2	The Standard Stars	51
4.3.3	The error on the AGN light curves	54
4.4	Light Curves	57
4.4.1	NGC3783	57
4.4.2	AKN120	58
4.4.3	F51	65
4.4.4	F9	65
4.4.5	H0557	65
4.4.6	MARK1239	65
4.4.7	ESO323	65
4.4.8	MARK509	74
4.4.9	NGC7213	74
4.4.10	IRAS09149	75
4.4.11	IC4329A	75
4.4.12	IzW1	75
4.5	Transfer Functions	75
4.5.1	Accretion Disk Transfer Function contribution	79
4.5.2	Dust Torus Transfer Function contribution	79
5	MCMC algorithm	80
5.1	Markov Chain Mote Carlo	81
5.1.1	Markov Chain Monte Carlo Principle	82
5.1.2	Fixed Transfer Function MCMC	82
5.1.2.0.1	Temperature of the Dust Torus (T):	85
5.1.2.0.2	The natural log of the thermal lag ($\mu_{thermal}$):	85
5.1.2.0.3	The natural log of the width of the thermal lag ($\sigma_{thermal}$):	85
5.1.2.0.4	The thermal fraction of the observed flux (A_T):	86
5.1.2.0.5	The BLR transfer function normalisation (N_{AD}):	86
5.1.2.0.6	The natural log of the Accretion Disk lag (μ_{AD}):	87
5.1.2.0.7	The natural log of the width of the Accretion Disk lag (σ_{AD}):	87
6	Discussion	91
6.1	Flux Calibrations	91
6.2	The MCMC Modeling	92

7 Conclusion	94
Appendices	96
A Individual Light Curve Plots	97
B AGN Signal-to-Noise Ratio Plots	119
C Structure Function Plots	143
7.1 Reading List	156

Chapter 1

Introduction

This paper will discuss the reduction of observed data of local universe AGNs, obtained using the Rapid Eye Mount (REM) telescope on the La Palma site in Chile, into AGN light curves usable for reverberation mapping. The aim of this paper is to demonstrate the possibilities in using observations of AGNs, from different bands, to determine thermal and optical lags inherent in the AGN. To do this the project will discuss the process of determining the light curves based on local reference stars, as well as the magnitude calibrations of these reference star, where applicable. Further the theoretical considerations for the creation and running of a Markov Chain Monte Carlo algorithm to be used to for lag determinations are discussed.

The project has been approached as two part. Initially the aim was to produce reliable light curves from the observational images obtained by the INAF REM Telescope. The observations from REM are done across the J,H,K,g,r,i,z bands. The second part of the project consists of creating a python program capable of determining the UV-continuum light curve of the AGNs, and the associated transfer functions, and thusly the lag-times.

1.1. AGN AND COSMOLOGY¹

Edwin Hubble showed a relationship in cosmological measurements between distance and redshift (*equation 1.1*), and thus concluded that the recession velocity of astronomical objects, not bound gravitationally, was a function of distance. This is explained by the theory of the expanding universe.

$$z = \frac{\lambda}{\lambda_0} - 1 \quad (1.1)$$

The motion of galaxies, as they experience the expansion of the universe, is called *the Hubble flow*. Generally galactic movements can be described by two distinguishable motions. The locally influenced velocity *through* space, called their *peculiar velocity*,

¹Apart from the, when relevant, specified papers this section relies heavily on Mo, Bosch & White 2010 [21], Carroll and Ostlie 2014 [?] and Neal Jackson *The Hubble Constant* 2015 [?]

often associated with gravitational interactions with other galaxies, and the movements spawned and maintained through the expansion of the universe, the *recessional velocity*. The latter is not due to galactic motion through surrounding space, rather it is the galaxy being "*carried*" along with the surrounding space due to the expanding universe. Similarly the *Cosmological redshift*, caused by the expanding universe, is not an expression of the observed galaxy movement by itself, but rather an expression of the light wave being "*stretched*" as the universe expands along the path traveled by the wave. The knowledge of the expanding universe and the *Hubble Constant* (H_0) allows the calculation of inter-galactic distances of non-gravitationally bound systems by calculating the redshift (*equation 1.2*) and is called the *Hubble law*.

$$d \simeq \frac{c}{H_0} \frac{(z+1)^2 - 1}{(z+1)^2 + 1} \quad (1.2)$$

The main difficulty in utilising the Hubble Law is the determination of the Hubble Constant. This is historically a difficult calibration due to the importance on the accurate determination of the distance to remote galaxies, through secondary distance indicators, as well as the peculiar velocity of the observed galaxies. Additional uncertainty can occur due to the skewing of statistics originating from the *Malmquist bias*, which is the bias inherent in Magnitude-limited samples, causing the astronomers to look only below a given apparent magnitude, thus as the distance increases only object of increasing absolute flux will be included.

The increasing accuracy in the measurements of the Hubble constant from the local universe, in the last half a decade, has led to the realisation of a significant discrepancy between the measurements obtained from the local universe, through observations of Cepheids and Type Ia Supernovae (SNe Ia) with $H_0 = 73.24 \pm 1.74 \text{ km s}^{-1} \text{Mpc}^{-1}$ (Riess et al. 2016 [29]), $H_0 = 72.8 \pm 2.4 \text{ km s}^{-1} \text{Mpc}^{-1}$ (Bonvin et al. 2017 [10]), $H_0 = 71.0 \pm 2.8 \text{ km s}^{-1} \text{Mpc}^{-1}$ (Arenas et al. 2017 [16]) and $H_0 = 73.48 \pm 1.66 \text{ km s}^{-1} \text{Mpc}^{-1}$ (Riess et al. 2018 [28]). And the observations from the opposite end of the observable universe, at the sound horizon, of Cosmic Microwave Background (CMB). This is done by the Planck Collaboration, using a flat Λ CDM cosmology. The Planck Collaboration et al. 2016 [12] determined the H_0 value to be $H_0 = 66.93 \pm 0.62 \text{ km s}^{-1} \text{Mpc}^{-1}$, and previous Planck releases has determined comparable values. This is a discrepancy of 3.4σ (Riess et al. 2018 [28]), and thus the disagreement provides evidence of physics not included in the *Standard Model*. The Standard Model does not include, among other theories, features such as *Time-dependent or early dark energy*, *Gravitational physics beyond general relativity*, *additional relativistic particles* or *non-zero curvature*, despite the main argument for their exclusion being the attempt at simplicity (Riess et al. 2016 [29]). It is beyond the scope of this project to investigate or explain the intricacies of the standard model, and the excluded physical theories, it is however of interest to the purpose of this project to understand the role AGN, or at further distances Quasars, can play in the future investigations into the Hubble Constant.

1.1.1. Measuring the Hubble Constant in the local universe²

The Hubble Constant is as shown in *equation 1.2* dependent upon the distance to the observed galaxy, and the recession velocity of said galaxy. Thus calculation of the Hubble Constant necessitates an accurate determination of both these parameters. The recession velocity can typically be calculated through the redshift (*equation 1.1*), assuming the recession velocity dominates over the peculiar velocity. The relative error in the recession velocity, due to the peculiar velocity, is decreasing by distance as the recession velocity gains dominance. It is assumed that the relative error caused by the peculiar velocity decreases to under 10% at distances in excess of 50 *Mpc*. The main difficulty in calculating an accurate value of the Hubble constant, based on observations of the local universe, originates in the issues inherent in distance measurements. The common method of distance estimation in the local universe, not utilising the Hubble law, is through the use of either *standard candles* or *standard rulers*. A *standard candle* is an astronomical object of known, or accurately predictable luminosity, and a *standard ruler* is an object of known, or accurately predictable, size. The determination of usable standard candles and/or rulers is a non-trivial issue, due to the significant spread in size and luminosity of galaxies and stars, regardless of their colour. Thus the perfect object for calculation of the Hubble constant is an object that

- Has physical properties allowing the identification as a standard candle or ruler
- Can be independently calibrated e.g. does not build upon previous distance or luminosity determinations (a one-step process), as errors stack
- At sufficient distance that error associated with peculiar velocity is small
- Astrophysically simple i.e. distance determination is independent on internal properties of the object
- Determines the Hubble constant independently of other cosmological parameters.

There are a number of *one-step* methods of determining the Hubble constant. A full discussion of the various modes of Hubble determination in the local universe is somewhat outside the scope of this paper. Thus only the *Megamaser cosmological method* will be discussed, due to its familiarity with AGN cosmology, but neither the *Sunyaev-Zel'dovich effect* nor the *Gravitational lens model* will be discussed, however a full description is found in Neal Jackson *The Hubble Constant 2015* [?].

The *Megamaser cosmological method* relies on the use of Very Long Baseline Interferometry (VLBI) of frequencies around $\nu \simeq 22$ GHz, allowing resolution on the milliarcsecond scale. The Megamaser system in galaxies involves clumps of gas circulating the central galactic Supermassive Black Hole (SMBH) at radius $r \sim 0.1$ pc. It becomes possible, in not too distant galaxies, to resolve the rotating clumps, and through continuous

²Apart from the, when relevant, specified papers this section relies heavily on Mo, Bosch & White 2010 [21], Carroll and Ostlie 2014 and Neal Jackson *The Hubble Constant 2015*

observation determine the clump velocities and accelerations. If one is to assume a Keplerian motion of the observed gas it becomes possible to determine the radius of the rotating gas, and the SMBH mass. This allows a trigonometric determination of the galactic distance, and thus a Hubble constant determination by comparing the galactic redshift with the distance obtained by the *standard ruler*, that is the Megamaser system. This method however is vulnerable to systematic errors, although assumed to be small, originating from the understanding of the physical parameters of the disk, such as eccentricity, position angle, periapsis angle and inclination (Neal Jackson 2015 [?]).

The more traditional method of determining the distance to astronomical objects in the local universe is through the *Local Distance ladder*. This approach relies on gradually expanding the distance estimation through understanding of the observed behavior of specific astronomical objects relative to comparable objects at already known distances, thus it becomes a ladder (Neal Jackson 2015 [?])

1. **Parallax approach:** Close stars will change angle in the sky dependent on the Earth position in its orbit around the sun. The parallax approach thus relies on the observed motion of close stars on the sky, relative to more distant stellar objects. The *parsec (pc)* is defined as the distance an arbitrary star must be from the solar system to achieve a 1 arcsec angular change due to the Earth orbit.
2. **Open Clusters:** The Parallax approach can be used to accurately determine the distance to close open clusters with an error $< 1\%$. The stellar population of open clusters can be fitted on a *Hertzsprung-Russell diagram* of the stellar temperature (determined through stellar colour and Wien's law) against apparent magnitude (discussed later), revealing a characteristic sequence of stars, the so-called "main sequence stars". These nearby clusters can then be utilised in the calibration of distance to clusters outside the reach of the Parallax approach through "*main sequence fitting*". This method can be applied to nearby galaxies, in which it is possible to resolve individual stars, such as the Large and Small Magellanic Clouds and is liable to have errors of a few percent.
3. **Cepheids:** The open cluster approach allows for the calibration of Cepheid variable stars. These stars are the intrinsically most luminous of the variable stars. Cepheids are pulsating Giant Blue stars located in a narrow range on the Hertzsprung-Russell diagram between $7000 - 8000 \text{ K}$. Observations show that the pulsation period is directly proportional with the luminosity, thus creating a standard candle, that can be calibrated through Cepheids observed in, or nearby to, open clusters. They are observed in the Large Magellanic Cloud and in galaxies at distances up to $20 - 30 \text{ Mpc}$, still significantly closer than the recommended $d > 50 \text{ Mpc}$ for Hubble constant calibration.
4. **Type Ia Supernovae (SNe Ia):** A binary system of a Giant star dumping mass onto a white dwarf triggering a Supernovae explosion. The Type Ia SNe has same characteristic of the observed time-dependent light curve regardless of distance, and despite variation in the absolute luminosity between separate events, the

similarities in light curves and the well understood degree of fading in the 15 days following peak brightness (m_{15}) allows for the calibration of SNe Ia events for distance measurements, if they can be observed in galaxies with well calibrated Cepheid distances. Due to the brightness of the SNe Ia event this allows further distance calibration of galaxies, past the $d = 50 \text{ Mpc}$ line at which the peculiar velocity driven error on the recession velocity decreases to $< 10\%$.

5. ***Other relations:*** The SNe Ia is not the only distance measurement usable in the attempt to estimate distances in the local universe. The *Tully-Fisher relation* allows for luminosity estimation of edge-on spiral galaxies through the relation $L \propto v^4$, similarly the elliptical galaxies has the *Faber-Jackson relation*. There are several more complex methods of measuring distances to galaxies, however an in-depth discussion is not relevant.

The main issue arising from the Local Distance ladder is the stacking of uncertainties, thus any uncertainty at the early stages of the ladder will propagate through the ladder (the math of error propagation is discussed later).

1.1.2. The Hubble constant and reverberation mapping

The main problematic of the Local Distance Ladder, with respect to determining the origin of the 3.4σ tension between the locally determined Hubble constant, and the CMB determined value, is the limited reach of the ladder, as well as the propagating uncertainties. Thus it becomes relevant to attempt to identify possible standard candles, or rulers, available in one-step jumps at larger distances. Despite the AGN or, at larger distances, Quasars being the most powerful observables in the known universe, their functionality as standard candles are non-existent due to the varying luminosity, while having a mostly unchanging SED, thus not allowing for luminosity predictions to be made through the SED (Risaliti and Lusso 2015 [30]). AGNs are however excellent for high redshift observations, and thus if the internal dimensions of the AGN can be accurately determined, and then resolved, it would become possible to accurately utilise the observed AGN as a standard ruler, and thus allow determination of the Hubble constant at increasing redshift.

This project aims at determining the inner scales of observed AGNs through the use of reverberation mapping. It is the aim of this project to lay the groundwork for an algorithm that can be utilised for *reverberation mapping* of AGN without complete knowledge of the driving function. If such an endeavor should prove successful it would allow for future H_0 calibrations to provide a deeper understanding of the expansion of the apparent tension in the local universe and CMB measurements of the Hubble Constant by providing a means of determining the Hubble constant at intermittent redshifts.

1.2. ACTIVE GALACTIC NUCLEI

Active Galactic Nuclei, or AGN for short, is a term used to describe a powerful, energetic and luminous phenomena in the galactic center that does not originate from the galactic stellar population. It is generally believed that these phenomena is powered by accretion onto a Supermassive Black Hole (SMBH). This accretion however radiates in the X-RAY bands, rather than the optical and NIR bands studied in this project. Therefore it becomes of paramount importance to understand the workings of the AGN and the various processes by which light is emitted. This section will thus discuss the AGN phenomena, how it originates as well as its importance in modern astrophysics.

1.2.1. Observing and identifying the AGN

AGN identification and observation historically follow a list of observable properties. The earlier identification methods as described by both Schmidt (1969) [?] as well as Peterson (1997) [26] and later Peterson (2008) [?] allows AGN identification based upon datasets of similar nature as the ones used in this project. These identification properties are;

1. The pointlike representation of an AGN upon an imaging detector
2. Strong emission lines
3. The Continuum Luminosity varies over time
4. Evidence of strong non-stellar emission
5. Strong X-RAY emission
6. Radio emission
7. Non-stellar UV through IR emission
8. Broad emission lines in the UV through IR.

it is important to note however that not all observables is always registered. In the datasets providing the foundation for this project the observed AGN appear as point-like, time-varying emission in the center of resolved galaxies (the so-called Seyfert Galaxies discussed later) with non-starlike SEDs.

1.2.2. AGN morphology

It can generally be said that AGN falls into two different categories. The Seyfert Galaxies and the Quasars. These categories each have identifying points, however it is somewhat unclear to which degree they are distinctly different objects, or if the difference is mostly due to possibilities of observation. The distinction is of general

importance and interest, however for the majority of this project it makes little actual difference in the results obtained, although it should be said that the available data did belong to Seyfert galaxies.

1.2.2.1. Seyfert Galaxies

Discovered by Carl Seyfert (1943) these galaxies are Active Galaxies characterized by being spiral galaxies with a bright star-like nuclei in the center. Spectroscopically these galaxies contains both non-thermal continuum radiation, and broad emission lines in their spectra. In addition observations show that the Luminosity output from the Nuclei originating in these Active Galaxies can at times vary by more than a factor of two in a year (Peterson 1997 [26]).

The first Active Galaxy observed in 1908 by E. A. Fath at the Lick Observatory was NGC 1068. However not until 1943 did Carl Seyfert identify these as a distinct class of galaxies, now called Seyfert Galaxies. Not until the late 1950's did these galaxies become relevant again, with their identification as radio sources. Woltjer (1959) [38] identified these Seyfert galaxies as having:

1. Unresolved nuclei, so at the then observational quality, a nucleus smaller than 100 pc.
2. Lifetimes in excess of 10^8 years. This being concluded from the realisation that Seyfert Galaxies makes up 1/100 of all spiral galaxies. Leading to two possible conclusions. Either all Spiral Galaxies pases through a Seyfert phase, or they are fundamentally different from other spirals, making it logical to assume they have lifetimes comparable to other spiral galaxies (of order 10^{10} yrs).
3. If it is assumed the material in the Nucleus is gravitationally bound, then based on the widths of the emission lines (excess of 10^3 kms^{-1}) and the viral argument *equation 1.3*,

$$M \approx \frac{v^2 r}{G} \quad (1.3)$$

then it must be assumed the Mass of the Nucleus is of the order $10^6 M_\odot$.

It is of note that the Seyfert Galaxies fit into two types. Seyfert I galaxies has permitted emission lines originating primarily from Hydrogen with very broad characteristics and giving FWHM corresponding to velocities in excess of 10^3 kms^{-1} . Additionally the Seyfert I galaxies also contain forbidden lines (such as [OIII]) with much narrower profiles ($10^2 - 10^3 \text{ kms}^{-1}$). Seyfert II galaxies differs in that the emission observed is originating in the Narrow Line Region (NLR) entirely. This does not necessarily imply an absence of a Broad Band Region (BLR), as this region could be unobservable in this galaxy (Peterson 1997 [26]; Mo, Bosch & White 2010 [21]).

Most galaxies contains a SMBH in their center, however only few becomes Seyfert Galaxies. Studies seems to suggest that the SMBH becomes "active" due to disturbances in the gravitational potential, caused by either tidal interaction with foreign galaxies or galactic mergers. It is suggested that the disturbances in the gravitational potential is essential for the gas to overcome the angular momentum barrier (discussed later), allowing the accretion of gas onto the SMBH (Schneider 2006 [31]).

1.2.2.2. Quasars³

Quasars, or as originally called Quasi-Stellar Radio Source, are the most luminous AGNs observed. A subset of these are also strong radio sources (5-10%), and it was originally these objects that defined the quasars distinction and name. Generally quasars have strong similarities with Seyfert Galaxies, however they have very weak stellar absorption features and the Narrow Lines tends to be weaker when compared to the Broad Lines than observed in the Seyfert Galaxies. The optical spectrum observed from quasars are similar to those observed in the Seyfert Galaxies. In formal classification the distinction is made from the absolute magnitude with *equation 1.4* defining a quasar.

$$M_B \leq -21.5 + 5\log(h_0) \quad (1.4)$$

This distinction is however a historical construct, based upon the observable qualities of the respective AGNs, as it appears the only fundamental difference between Quasars and Seyfert Galaxies is the Luminosity of the object. The quasar Luminosity can be of the order 10^3 larger than that of a galaxy, and therefore only at low redshift high resolution quasars will the host galaxy be observable.

1.2.2.3. Radio Galaxies⁴

The normal spiral galaxies will have weak radio emission (mostly powered through SN remnants) and therefore have power (*equation 1.5*),

$$P_{1.4GHz} \leq 2 * 10^{23} W Hz^{-1} \quad (1.5)$$

this allows the definition of radio galaxies of being galaxies with $P_{1.4GHz}$ larger than *equation 1.5*.

Radio Galaxies were originally identified through the third survey at Cambridge, and it has since been realised that almost all radio galaxies are AGN ellipticals. Much like the Seyfert Galaxies two types are identified, the Broad-Line Radio Galaxies (BLRG) and Narrow-Line Radio Galaxies (NLRG). The BLRG and NLRG differs from their corresponding Seyfert Galaxies partly in being radio loud, and the morphology of the host galaxy, but also in the existence of mostly asymmetric stretching radio jets stretching several hundred kiloparsec or even megaparsec from the AGN.

³Peterson 1997 [26] and Mo, Bosch & White 2010 [21]

⁴Peterson 1997 [26] and Mo, Bosch & White 2010 [21]

1.2.3. Stellar Radiation⁵

An understanding of the observed properties of stars becomes necessary to identify, and understand the properties of AGNs. The most important characteristic of the AGN spectrum utilised in this project is the time-varying *non-stellar* characteristics of the radiation emitted by the AGN. The *AGN Radiation Spectrum* differs from the *Stellar Radiation Spectrum* by both the varying luminosity created by the AGN, as opposed to the constant Luminosity Function from the Stellar Light-Source, and the non-*Black Body Radiation* of the AGN.

Despite the lack of any astronomical objects emitting like a perfect *Black Body*, observations show that it is a good first order approximation for the spectral energy distribution of *stellar radiation*. Thus the specific intensity (B_ν) of the stellar radiation can be approximated by the *Planck law*

$$B_\nu(T) = \frac{2h\nu^3}{c^2} \left[e^{\frac{h\nu}{kT}} - 1 \right]^{-1}. \quad (1.6)$$

In the model of the radiation emitted by a star is described as a Black Body spectrum the luminosity (L) is dependent on the temperature (T) and radius (r) of the star

$$L = 4\pi r^2 \sigma_{SB} T^4, \quad (1.7)$$

with σ_{SB} being the *Steffan Boltzmann constant*. Thus the *effective temperature* (T_{eff}) is often discussed, as the temperature of a Black Body, of identical radius, emitting the same luminosity and spectral energy distribution as the star.

Additionally stellar observations identify the relationship between stellar luminosity and stellar mass as being

$$\frac{L}{L_O} = \left(\frac{M}{M_O} \right)^{3.5}, \quad (1.8)$$

and thus a main-sequence star of mass $10M_O$ emits $\sim 3200L_O$. This increase in luminosity causes a decrease in the main-sequence lifetime following

$$t_{MS} = 8 \times 10^9 \left(\frac{M}{M_O} \right)^{-2.5} \text{yr.} \quad (1.9)$$

Thus the previously mentioned star would have a main-sequence lifetime of $t_{MS} \sim 2.5 \times 10^7 \text{ yr.}$

1.2.4. AGN structure

The AGN is the most powerful and luminous objects known in the universe. Evidence shows quasars as early as redshift $z = 7$, leading to a formation time-scale of the

⁵This section is build upon Léna, Rouan, Lebrun & Pelat 2012 [?] and Schneider 2006 [31]

first AGNs of $t_{AGN} < 0.5 \text{ Gyr}$ (Mo, Bosch & White 2010 [21]). The AGN, being the most powerful astronomical process known, is the cause of a massive energy output throughout its lifetime. Some of the most powerful AGNs known have an energy output, integrated over their entire lifetime, of $E \geq 3 \times 10^{61} \text{ erg}$. Such massive energy outputs can only be generated through nuclear processes or accretion of matter. It is however not feasible for the energy output to be the result of nuclear fusion, as in the stellar core, as this has an efficiency of around 0.007 (Mo, Bosch & White 2010 [21]). This efficiency (ϵ) for converting mass to energy, when applied to Einsteins equation means $E = \epsilon mc^2$ necessitating the mass of a Black Hole fueled by fusion of $2 \times 10^9 M_\odot$ (Schneider 2006 [31]). This far exceeds the upper limit of $150 M_\odot$ observationally determined for the stellar mass for our local universe (Weidner & Kroupa 2004 [37]), as well as following *equation 1.9* it becomes apparent that the expected stellar lifetime would be far too short, making it unfeasible for the AGN to be powered by nuclear fusion. In comparison, however, the accretion process of free-falling material onto a Black Hole devoid of angular momentum has an efficiency of around 0.06 and in the case of the accreting material onto a Black Hole being subject to the maximum rotation allowed the accretion can be as large as 0.29 (Schneider 2006 [31]). Thus it is most feasible for the AGN to be powered through the accretion method, both due to the higher efficiency, and due to the mass, of the AGN, being far higher than any observed, or theorised, stars. This leads to the theory of accretion onto a SMBH with the AGN situated around a SMBH being the accepted theory. In this accretion theory the AGN is powered by gas being accreted onto the central SMBH. The energy originates from the potential energy stored in the accretion disk with respect to the SMBH.

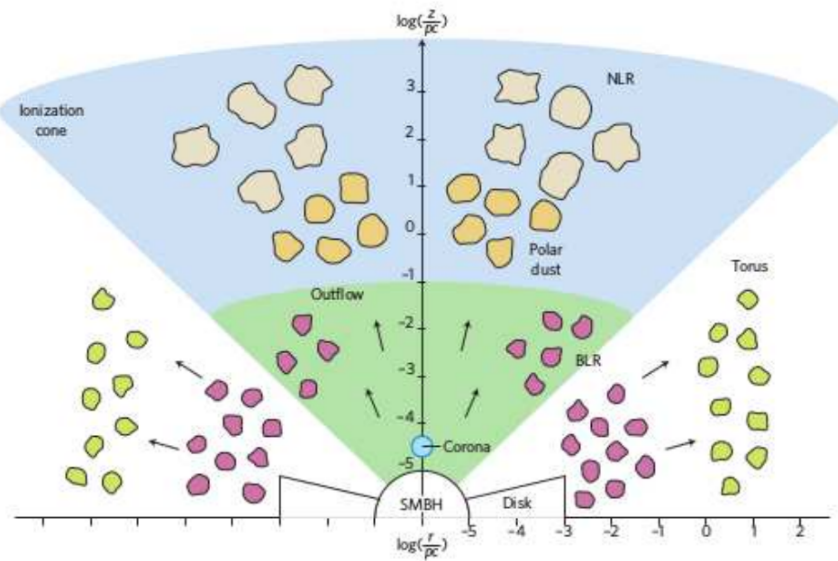


Figure 1: Sketch of the main AGN structures seen along the equatorial and polar direction. From the center to host-galaxy scales: SMBH, accretion disk and corona, BLR, torus and NLR. Different colours indicate different compositions or densities.

Figure 1.1: Almeida & Ricci 2017 [7]

1.2.4.1. The Driving Engine

It is assumed that the energy output from an AGN is generated by accretion onto a Supermassive Black Hole (SMBH), this is generally called the *Supermassive Black Hole Paradigm*. In this model the energy source from the AGN is the potential energy release as material is accreted from the accretion disk onto the SMBH.

1.2.4.1.1 The Black Hole:⁶

In the case of gaseous material surrounding an energy source like a star or AGN, in a spherical geometry, the surrounding material will experience an outward pressure scaling with the luminosity (L) and inversely proportional with the radius (r) squared,

$$P_{rad}(r) = \frac{L}{2\pi r^2 c} \quad (1.10)$$

thus in a region of ionized gas, like the one created by the photo-ionization from stars and AGN, the pressure will exert a force on the gas due to the scattering of photons by electrons given by,

$$\mathbf{F}_{\text{rad}} = \sigma_T P_{rad}(r) n_e(r) \hat{\mathbf{r}} = \frac{\sigma_T L n_e(r)}{2\pi r^2 c} \hat{\mathbf{r}} \quad (1.11)$$

with σ_T being the Thomson scattering cross-section ($\sigma_T = \frac{8\pi}{3} r_0^2$) and $n_e(r)$ the electron density at radius r . Thus, if the cloud surrounding the AGN has to be maintained, it must be assumed that it is held by the gravitational potential of the AGN and thus it must be true that

$$|\mathbf{F}_{\text{rad}}| \leq F_{grav} = \frac{GM_{BH}\rho(r)}{r^2}, \quad (1.12)$$

with G being the gravitational constant, M_{BH} the mass of the Black Hole and $\rho(r)$ the density of the gas. Thus the maximal accretion luminosity that can be reached by this spherical accretion, the Eddington Luminosity (L_{Edd}), can be found to be

$$L_{Edd} \equiv \frac{4\pi G cm_p}{\sigma_T} M_{BH}, \quad (1.13)$$

with m_p being the proton mass. A SMBH does not necessarily accrete at the Eddington Luminosity, thus assuming an *accretion rate* of \dot{M}_{BH} , where the material being accreted crosses a shell at radius r , the AGN luminosity can be calculated as

$$L_{AGN} = \frac{GM_{BH}}{r} \dot{M}_{BH}. \quad (1.14)$$

The Schwarzschild radius, or gravitational radius, of Black Holes (r_S) is given as

$$r_S = \frac{2GM_{BH}}{c^2}, \quad (1.15)$$

⁶This section build heavily on Mo, Bosch & White 2010 [21]

and is the radius at which the escape velocity in the solution to the viral theorem exceeds the speed of light (c). The Schwarzschild radius can be used to determine the efficiency at which accretion occurs, or given the latter the radius at which it occurs

$$\epsilon_r = \frac{L}{\dot{M}_{BH}c^2} = \frac{1}{2} \frac{r_S}{r}. \quad (1.16)$$

Observations indicates that the continuum radiation from AGNs originates primarily from $r \sim 5r_S$. Thus the efficiency at which mass is converted into radiation is around 0.1. Thus it must be concluded that the Black Hole is rotating to induce a higher mass conversion efficiency than the non-rotating Black Hole efficiency of 0.06.

1.2.4.1.2 The Accretion Disk:⁷

Accretion is the process at which material fall onto a compact object, such as a protostar or a Black Hole. During this process the gravitational potential energy of the material is converted into kinetic energy. In the case of unimpeded accretion there will be no release of radiation, as AGNs are some of the most energetically powerful and luminous objects in the universe the accretion cannot be unimpeded. This impediment is provided through the laws governing conservation of angular momentum ($L = I\omega$), as the gas, and other material, orbiting in galaxies, also in the galactic center, has a finite angular momentum, and, as angular momentum is always preserved, free-fall accretion onto the Black Hole is prohibited. Gas particle friction, from the viscosity of the materials, resulting in angular momentum transfer will result in a disk like structure, perpendicular to the direction of the angular momentum. It is possible to view the disk as a series of concentric rings all rotating with approximately the Kepler velocity (equation 1.17)

$$v_{Kepler} = \sqrt{\frac{GM_{BH}}{r}} \quad (1.17)$$

causing friction between them, causing heating of the disk. This heating de-accelerates the gas causing inward motion of the material. This inward motion provides released potential energy, which in turn is the energy observed being radiated away as thermal radiation.

Thus when the mass m in the accretion disk moves from radius $r + \Delta r$ to radius r , the energy generated will be

$$\Delta E_{pot} = \frac{GM_{BH}m}{r + \Delta r} - \frac{GM_{BH}m}{r} \approx -\frac{GM_{BH}m\Delta r}{r^2}. \quad (1.18)$$

Equation 1.18 assumes that the SMBH mass is dominant in the system, as to ignore the self-gravitational potential energy of the accretion disk itself. The viral theorem dictates that half the converted energy generates kinetic energy, and the second half

⁷This section build heavily on Schneider 2006 [31]

can be lost in internal energy. If the energy released is emitted locally in the disk the luminosity release of the disk as a result of mass m moving a radial distance of Δr is

$$\Delta L = \frac{GM_{BH}\dot{M}_{BH}}{2r^2} \Delta r. \quad (1.19)$$

\dot{M}_{BH} is radially independent as to avoid accumulation of material at any given radius, and thus all concentric rings of width Δr experiences a mass flow of \dot{M}_{BH} . In the case of optically thick disks the radiation emitted will become Black Body radiation, thus *equation 1.19* becomes

$$\Delta L = 2 \times 2\pi r \Delta r \sigma_{SB} T^4(r), \quad (1.20)$$

with σ_{SB} denoting the Steffan-Boltzman constant and the factor 2 the double sided nature of a disk. Thus determining the actual temperature of the disk becomes relevant in order to accurately calculate the emitted luminosity. This question is two sided. In the case of $r_S \ll r$

$$T(r) = \left(\frac{3GM_{BH}\dot{M}_{BH}}{8\pi\sigma_{SB}r^3} \right)^{1/4}, \quad (1.21)$$

and in the case of the former condition not being true the temperature is given by

$$T(r) = \left(\frac{3c^6\dot{M}_{BH}}{64\pi\sigma_{SB}G^2} \right)^{1/4} M_{BH}^{-1/2} \left(\frac{r}{r_S} \right)^{-3/4}. \quad (1.22)$$

The disk emission is, due to the temperature increasing $\propto r^{-3/4}$, to a first order approximation a superimposition of concentric black body rings at differing temperatures. Additionally the temperature increases at increased accretion rate, and lowers at more massive black holes. This explains the lack of X-Ray emitted from AGN accretion disks due to thermal radiation, as opposed to X-Ray binaries such as neutron stars and stellar-mass black holes.

1.2.4.2. Broad-Line Region⁸

The Broad-Line Region (BLR) is located in a halo surrounding the accretion disk, and is observable in the optical spectra of Seyfert I galaxies, and in some Quasars, with strong emission lines with velocity width (Δv) of $500 \text{ km s}^{-1} \leq \Delta v \leq 10000 \text{ km/s}$. The observed velocity dispersion of the BLR emission lines could have two origins. Either the velocity dispersion originates through thermal velocity

$$v(T_{gas}) \approx \left(\frac{kT_{gas}}{m_p} \right)^{1/2}, \quad (1.23)$$

or the origin of the observed broadening of emission lines is attributed to the rotational motion of the gas in the BLR

$$v_{rot} \approx \sqrt{\frac{GM_{BH}}{r}} = \frac{c}{\sqrt{2}} \sqrt{\frac{r_S}{r}}, \quad (1.24)$$

⁸Unless otherwise referenced this section build heavily upon Bianchi, Maiolino & Risaliti *AGN Obscuration and the Unified Model* 2012, Schneider 2006 [31], Peterson 1997 and Mo, Bosch & White 2010 [21].

thus becoming Doppler Broadening. In order to obtain such velocity dispersion from the temperature of the gas in the BLR, a gas temperature of the order 10^{10} K would become necessary. This is not the case, as at this temperature all atoms would be fully ionized, eliminating all emission lines, as well as the lack of the elimination of the 511 KeV line in Gamma radiation, which would result from the plasma generated e^+e^- -pairs at such temperatures (Schneider 2006 [31]). Thus the velocity dispersion is Doppler Broadening of the emission lines, as a result of the rotational motion of the gas in the BLR, and thus a different method of estimating the gas temperature must be considered. The observed Doppler Broadening would be attainable at radii of $r \sim 1000r_S$ (Schneider 2006 [31]).

Despite the difficulty in determining the gas temperature originating in the BLR, due to electron densities being sufficiently large as to collisionally suppress almost all forbidden line emissions, the relative line intensities of ionized gases indicates a temperature of order 10^4 K, corresponding to a velocity dispersion of $\approx 10 \text{ kms}^{-1}$, leading further credence to the theory that the velocity dispersion is due to the Doppler Broadening.

The large Doppler broadening of the line observed in the BLR causes many of the normally observable features of a spectrum to become blended, and some features can become unresolved in the obtained AGN spectra. It is important to note that the emission lines varies with time dependent of the comparable variations in the continuum flux indicating a photoionization in the BLR driven by the central source (the SMBH).

The gas density of the BLR can be estimated through the observed emission lines. While the forbidden transitions are all collisionally suppressed in the BLR, allowed and semi-forbidden lines are not. The distinction between allowed, forbidden and semi-forbidden emission lines are done by basis of quantum mechanical transitional probability, and thus the distinction can be used to predict the probability of de-excitation being through spontaneous emission rather than through collisional energy loss. Allowed transitions has high transitional probabilities, and thus short lifetimes (of order $t \lesssim 10^{-8}\text{s}$), thus reducing the chance of collisional suppression. Forbidden transitions by comparison have lifetimes typically around 1s, with the semi-forbidden ones being somewhere between the two. Examples of allowed transitions observed in the BLR spectrum are $Ly\alpha$, Mg_{II} and C_{IV} , with semi-forbidden ones being C_{III}] and N_{IV} . The *mean free path* (λ) and thus the *mean travel time* (τ_t) of an ideal gas can be described through the gas radius (d), Avogadro's number (N_A), the temperature (T), the gas constant (R) and the gas pressure (P) and is given by⁹

$$\lambda = \frac{RT}{\sqrt{(2)\pi d^2 N_A P}}. \quad (1.25)$$

⁹<http://hyperphysics.phy-astr.gsu.edu/hbase/Kinetic/menfre.html>

Thus it can be concluded that the chance for collisional de-excitation is dependent on the physical conditions in the gas, while radiational transitions are dependent on the atomic parameters, and thus a well known quantity. Thus the lack of forbidden emission lines are indicative of the lower bound on the gas density, such as the $[O_{III}]$ $\lambda 4363$, $\lambda 4959$ and $\lambda 5007$ transitions that is usually strong in ionized gases, but is suppressed at electron densities exceeding $10^8 cm^{-3}$. Additionally the presence of the semi-forbidden lines can be utilised for estimation of the upper bounds for the gas densities. In Schneider 2006 [31] the estimate of the electron density in the BLR gas is estimated at $n_e \sim 3 \times 10^9 cm^{-3}$ based upon $[O_{III}]$ and C_{III} lines. Further, the total number of emitted line photons can be measured using the AGN distance and the observed line strength. These calculations allows for determination of the total emitting volume from the BLR, and thus the BLR gas filling factor of 10^{-7} . This indicated the BLR gas is concentrated in clouds of gas (Schneider 2006 [31]).

Observations comparing the continuum radiation of the central engine, and the BLR line emission flux indicates a fraction of 0.1 of the AGN energy is being absorbed by the BLR. Thus it must be concluded that the total surface area of the BLR clouds, as they are optically thick, spans 10% of the solid angle of the AGN. From this, combined with the filling factor it is found that there are of order 10^{10} clouds in the AGN with a typical size of $\sim 10^{11} cm$ (Schneider 2006 [31]).

This project occupies itself with the reverberation mapping of the AGN, although not the BLR itself. Reverberation mapping of the BLR occupies itself with determining the structure of the BLR by observing the BLR response to continuum variations. As the AGN driving function varies it must be assumed that the physical conditions in the BLR exhibits comparable variations. The reverberation mapping attempts to determine the transfer functions governing the delay between the UV-driving function variations of the AGN and the BLR response, which is governed by the light travel-time effects within the BLR ($\tau = r/c$). The strength of the reverberation mapping technique is its ability to work independently of assumed BLR geometry and infer the geometry through the BLR response to continuum variations. The reverberation mapping techniques is based upon a series of assumptions as described by Peterson (1993).

1. The Continuum emission originates at a single compact and central source. Thus follows the SMBH model of the AGN.
2. The BLR has a small filling factor (the majority of the volume attributed to the BLR is a vacuum), hence photons are able to propagate freely inside the BLR. This seems to be supported by the low *filling factor* of the BLR, and no evidence of is observed for an Inter-Cloud Medium scattering the wave fronts.
3. There is a simple relationship between the ionizing continuum and the observable UV/optical continuum flux.
4. The light travel-time $\tau_{LT} = r/c$ across the BLR is the most important time scale.

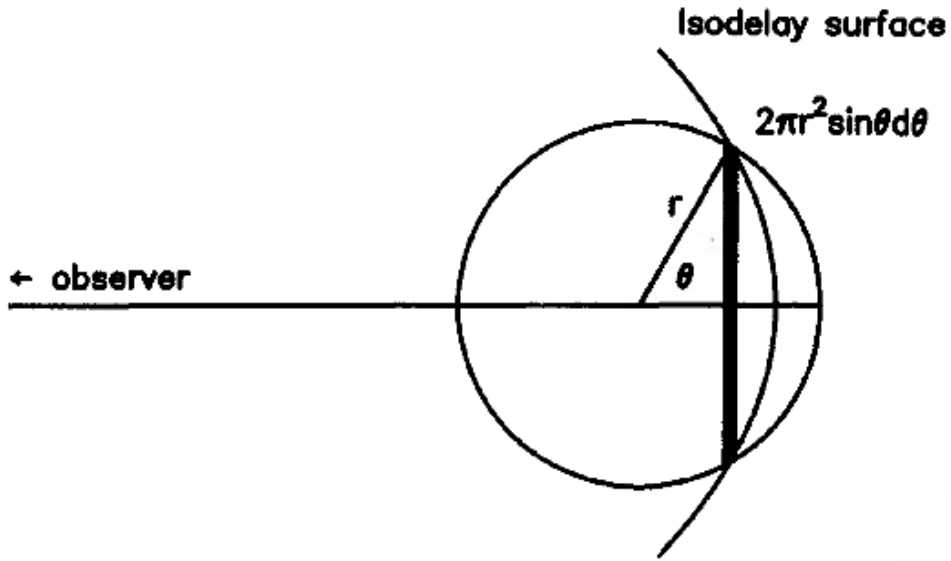


FIG. 2—The intersection between a thin spherical shell BLR and an arbitrary isodelay surface whose locus is specified by $\tau = (1 + \cos \theta)r/c$. At delay τ , the observer (to the left at infinity) sees response to the continuum flux at time $\tau=0$ from clouds within the instantaneous area of intersection $2\pi r^2 \sin \theta d\theta$.

Figure 1.2: Figure and text from Peterson 1993 [25].

- (a) The BLR variations as response to the continuum variations is short compared to τ_{LT}
- (b) Significant geometrical changes to the BLR (dynamical time scale) happens over significantly larger time scales than the τ_{LT} , τ_{dyn} can be estimated as the time taken for cloud of gas to cross the BLR; $\tau_{dyn} = r/\Delta v_{FWHM}$
- (c) τ_{rec} , the time scale for the cloud to reprocess ionizing radiation, is virtually instantaneous

The observed light from the BLR at any given time (t) is the sum of the light emitted from all the isodelay surfaces in the BLR, with all parts of the sum being each surface reaction to the continuum level at different points in the past. If the BLR is assumed to be a thin spherical shell of radius r , with θ being the angle between the line-of-sight to the central source and a vector to a given point on the BLR shell, then this given iso-delay surface has a intersection ring of radius $rsin\theta$ and area $2\pi r^2 sin\theta d\theta$ (figure 1.2). If we assume that the *responsivity* (ϵ) of all clouds are constant, the response to driving function variations can be written as a function of θ by (Peterson 1993 [25])

$$\Psi(\theta)d\theta = 2\pi\epsilon r^2 sin\theta d\theta. \quad (1.26)$$

Thus any clouds on this iso-delay surface is observed with delay

$$\tau = (1 + \cos\theta)r/c, \quad (1.27)$$

thus following

$$d\tau = -r/c \times \sin\theta d\theta. \quad (1.28)$$

This allows the line response and thus the transfer function ($\Psi(\tau)$) to be determined as

$$\Psi(\tau)d\tau = \Psi(\theta) \left| \frac{d\theta}{d\tau} \right| = 2\pi\epsilon r c d\tau. \quad (1.29)$$

In the case of the thin BLR shell described the transfer function will be constant and non-zero between $\tau = 0$ at $\theta = 180^\circ$ and $\tau = 2r/c$ at $\theta = 0^\circ$ (Peterson 1993 and Peterson 1997). The actuality is that the BLR is vastly more complicated. It is probably better represented by continuous concentric circles of iso-delay surfaces, none of which are covered along the entirety of the shell due to the low *filling factor*. Thus the reverberation mapping analysis of the BLR can be utilised to estimate the mass of the SMBH (M_{SMBH}), due to the accurate size estimations, originating from the reverberation mapping techniques, combined with the *characteristic velocity dispersion* obtained through spectroscopic analysis (Schneider 2006 [31]).

The BLR, as previously discussed, owes its ionization and heating variations to the varying central continuum source of the AGN. As the central source luminosity varies in the AGN, so should the BLR emission line fluxes and physical conditions. The physical size of the BLR is finite and as such the BLR response to changes in the X-RAY-continuum will be delayed. This delay is examined using *Reverberation mapping*. The delay Δt of the BLR response correspond to the *light travel time* across the BLR (r/c). Thus it becomes possible to measure the physical extend of the BLR based upon the delay in the response function, allowing the analysis of the individual *iso-delay surfaces* of the BLR. Additionally in spectroscopic analysis it becomes possible to identify the delay caused in different line transitions and thus the possibility of analysing different parts of the BLR, given sufficient resolution (Schneider 2006 [31]).

The BLR appears to scale with the luminosity of the AGN, much like would be expected in the assumption that the outer edge of the BLR and inner edge of the durst torus is defined by the sublimation radius, and thus depending on the energy output by the AGN. Additionally reverberation mapping indicates a varying ionization structure of the BLR as a function of the distance from the central AGN. Thus it appears the higher the ionization energy required by a transition, the smaller the radius, thus construing the BLR as an inhomogeneous region of the AGN. This is exemplified by the NGC5548 AGN (not investigated by this project) with a delay of $\Delta t \sim 12$ d for the $Ly\alpha$ -transition and 26 d and 50 d for C_{III}] and Mg_{II} respectively. This is found through both the use of reverberation mapping, and cooperated by the Doppler broadening of the various lines, with high energy lines being broader. Thus it must be concluded through existing reverberation mapping investigations of observed

AGNs that an inhomogeneous BLR is present, spanning a large radius (r) comprised of different "layers", as demonstrated by the radial dependence of ionizing transitions in the BLR (Schneider 2006 [31]).

1.2.4.3. Reverberation Mapping¹⁰

The sub-parsec scale structure of AGNs, driving engine, accretion disk and BLR, are unresolved even in the closest AGNs and as such reverberation mapping becomes a vital, and time consuming, tool in AGN investigations (Fausnaugh et al. 2017). It is the only tool available that allows the study of the central engine of the AGN, irrespective of the telescopic spatial resolution. It utilises spectroscopic, and photometric, observations to determine the light travel time between different components of the AGN (Nuñez, Chelouche & Kaspi 2018). Previously BLR reverberation mapping, for a highly simplified BLR model, was discussed, however the usefulness of this method spans further than the BLR. In this project the reverberation mapping will focus on the dust torus as well as the accretion disk.

Reverberation mapping can be used, as already discussed, to determine the time delay between the hot continuum radiation of the accretion disk, and the broad-emission lines of the BLR or the dust torus. It is however an additional possibility to utilise this approach to map the accretion disk itself. The time delays in the different observed bands of the accretion disk can be used to determine the light-travel time (τ_{AD}) across the adccretion disk, thus providing information regarding the size, and temperature of the disk (Nuñez, Chelouche & Kaspi 2018).

As the standard geometrically thin, optically thick, accretion disk theory has a $T \propto r^{-3/4}$ temperature, radius relation, it follows that the Black Body emission is highly spatially dependent. The inner, hot, parts of the accretion disk radiate UV emission in the range $\sim 10 - 3,000 \text{ \AA}$, whereas the outer parts are emitting in the optical and IR spectrum of $\sim 3,000 - 10,000 \text{ \AA}$. As the X-RAY emission from the corona, irradiating the disk, undergoes variations, the disk radiation must respond to the changed physical conditions. It must then be expected that a time delay, corresponding to the disk size, can be observed between the UV- and IR-emission (Fausnaugh et al. 2017 and Krolik et al. 1991).

The results from Fausnaugh et al. 2017 (*figure 1.3*) indicates that the that the $T \propto r^{-3/4}$ may not be entirely accurate, and these results suggests a temperature profile of $T \propto r^{-1}$ may indeed be more accurate. This shows the importance of the reverberation mapping technique, in the ability to infer the disk structure without the capability to resolve the disk itself. The difficulty in reverberation mapping is the time scale of AGN variations. The variations occurring in the AGN luminosity happens over periods spanning from months to years, and as such any level of Reverberation mapping

¹⁰Schneider 2006 [31] is used for additional information.

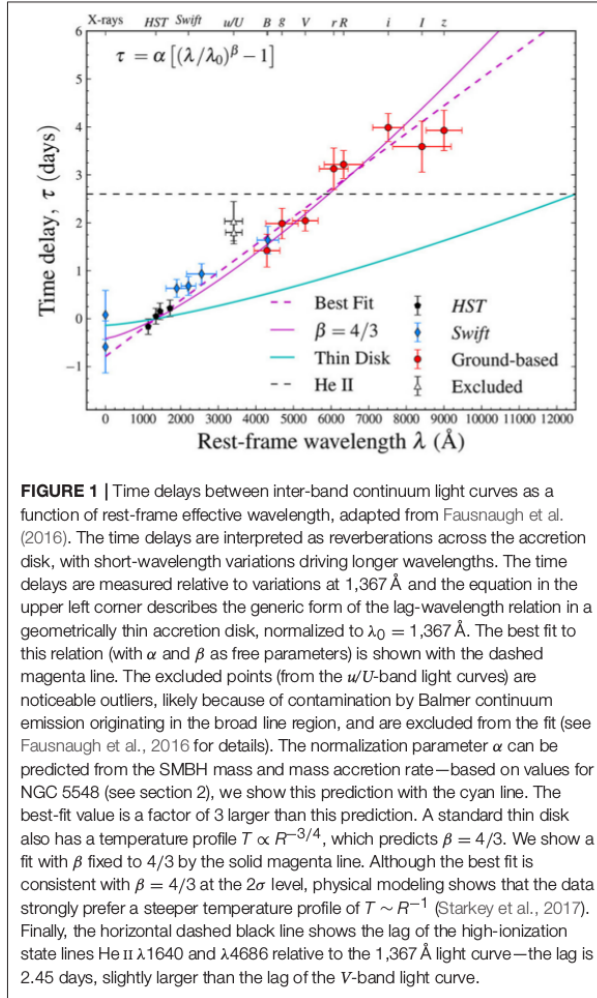


Figure 1.3: Image and text from Fausnaugh et al. 2017 and references therein

investigation must be based upon data collected over a period of years.

In this project the reverberation mapping is utilised in an additional attempt to estimate and model the X-RAY driving function. This is done in an attempt to compensate for significantly more sparse sampling than that traditionally used.

1.2.4.4. Narrow-Line Region

The Narrow-Line Region (NLR) are the largest spacial scale at which the ionizing radiation from the central engine is dominant as compared to other sources (Peterson 1997). This region in the Seyfert Galaxies extends from $\sim 10pc$ up to $\sim 1kpc$ (Almeida & Ricci 2017 [7]), and thus exists on sufficiently extended spatial scales as to allow the physical and kinematic distribution to be mapped out to some extend (Mo, Bosch & White 2010 [21]). Additionally the NLR position outside the sublimation radius, and thus outside the *Torus* (section 1.2.4.5), leads to the observed collimation of the NLR into the bi-conical shapes that are known as ionization cones (Almeida & Ricci

2017 [7]). The NLR spectrum as opposed to the BLR spectrum contains emission lines from forbidden interactions, thus allowing the conclusion that the electron density is significantly lower and therefore not collisionally suppressing the forbidden interactions. The forbidden line emission from the NLR is isotropic, due to the low chance of self-absorption of forbidden emission lines. Thusly it becomes possible to utilise the intensities of forbidden lines to determine physical properties of the NLR such as the temperatures and electron densities. An additional key difference between the BLR and NLR is the precense of dust in the latter, thus one can infer that the NLR is located outside the dust sublimation radius (Peterson 1997).

The physical conditions in the NLR can be inferred from the observed emission lines. Two key observable that it is possible to constrain well in the NLR as opposed to the BLR is the electron density and the electron temperature. In both cases emission lines originating from forbidden transitions from the same ion, to prevent bias in the result originating from the chemical composition of the NLR, is compared.

1. The electron densities are constrained using the forbidden transitions generating the $[OII]\lambda\lambda 3726, 3729$ and the $[SII]\lambda\lambda 6716, 6731$ emission lines. It is important in the constrain on the electron densities to utilise emission lines of comparable energy requirements, so as to minimize the temperature impact. The $[OII]$ emission lines are rarely used in this respect however, due to the high degree of overlapping due to Doppler broadening. The electron density is given by *equations 1.30-1.32*. The emissivity in an emission line can be given as

$$j_{21} = n_2 A_{21} \frac{hv_{21}}{4\pi}, \quad (1.30)$$

with n_2 being the number density af atoms at the $n=2$ state, A_{21} the Einstein coefficient, j_{21} is the emissivity in the line and hv_{21} the transition photon energy. In the case of a statistical equilibrium in the region the net line emission (through spontaneous emission) must be in balance with the rate of collisional excitation ($\langle\sigma_{12}v\rangle$) and collisional de-excitation ($\langle\sigma_{21}v\rangle$), with σ being the *velocity-dependent cross-section* and v the *velocity*. Thus the balance becomes

$$\langle\sigma_{12}v\rangle n_e n_1 = n_2 A_{21} + \langle\sigma_{21}v\rangle n_e n_2, \quad (1.31)$$

with n_e being the electron density. Thus *equation 1.31* can be solved for n_2 and combined with *equation 1.30*

$$j_{21} = n_e n_1 \langle\sigma_{12}v\rangle \frac{A_{21}}{A_{21} + n_e \langle\sigma_{21}v\rangle} \frac{hv_{21}}{4\pi}. \quad (1.32)$$

It is then possible to solve for the electron density (Peterson 1997).

2. The NLR electron temperature is determined by comparing emission lines from forbidden transitions from same ions at different exitation potentials (χ), leading

to the relative intensities being highly temperature dependent. Often used emission lines are $[OIII]\lambda\lambda 4363, 4959, 5007$ and $[NII]\lambda\lambda 5755, 6548, 6583$ although the $[NII]\lambda 5755$ relatively weak and therefore sub-optimal. The temperature is determined using *equation 1.33* (Peterson 1997).

$$\frac{F(\lambda 4959 + \lambda 5007)}{F(\lambda 4363)} = \frac{7.33e^{3.29 \times 10^4/T_e}}{1 + 4.4 \times 10^{-4}n_e T_e^{-1/2}} \quad (1.33)$$

Utilising the emission lines originating from forbidden transitions in the NLR typical values for the electron density and temperature is found to be; $10^2 cm^{-3} < n_e < 10^4 cm^{-3}$ with the average value around $2000 cm^{-3}$ and the temperature is found to be between 10,000 and 25,000 K and typically around 16,000 K (Peterson 1997, Schneider 2006 [31] and Mo, Bosch & White 2010 [21]).

The NLR gains its name due to the *Full Width Half Maximum* of the emission lines in the region of $200 \leq v_{FWHM} \leq 900 km s^{-1}$ (Peterson 1997), that despite indicating significantly broader characteristic velocities than normal galaxies, is still significantly narrower than those found in the BLR (Schneider 2006 [31]).

The NLR does not lend itself to reverberation mapping analysis, as it due to its vast spatial scale does not undergo variations on an observable time-scale. The NLR however can be spatially resolved and therefore indirect observational techniques becomes less vital (Schneider 2006 [31]).

1.2.4.5. Dust Torus

Evidence of the existence of an obscuring toroidal structure surrounding the central engine, called the *Torus*, was originally achieved through spectropolarimetric observations of Type II Seyfert galaxies. In these investigations it was noted that it was possible to detect BLR emission in polarized light from the AGN hidden in light being reflected by material located along the axial line of the AGN. Thus the early evidence of the Torus was not direct observations of the Torus itself, rather it was the obscuring effect of the Torus leading to the detection (Nenkova, Ivezić & Elitzur 2002 [22] and Almeida & Ricci 2017 [7]).

The Torus is powered by the emission from the AGN accretion disk by absorbing and re-emitting the energy released in the accretion disk. The temperature in the Torus is dependent on the distance to the center of the AGN in question, as the Torus temperature varies from 100 K up to the sublimation temperature (T_{sub}), thus the inner wall of the Torus is at the sublimation radius (R_{sub}), and thus it is possible from the thermal lag in the AGN spectrum to infer the sublimation radius. Hönig & Kishimoto (2010) [17] estimates the relationship between the radius and temperature in the Torus (*equation 1.34*)

$$\frac{r}{r_{sub}} = \left(\frac{T}{T_{sub}} \right)^{-2...-2.8} \quad (1.34)$$

Understanding of the Torus and its obscuring effect on observed AGNs are important due to the significant altering effect it has on the observed characteristics of the AGN. The Torus obscure, given the right inclination angle, of the AGN both the Driving function (X-Ray and UV-radiation) and the BLR radiation, and thus understanding of the components and composition of the Torus becomes of importance in the attempt to understand the AGN phenomena. It is possible from the observations of the Dusty Torus to conclude that the Torus must be both optically and geometrically thick, additionally Type II Seyfert Galaxies with their Dusty Torus' usually reveal the existence of hight column densities of Hydrogen. The observed column densities of Hydrogen appear to be ranging from $\sim 10^{23} - 10^{25} \text{ cm}^{-2}$. It is generally assumed that the high column densities of Hydrogen originates in the Torus, thus indicating a gaseous component of the Torus that dominates in mass (Hönig and Kishimoto, 2010).

Mid-IR, imaging and Interferometry, and more recently sub-millimeter observations, has constrained the Torus to a size of $0.1 - 10 \text{ pc}$. Radio observations of the toroidal structure also infer, through the 22 GHz maser line, the presence of the *maser disk* (discussed briefly in *section 1.1.1*) in this region. It is generally assumed that the maser disk spacial distribution is overlapping the Torus itself (Almeida & Ricci 2017 [7]). The Torus is of interest, in this project, due to the possibility of the AGN Torus to be used as a *standard ruler*, like the maser disk in non-AGN galaxies, thus providing a possible avenue for additional investigations into the Hubble constant. The benefit of the Torus in the constraining of the Hubble constant is the luminous nature of the AGN combined with the possibility for precision determination of the spacial scale due to reverberation mapping, that is allowed due to the dependence of the torus luminosity on the accretion disk variations.

The Torus does not equally obscure all observed AGN due to the geometrical distribution of the phenomena. The fraction of Type II seyfert Galaxies compared to Type I Seyfert Galaxies can be represented through the Geometrical Covering Factor of the Torus, denoted as f_2 (defined in *equation 1.35*),

$$f_2 = 1 - \int_0^{\pi/2} P_{esc}(\beta) \cos(\beta) d\beta \quad (1.35)$$

with $P_{esc}(\beta)$ being the probability that AGN emitted light will escape unhindered at an angle β from the equatorial plane of the torus (Mateos et al. 2018),

$$P_{esc}(\beta) = e^{-N_0 \times e^{-\beta^2/\sigma^2}} \quad (1.36)$$

with N_0 being the mean number of clouds along the equatorial direction and σ being the angular width of the Torus.

1.2.4.6. Unification Theory¹¹

The unification theory (*figure 1.1*) aims at providing a singular explanation for the AGN phenomena by attributing the observed differences of the AGN types to the conditions of the observation, as opposed to intrinsic differences between the observed AGN phenomena. The unification theory predicts the AGN symmetry to be much like galaxies and solar systems not spherical, but rather axisymmetric systems. This allows for differences in the observational results to occur based upon the inclination angle of the system being observed.

Observational analysis of observed Type I and Type II AGN demonstrates uncanny similarities considering they should be different astrophysical phenomena. Despite the apparent lack of a BLR in Type II Seyfert Galaxies both Seyfert types has strong high- and low ionization narrow lines, such as O_{III} , N_{III} , O_{II} , O_I , N_{II} and S_{II} , as well as high ionization corona lines (Fe_X , Fe_{XI} , Si_{IX} and Si_{IX}). These common emission lines further demonstrates strong similarities, between Seyfert I and Seyfert II galaxies, in the observed line ratios in the Narrow- and Corona emission lines.

The Unification Theory assumes the AGN being powered by a central SMBH of order $10^6 - 10^{10} M_\odot$ that is surrounded by an accretion disk. Surrounding the accretion disk is a region of hot, fast-moving dense gas, the so called BLR discussed earlier. In Type I Seyfert Galaxies this BLR is the cause of a significant amount of the observed Luminosity. In the Unification World view the BLR is photoionized by UV radiation from the central engine, the SMBH accreting from the accretion disk, and thusly the BLR emission lines changes intesity following changes in the UV continuum.

Surrounding the BLR is a dusty region with the inner radius being the sublimation radius from the SMBH. This is also the region called the Torus. This dusty region reprocesses the UV continuum emission and emits the energy in the IR regime. Further out is the Narrow line region comprised of cool and low density gas. In this region the velocity caused by the gravitational rotational motion is of the order $10^2 km s^{-1}$ and is located at pc scale distances from the central engine of the AGN.

Thus it is possible under the Unification Theorem to represent Seyfert I and Seyfert II galaxies as being fundamentally identical, with the main difference being the inclination angle of the host galaxies, and thus in Seyfert II Galaxies the BLR is only not observed due to the energy being blocked by the orientation of the Torus. Additionally it would then stand to reason that Quasars are either Seyfert Galaxies with sufficiently bright AGNs as to overshadow the host galaxy, or sufficiently distant as to have the Luminosity from the host galaxy being undetectable or a combination of the two.

The Unification Theory originates in the attempt to explain the observed differences in what appears observationally to be two distinctly different types of Seyfert Galaxies.

¹¹Unless specified otherwise the information in this section relies heavily on Peterson 1997, and Bianchi, Maiolino & Risaliti 2012 *AGN Obscuration and the Unified Model* [9]

The main observationally differences between the two are the seeming lack of broad emission lines in Seyfert II Galaxies and the AGN continuum appears weaker in Seyfert II Galaxies. A logical assumption, if one assumes they are not intrinsically different phenomena, is that in the Type II case one observes the phenomena through a attenuating medium responsible for the partial or complete extinguishen of the BLR lines and UV continuum. This extinguishing medium has to operate over a broad wavelength range, and as such dust is the most fitting theory as well as block 3/4 of the sky as seen from the Central Engine, as this is the fraction of observable Type II to Type I Seyfert Galaxies. Some of the major questions to be answered is;

1. Why does the Seyfert II continuum appear to be a power law, much like the Seyfert I continuum, if it is reddened it would no longer be a power law?
2. Why is Seyfert II galaxies only one order of magnitude fainter than their Seyfert I counterparts, despite the BLR lines being completely suppressed in the spectrum?

Chapter 2

Absolute Flux and Absolute Magnitude

Identifying the absolute magnitude and flux of the observed AGN's necessitates the use of observed standard stars. Structure function observations made by Vries et al. 2004 shows the stellar Structure Functions to be flat, whereas AGN Structure Functions show a significant slope. This fits the known characteristics of stellar flux of being constant over long time-scales. This quality of stellar flux can be utilised in determining the absolute flux, and magnitudes of observed variable sources.

Ground based astronomical observations does not demonstrate a constant observed flux on stellar objects as they are heavily influenced by various noise parameters associated with the earth atmosphere. This section will cover these noise parameters associated with the earth atmosphere, and describe the solution utilised in this project.

2.1. EARTH ATMOSPHERE AND ASSOCIATED UNCERTAINTIES¹

The atmosphere of earth consists of different layers of varying temperature. These layers all have different impact upon the observations made. The different layers of the atmosphere is shown in (FIGURE 2.1 FROM OBS. AST. BOOK) and the temperature, altitude and pressure relations in (FIGURE 2.2 FROM OBS. AST. BOOK).

Astronomic observations can be influenced by the earth atmosphere by either *total* or *partial* absorption. In the case of *partial*-absorption the atmosphere through which the observations are carried out alters the spectra of the observed sources. These changes are caused by *telluric absorption bands* that can be identified, to avoid misinterpreting the spectra obtained. In the case of *total*-absorption it is possible to determine *transmission windows* at any relevant altitude, and thus identify the altitude at which observations becomes impossible and thus the optical placement of the telescope based upon the local *transmission windows* and the local *partial*-absorption. This project is not interested in the process behind the location of the relevant telescope. It is however necessary to understand the importance of the noise generated by the local conditions.

¹This section builds heavily on Léna, Lebrun & Pelat, Observational Astrophysics, Third Edition.

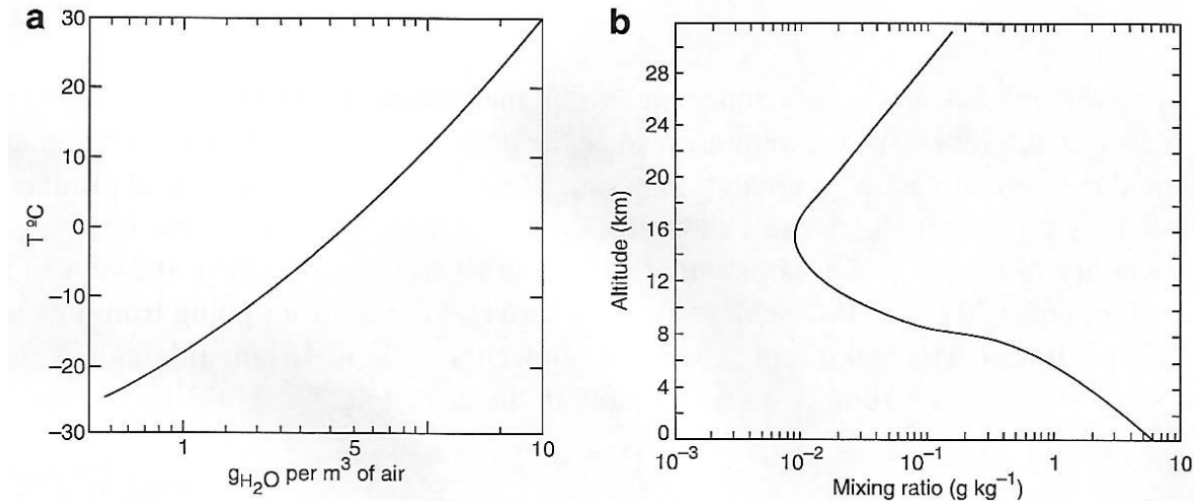


Fig. 2.3 (a) Mass concentration of water vapour in saturated air, at normal pressure, as a function of temperature. (b) Mixing ratio $r(z)$ of water vapour in air as a function of altitude for an average atmosphere. $r(z)$ is measured in g kg^{-1} , so that it is close to unity for the most frequently encountered meteorological conditions near ground level

Figure 2.1: Copy from Léna, Lebrun & Pelat [?], *Observational Astrophysics, Third Edition*.

In figure 2.5 and 2.6 atmospheric weather data for two nights are shown. These nights differs significantly in the air humidity and cloud coverage, and the changes in same over the course of the night.

The Earth atmosphere is composed of several gases that influences the observed spectra of astronomical objects from ground based observations. The absorption spectra of several of these gases are demonstrated in figure 2.3.

2.1.0.0.1 Water Vapour:

Water vapour in the atmosphere is highly dependent of altitude and local geographics. It is as shown in figure 2.3 the cause for absorption over a great range of wavelenghts. The water vapour can be described by either the *humidity*, being the expression of the amount of water vapour as compared to the maximum possible water vapour at a given volume at the relevant temperature, or the *mixing ratio*. The *mixing ratio* is an expression of the mass of water vapour in 1kg of air (equation 2.1) and is altitude dependent,

$$r = \frac{m_{H_2O}}{m_{air}} \quad (2.1)$$

with r being the mixing ratio, that can vary between 0 and $r_s(T)$, the latter being the saturation mixing ratio, varying by altitude and temperature as shown in figure 2.1.

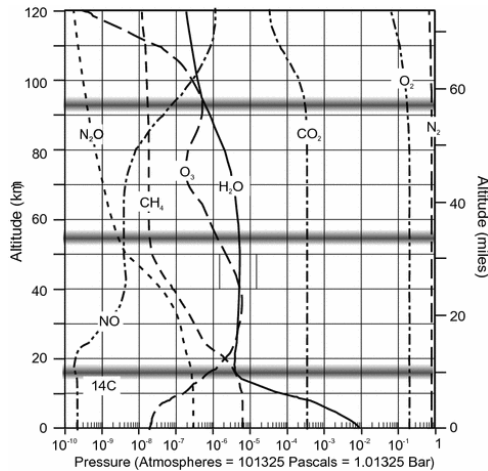


Figure 2.2: The contribution to the atmospheric pressure from various atmospheric gases.

Copy from Hay W.W. (2013) *The Atmosphere*. In: *Experimenting on a Small Planet*. Springer, Berlin, Heidelberg.

It is thus possible to determine the column density of water vapour in the atmosphere through equation 2.2,

$$h_{H_2O}[cm] = \rho_0[g cm^{-3}] \int_{z_0}^{\infty} r(z) e^{-z/H} dz, \quad (2.2)$$

with z being the altitude, ρ_0 being the density at $z = 0$ and H being the scale height.

Water vapour absorption arise from both *pure rotational molecular transitions* and *electronic molecular transitions* and this, combined with its distribution throughout the atmosphere, causes the varied absorption seen in figure 2.3.

2.1.0.0.2 Ozone:

The Ozone layer absorbs mainly in the ultraviolet range ($\lambda < 300nm$) and is a very significant absorber in a narrow range of absorption as shown in figure 2.3. The highest concentration of ozone is at an altitude of $\sim 16 km$, as such it cannot be avoided in ground based observations. Ozone absorbs by *pure rotational molecular transitions* and *electronic molecular transitions*. The contribution towards the ozone pressure can be seen in figure 2.2.

2.1.0.0.3 CO₂:

With a constant mixing ration, independent of altitude (figure 2.2.), CO₂ is an important source of infrared absorption, particularly mid-IR, in the atmosphere. CO₂

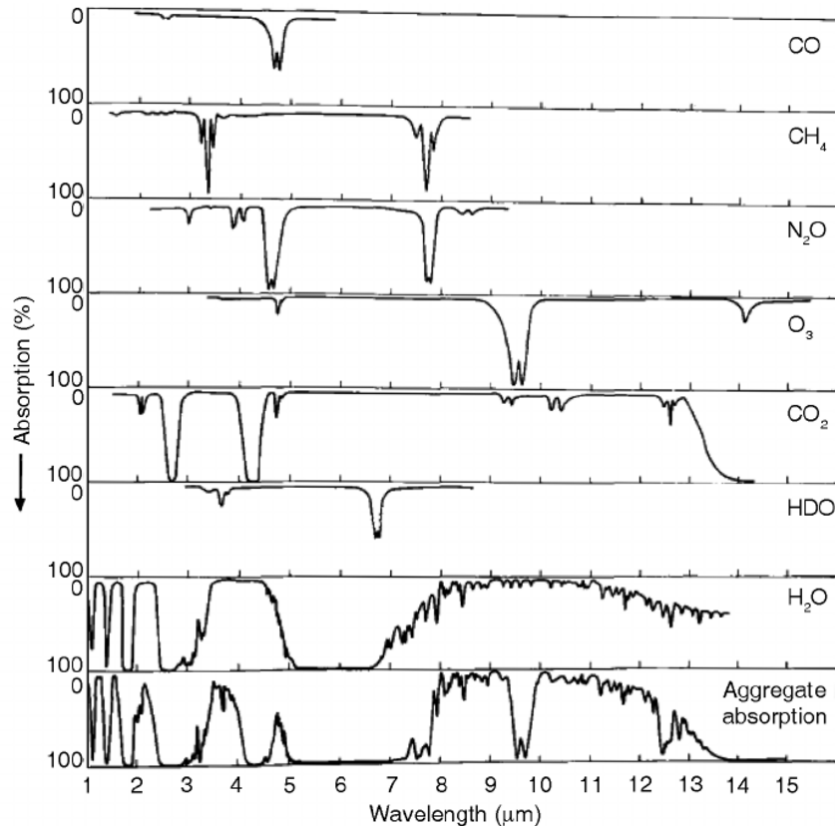


Figure 2.3: The absorption features of various absorbing gases in the Earth atmosphere. Brunetti and Prodi 2015 [11]

absorbs through *pure rotational molecular transitions* and *rotational-vibrational molecular transitions*

2.2. MAGNITUDES AND FLUXES:²

The magnitude scale is a logarithmic flux scale utilised to compare luminosities between separate astronomical objects. It was implemented prior to the invention of precision measurement tools utilised for accurate flux measurements. The logarithmic nature of this scale originates in the human eye, as the human eye ability to identify differing light intensities is not linear, rather it scales roughly logarithmically.

2.2.1. Apparent magnitude:

The original measuring scale was based upon the observed differences between astronomical object, independent on distance and is called *apparent magnitude*. The magnitude scale is for historical purposes, due to the inherent historical difficulty in observing outside the optical spectrum, only used in optical astronomy. It has however

²This section builds heavily on Schneider 2006 [31]

Table 2.1: The differences between the AB zero magnitudes and the Vega zero magnitudes in the filters used by this project.³

Filter	$m_{AB} - m_{Vega}$
g	-0.08
r	0.16
i	0.37
z	0.54
J	0.91
H	1.39
K_s	1.85

been modified with a more precise modern definition (*equation 2.3*)

$$m_1 - m_2 = -2.5 \log\left(\frac{F_1}{F_2}\right), \quad (2.3)$$

with m_1 and m_2 being the *apparent magnitudes* of the astronomical objects 1 and 2 and F_1 and F_2 the fluxes of same. The constant 2.5 is chosen as to achieve the closest agreement between the historically based visual magnitudes and the modern precision based magnitude system.

As demonstrated in *figure 2.3* the flux observed in ground based observations are heavily influenced by the wavelengths bands chosen for observation as well as the differing energy spectral distributions vary between objects. As such a series of filters are designed with magnitudes defined for all relevant observational filters. In this project the filters of note are the SDSS filters g, r, i , and z and the Johnson-Cousins filters J, H and K as shown in *figure 2.4*.

Magnitudes are thus filter dependent and the denotation for the magnitude in filter K is $m_K = K$. In order to determine the relationship between the magnitudes measured in different filters, and have a comparison table between astronomical objects a zero magnitude star is chosen, the type A0 star with Vega as the normal example. In this Vega system $U = B = V = R = I = J = H = K\dots = 0$. The alternative to the Vega system is the AB system for apparent magnitudes. In this system it is assumed that the zero magnitude definition for all filters is not the SED of an actual star, but rather the constant flux in all bands of $F = 2.89 \times 10^{-21} \text{ erg s}^{-1} \text{ cm}^{-2} \text{ Hz}^{-1}$. The conversion between AB and Vega magnitudes are demonstrated in *table 2.1*.

2.2.2. Absolute magnitude:

The apparent magnitude discussed so far is an interpretation of the strength of the flux observed, and not a representation of the luminosities of the objects observed.

The apparent magnitude does not consider the distance (D) of the observed objects. To overcome this short-coming the absolute magnitude is used. For an isotropically emitting source of distance D and luminosity L the flux F is found by *equation 2.4*

$$F = \frac{L}{4\pi D}. \quad (2.4)$$

In the same manner that the *apparent magnitude* (m) is an interpretation of the observed flux F , the *absolute magnitude* (M) becomes an expression for the luminosity L . The absolute magnitude is defined to be the apparent magnitude in the case of the emitter being located at a distance of 10 pc and the relationship is given by *equation 2.5*

$$m - M = 5\log\left(\frac{D}{1 \text{ pc}}\right) - 5 \equiv \mu, \quad (2.5)$$

with μ being the *distance modulus*, and thus a logarithmic measure of the distance to the source.

Bolometric magnitudes:

The *apparent bolometric magnitude* (m_{bol}) is the magnitude of a light emitting source calculated from the flux integrated over all wavelengths

$$m_{bol} = -2.5\log(F) + \text{const.}, \quad (2.6)$$

with the constant being calculated based upon reference stars. The *absolute bolometric magnitude* (M_{bol}) is identical to the *apparent bolometric magnitude* just based upon the luminosity integrated over all frequencies.

2.2.3. Flux:

The flux, the energy received on a given area over a given time-frame, provides an easier foundation to calculate the individual energy contributions to the observed signal than the more intuitively comparable *magnitude*. The flux observed by a telescope is dependent upon the luminosity of the source, and the distance between source and observer (see *equation 2.4*), as well as, in the case of ground based observations, the atmospheric conditions at the time and location of the observation (*section 2.1*). As such the flux measured is not in itself an absolute expression of the energy output by the emitter, nor the change in energy output from the emitter. The former variable being dependent on distance and atmospheric conditions, while the latter is dependent on changes in the line-of-sight, and thus the atmospheric conditions. This project does not concern itself with the *absolute flux* of the observed AGN, rather it is purely the time-dependence of the flux that becomes of interest. Thus it becomes a necessity to minimize the influence of the changing atmospheric based noise, and all reported fluxes is *apparent flux* rather than *absolute flux*.

The initial stage of this project focused upon the creation of AGN light curves based upon the REM data for *reverberation mapping* investigations. Thus it is not the interest,

Table 2.2: The zero magnitude fluxes in the relevant wavebands, and magnitude systems for this project

	Jy	$\text{erg s}^{-1}\text{cm}^{-2}\text{\AA}^{-1}$
<i>J</i>	1594 ± 27.8 [1]	$3.13 \pm 0.05 \times 10^{-10}$
<i>H</i>	1024 ± 20.0 [1]	$1.11 \pm 0.02 \times 10^{-10}$
<i>K</i>	666.7 ± 12.6 [1]	$3.96 \pm 0.08 \times 10^{-11}$
<i>g</i>	3631 [2]	466.9×10^{-11}
<i>r</i>	3631 [2]	278.0×10^{-11}
<i>i</i>	3631 [2]	185.2×10^{-11}
<i>z</i>	3631 [2]	131.5×10^{-11}

nor the aim, of this project to determine the *absolute flux* of the observed AGNs, rather it is the relative time-dependent difference between the different observational bands that becomes relevant. Due to the importance of the time-dependent flux variations, considerations must be given to the attempt to minimize the atmospheric based errors in the observations. In the case of ground based observations this is done through the identification of suitable observational wavebands (*figure 2.3*), and the use of flux calibration based upon simultaneous observations of non-energy varying emitters (*photometric standard stars*). These *standard stars* are the only reliable method of convert instrumental magnitudes, or fluxes, into calibrated magnitudes. A standard star is a pre-observed star of known, and reliable, magnitude, allowing the flux determination of observed objects to occur based on the *relative observed flux* of the *standard star*, assuming the observations occurred both spacially and temporally close together (J. Palmer & A.C. Davenhall 2001 [24]). Preferably multiple standard stars are observed simultaneously to allow for error reductions. In this project the observed AGN have been observed with a number of standard stars (1-3) in the image frame, it is however important to note, that the not all stars are present in all frames.

Flux calibration done this way lends much of its derivation to the previous discussion of *apparent magnitude*. The apparent magnitude calculation is dependent upon the observed fluxes of two objects observed under identical conditions, while knowing the expected magnitude of one of them. In the case of this project the known standard star magnitudes are obtained using a magnitude determination made by two larger surveys (PanSTARRS and 2MASS). The flux calibrations can be done through *equation ??*. The 2MASS survey utilises calibrated version of the VEGA magnitude system (Cohen et al. 1992 [?] [1]) and PanSTARRS magnitudes are done based upon the AB system (Tonry et al. 2012 [?]). The relevant zero magnitude flux' is tabulated in *table 2.2*.

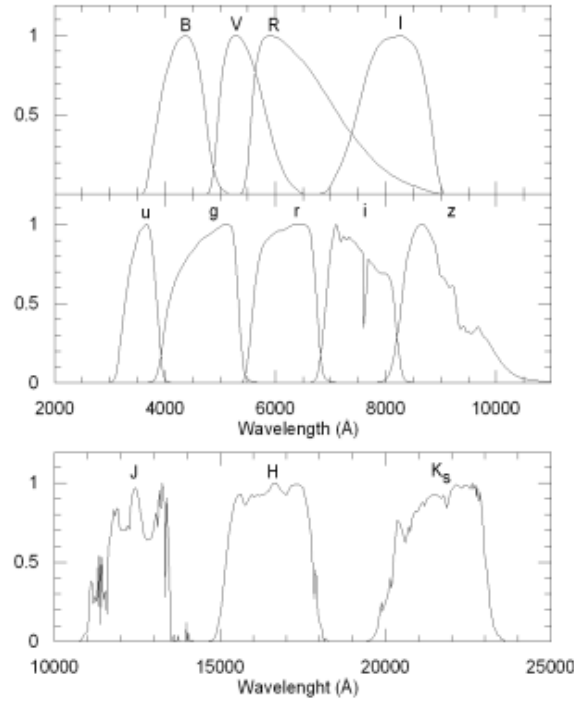


Figure 2.4: The filters used in this project. The SDSS filters g,r,i and z and the Johnson-Cousins J,H and K filters. Figure from Bilir et al. 2007.

2.2.4. Error in Fluxes⁴

Astronomical observations are subject to observational uncertainties. These uncertainties arises through atmospheric disturbances, as previously discussed, as well as interstellar and intergalactic material blocking part, or entire, emission lines thus skewing the observed data in the observed bands. In this project astronomical disturbances, beyond those inherent in the AGN structure, is of little actual interest. It is essentially assumed that the AGN is sufficiently close as to ignore the intergalactic material, or that the influence of same would be evenly distributed across all observed bands.

The flux based error of interest in this project is the measure of the relative strength of the noise in the observation, in relation to the signal strength, called the *signal-to-noise ratio (SNR)*. The *signal-to-noise ratio* is a multi-component expression (equation 2.9). Noise can be itemized as either *technical-* or *fundamental noise*. Any observational setup will have a *fundamental noise limit* that cannot be overcome, like diffraction limited or seeing limited, as well as a *technical noise*, which can be reduced. The SNR parameters are [23];

- **Signal:** The number of photons detected by the detector, not the number of arriving photons, as the detector is limited by the quantum efficiency.

⁴This section inspires heavily from Hughes & Hase 2010 *Measurements and their Uncertainties A practical guide to modern error analysis* [18]

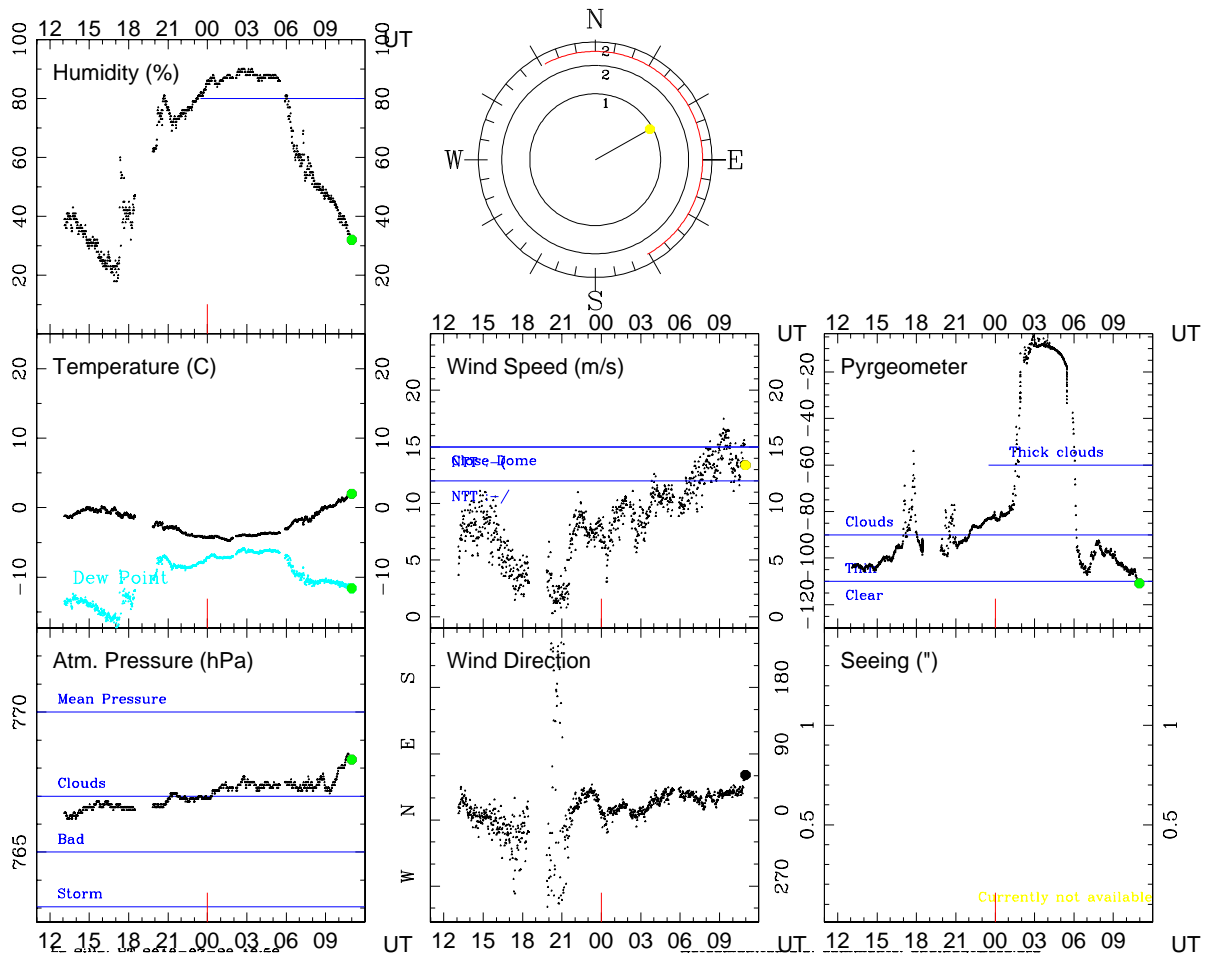


Figure 2.5: Atmospheric data for the La Silla Observatory Site in Chile at the night of 20th July 2018. This night demonstrates significant and varying cloud coverage of the observatory site as well as significant and changing humidity. At this night comparing observations obtained at midnight and 03.00 should not be compared, due to the significant difference in the cloud coverage influencing the results. Data from the La Silla - Meteominitor.

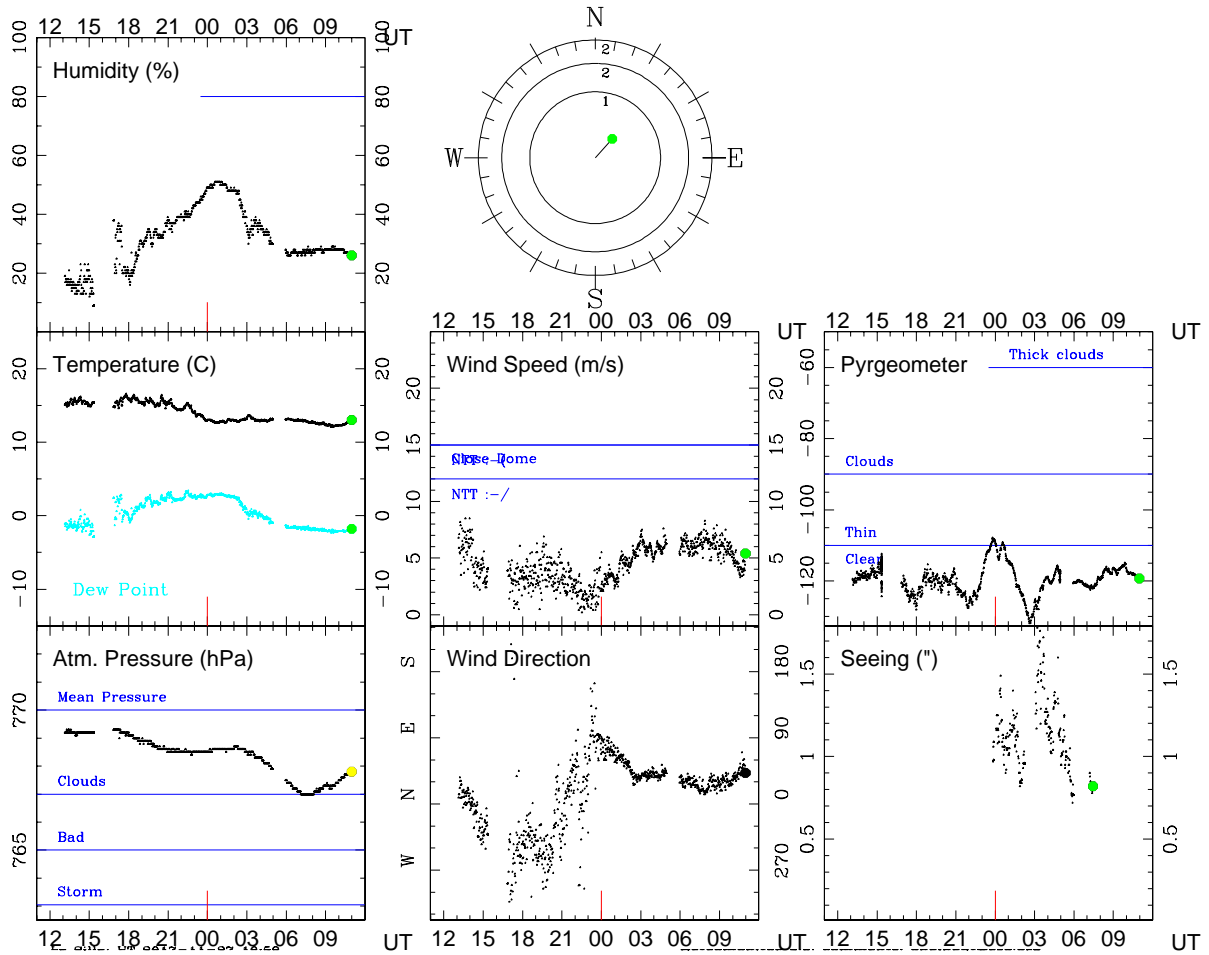


Figure 2.6: Atmospheric data for the La Silla Observatory Site in Chile at the night of 27th November 2017. This night demonstrates lower and more constant cloud coverage of the observatory site as well as lower but changing humidity. This night will be a significantly improved night to compare observations of different astronomical objects at different parts of the night sky. Data from the La Silla - Meteominitor.

- **Shot Noise:** The shot noise arises as even a non-intensity varying light source will have *Poisson distribution* of the registered signal around the mean *Poisson noise* (equation 2.7).

$$SNR_{shot} = \sqrt{signal} \quad (2.7)$$

The shot noise takes several forms;

- *Signal Noise:* The Poisson fractional uncertainty on the signal itself.
- *Sky Noise:* Any measurements will inevitably include the background noise generated by the sky. As the laws of error propagation predicts [18]

$$Z = A \pm B \quad \alpha_Z = \sqrt{\alpha_A^2 + \alpha_B^2}, \quad (2.8)$$

the Sky Noise is propagated.

- *Dark Noise:* The error originating in the thermal radiation pr. unit time (t) of the detector itself. Propagates like the *sky noise*, but can be limited by cooling the detector.
- **Read-out-noise (RON):** The amplifier added noise at the read-out. It is measured in electrons pr. pixel.

Thus the signal-to-noise ration is given by

$$SNR = \frac{N_{signal}}{\sqrt{N_{signal} + n_{pixels} \times (N_{sky} + N_{dark} \times t + RON^2)}} \quad (2.9)$$

In this project the sky background was pre-subtracted by the REM team, and as such the *Sky Noise* was determined as the variation in the "dark" parts of the images for the JHK-bands. It is important to note that the JHK-bands are given as "stacks", and as such all values must be multiplied with the number of images in the individual "stacks".

Chapter 3

Defining a Light Curve

The second part of this project was an attempt at creating a computer algorithm capable of running a reverberation mapping analysis based on optical- and infrared light curves without the initial driving function. To succeed in this it became necessary to find a method of generating a physically reliable driving function, to work as a basis for the reverberation mapping analysis. This project investigated three different methods of characterising Light Curves. Each methods have their own advantages and disadvantages, and to formulate a working model for the continuum Light Curve all three has their uses. The methods are;

1. The Stochastic model described in Kelly et al. (2009) [20]. This model builds on the assumption of AGN variability being described as a *Continuous Time First-Order Autoregressive Process* (CAR(1)).
2. Modeling the AGN variability as a Power Spectrum with Power Spectral Density slope of $\alpha = -2.3 \dots -3.4$.
3. Using Structure Functions to analyse AGN variability.

These three approaches allows for the identification and evolution of different aspects of AGN light curves. The Structure Function allows for the understanding of certain key characteristics of the observed and modeled Light-Curves, whereas both the Kelly et al. (2009) and the Power Spectrum approach allows for the modeling and evolution of AGN

3.1. KELLY MANIPULATIONS¹

Light Curve sampling is dependent on atmospheric conditions, the visible night sky and observation time on the telescope. As such observed light-curves will often be unevenly sampled with time intervals of days or perhaps weeks. Thus a method of modeling the missing data can be necessary, this is the aim of the Kelly et al. (2009) described Stochastic model (from here named "*Kelly model*"). In the data obtained, for the purpose of this project, considerable and uneven time intervals presents itself. The

¹This section relies upon the paper Kelly et al. 2009 [20]

Kelly model is a model build over the assumption that a Light-Curve observed in an AGN can be modeled as a *Continuous Time First-Order Autoregressive (CAR(1)) Process*. The Kelly model is consistent with a power spectra of the form $P(f) = 1/f^2$. This as described later, despite previously being a common assumption for AGN variability, is not an entirely accurate representation of the observed AGN variability, thus the Kelly model cannot, standalone, define an actual AGN Light-Curve without additional development.

The Kelly model is, as mentioned, a Continuous Stochastic model, rather than modeling Light-Curves using Fourier (Spectral) techniques. It is modeled as Continuous time, as the physical processes occurring in the accretion disk is continuous, and it provides a natural way of handling irregular sampling. The model uses 3 different parameters to define the Light-Curve created;

1. A characteristic time-scale, called the "*relaxation time*" (τ_{Kelly})
2. Amplitude of short time-scale variability
3. Mean value of the Light-Curve

The "*relaxation time*" is given as the time-scale at which the time series becomes uncorrelated and is easily associated with the various characteristic time-scales inherent in the accretion disk physics such as the light crossing time, the orbital time-scale and the thermal time-scale.

$$t_{lc} = 1.1 \times \left(\frac{M_{BH}}{10^8 M_O}\right) \left(\frac{R}{100 R_S}\right) \text{ days} \quad (3.1)$$

$$t_{lc} = 104 \times \left(\frac{M_{BH}}{10^8 M_O}\right) \left(\frac{R}{100 R_S}\right)^{3/2} \text{ days} \quad (3.2)$$

$$t_{lc} = 4.6 \times \left(\frac{\alpha}{0.01}\right)^{-1} \left(\frac{M_{BH}}{10^8 M_O}\right) \left(\frac{R}{100 R_S}\right)^{3/2} \text{ yr} \quad (3.3)$$

In Kelly et al. 2009 the relationship between the Characteristic time-scales in *equations 3.1, 3.2 and 3.3* and the *relaxation time* is investigated. They conclude that although both the t_{orb} and the t_{th} provides reasonable fits, the best fit is the thermal time-scale. The differential equation governing the *Kelly model* is given through *equation 3.4*.

$$dX(t) = -\frac{1}{\tau_{Kelly}} X(t) dt + \sigma \sqrt{dt} \epsilon(t) + b dt \quad (3.4)$$

with $b\tau_{Kelly}$ being the observed mean value of the observed light curve and τ_{Kelly} is the relaxation time additionally the variance on the Light-Curve is given by $\tau\sigma^2/2$. Additionally the $\epsilon(t)$ a white noise function of zero mean and variance of one, and $X(t)$ represents the Light-Curve. The Kelly approach introduces a slight shifting on the axis dependent on the direction of evolution and the direction in which the Light-Curve is read. Due to this bias in the *Kelly model* it has been chosen during the course of

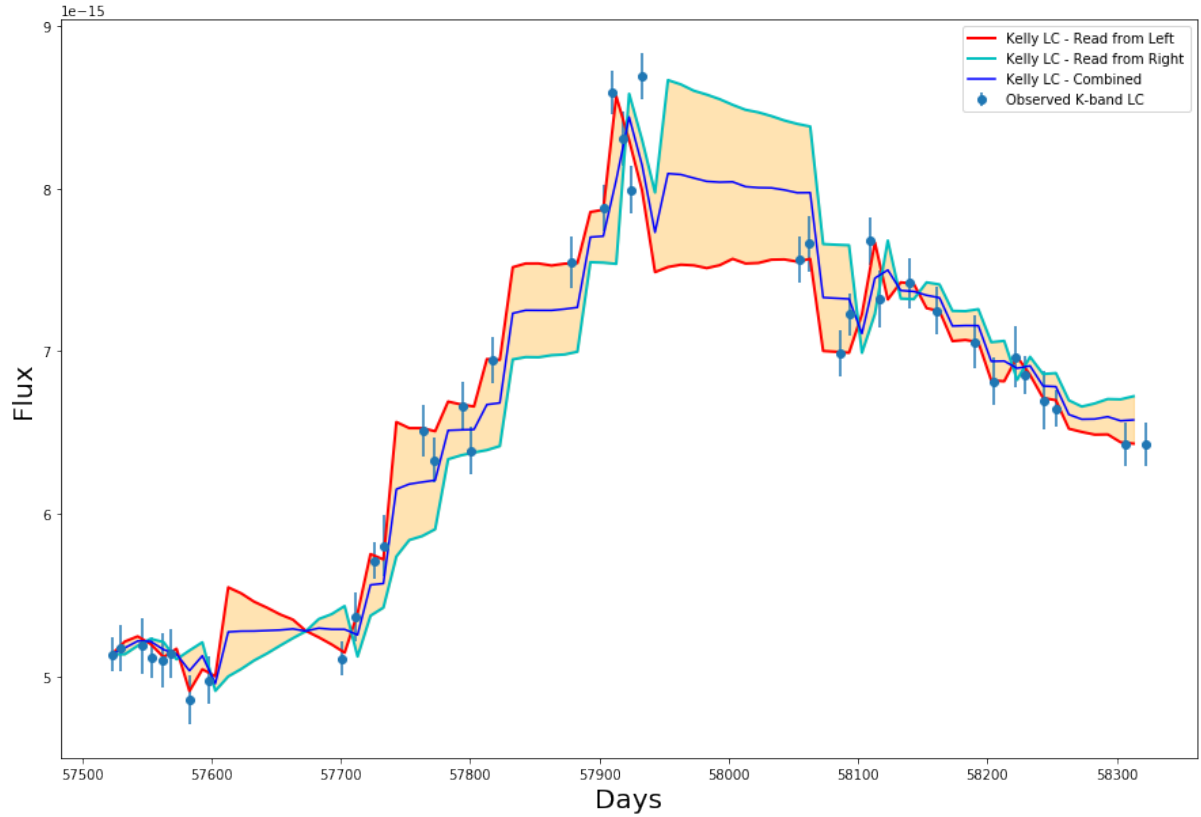


Figure 3.1: The Kelly function applied to the NGC3783 K-band spectrum. The red curve is the Kelly method interpretation as applied from left to right, and the green is the opposing direction. It becomes apparent that significant bias can be found in the Kelly method as only applied in one direction.

this project to generate the *Kelly Light-Curve* from both directions and use the mean Light-curve. This is exemplified in figure 3.1

The three parameters defining the *Kelly model* can be determined through the use of a maximum likelihood estimate from equations 3.5 through 3.11.

$$p(x_1, \dots, x_n | b, \sigma, \tau) = \prod_{i=1}^n [2\pi(\Omega_i + \sigma_i^2)]^{-1/2} \times \exp\left[-\frac{1}{2} \frac{(\hat{x}_i - x_i^*)^2}{\Omega_i + \sigma^2}\right] \quad (3.5)$$

$$x_i^* = x_i - b\tau_{Kelly} \quad (3.6)$$

$$\hat{x}_1 = 0 \quad (3.7)$$

$$\Omega_1 = \frac{\tau_{Kelly}\sigma^2}{2} \quad (3.8)$$

$$\hat{x}_{i>1} = a_i \hat{x}_{i-1} + \frac{a_i \Omega_{i-1}}{\Omega_{i-1} + \sigma_{i-1}^2} (x_{i-1}^* - \hat{x}_{i-1}) \quad (3.9)$$

$$\Omega_{i>1} = \Omega_1 (1 - a_i^2) + a_i^2 \Omega_{i-1} \left(1 - \frac{\Omega_{i-1}}{\Omega_{i-1} + \sigma_{i-1}^2}\right) \quad (3.10)$$

$$a_{i>1} = \exp\left[-\frac{t_i - t_{i-1}}{\tau_{Kelly}}\right] \quad (3.11)$$

The *Kelly method* as a CAR(1) process has a power spectrum given by *equation ref eq : Kelly power spec*

$$P(f) = \frac{2\sigma^2\tau_{Kelly}^2}{1 + (2\pi\tau_{Kelly}f)^2} \quad (3.12)$$

allowing the resulting Light-Curve to be separated in two different regimes. In the case of time-scales being short as compared to the *relaxation time* the power spectrum falls as $1/f^2$ and in the case of time-scales longer than the *relaxation time* the power spectrum becomes constant.

Analysing *figure ??* one can identify one of the key weaknesses in the *Kelly method* in the significant time-gaps displayed. The Kelly Function provides a generally reasonable fit in areas of reasonable coverage for the observations, however it proves unable to successfully predict reasonable suggested data for time-gaps of significant size. As such utilising the range of suggestions provided by the twin interpretations from opposing sides becomes useful. It may be possible to adjust this somewhat by introducing a dependence of time from the points of observation that the estimate is based upon. This however is not the focus at this time.

3.2. POWER SPECTRAL DENSITY

The Power Spectral Density (PSD) is an expression of the variability of a function as a function of temporal frequency. The PSD is determined by calculating a periodogram (*equations 3.13, 3.14 and 3.15*). The *periodogram* generated through calculating the Power Spectral Density of real observable data is an *inconsistent estimator* of the PSD, as the scatter observed in the periodogram is not inversely dependent on the number of observations, necessitating averaging the periodogram. This can be done by either binning the calculated frequencies, or averaging over data segments, thus allowing an averaged periodogram to become a *consistent estimator* of the PSD (Vaughan et al. 2003 [36]).

In the case of AGN Light-Curves the interesting aspect of the PSDs becomes the slope of the *consistent estimator*. This PSD slope (denoted α) can be an indication of the time-dependent variability of AGN Light-Curves should a general tendency be identified. It is important to acknowledge that AGNs vary and as such, despite early assumptions of $\alpha = 2$ the PSD slope is not identical across observed AGNs.

The PSD can be obtained from both evenly and unevenly sampled light-curves. To calculate the PSD from a discrete Light-Curve ($X(t_i)$) with N observed data points it is necessary to remove the zero-frequency power, by subtracting the mean from the Light-Curve,

$$X_{PSD}(t_i) = X(t_i) - \mu(X(t_i)) \quad (3.13)$$

and calculate the modulus squared of the discrete Fourier transform

$$|F_N(\nu)|^2 = \left[\sum_{i=1}^N X_{PSD}(t_i) \cos(2\pi\nu t_i) \right]^2 + \left[\sum_{i=1}^N X_{PSD}(t_i) \sin(2\pi\nu t_i) \right]^2 \quad (3.14)$$

with ν being the sampled frequencies of the discrete Fourier transform occurring at evenly spaced intervals at $\nu_{min}, 2\nu_{min}, 3\nu_{min}, \dots, \nu_{Nyq}$, with $\nu_{min} = T^{-1}$ (T being total length of Light-Curve) and ν_{Nyq} being the Nyquist frequency of $(2T/N)^{-1}$. The power of the relevant function is obtained by normalising $|F_N(\nu)|^2$ (Uttley et al. 2001 [35])

$$P(\nu) = \frac{2T}{\mu^2 N^2} |F_N(\nu)|^2. \quad (3.15)$$

This Power Spectra allows the integration of the Power Spectra over a range ν_1 to ν_2 to determine the contribution to the fractional rms squared variability (σ^2/μ^2) of the Light-Curve generated by variations on the time-scale T_2 to T_1 . (FIND AND CHECK van der Klis 1997). The total fractional rms variability observed is thus determined by the square root of the integrated power spectrum. It is observed in Uttley et al. 2001 [35] that the actually observed power spectra for AGN demonstrate either a Knee Model power spectra, by flattening to a slope of $\alpha = 0$ at low frequencies or a high-frequency break model (by flattening to a slope of $\alpha = 1$ at low frequencies). The PSD slope is obtained through linear fitting in loglog-space past the "Knee" or "Break".

In a study by Smith et al. 2018 [34] of 21 Type I AGN Light-Curves from Kepler the PSD slopes has been studied. The AGNs studied by Smith et al. 2018 [34] are comparable to AGNs studied in this project, in them being of the local universe, all but one of them with redshift $z < 1$. In the study it is determined that the PSD slope (α) ranges from -1.7 to -3.4 with a mean value of $\alpha_{mean} = -2.51$ and standard deviation of $\alpha_{std} = 0.42$. This allows for better indications of the Physical relevance of the generated driving function of the observed AGNs, that is attempted in this project.

3.3. STRUCTURE FUNCTION

The structure function is used to understand the behavior of long-term AGN variability. Short-term AGN variability is generally accepted to be attributed towards relativistic beaming effects (READ UP ON THIS AND WRITE EXPLANATION FOR THIS IN THEORY), however long-term AGN variability is more difficult to ascertain the cause of. Suggestions towards possible causes is (as given in Vries et al. 2004 and Kawaguchi et al. 1998):

1. Disk Instability (described in Starling et al. 2004 READ UP ON IT AND WRITE HERE)
2. Super Novae event bursts close to the AGN
3. Source extrinsic variations due to microlensing events along line-of-sight

The structure function, as described by Kawaguchi et al. (1998) and Simonetti et al. (1985) (FIND THIS PAPER), is given by *equation 3.16*

$$V(\tau) = \frac{1}{N(\tau)} \sum_{i < j} [m_{opt}(t_i) - m_{opt}(t_j)]^2 \quad (3.16)$$

with $m_{opt}(t_i)$ being the optical magnitude at the time t_i , τ being the time-difference $t_i - t_j$ and $N(\tau)$ being number of pairs of $\tau = t_i - t_j$. The structure function itself applied to an observed AGN Light-Curve will demonstrate three regimes (Kawaguchi et al. 1998, Hughes et al. 1992 (FIND THIS PAPER AND CONFIRM));

1. A plateau at time-lags exceeding the longest correlation time-scale, with a value twice the variance of fluctuations in the measurements
2. Plateau at short time-lags with value twice the measurement noise (not in models without arbitrary measurement noise)
3. Power-law increase with time-lag as $[V(\tau)]^{1/2} \propto \tau^\beta$ between the two plateau'

Additionally there is a comparability between the PSD slope (α), discussed previously, and the structure function slope (β) of $\alpha = 1 + 2\beta$ assuming $1 \leq \alpha \leq 3$ (FIND REFERENCE EITHER KAWAGUCHI OR VRIES).

Chapter 4

Reducing the Data¹

The main aim of this project was the reduction of the observed data into light curves usable for reverberation mapping. In this section the observational images of 7 different AGNs, from both Type I and Type II Seyfert Galaxies (*table ??*) will be reduced into AGN light curves in the optical *SDSS-* (g,r,i,z) and infrared *Johnson-Cousins J,H,K* observational bands.

Initially the task was geared towards determining the best solution for isolating the AGN from the surrounding galaxy, through choice of aperture size, and astrometrical calibrations. The AGNs treated in this project belong to the local universe, and as such the surrounding galaxy was resolved, thus making the observed AGNs Seyfert Galaxies. This creates an issue in the calibration of the AGN Light-Curves, as the host galaxy will have a non-negligible contribution towards the observed signal. In the case of a Quasar the chosen aperture and exact precision on the astrometrical calibration would be of secondary importance, as the AGN emission overpower the stellar contribution from the galaxy, and thus including the entirety of the galactic light would not be a major issue. A Seyfert Galaxy however does not have an AGN of sufficient strength to out-shine the stellar component of the observed galaxy, and as such reducing the calculated stellar emission becomes a priority. *figure 4.1* show this in the observed *NGC7213 Seyfert I Galaxy*, demonstrating the extend of the galaxy as compared to the central point source like quality of the AGN, the central groupings of pixels.

Due to the non-negligible nature of the stellar contribution towards the observed emission, it becomes necessary to separate the two components. This presents two separate challenges;

1. how to identify and locate the center of the AGN in the obtained image - so an astrometrical challenge
2. how to determine the angular size of the AGN in the observed image - so an aperture challenge

¹AGN classifications from <http://simbad.u-strasbg.fr/> [3]

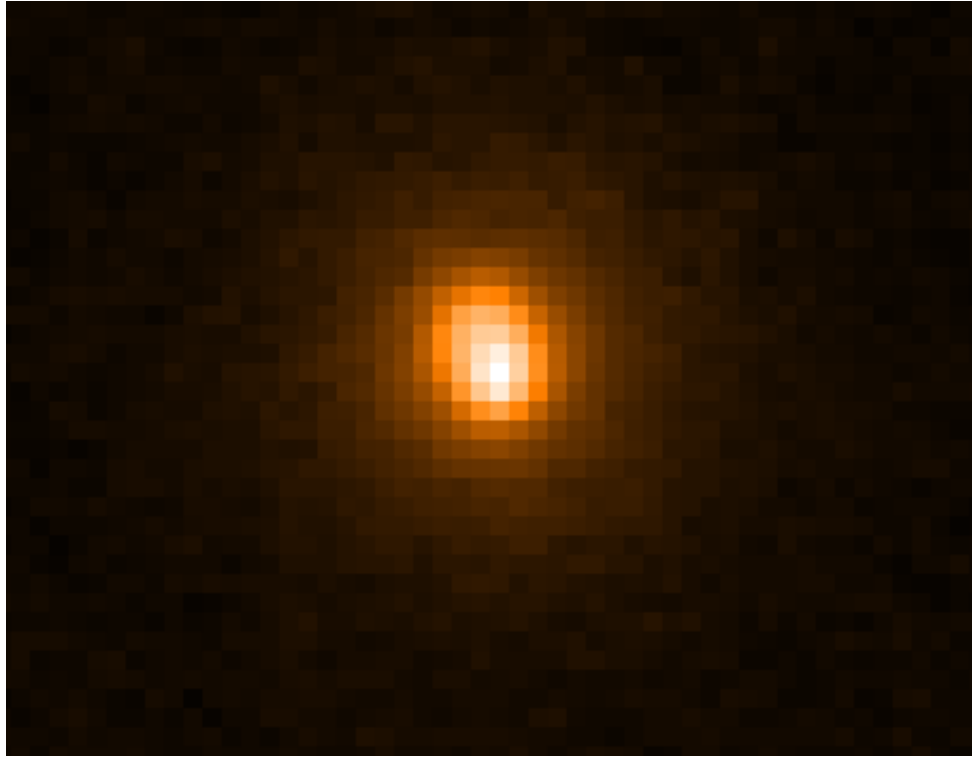


Figure 4.1: Image of NGC7213, one of the AGNs in the sample. Only the central groupings of pixels are dominated by AGN emission, the rest are dominated by stellar emission.

following this challenge it became necessary to identify relevant stars for use as standard stars in the aim to create light curves independent of nightly observational conditions (as discussed section 2.2.3). In this regard it became an issue that the Pan-STARRS survey does not extend below a declination of -30° , this necessitated the use of REM data to calibrate relevant southern Standard Stars in the g,r,i and z bands.

4.1. THE REM TELESCOPE²

The REM telescope, the origin of this data, is a INAF operated 60 cm fast reacting telescope at the ESO La Silla observatory site in Chile. The REM telescope itself consists of two simultaneously operated components; the IR imaging *REMIR* camera, and the optically imaging *ROSS2* camera.

The ROSS2 camera is imaging in 4 simultaneous passbands on its 2048:2048 detector plate. Thus it allows simultaneous imaging of the griz bands. The *field of view* is $9.1 \times 9.1 \text{ arcmin}$ with a *plate scale* of $0.58 \text{ arcsec/pixel}$. It has not been possible to find a specification sheet for either detector, but taking the cross-section of a saturated star (figure 4.2 of HD 101274 in the NGC3783 frame) indicates a saturation of $\sim 64.500 \text{ ADU}$.

The REMIR camera operates the JHK filters from this project. The detector has a

²If not otherwise specified the origin of this information lies with <http://www.rem.inaf.it/> [19]

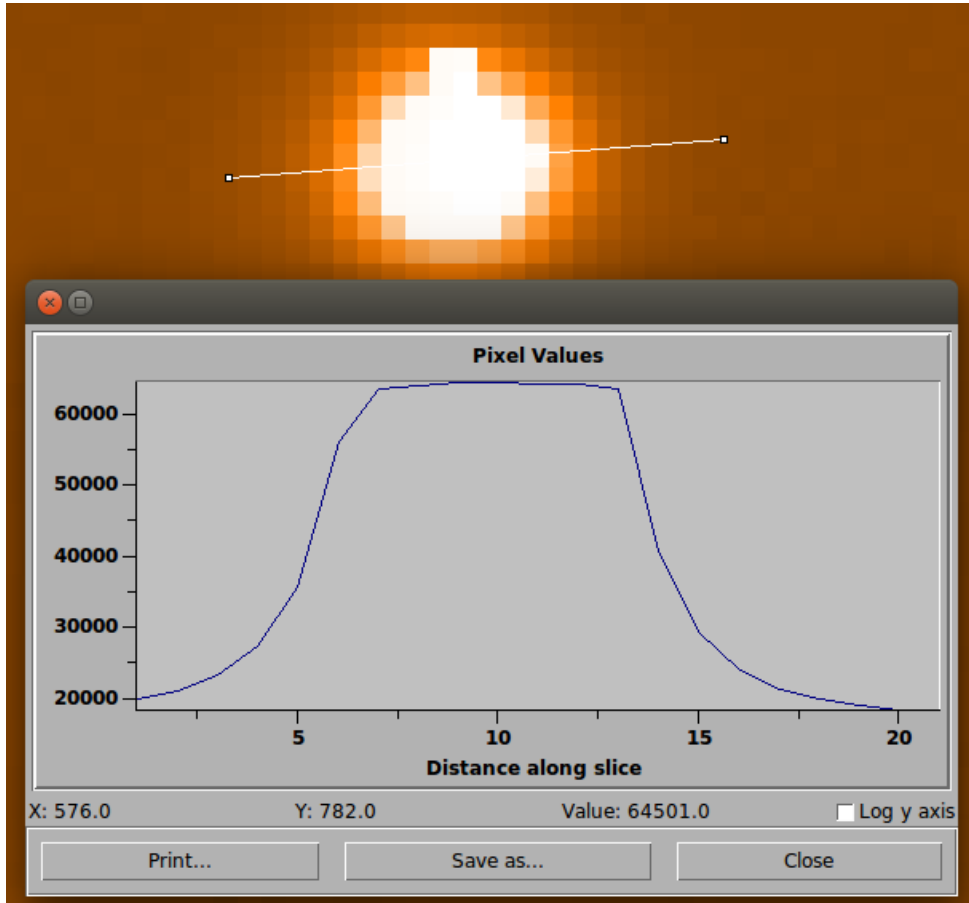


Figure 4.2: Finding the saturation limit of the ROSS2 detector from REM through the analysis of the cross-section of the saturated (flat topped psf) HD 101274 star, with the use of the Starlink:Gaia::Skycat software [14].

pixel scale of 1.2 arcsec/pixel and a field of view of $10 \times 10 \text{ arcmin}$. The detector has a saturation (given by the fits headers) of 65536 ADU and a linearity limit of 15.000 ADU .

4.2. FINDING THE AGN

4.2.1. Astrometry of the AGN

This project investigated two different approaches to locating the center of the AGN in the obtained REM images. Both approaches had their own individual strengths and shortfalls. The initial approach relied on the use of the existing astrometrical calibration of the images, as done by the REM Telescope, or updating them later using a third party software package like Pin-Point, or equivalent (hereon called the *accurate astrometry method*). The second approach investigated the use of the SEXtractor software (the *SEXtractor method*). SEXtractor identifies abnormal pixel values in the image, based upon a search criteria and an underlying algorithm, that is neither the scope nor interest of this project, and returns a list of pixel groupings fitting the search criteria. Knowing the approximate pixel location of the stellar object of interest allows

identification of the observed center of this astronomical object.

Both methods has advantages and disadvantages. Utilising accurate astrometry, when applicable, is a fast mode of investigation, both due to the use of broadcasting operations on numpy arrays, and due to the convenience of pre-identifying the correct object for later investigation, as opposed to searching a list of all possible objects everywhere in the image. Additionally, assuming accurate geometry in the image, this method allows investigation of the center, as it is determined by larger surveys, of the AGN, as opposed to attempting to find the spatial location of the SMBH in the AGN, and risk stellar noise combined with galactic inclination angle skewing the results. Conversely the same advantage is also the primary disadvantage of the accurate astrometry method of identifying the AGN in the obtained images. The accurate astrometry method does not take into consideration the actual pixel configurations on the image, only the pixels that, according the the astrometry, is expected to be of relevance. This then leads to the risk, that in the case of non-perfect astrometry, the program may exclude some, or the entire light contribution from the AGN. This could be counteracted by using a larger aperture, but this has its own issues, as discussed later.

The second method investigated for use in this project utilises, as mentioned, the SEXtractor software. The main advantage of this method is that even in the case of slightly inaccurate, although not missing, astrometry, it is still possible to find the peak intensity of the observed astronomical objects. Thus this method allows for inaccurate astrometry on the obtained images, and thus theoretically allows the determination of the location of the AGN engine itself, should such location be unknown. The disadvantage in return is the significantly slower speed by which the light curves are generated, as well as the increased impact of noise, stellar light and inclination angle, of the host galaxies, on the obtained light curves.

Figures 4.3 and 4.4 shows the difference between the expected location of the AGN of NGC3783 and the standard star Tycho-2 7740-22-1 respectively and the by SEXtractor determined locations, based on the, by the REM team, determined image coordinates. The errors observed in *Figures 4.3 and 4.4* are compounded by two sources of error that can be distinguished between. In the plot for Tycho-2 7740-22-1 it is observed that the difference between the expected location of the Standard Star and the, by SEXtractor, determined location coordinates, in the astrometrical calibration inherent in the images, is dispersed in a random circle, with no regards to time of observation, around the expected location. This must conceivably, should one assume that the located center of the Standard Star is not otherwise affected, give an accurate demonstration of the inaccuracy in the supplied astrometry. *Figure 4.3*, however, shows the location error associated with the AGN of NGC3783. In this case it is clear that the average SEXtractor location is shifted away from the expected location, in addition to showing the same relative scatter. Thus, if one accepts the results from the point-like Tycho-2 7740-22-1 as an accurate estimation of the error in the astrometry, and the official location of the

center of NGC3783, as determined by larger, more extensive surveys, then it must be clear that the SEXtractor software is not capable of accurately determining the center of the AGN based upon the peak intensity of the light emitted from NGC3783. This error likely arises based upon the inclination angle of the galaxy skewing the Point Spread Function of the entire galaxy by "hiding" some of the light from stars in the part of the galaxy "leaning away" from the line-of-sight. Thus the SEXtractor method might see the inclusion of excessive stellar light, however the astrometry accuracy method might lead to missing the AGN, and the Starndard Stars, either partly or entirely. In this project the choice thus became the use of the SEXtractor software, as the astrometry precision method was deemed too unreliable, and the image quality was such that third party software, such as Pin-Point, designed to improve astrometry often either failed to provide significantly improved astrometry, or failed entirely in providing an astrometric coordinate system.

4.2.2. Aperture Choice

The aperture choice is a two-fold problem. A small aperture in a astrometrically inaccurate setting risk missing part of the AGN emission, and increase shot noise contribution due to the lower flux rate of both star and AGN (*section 2.2.3 & 2.2.4*), whereas a large aperture will include unwanted stellar emission in the calculations.

If the dust torus temperature were of no relevance for this project, and the AGN driving function pre-known, it may have been of lesser importance to reduce the hos galaxy pollution of the reduced light curves. This project, however, aims at providing AGN light curves of sufficient quality, so as to be usable for reverberation mapping of the accretion disk, and the dusty torus without available X-RAY observations of the AGN. Thus while larger apertures will ensure the inclusion of the light from the entirety of the AGN, it allows grater galactic pollution. The choice of aperture in this project was based on empirical experiments upon the available data,

In *figure 4.5 and 4.6* the NGC3783 generated light curves for apertures of radius 0.72 arcsec , 1.8 arcsec and 3.6 arcsec are shown. Additionally *figure 4.5* demonstrates the aperture sizes 2.88 arcsec and 2.57 arcsec . The AGN flux difference between the 1.8 arcsec - and 3.6 arcsec apertures, in gradual jumps for each successive aperture increase, indicates the inclusion of galactic pollution in the aperture. The 0.72 arcsec - and 1.8 arcsec apertures appears to be in agreement on the AGN magnitude, however they each demonstrate a significant scatter in the data. Additionally with a *Johnson-Cousins waveband* pixel-scale of $1.221 \text{ arcsec/pixel}$ it would be unreasonable, given the astrometry precision, to reduce the aperture size below 1.8 arcsec . The SDSS filters has pixel-scale of $0.581 \text{ arcsec/pixel}$, thus making a smaller aperture more feasible. *Figure 4.6* however, indicates a significantly enlarge scatter in particularly the *i*-band. Despite the inclusion of additional pollution it appears that an aperture choice of 2.57 arcsec would be most feasible. It appears that this aperture retains sufficient size as to reduce the scatter from incomplete astrometry, as well as being sufficiently narrow as to reduce

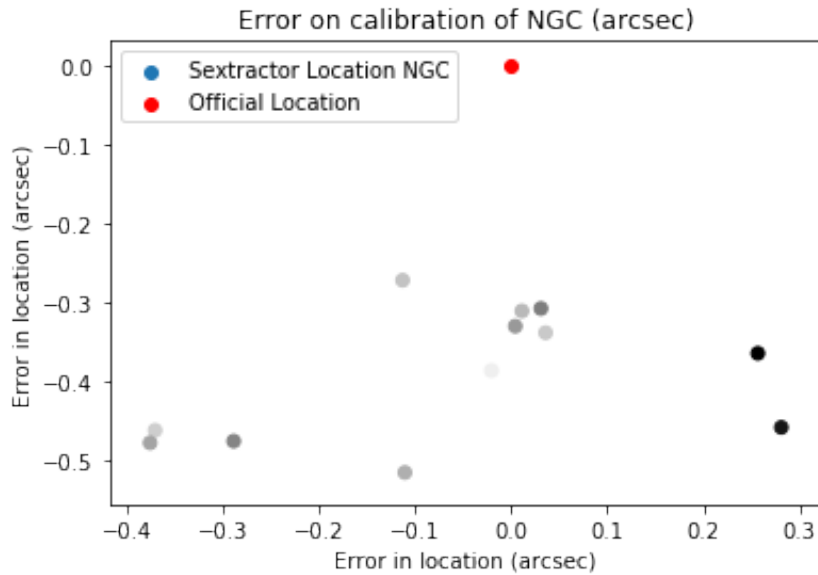


Figure 4.3: The Astrometric precision on the obtained images with respect to the center of the AGN NGC3783. The x-axis is the error in the Right Ascension and y-axis the error in Declination Angle, the lightening colour of the SExtractor Locations are in response to the time of observation, demonstrating a lack of relation in this regard.

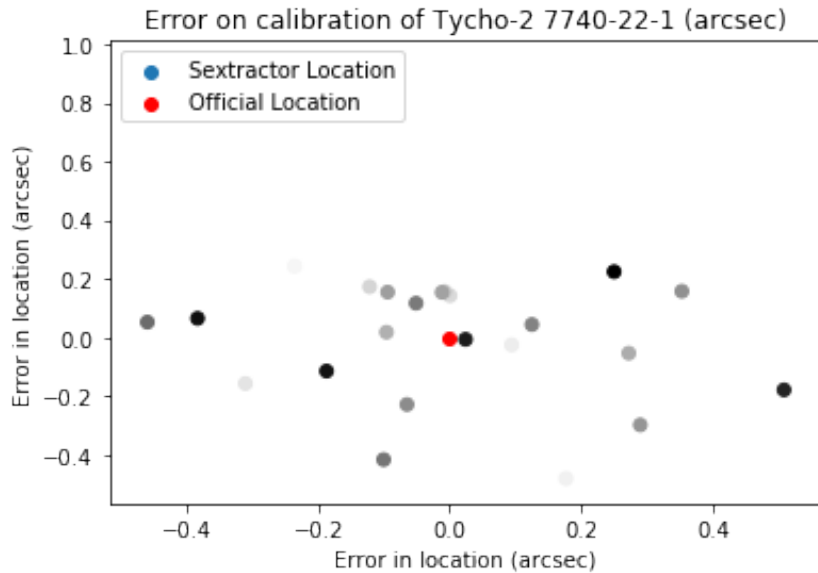


Figure 4.4: The Astrometric precision on the obtained images with respect to the center of the standard star Tycho-2 7740-22-1. The x-axis is the error in the Right Ascension and y-axis the error in Declination Angle, the lightening colour of the SExtractor Locations are in response to the time of observation, demonstrating a lack of relation in this regard.

some of the galactic pollution. It will be inevitable, given the angular resolution of the telescope, that galactic pollution is included. Thus the decision of this project is to retain an aperture of 2.57 arcsec .

4.3. THE LIGHT CURVE ALGORITHM

The algorithm for recovering the AGN light curves relies heavily on the *SEXtractor* [4] software [8] and the reference star catalogues of *PanSTARRS* [5] and *2MASS* [6].

4.3.1. The use of *SEXtractor*³

The *SEXtracotor* software determines a global background map and uses it to isolate pixels, or groupings of pixels, not belonging to the background (for more information see the *SEXtractor User's Guide* [8]). The *SEXtractor* call specified the parameters that should be returned:

```
In [19]: def Sxtable(quas,aperture):
    header = pyfits.getheader(quas)
    phot_app = aperture*3600/header['PIXSCALE']
    np.set_printoptions(threshold=np.inf)
    sew = sewpy.SEW(params=['XMODEL_WORLD', 'YMODEL_WORLD', 'X2MODEL_WORLD', 'Y2MODEL_WORLD',
                           'XMODEL_IMAGE', 'YMODEL_IMAGE', 'FLUX_RADIUS(1)', 'FLUX APER', 'ELLIPTICITY'],
                    config=[{"DETECT_THRESH":3, "DETECT_MINAREA":5, "DETECT_MAXAREA":10000,
                             "PHOT_FLUXFRAC":"0.5", "PHOT_APERTURES":2*phot_app,
                             "PIXEL_SCALE":header['PIXSCALE']}]
                    , sexpath='/usr/bin/sextractor')
    out = sew(quas)
    #print out
    return out
```

Figure 4.7: The *SEXtractor* call in the light curve code.

The "*XMODEL_WORLD*", "*YMODEL_WORLD*", "*XMODEL_IMAGE*" and "*YMODEL_IMAGE*" gives the location of the objects found in *SEXtractor* in Celestial Coordinates and pixel coordinates respectively. The "*FLUX_RADIUS(1)*" and "*FLUX_APER*" designates that the sampling method is aperture, and that the entirety of the flux in the aperture is to be returned (the *SEXtractor* standard is 0.5). The "*DETECT_THRESH*" and "*DETECT_MINAREA*" commands designates the required expectation for an object to be returned in σ above background noise and minimum size of the pixel groupings. "*PHOT_FLUXFRAC*" should be considered legacy code, and specifies the fraction of light inside the *half-light radius* of the object, should such be queried. "*PHOT_APERTURES*" is the diameter of the aperture chosen (in pixels). Aperture photometry in general risks running the danger that the number of pixels inside the aperture changes dependent of small changes in the observed coordinates. This problem is resolved in *SEXtractor* by dividing all pixels into groups of 5×5 sub-pixels.

A search algorithm was created to determine the closest *SEXtractor* object to the expected location of the astronomical object of interest. This search algorithm was

³The information in this section relies heavily on [8] and the website sextractor.readthedocs.io [32]

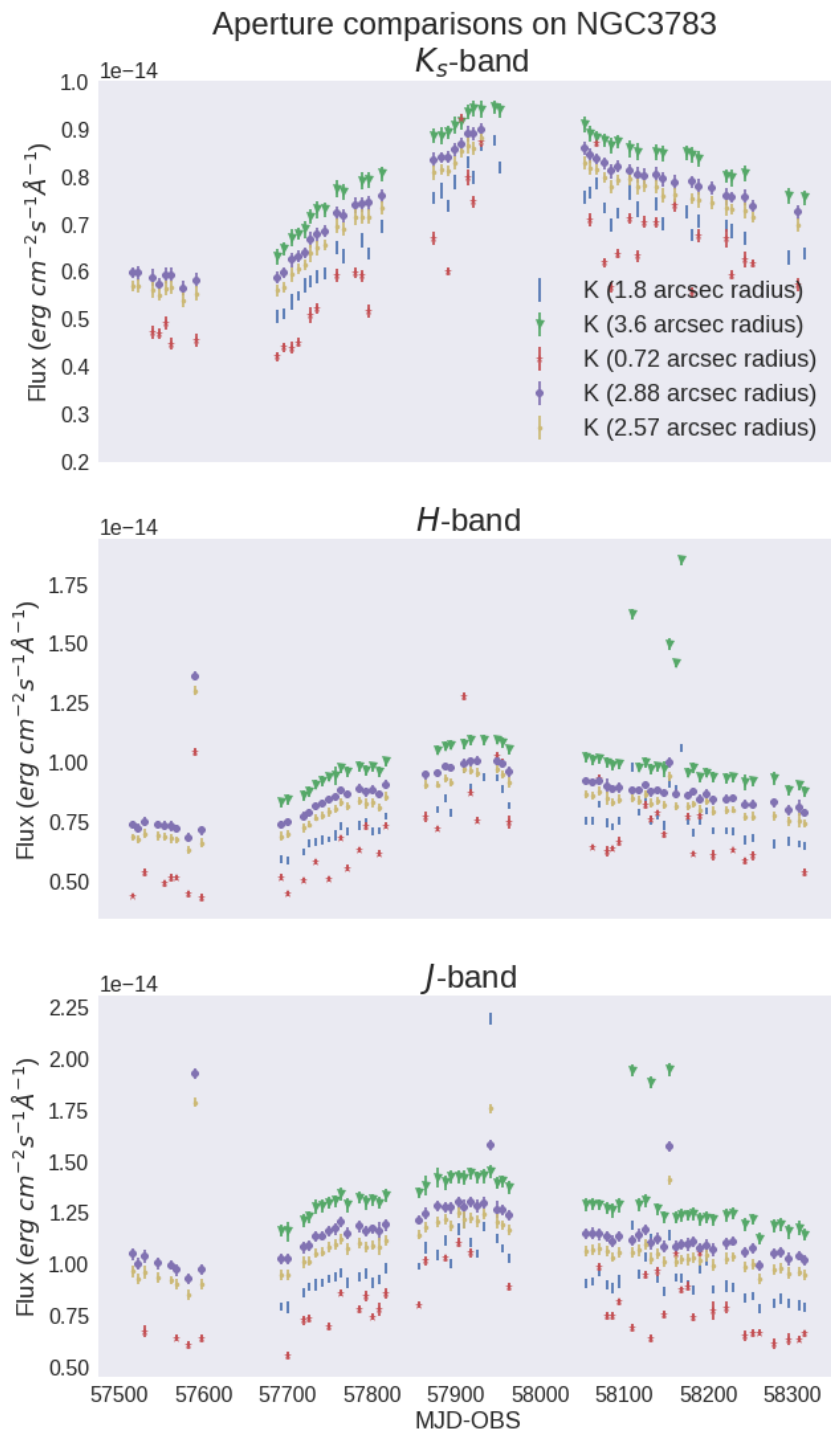


Figure 4.5: Aperture comparisons of the NGC3783 JHK bands for apertures of radius 1.8 arcsec (blue), 3.6 arcsec (green), 0.72 arcsec (red), 2.88 arcsec (purple) and 2.57 arcsec (yellow). The jump from the 1.8 arcsec- to the 3.6 arcsec aperture indicates the greater flux in the latter aperture associated with the host galactic pollution, however it appears that the scatter increases significantly below an aperture of 1.8 arcsec.

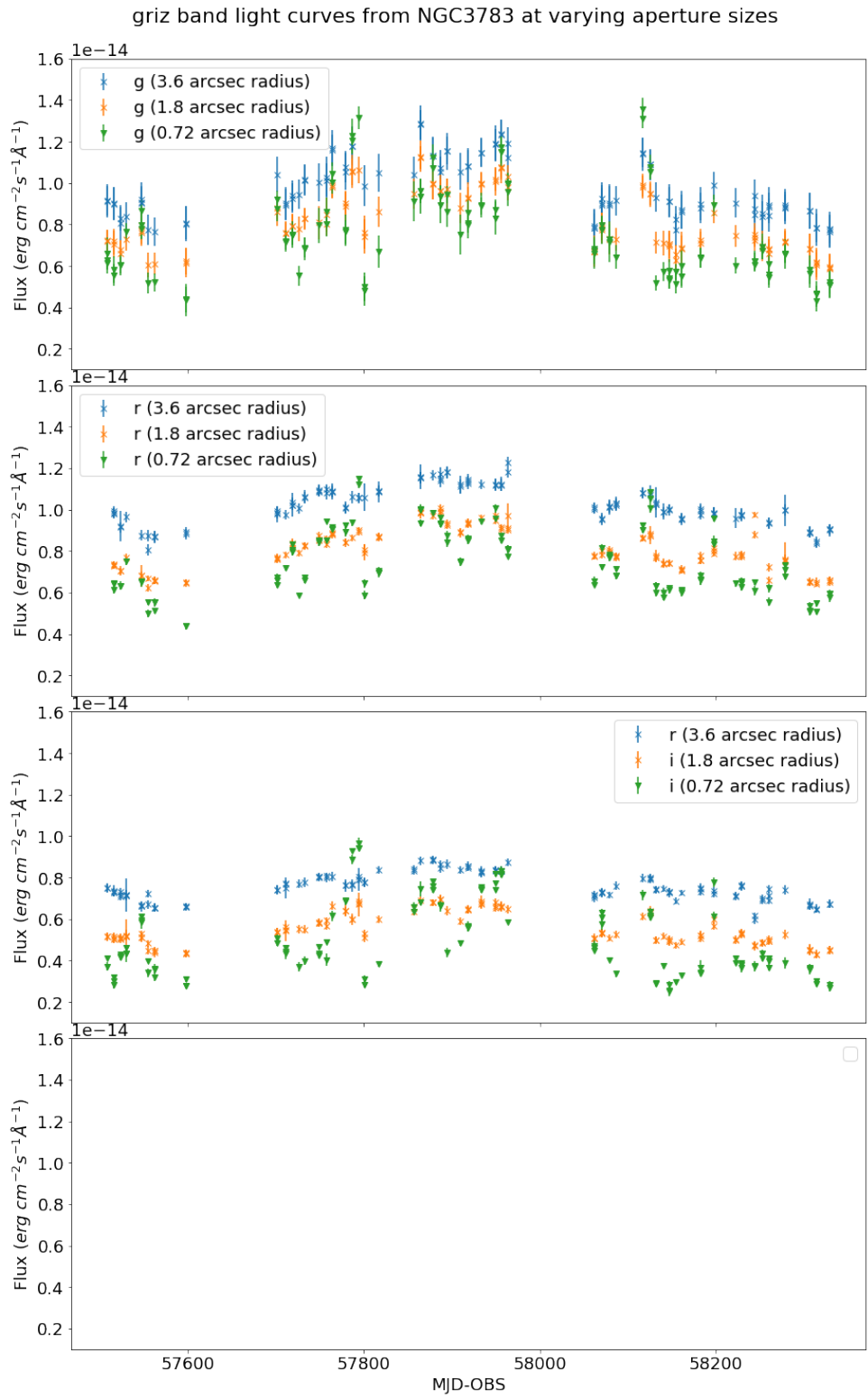


Figure 4.6: Aperture comparisons of the NGC3783 JHK bands for apertures of radius 1.8 arcsec (blue), 3.6 arcsec (orange) and 0.72 arcsec (green). The jump from the 1.8 arcsec- to the 3.6 arcsec aperture indicates the greater flux in the latter aperture associated with the host galactic pollution. The 0.72 arcsec aperture show greater scatter in the *i* band especially.

created to exclude the outer 15 pixels of the images as allowed locations for the reference star psf center points, due to the early realisation that it was an oft occurring phenomenon that parts of the stellar psf would otherwise fall outside the image, thus creating unaccounted scatter by reducing the effective size of the stars. It was decided to allow an astrometrical inaccuracy of ± 10 pixels, this has not caused any undue confusion between astronomical objects in the image frames. The search algorithm is shown in *figure 4.8*.

```
In [9]: def flux(quas,aperture,main_RA_WORLD,main_DEC_WORLD):
    header = pyfits.getheader(quas)
    RAmain = WCS(quas).all_world2pix(main_RA_WORLD,main_DEC_WORLD,1)[0]
    DECmain = WCS(quas).all_world2pix(main_RA_WORLD,main_DEC_WORLD,1)[1]
    output = float('nan')
    if 15 < RAmain < header['NAXIS1'] - 15 and 15 < DECmain < header['NAXIS2'] - 15:
        out = SXTable(quas,aperture)
        RAmain = WCS(quas).all_world2pix(main_RA_WORLD,main_DEC_WORLD,0)[0]
        DECmain = WCS(quas).all_world2pix(main_RA_WORLD,main_DEC_WORLD,0)[1]
        #print out['table'][['XMODEL_IMAGE']], out['table'][['YMODEL_IMAGE']]
        #print RAmain, DECmain

        for j in range(len(out['table'][['XMODEL_IMAGE']])):
            #output['time'][j] = header['MJD-OBS']
            if RAmain - 10. < out['table'][['XMODEL_IMAGE']][j] < RAmain + 10. and \
                DECmain - 10. < out['table'][['YMODEL_IMAGE']][j] < DECmain + 10.:
                #print 'YES'
                output = out['table'][['FLUX_APER']][j]
                break
        else:
            output = float('nan')
            #print 'Done'
    return output
```

Figure 4.8: The search algorithm to identify the relevant astronomical objects in the image frames.

4.3.2. The Standard Stars

The AGN flux was found through the use of simultaneously sampled standard stars, in the same image, by the use of a re-arranged version of *equation 2.3* and the known standard star magnitudes obtained from *PanSTARRS* and *2MASS* combined with the known zero-magnitude flux rates (*table 2.2*). The standard star role in the creation of AGN light curves from observational data is, crucial (J. Palmer & A.C. Davenhall 2001 [24]). Where applicable multiple standard stars has been utilised in this project in an attempt to confirm the obtained fluxes, to have alternatives for overexposed stars, such as the NGC3783 plate HD 101274 in the griz bands (*figure 4.2*) and to counter the possibility of a star being out of the frame due to the image orientation (like the NGC3783 plate Tycho-2 7740-529-1). In this project a plethora of standard stars has been utilised, however as the *PANSTARRS survey* does not extend below a declination angle of -30° it has been necessary to do a magnitude calibration on all reference stars in the griz bands below this limit. This has been done through the utilisation of the same code as the AGN flux determination and utilising *equation 2.3*, with F_1/F_2 being the relative observed fluxes. The Standard Stars and their magnitude calibrations, whether they be from *2MASS*, *PANSTARRS* or done in the course of this project can be seen in *tables 4.1 & 4.2*.

AGN	Standard Star	Magnitudes:		
		K _s -band	H-band	J-band
NGC3783	HD 101274	8.909	8.982 ± 0.023	8.997 ± 0.026
	Tycho-2 7740-22-1	10.611 ± 0.024	10.726 ± 0.023	10.919 ± 0.026
	Tycho-2 7740-529-1	9.580 ± 0.023	9.625 ± 0.022	9.902 ± 0.023
NGC7213	UCAC3 86-422902	9.925 ± 0.019	10.024 ± 0.023	10.560 ± 0.024
	CD-47 14075	9.608 ± 0.023	9.687 ± 0.025	9.891 ± 0.023
	TYC 8438-57-1	9.584 ± 0.021	9.661 ± 0.025	9.917 ± 0.023
ESO323	TYC 7777-7-1	10.207 ± 0.025	10.226 ± 0.022	10.513 ± 0.026
	RAVE J130620.8-402401	7.105 ± 0.026	7.447 ± 0.038	8.294 ± 0.027
	UCAC2 14614825	10.005 ± 0.021	10.142 ± 0.024	10.672 ± 0.022
F51	2MASS 18450869-6222189	10.644 ± 0.021	10.762 ± 0.024	11.335 ± 0.022
	2MASS 18450354-6219212	11.896 ± 0.023	11.939 ± 0.024	12.248 ± 0.024
F9	2MASS 01240183-5849456	11.534 ± 0.026	11.597 ± 0.025	11.961 ± 0.024
	2MASS 01233777-5849372	12.218 ± 0.027	12.361 ± 0.025	12.994 ± 0.026
	TYC 8480-374-1	10.938 ± 0.025	10.961 ± 0.024	11.307 ± 0.026
AKN120	2MASS 05161394-0009031	9.772 ± 0.022	9.922 ± 0.025	10.410 ± 0.022
	HD 290133	8.734 ± 0.021	8.842 ± 0.057	9.303 ± 0.021
	HD 290134	8.018 ± 0.024	8.171 ± 0.038	8.616 ± 0.024
MARK509	TYC 5760-1417-1	9.085 ± 0.023	9.187 ± 0.025	9.676 ± 0.022
	TYC 5760-1435-1	8.845 ± 0.020	8.946 ± 0.022	9.421 ± 0.023
	TYC 5760-1396-1	11.072 ± 0.023	11.114 ± 0.026	11.363 ± 0.023
MARK1239	2MASS 09523087-0135070	11.017 ± 0.025	11.081 ± 0.024	11.392 ± 0.024
H0557	2MASS 05580396-3819155	12.737 ± 0.035	12.771 ± 0.030	13.188 ± 0.028
	2MASS 05581248-3819318	11.424 ± 0.026	11.467 ± 0.023	11.757 ± 0.023
	2MASS 05581134-3818299	11.796 ± 0.029	11.855 ± 0.025	12.068 ± 0.023
IzW1	2MASS 00533318+1242209	13.512 ± 0.037	13.600 ± 0.033	14.237 ± 0.031
IC4329A	2MASS 13490656-3020366	11.308 ± 0.022	11.402 ± 0.025	11.807 ± 0.024
	2MASS 13491045-3016218	14.041 ± 0.062	14.041 ± 0.049	14.320 ± 0.034
	2MASS 13492434-3020197	13.501 ± 0.038	13.444 ± 0.031	13.830 ± 0.029
IRAS09149	TYC 8944-295-1	11.308 ± 0.022	11.402 ± 0.025	11.807 ± 0.024

Table 4.1: The Standard Star magnitudes and errors as given by the 2MASS survey [6]. Stellar names originates from the Simbad database [3] where applicable, the remainder are referred to by their 2MASS id's.

AGN	Standard Star	Magnitudes:			
		g	r	i	z
NGC3783 [†]	HD 101274	*	*	*	*
	Tycho-2 7740-22-1	13.247± 0.065	12.810± 0.061	12.712± 0.027	12.904± 0.229
	Tycho-2 7740-529-1 [‡]	12.337± 0.005	12.095± 0.003	11.799± 0.001	11.637± 0.001
NGC7213 [†]	UCAC3 86-422902	13.993± 0.097	13.049± 0.133	12.878± 0.044	12.345± 0.138
	CD-47 14075 [‡]	12.141± 0.006	11.936± 0.005	11.723± 0.005	11.343± 0.004
	TYC 8438-57-1 [‡]	12.333± 0.004	12.201± 0.003	11.821± 0.003	*
ESO323 [†]	TYC 7777-7-1	12.592± 0.348	11.725± 0.238	11.503± 0.083	11.447± 0.066
	RAVE J130620.8-402401	13.300± 0.387	12.003± 0.314	10.702± 0.141	10.064± 0.136
MARK509	TYC 5760-1417-1	11.772± N/A	11.123± N/A	10.878± N/A	10.758± N/A
	TYC 5760-1435-1	11.604± N/A	10.939± N/A	10.666± N/A	10.520± N/A
	TYC 5760-1396-1	12.663± N/A	12.364± N/A	12.262± N/A	12.232± N/A
F9	2MASS 01240183-5849456	13.723± 0.040	13.239± 0.023	13.068± 0.006	12.999± 0.009
	2MASS 01233777-5849372	16.323± 0.040	15.222± 0.023	14.628± 0.006	14.440± 0.053
	TYC 8480-374-1 [‡]	12.746± 0.007	12.668± 0.007	12.322± 0.003	12.274± 0.009
F51	2MASS 18450869-6222189	14.271± 0.240	13.382± 0.261	12.853± 0.093	12.632± 0.084
	2MASS 18450354-6219212	14.400± 0.244	13.785± 0.165	13.425± 0.061	13.223± 0.125
AKN120 [†]	2MASS 05161394-0009031	12.852± N/A	12.100± N/A	11.767± N/A	11.575± N/A
	HD 290133	13.104± 0.005	10.634± 0.022	11.112± 0.001	14.146± 0.001
	HD 290134	10.680± N/A	9.727± N/A	10.910± N/A	9.196± N/A

H0557 [†] FILL OUT	2MASS 05580396-3819155	14.883± 0.126	14.409± 0.075	14.239± 0.074	14.126± 0.168
	2MASS 05581248-381931	13.202± 0.110	12.865± 0.086	12.831± 0.154	12.681± 0.099
	2MASS 05581134-3818299	13.313± 0.106	13.039± 0.080	13.045± 0.113	12.907± 0.118
IC4329A [†]	2MASS 13490656-3020366	13.724± 0.014	13.110± 0.001	12.929± 0.003	12.768± 0.049
	2MASS 13491045-3016218	15.951± 0.013	15.501± 0.033	15.262± 0.011	*
	2MASS 13492434-3020197	15.465± 0.017	15.023± 0.004	14.883± 0.010	14.583± 0.013
IRAS9149 [†]	TYC 8944-295-1	12.499± 0.005	11.787± 0.003	11.394± 0.034	11.181± 0.001
	2MASS 09162418-6219030	15.408± 0.064	14.492± 0.080	14.033± 0.031	13.711± 0.096
IzW1 [†]	2MASS 00533318+1242209	17.058± 0.004	16.057± 0.003	15.646± 0.003	15.442± 0.003
MARK1239 [†]	2MASS 09523087-0135070	13.069± N/a	12.633± N/A	12.446± N/A	12.354± N/A

Table 4.2: The Standard Star magnitudes and errors as given by the PanSTARRS survey [5] where applicable, and as determined through this project otherwise. [†] indicates AGN at declination below -30° , thus not being present in PanSTARRS, and [‡] indicates a standard star determined in this project based on single night observations due to the low sampling of the AGN, at the time of the Standard Star calibration, and the lack of good nights of constant visibility in the area coinciding with the AGN sampling. * indicates Standard Stars that in some or all bands saturates the detector to the point of loss in linearity. N/A indicates Standard Stars in the outer fringes of the observed sky area, thus by happenstance not visible in the frames at the nights, of good constant visibility, that can be used for Standard Star calibration.

4.3.3. The error on the AGN light curves

The *signal-to-noise ratio* (see section 2.2.4) was determined based on the sampling of background sky variation (the sky-background contribution to the shot-noise in the pre-background subtracted JHK band images (for further discussion on the nature of shot noise see *Hughes & Hase 2010 [18]*)) in three different locations, located around the AGN, that were pre-determined to have no expectation of viewable astronomical objects. For this purpose the previously *accurate astrometry method* was utilised, due to the unimportance of the exact sky location in an uninhabited area. The use of three different locations was chosen to minimize the potential effect of cosmic ray hits, and

any effects originating from differences arising across the image plate. The different sky-background variations obtained was combined and analysed as one and the error obtained from the different objects (AGN and standard stars) becomes (*Hughes & Hase 2010 [18]*)

$$\begin{aligned} F_{AGN} &= k \frac{signal_{AGN}}{signal_{standardstar}} \quad \Rightarrow \\ \alpha_{F_{AGN}} &= F_{AGN} \sqrt{\left(\frac{\alpha_{signal_{AGN}}}{signal_{AGN}} \right)^2 + \left(\frac{\alpha_{signal_{standardstar}}}{signal_{standardstar}} \right)^2}, \end{aligned} \quad (4.1)$$

with α being the *signal-to-noise ratio* and F the flux. The *signal-to-noise ratio* were further analysed to understand the contribution from either the *signal*, the *sky-background* or the *RON*. The error propagated through rearrangement of *equation 2.3* is

$$\begin{aligned} F_* &= F_{ref} 10^{\frac{m_{ref} - m_*}{2.5}} \quad \Rightarrow \\ \alpha_{F_*} &= \frac{\ln(10)\alpha_{m_*}}{2.5} F_{ref} 10^{\frac{m_{ref} - m_*}{2.5}}, \end{aligned} \quad (4.2)$$

with F_{ref} and m_{ref} being the reference flux and magnitude respectively that is being used for calibration, in this project the vega zero-magnitude for the JHK bands, and the AB zero-magnitude values for the griz bands. F_* and m_* is the standard star flux and magnitudes, while α_{m_*} is the error in the standard star magnitude, either as determined in this project for the griz bands at declination below -30° , or the relevant PanSTARRS (griz) or 2MASS (JHK) values. As

$$\alpha_{Signal_{AGN}} = \frac{Signal_{AGN}}{SNR_{AGN}} \quad (4.3)$$

and the propagated error of multiplied variables are

$$Z = A \times B \quad \alpha_Z = Z \sqrt{\left(\frac{\alpha_A}{A} \right)^2 + \left(\frac{\alpha_B}{B} \right)^2}, \quad (4.4)$$

thus reducing the total error to

$$\begin{aligned} F_{AGN} &= \frac{signal_{AGN}}{signal_*} F_{ref} 10^{\frac{m_{ref} - m_*}{2.5}} \quad \Rightarrow \\ \alpha_{F_{AGN}} &= \frac{signal_{AGN}}{signal_*} F_{ref} 10^{\frac{m_{ref} - m_*}{2.5}} \times \sqrt{\left(\frac{1}{SNR_{AGN}^2} + \frac{1}{SNR_*^2} \right) + \frac{\ln(10)\alpha_{m_*}}{2.5}}. \end{aligned} \quad (4.5)$$

This is naturally baring the assumption that no error is found on the zero-magnitude flux itself, an assumption not entirely accurate (*table 2.2*), but compared to the *signal-to-noise ratio*, and the uncertainty in the standard star magnitude, this systematic, and minor, inaccuracy in the zero-magnitude flux is negligible.

The code for the calibration of the SNR is;

```
In [10]: def SNR(data1,data2,header,ap1,ap2):
    npix1 = np.pi*ap1**2/((header['PIXSCALE']/3600.)**2)
    npix2 = np.pi*ap2**2/((header['PIXSCALE']/3600.)**2)
    #print npix1
    #data2_1 = ((data2-data1)/npix2)*npix1
    data1_2 = data1
    data2_2 = abs(data2)

    return data1_2*header['DIT']*header['NDIT']*header['GAIN']/(np.sqrt(
        (data1_2*header['DIT']*header['NDIT']*header['GAIN']+
         float(header['GAIN']))*npix1*data2_2*header['DIT']*
         header['NDIT']+
         header['NDIT']*npix1*header['RON']**2))
```

Figure 4.9: The SNR calculation in the light curve algorithm.

with "header['DIT']" being the integration time (in seconds) pr. image, "header['NDIT']" being the number of images in a "stack" for the JHK bands, "header['GAIN']" being the gain in e^- / ADU (5 for the JHK bands, and 1 for the griz bands). The "data1" is the by SEXtractor determined ADU inside the aperture, while the data2 is the sky-background ADU pr. pixel. "npix1" is the number of pixels (including fractional pixels) expected inside the aperture ("ap1"), this does not provide an error, as the SEXtractor estimates the pixel area down to 1/25th of a pixel. The RON for the JHK bands is given as "header['RON']" and is given in the fits header as $100 e^-$, and the griz bands are given as "header['RONOISE']" and is given in the fits header as $4.5 e^-$. The Dark Noise is not given for the JHK bands, it is however present in the fits header for the griz bands and is given as $0.1 ADUs^{-1}$, and is thus included in that SNR estimation.

The sky-background is found by;

```
In [6]: def curve(quasar,header,w,center,apparature):
    '''Determines the FLUX of the stellar object given the the numpy array of the image, \
    the header of the fits file, the astropy coordinate representation, \
    the object position and the apparature of interest'''
    header,AGNdata,RAsstd,DECstd,pixspa,RAsstdpix,DECstdpix,exptime = Basic(quasar,header)
    #AGNdata = np.swapaxes(AGNdata,0,1)
    y, x = np.ogrid[0:header['NAXIS1'],0:header['NAXIS1']]
    #w = np.swapaxes(w,0,1)
    #F AGN = np.zeros((512,512,3)) #((int(2*apparature/pixspa)+1,int(2*apparature/pixspa)+1,3))
    #print center
    x1 = w.all2pix(center[0],center[1],0)
    x1,y1 = (x1[0]),(x1[1])
    if 15 < x1 < header['NAXIS1'] - 15 and 15 < y1 < header['NAXIS2'] - 15:
        try:
            mask = ((y-y1)**2 + (x-x1)**2) > (apparature/float(pixspa))**2
            AGNdata[mask] = float(0)
            mask = AGNdata == 0.
            rows = np.flatnonzero(~mask).sum(axis=1)
            cols = np.flatnonzero(~mask).sum(axis=0)
            AGNdata = AGNdata[rows.min():rows.max()+1, cols.min():cols.max()+1]
            #print apparature/float(pixspa)
        except:
            AGNdata = np.array([[float('nan'),float('nan')],[float('nan'),float('nan')]])
    else:
        AGNdata = np.array([[float('nan'),float('nan')],[float('nan'),float('nan')]])
    #if np.sum(AGNdata) < 500:
    #    AGNdata = np.array([[float('nan'),float('nan')],[float('nan'),float('nan')]])
    return AGNdata, x1, y1
```

Figure 4.10: The code determining the sky-background.

with "w" being the "astropy.wcs" of the fits image. The relevant value is then all the nonzero array elements.

The error calculation is done using equations 4.1-4.5 and the code is in figure ??.

```
In [12]: def error(SIGNAL_agn,SIGNAL_star,SNR_agn,SNR_star,star_mag,star_mag_err,vega_flux,vega_mag):
    SIGNAL_ERR = abs(SIGNAL_agn/SIGNAL_star)*np.sqrt(SNR_agn**(-2) + SNR_star**(-2))
    FLUX_CAL_ERR = star_mag_err
    SIGNAL = vega_flux*10**((VEGA_mag-star_mag)/2.5)
    FLUX_CAL = abs(SIGNAL_agn/SIGNAL_star)*VEGA_FLUX*((np.log(10)/2.5)*10**((VEGA_mag - star_mag)/2.5))
    return np.sqrt((SIGNAL**2*SIGNAL_ERR**2 + FLUX_CAL**2*FLUX_CAL_ERR**2))
```

Figure 4.11: The code determining the error in the light curves.

The qualification of "VEGA_FLUX" and "VEGA_MAG" for the reference flux and magnitude is legacy code, and retained as any one name is as good as another. Any star or magnitude system can be utilised for the flux calibration, assuming the stellar flux is well constrained. The griz bands utilises the AB system, as this is the PANSTARRS choice, and the JHK bands utilises the 2MASS system based on VEGA. The relative error on the light curves, excluding the error originating in the standard star magnitude determination is in *figure ??*.

```
In [13]: def relerror(SIGNAL_agn,SIGNAL_star,SNR_agn,SNR_star,star_mag,star_mag_err,vega_flux,vega_mag):
    SIGNAL_ERR = abs(SIGNAL_agn/SIGNAL_star)*np.sqrt(SNR_agn**(-2) + SNR_star**(-2))
    SIGNAL = vega_flux*10**((VEGA_mag-star_mag)/2.5)
    return np.sqrt((SIGNAL**2*SIGNAL_ERR**2))
```

Figure 4.12: The error determination excluding the magnitude error of the associated standard star.

4.4. LIGHT CURVES

The light curves generated throughout this project are subject to sampling infrequencies, weather conditions and the availability of standard stars and the information associated with them. The general trend is that the data is subject to high SNR, with the JHK bands providing the most consistent fitting with least scatter.

4.4.1. NGC3783

The AGN in NGC3783, located at (11:39:01.71 -37:44:19.01) in the ICRS coordinate system (all coordinates in this report is given in this system), is the best sampled AGN in this project that shows activity (*figures 4.14*). Due to its superior sampling, and its low magnitude, it is the most extensively used AGN in this paper for demonstration purposes. NGC3783 shows generally high SNR (*figure 4.15*), that for the JHK bands is in excellent agreement with the, by the REM website [19], expected SNR for the given magnitudes. The extreme scatter in the z-band is unaccounted for, but it is the general experience across the project that this band varies significantly. The JHK band light curves for this AGN (*figures 4.16*) allows for comparison of the flux calibration based upon several different standard stars, and shows a high level of agreement. The same comparison is not available in the griz bands due to the saturation of *HD 101274*, and

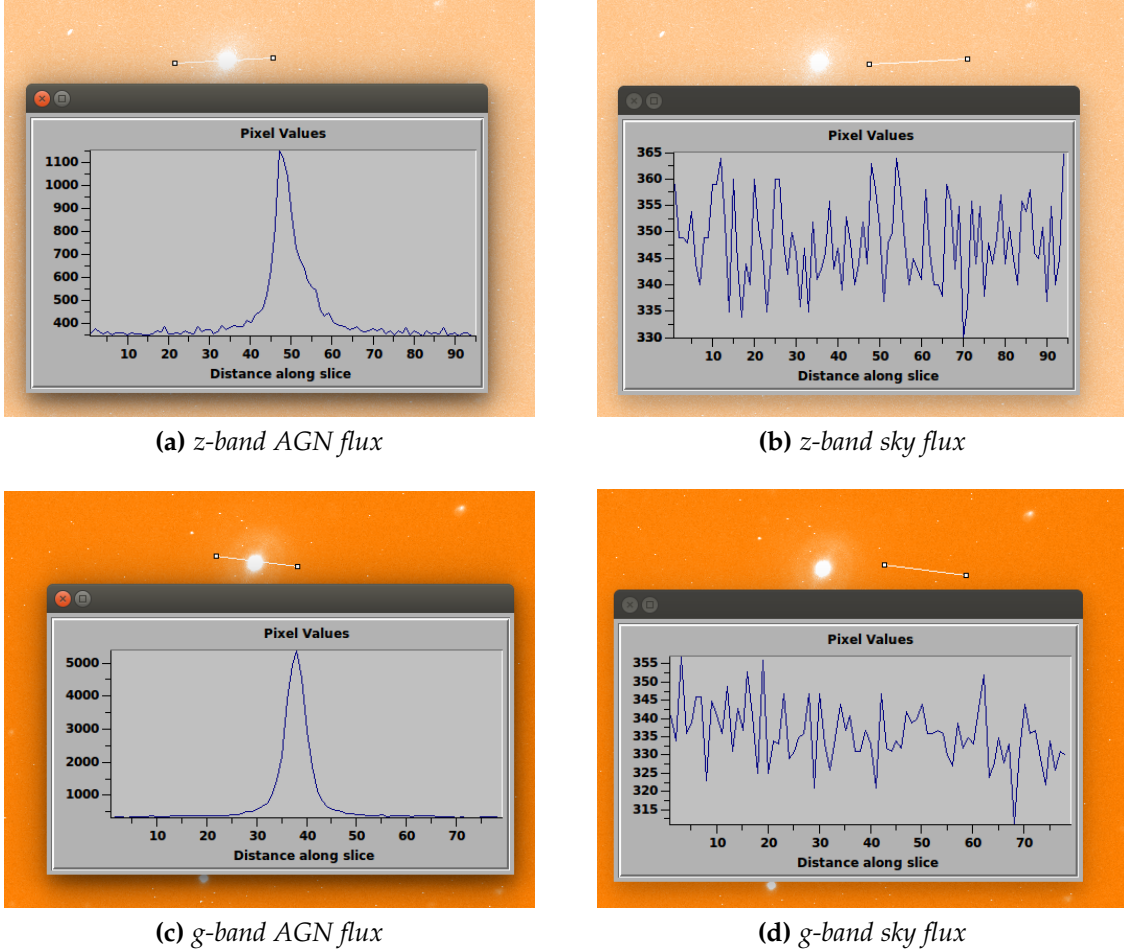


Figure 4.13: NGC3783 z- and g-band fluxes for the AGN and the sky background from 8th May 2016. The low z-band SNR originates in the low count level in the z-band despite comparable sky backgrounds.

the rare sampling of TYC 7740-22-1 due to the orientation of the image frames.

The structure function plot in *figure C.1* illustrates the data quality. The JHK bands structure functions, in particularly the K-band, is in agreement with the NGC3783 structure functions from Favre et al. 2005 [15]. However the griz bands all show significant variations from this standard. The early "turnoff point" of the griz bands seems to indicate that the scatter is sufficient that the temporal points becomes uncorrelated. It appears that most bands are in common agreement that the variability happens over 150-200 days.

4.4.2. AKN120

The AGN AKN120 (

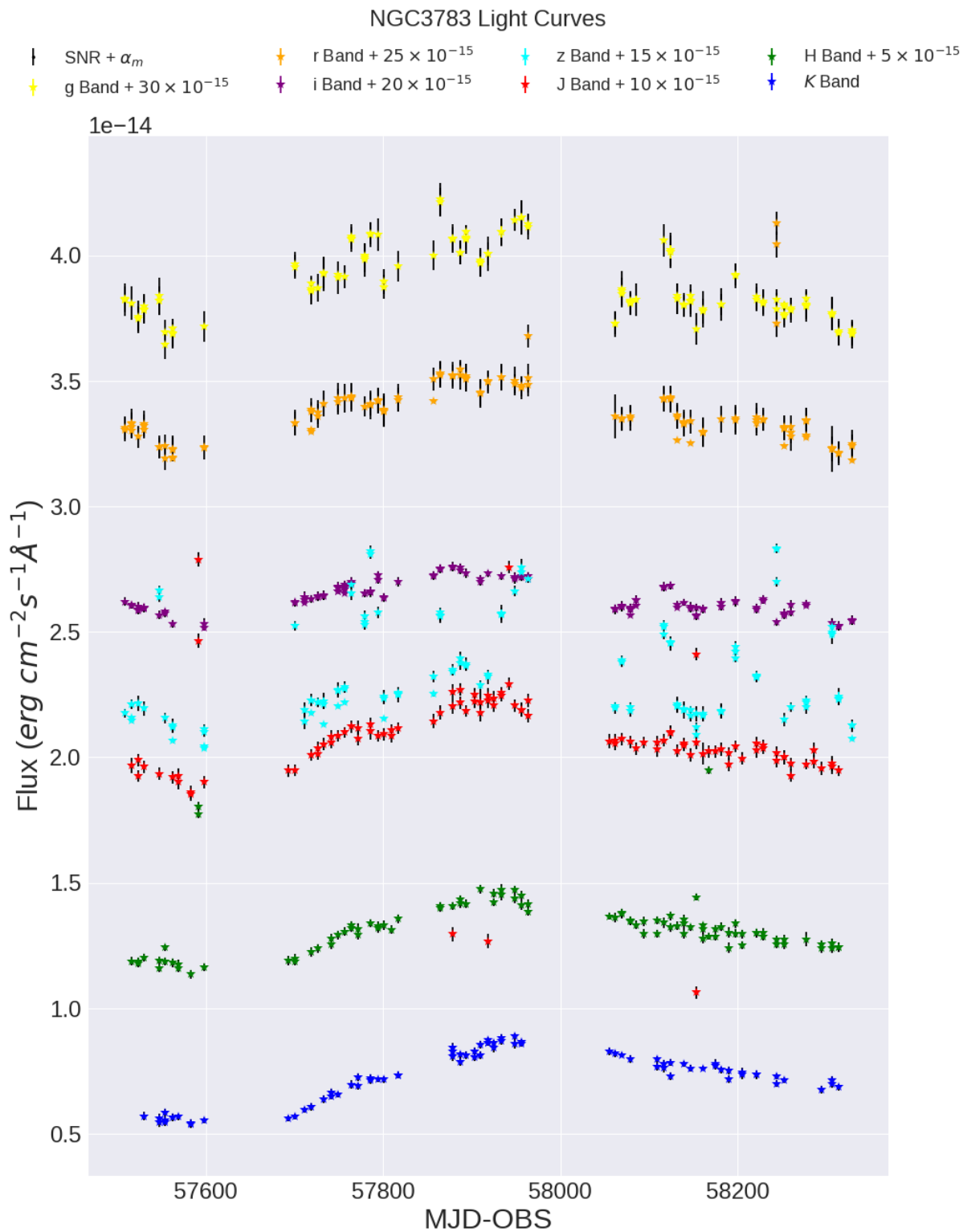


Figure 4.14: The NGC3783 fluxes in the various bands shown together for comparisons.

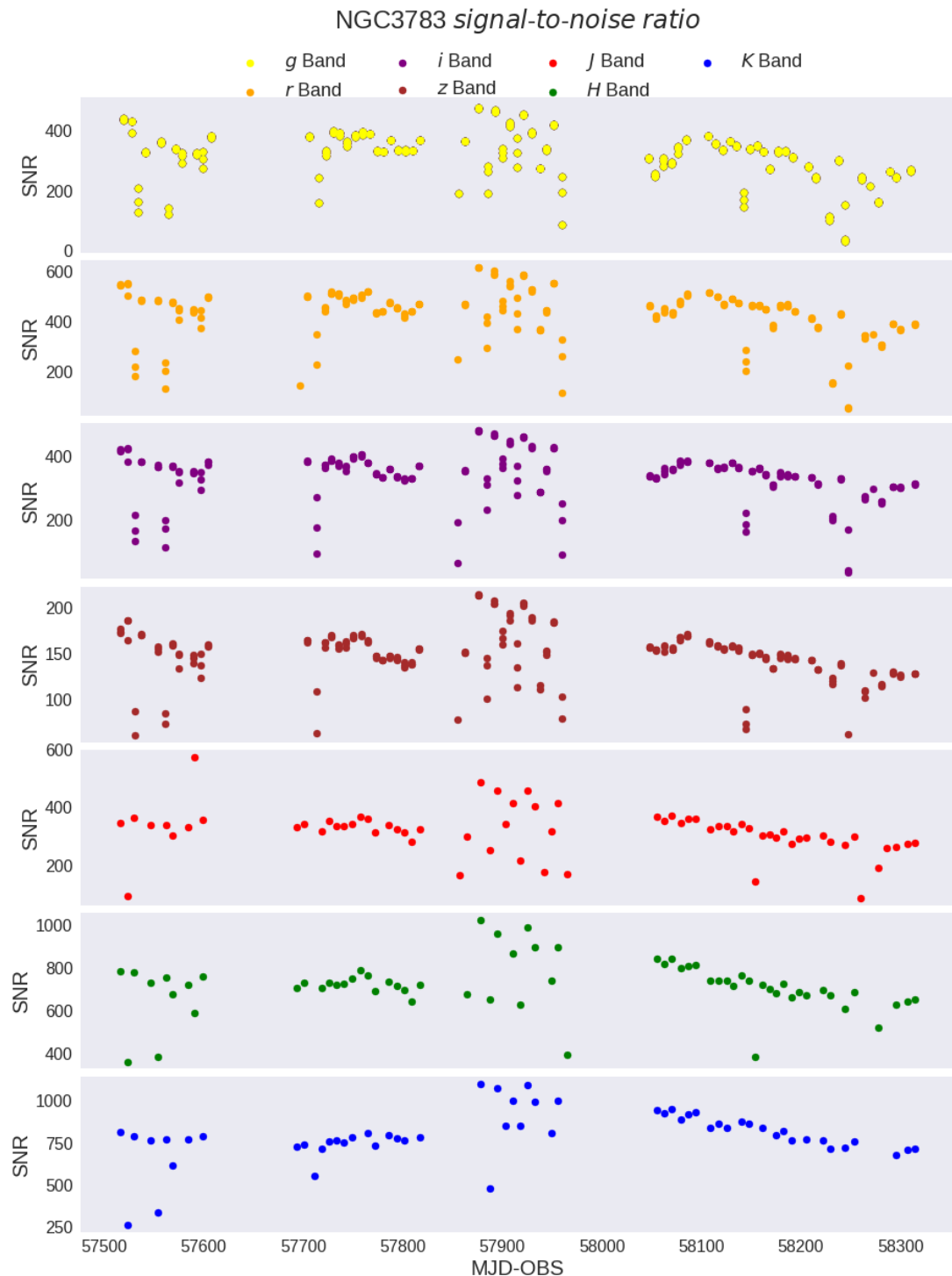


Figure 4.15: The NGC3783 signal-to-noise ratios for the various bands.

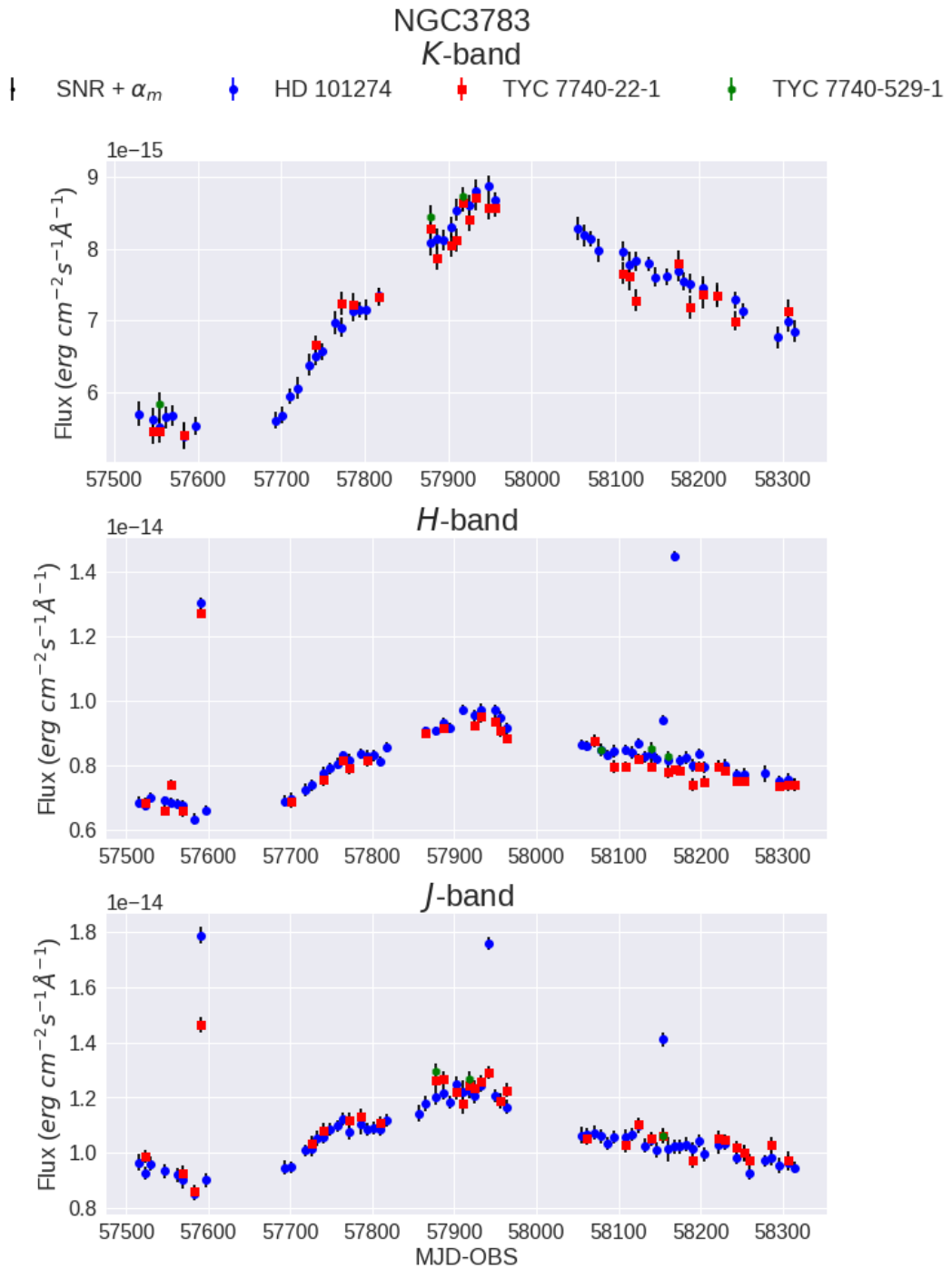


Figure 4.16: The observed light curves for the AGN in NGC3783 from the JHK bands shown individually showing excellent agreement between the different standard stars in the flux calibration.

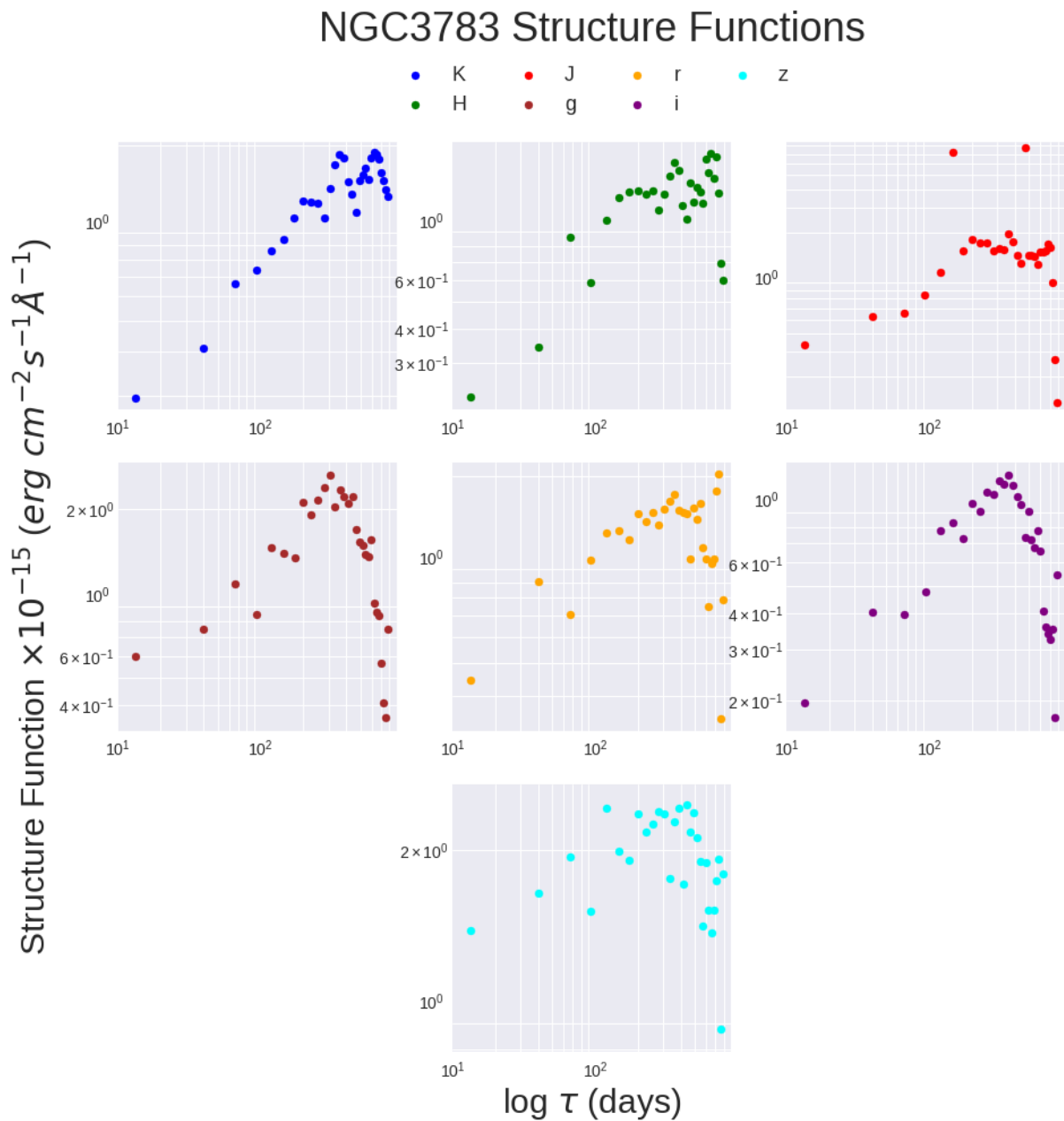


Figure 4.17: The NGC3783 structure function plots in the different observed bands.

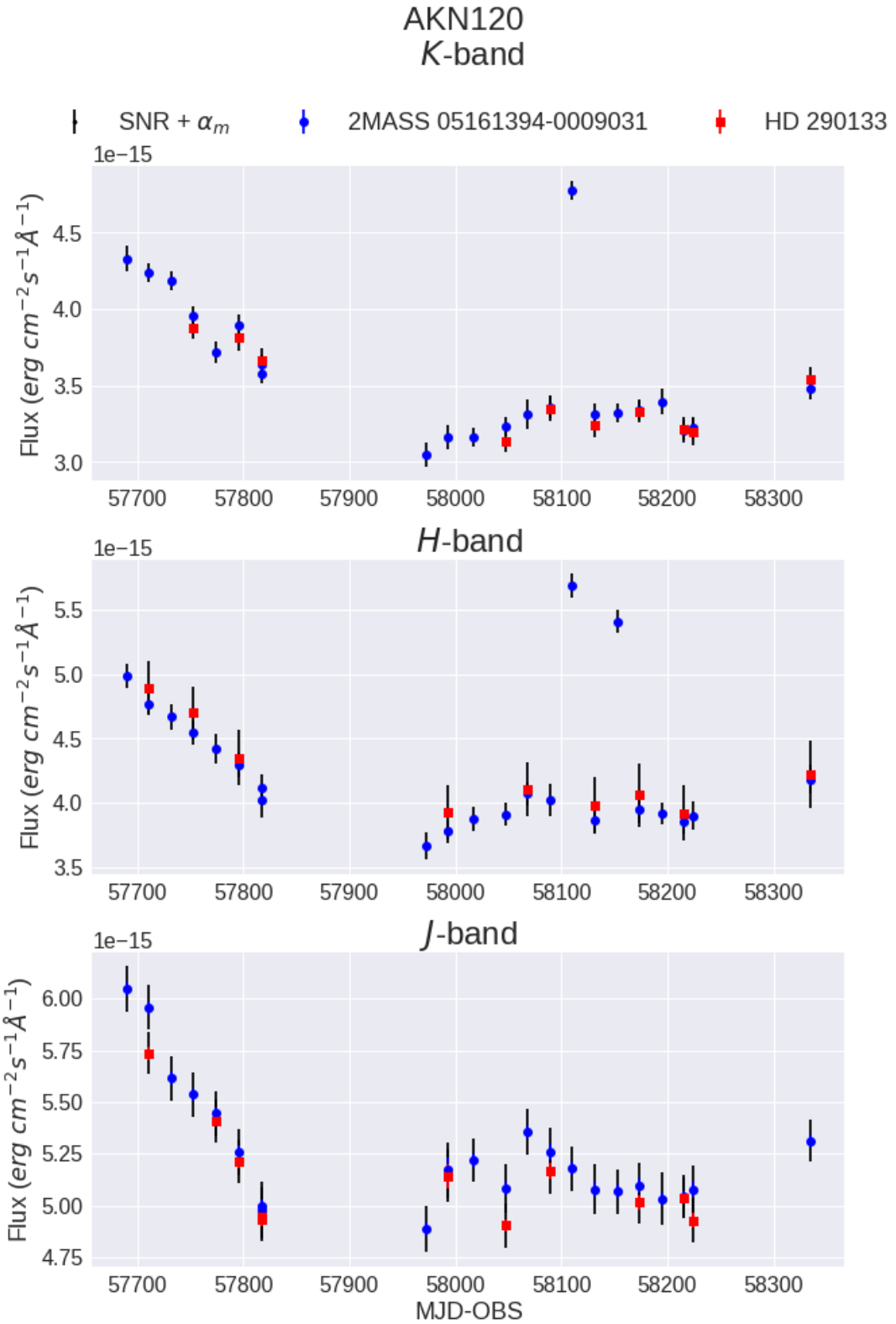


Figure 4.18: The observed light curves for the AGN in AKN120 from the JHK bands. The blue data is as compared to the reference star TYC 7777-7-1, the red data is compared to the star HD 290133 and the green data is compared to the standard star HD 290134.

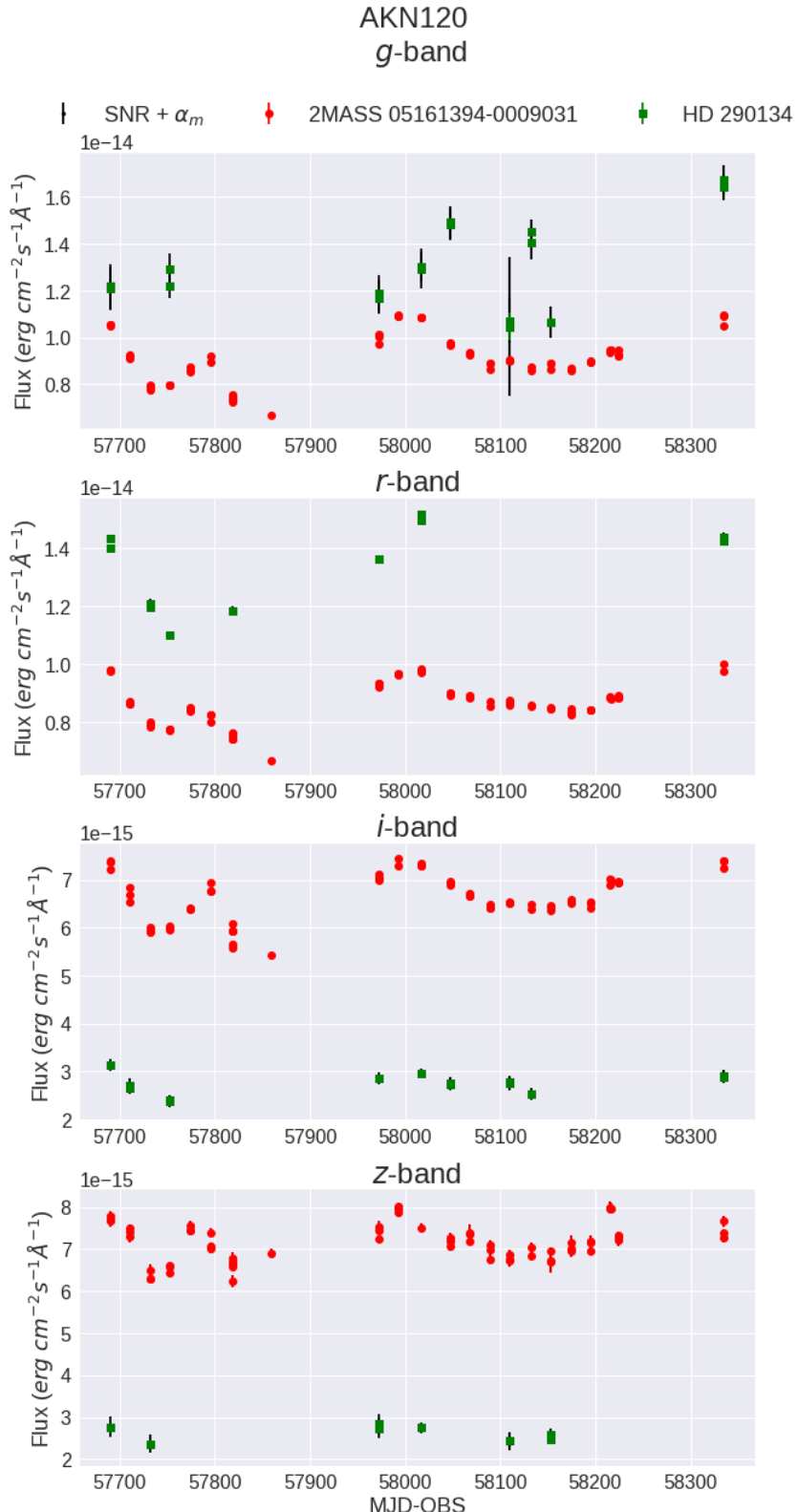


Figure 4.19: The observed light curves for the AGN in AKN120 from the griz bands. The blue data is as compared to the reference star TYC 7777-7-1, the red data is compared to the star HD 290133 and the green data is compared to the standard star HD 290134.

4.4.3. F51

F51 (18:44:53.991 -62:21:52.83) is one of the southernmost AGNs in this investigation. The standard star calibration in this frame was done using 3 different stars (*table ??*). As appears to be common when calibrating stellar magnitudes from differing standard stars, the magnitude associated error in the resultant AGN flux is vastly dominant (*figure 4.20*). The F51 is rare in this sample due to the clear trend demonstrated across all bands, despite the usual increased scatter in the z-band.

4.4.4. F9

F9 (01:23:45.764 -58:48:20.82) is only sampled once in the K band, and contrary to the norm, the F9 AGN appears to have the most obvious structure in the optical bands. *Figure 4.21* shows the F9 light curves.

4.4.5. H0557

H0557 (05:58:02.057 -38:20:04.43) shows excellent agreement between the 3 reference stars used for the flux calibration. The AGN has, over the course of observation, undergone a decrease in luminosity by around 25%. It again becomes obvious that the z-band is much more difficult to constrain. The calibration of the gri-bands utilised 3 standard star, of which the two were the *P525-E* star, and the latter the *SA092_342* star. It did however become apparent that the *P525-E* star observation on 10/11-17 provided extremely inaccurate measurements in the z-band. As such this observation was excluded.

4.4.6. MARK1239

The AGN MARK1239 (09:52:19.168 -01:36:44.10) (*figure 4.23*) provides a clear indication of lag between the gr- and JHK-bands (*figures 4.24 & 4.25*) through the delay, and smoothening of the slope seen early in the gr-bands. The i- and z-bands, when cleaned of the worst outliers in the dataset, appears far too support this somewhat despite the increased scatter.

4.4.7. ESO323

The ESO323 (13:06:26.115 -40:24:52.63) demonstrate the error from the imprecise magnitude calibrations. The ESO323 reference stars have been calibrated based upon 3 different stars, on three separate nights. Towards the end of the observational period the JHK-bands seems to indicate a break in the increasing luminosity, whereas this break appears to have happened in the r- and i-bands around 50-100 days earlier.

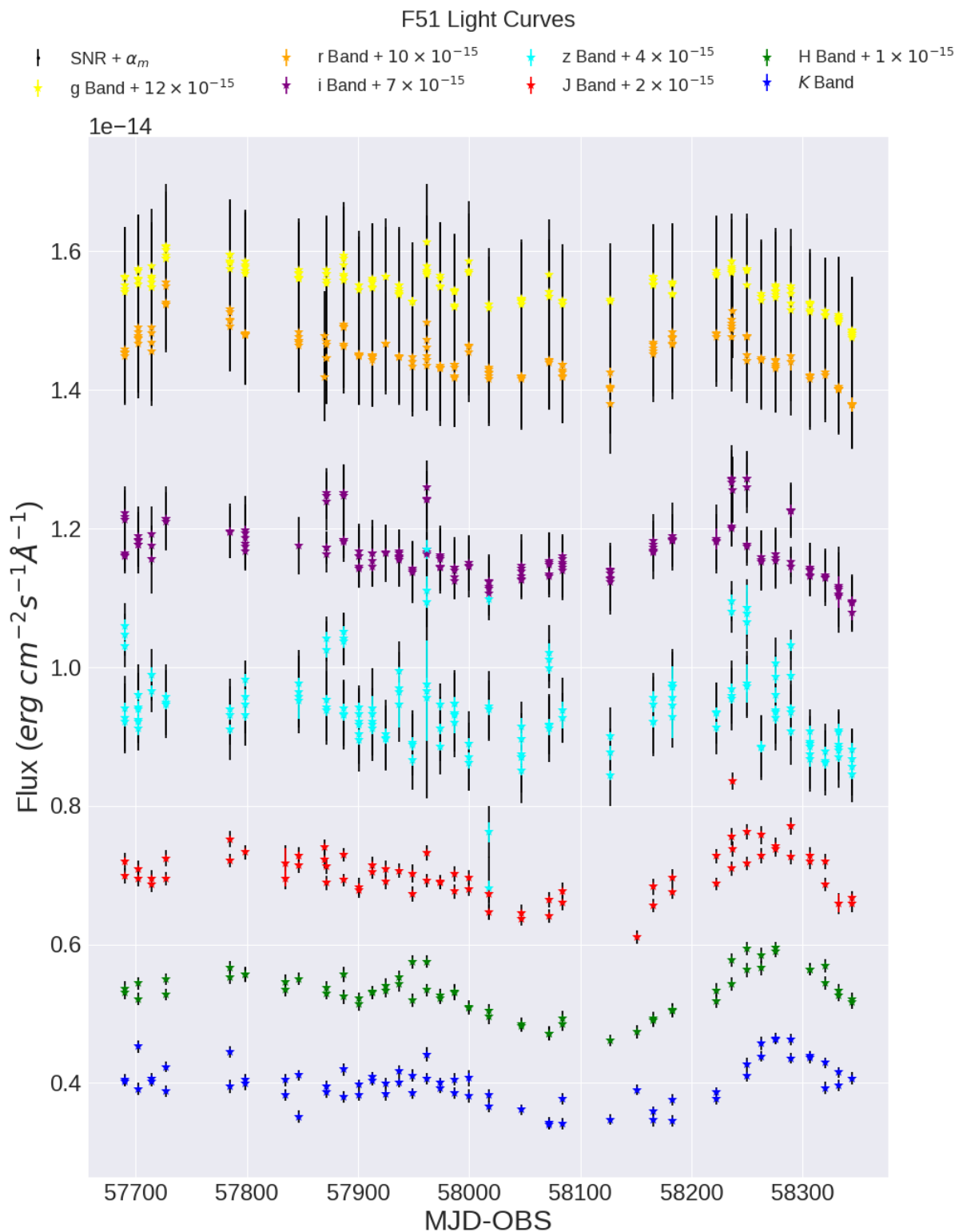


Figure 4.20: The F51 fluxes in the various bands shown together for comparisons.

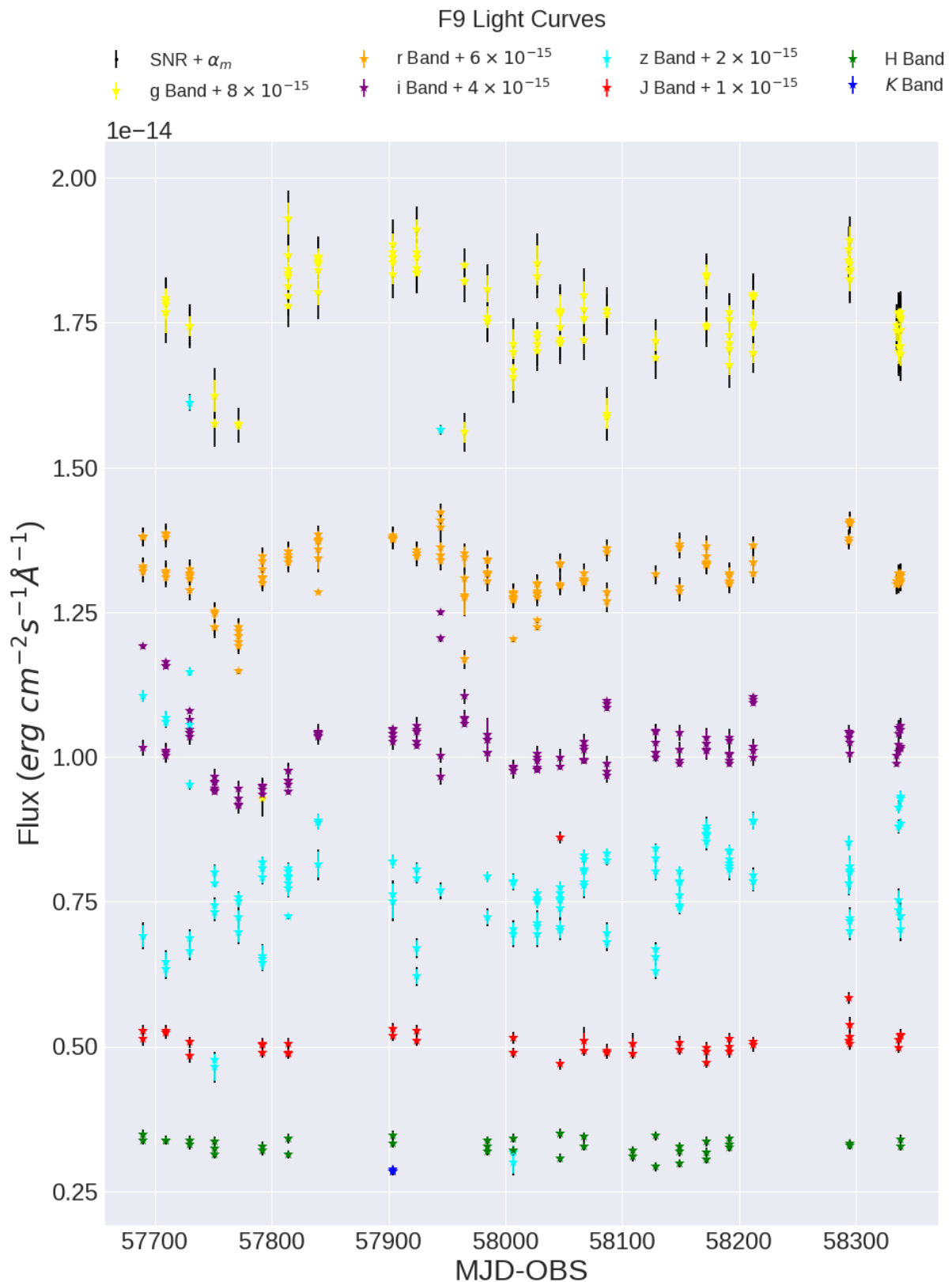


Figure 4.21: The F9 fluxes in the various bands shown together for comparisons.

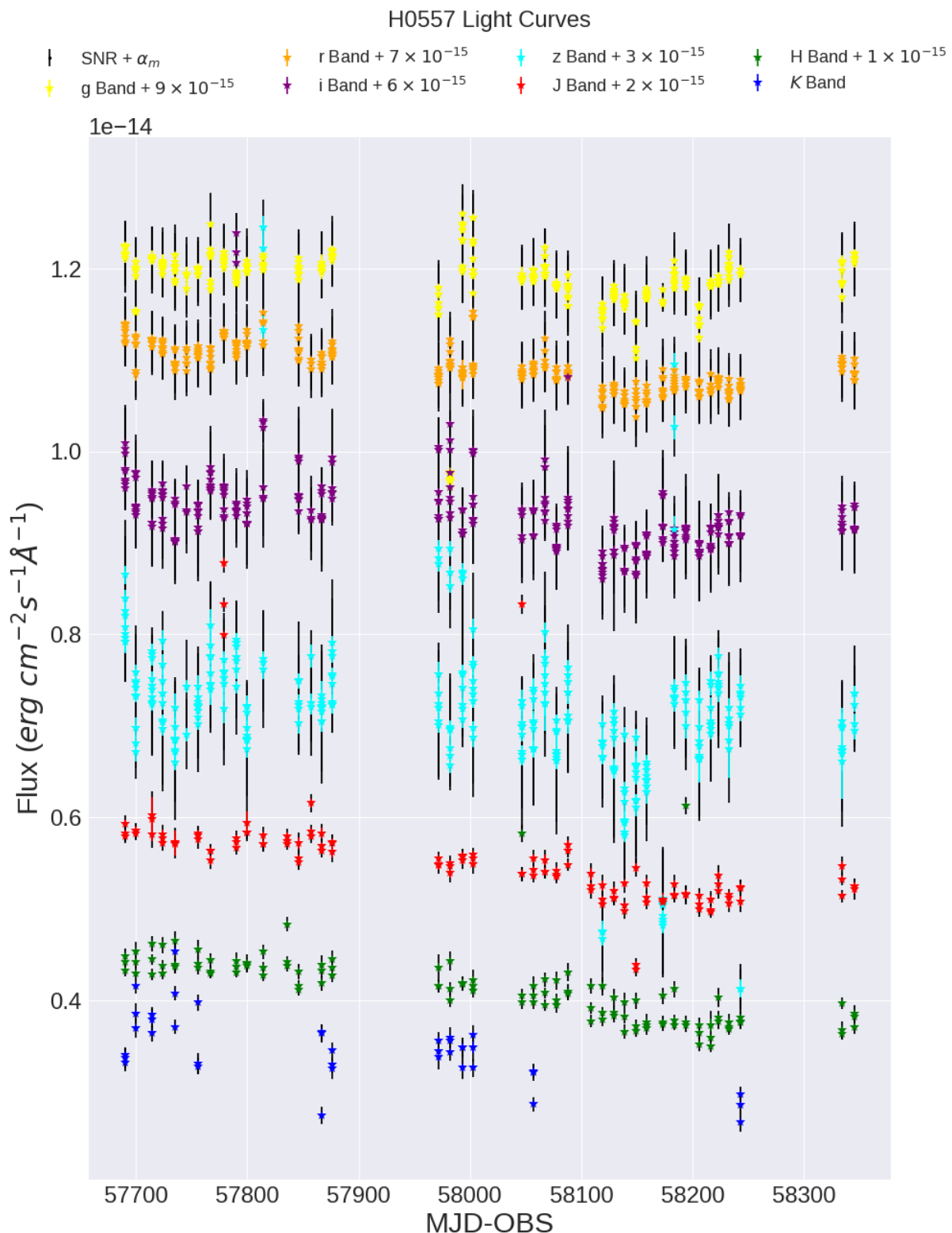


Figure 4.22: The H0557 fluxes in the various bands shown together for comparisons.

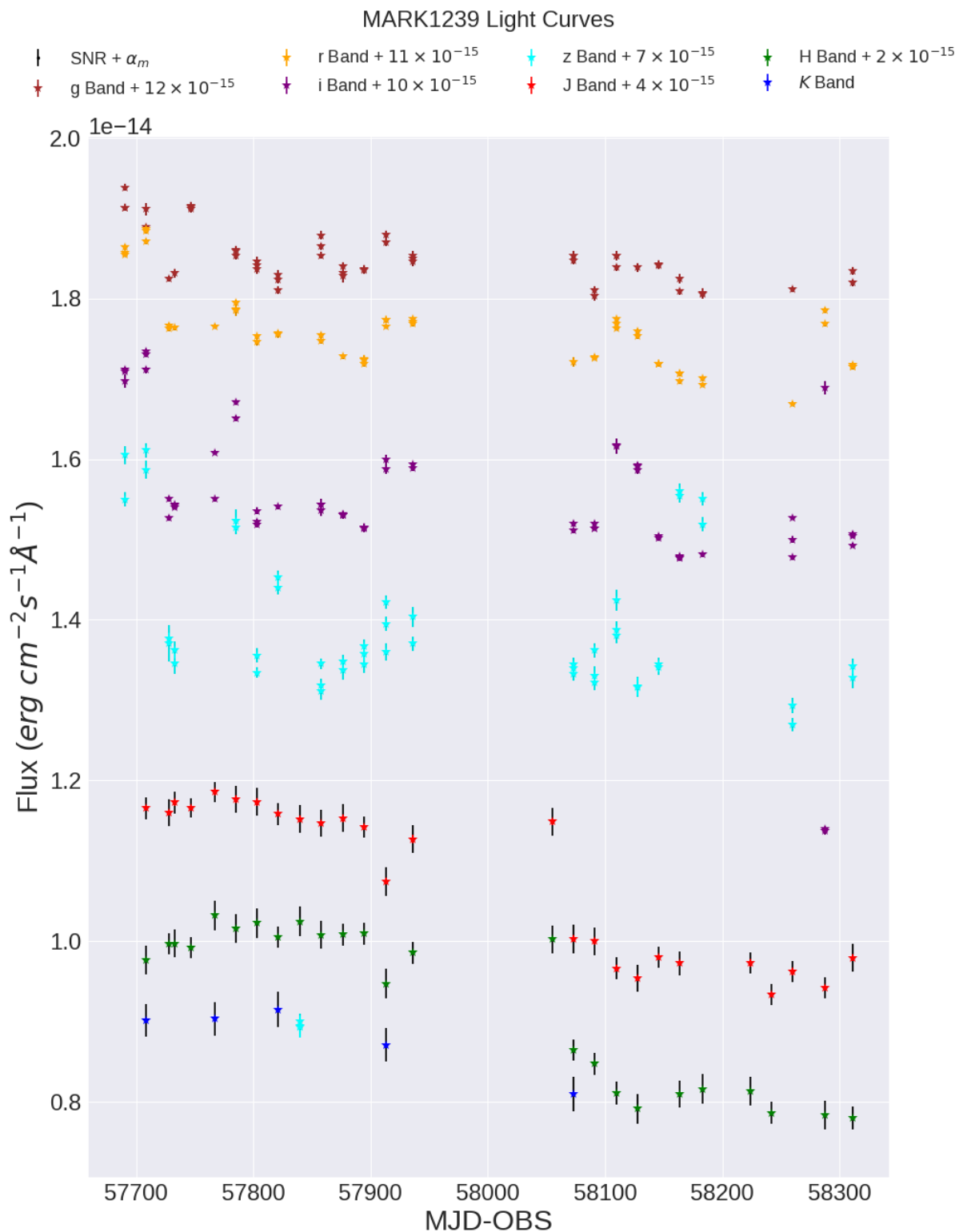


Figure 4.23: The MARK1239 fluxes in the various bands shown together for comparisons.

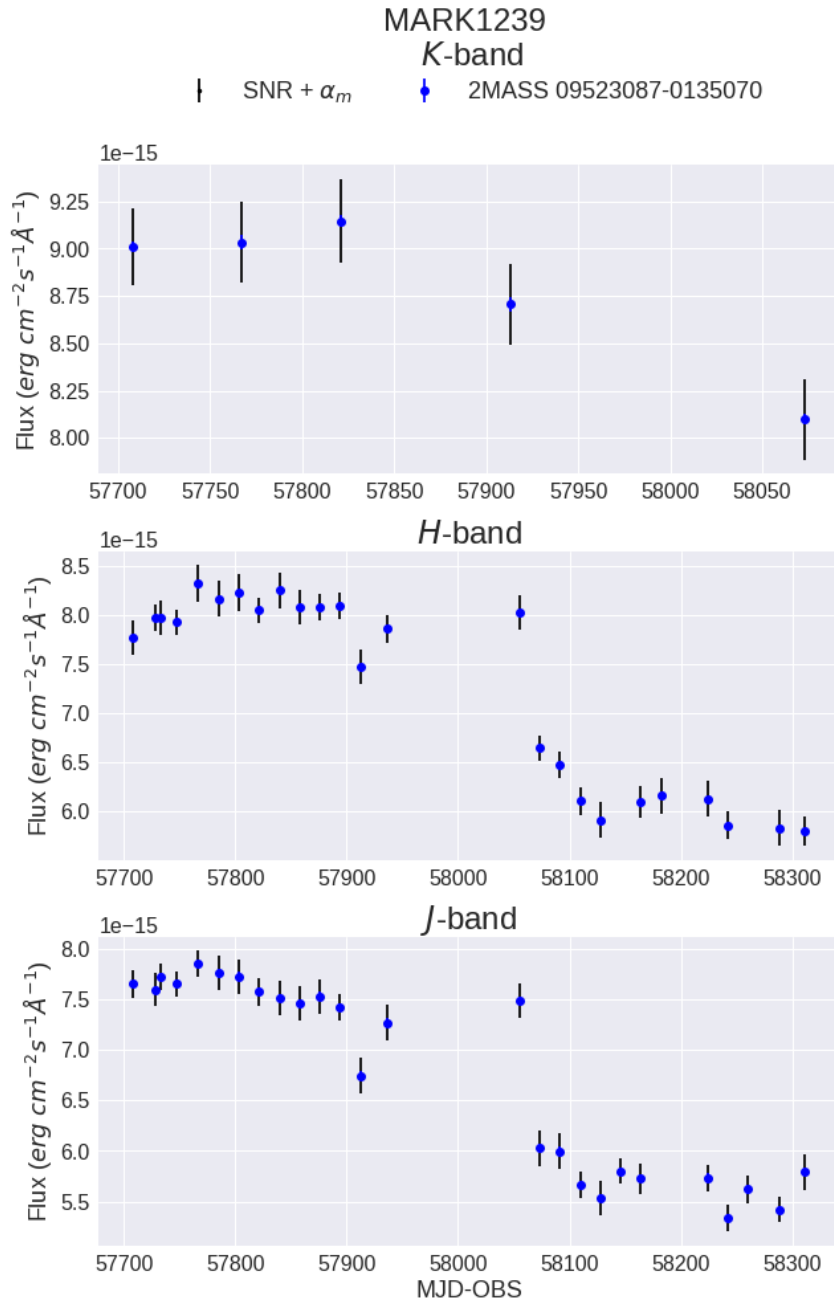


Figure 4.24: The observed light curves for the AGN in MARK1239 from the JHK bands shown individually. When taken in conjunction with the *g*- and *r*-band light curves they indicate the smoothening and delay of the light curve in the IR.

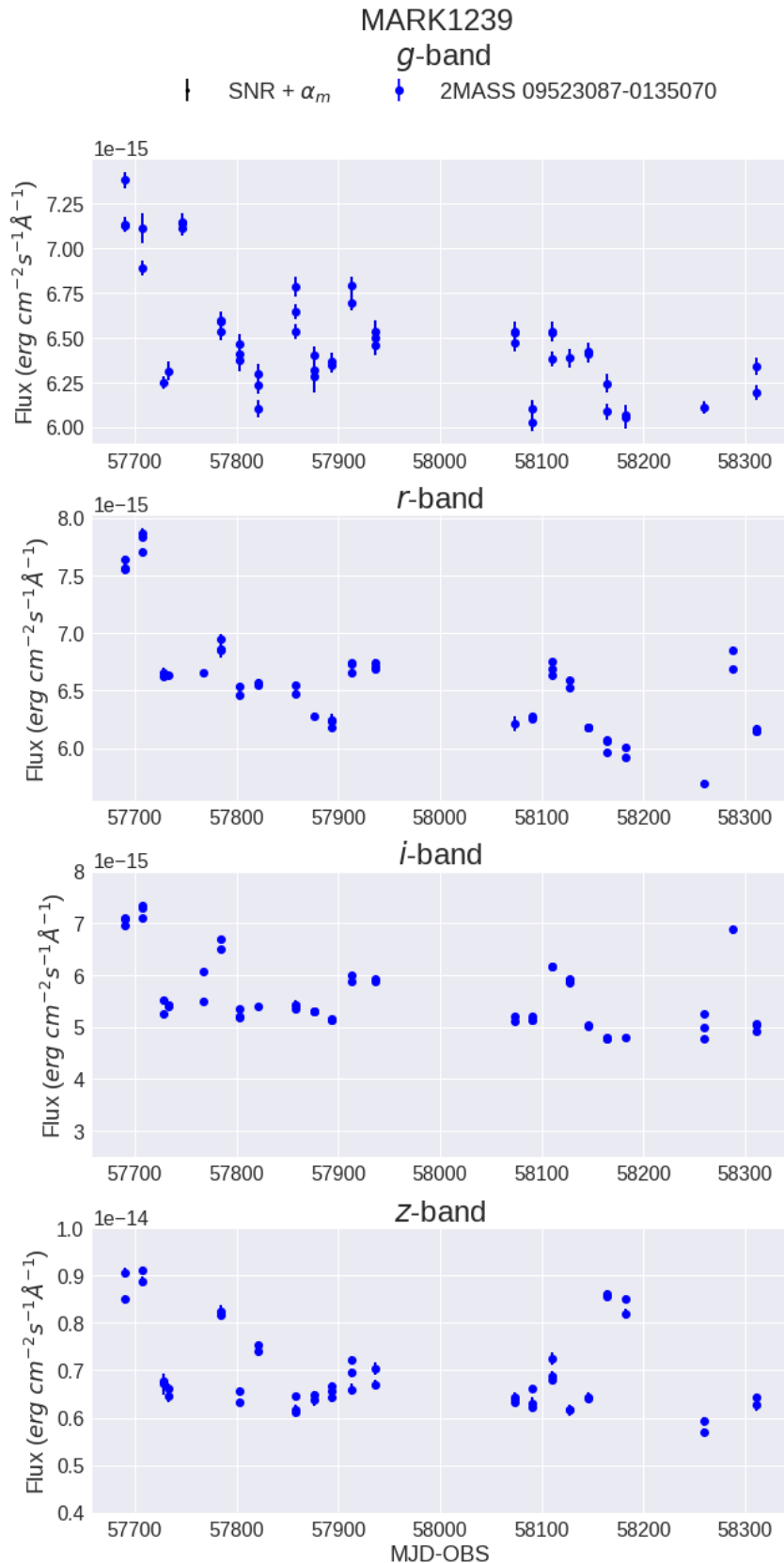


Figure 4.25: The observed optical light curves from MARK1239. Despite the scatter, the g- and r-band light curves can be seen in comparison with the JHK band light curves, and shows the indications of thermal lag.

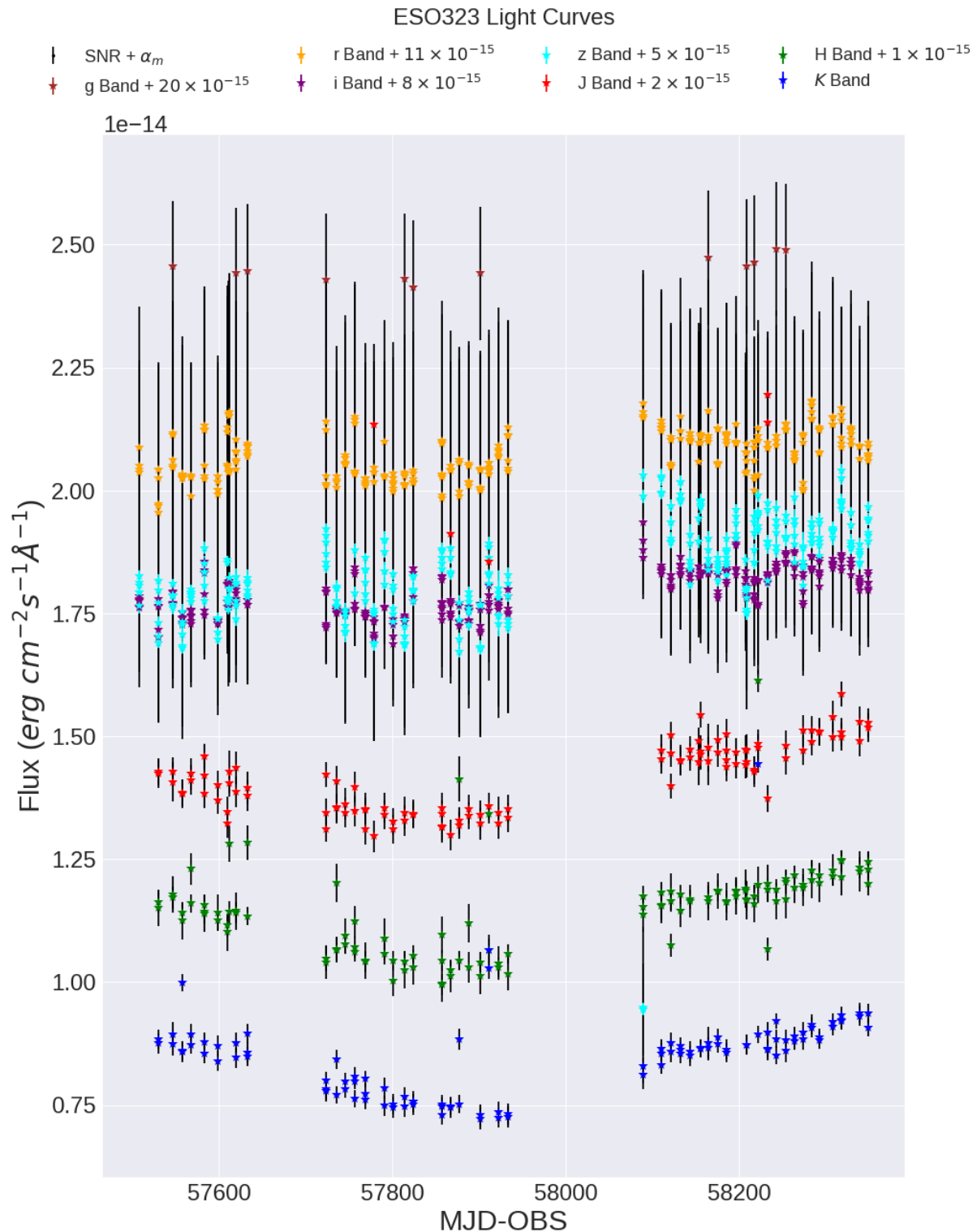


Figure 4.26: The ESO323 fluxes in the various bands shown together for comparisons. All flux calibrations has been scaled to TYC 7777-7-1.

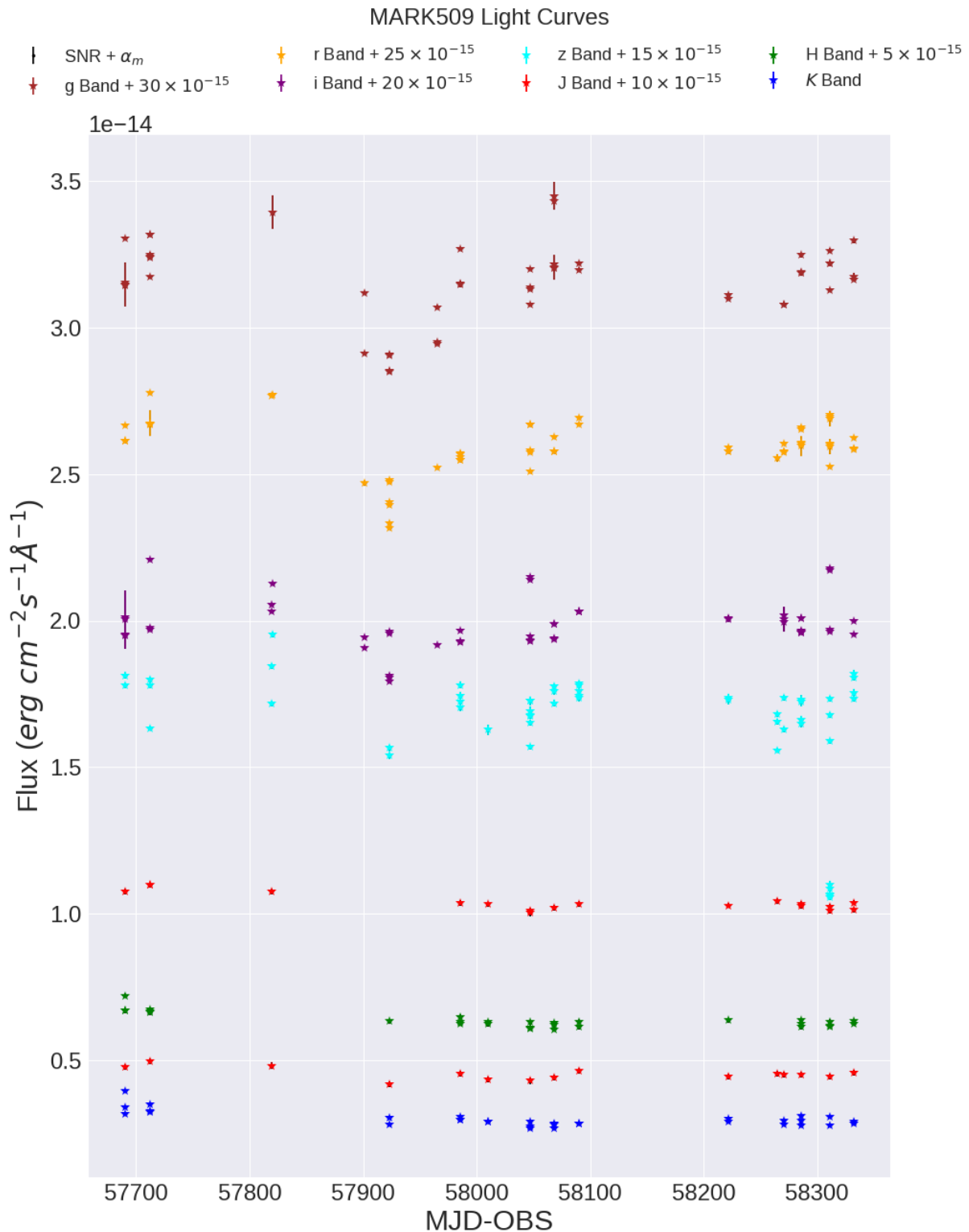


Figure 4.27: The MARK509 fluxes.

4.4.8. MARK509

4.4.9. NGC7213

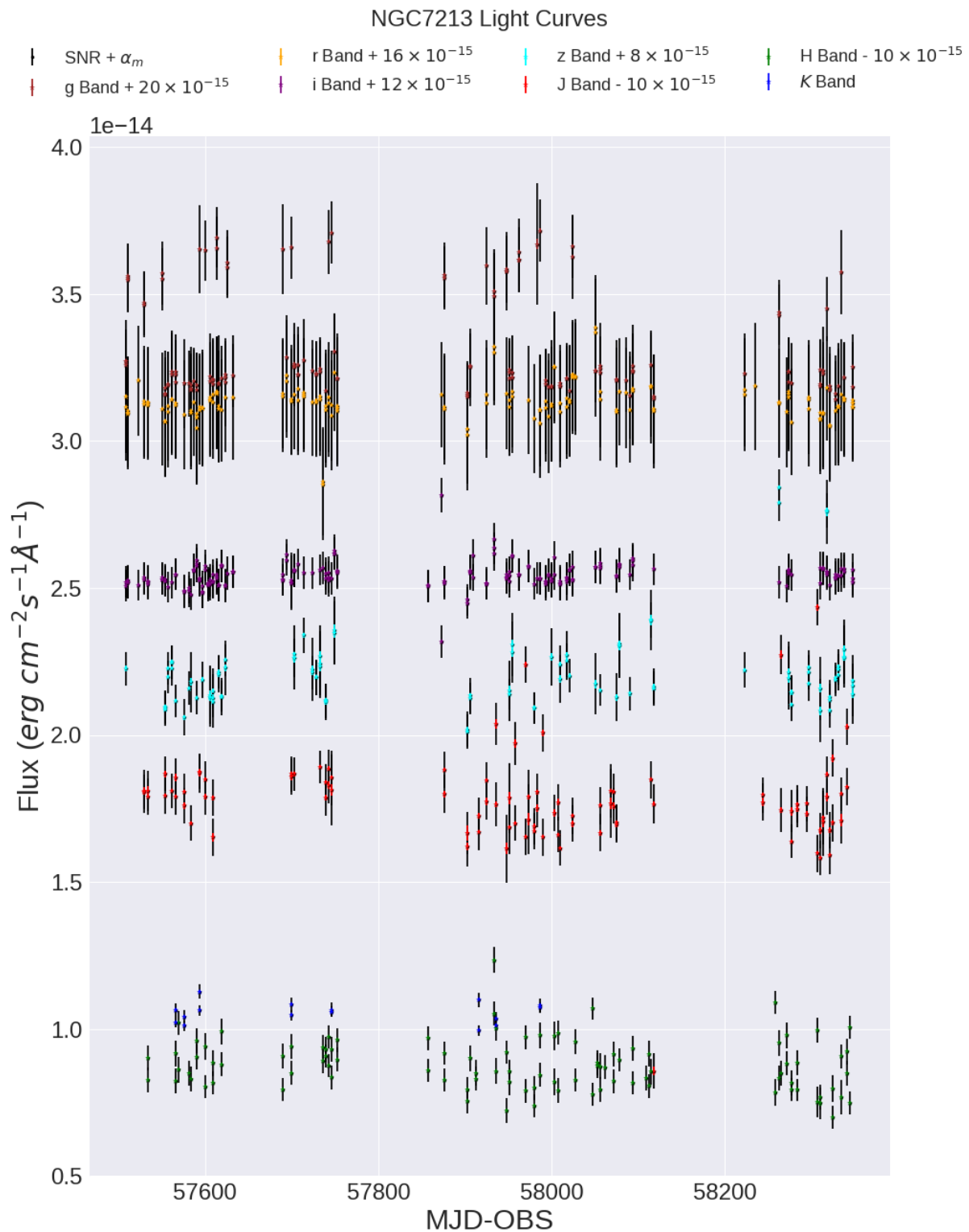


Figure 4.28: The NGC7213 fluxes.

4.4.10. IRAS09149

4.4.11. IC4329A

4.4.12. IzW1

4.5. TRANSFER FUNCTIONS

In order to determine the driving function one must have an understanding of how the LC behaves from the Quasar to the observation. If one were to determine the exact Transfer Function at all times, it would then be possible to determine the exact driving function. However the transfer function is an unknown quantity and as the observed light curve is the result of the transfer function and the observed light curve (*equation 4.6*) (Andreas Skielboe 2016 [33])

$$F_l(t, \lambda) = \int_{-\infty}^{\infty} \Psi(\tau, \lambda) F_C(t - \tau) d\tau \quad (4.6)$$

it is impossible to accurately determine the driving function. However this project is not concerned with the accurate driving function, it is however interested in the relative difference between the Transfer Functions. It is therefore decided to assume a Transfer Function for the K-band data. Using this arbitrary function, *equation ??* and an MCMC algorithm a possible driving function is determined. This possible driving function can then be utilised in compound with the observed light curve for the remaining observed bands and *equation 4.6* to determine the relative differences and hence the timelag between the Transfer Functions.

For arbitrary Transfer Function a log-normal is chosen (*equation 4.7*)

$$f(x) = \frac{1}{x\sigma\sqrt{2\pi}} e^{-\frac{(\ln(x)-\mu)^2}{2\sigma^2}} \quad (4.7)$$

The transfer function of an AGN however is not a simple singular log-normal function. In order to accurately determine the transfer function it is important to take into account the separate the individual transfer function contributions from the BLR and the Dusty Torus. The exact shape of the complete transfer function must thusly be a combination of the BLR and the Dust Torus contributions. The complete transfer function thus becomes

$$f(t, \lambda) = A_T \frac{1}{t\sigma_{Dust}\sqrt{2\pi}} e^{-\frac{(\ln(t)-\mu_{Dust})^2}{2\sigma_{Dust}^2}} + (1 - A_T) N_{AD} BB(T, \lambda) \frac{1}{t\sigma_{AD}\sqrt{2\pi}} e^{-\frac{(\ln(t)-\mu_{AD})^2}{2\sigma_{AD}^2}}, \quad (4.8)$$

with A_T being the fraction of the complete transfer function contribution originating from the dust torus, $BB(T, \lambda)$ the fraction of the Black Body radiation emitted at that wavelength and N_{AD} being the normalisation of the accretion disk flux transfer function.

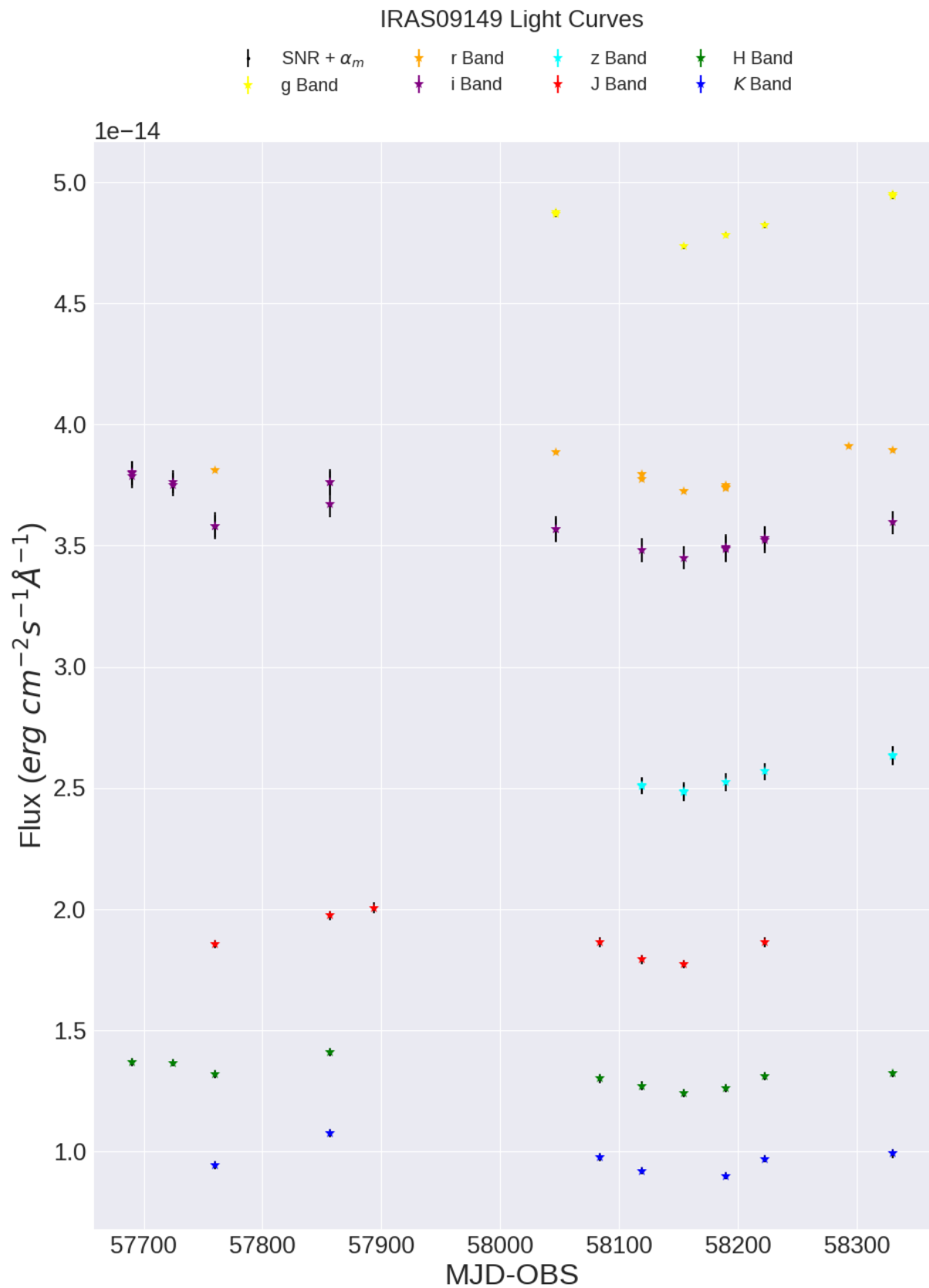


Figure 4.29: The IRAS09149 fluxes.

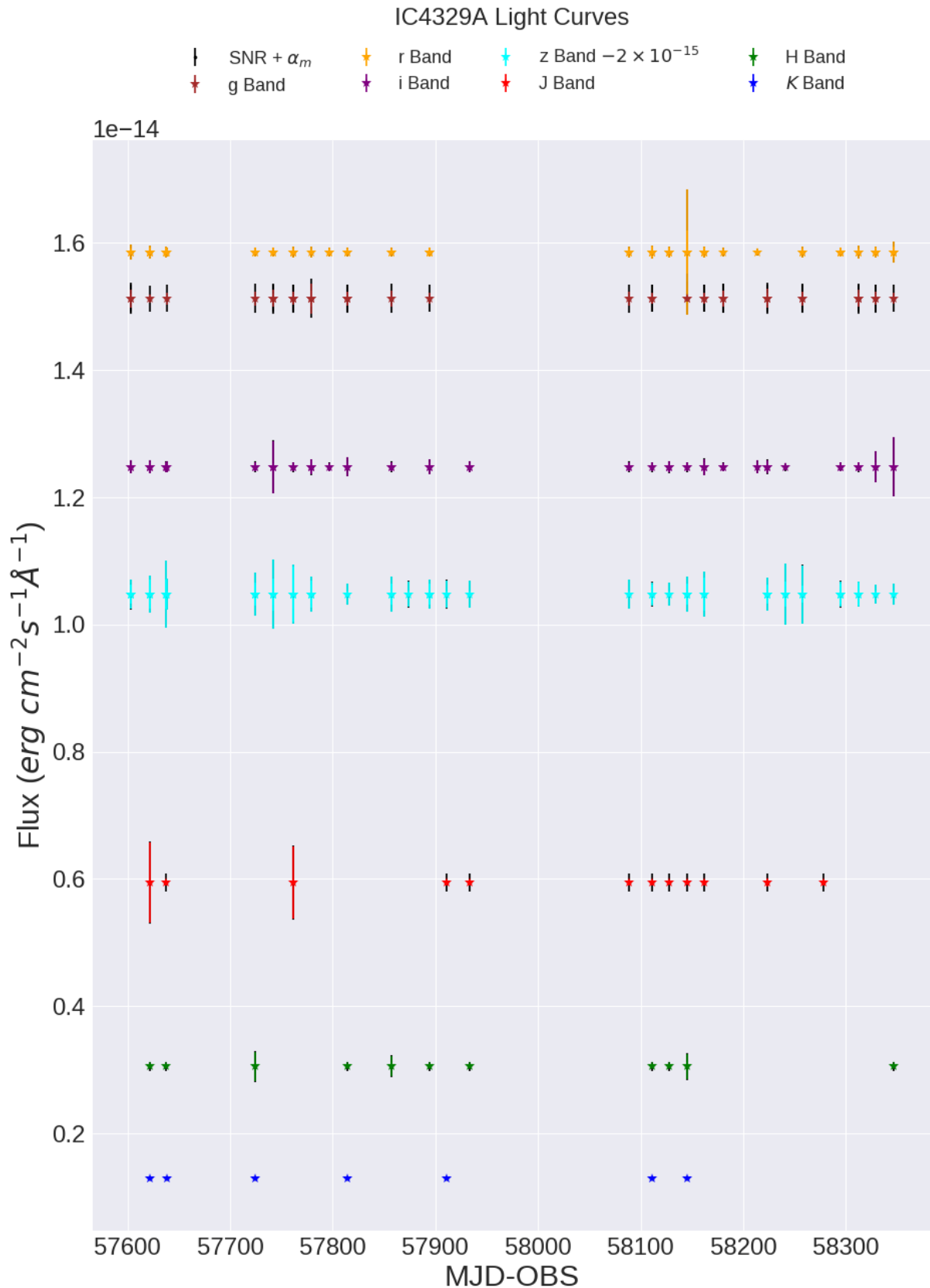


Figure 4.30: The IC4329A fluxes.

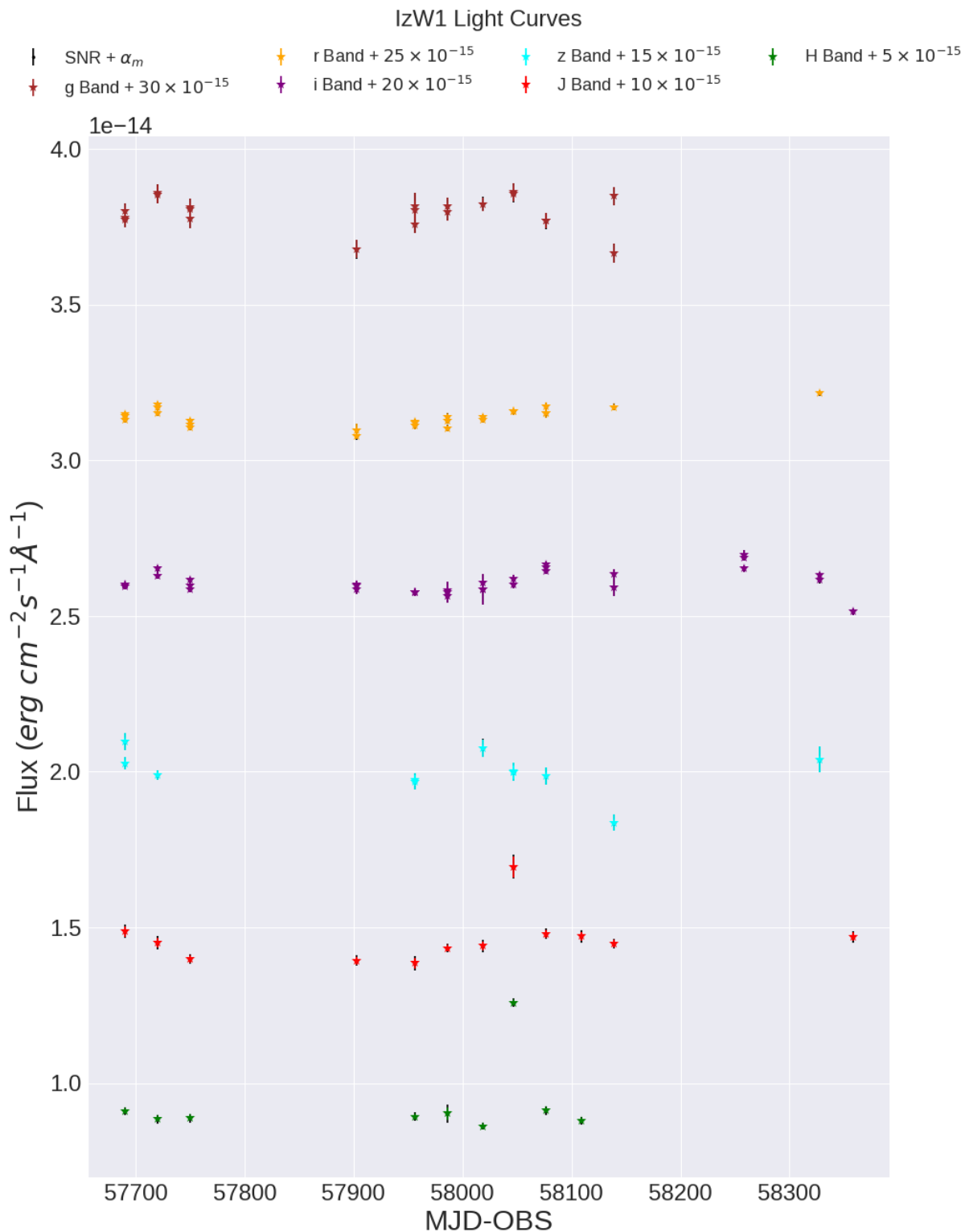


Figure 4.31: The IzW1 fluxes.

4.5.1. Accretion Disk Transfer Function contribution⁴

The accretion disk produces a

4.5.2. Dust Torus Transfer Function contribution

The Dust Torus undergoes heating from the central engine, and thus the contribution to the observed AGN radiation from this dusty area is thermal re-radiation. The dust torus is, as described previously, an area of varying temperature at depending on radius from the center of the AGN (*equation 1.34*) and Hönig & Kishimoto 2010 [17]. Thus the radiation from the dust torus should be represented by a series of concentric circles of varying temperatures all radiating as black bodies. It is however outside the scale of the program generated in this project to accurately depict such a complicated dust torus of unknown temperature and radial size. The program generated in this project therefore assumes the dust torus to be a uniform region of constant temperature and density, radiating as a black body.

⁴Nuñez, Chelouche & Kaspi 2018 [27]

Chapter 5

MCMC algorithm

The ultimate aim of the project was an attempt to successfully implement a reverberation mapping analysis of AGN in the local universe, without the knowledge of the X-RAY driving function of the central engine. As such the aim of the latter stages of the project became the creation of a computer algorithm that could back engineer the driving function based on observations in the J, H, K, g, r, i and z bands. Through the earlier parts of the project, aimed at obtaining the light curves, it was concluded that the data in the SDSS filters were generally of substandard quality as compared to the Johnson-Cousins filters, despite longer exposure times. It was found that particularly the z-band observations were of high uncertainty. The results obtained through such a program would naturally be subject to many uncertainties, it was however not possible to successfully develop a fully working program in the time allocated, thus this section will discuss the consideration that went into the program at this stage, and discuss possibilities for the failure of the algorithm developed.

Back engineering the driving function, in conjunction with the relevant two-part transfer functions (*equation 4.8*), of an AGN is a non-trivial task. The choice of using a Markov Chain Mote Carlo (MCMC) algorithm for such an undertaking was made due to its vast versatility. It was not feasible to believe the problem could be analytically solved, partly due to the low and uneven observation density, and partly due to the vast number of unknowns in the system of equations, prompting a complicated system of hundreds of overlapping equations, as each moment in time in the theoretical driving function can be treated as an individual unknown, through not independent, variable, if the problem was to be analytically solved, and partly due to the complications arising computationally from attempting to solve such a complicated system of simultaneous equations. The MCMC algorithm however allows for a more robust method of solving complicated systems should the algorithm be correctly set up.

The design of the MCMC was conducted in several steps, each aimed at addressing different parts of the issues arising from the MCMC analysing.

5.1. MARKOV CHAIN MOTE CARLO¹

Statistical problems in physics, economics etc. are oftentimes extremely complex systems that when solved would provide the *expectation value, confidence intervals* etc. They can however be extremely time consuming to solve, and or outright impossible, with the computational resources at hand. The Monte Carlo approach to statistical problem thus becomes the battle between precision and efficiency. In an ideal solution, to any statistical problems, the analytical solution could be determined, and thus able to provide the best possible understanding of the problem at hand. Solving statistical problems, or any multi-variable problems, analytically can however be an extremely complex undertaking, if at all possible in the first place.

In the problem undertaken in this project there is an understanding of the resultant product of the combined emitted light from an infinite number of infinitesimally small concentric spheres in the accretion disk, all of varying temperature, and electron number densities, and thus subject to differing transfer functions affected to various degrees by the driving function variations at all times prior to emission, combined with an infinite number of infinitesimally small concentric cylindrical shells of the dust torus of varying composition and temperature all being black body emitters of individual temperatures, reliant on energy released from the accretion process at all times prior to the time of emittance, depending on the varying relevant transfer functions for the individual shells. This is an impossible problem to solve analytically (or otherwise) with an impossible number of unknown parameters.

Despite the impossibility of the problem presenting itself in its entirety, it becomes possible to simplify the problem by several general assumptions. It is assumed that the dust torus is sufficiently uniform, in temperature, as to make the alterations to the black body emission, caused by the temperature gradient, fall inside the pre-accepted error. Additionally it is assumed that any light contribution not originating in the accretion disk or dusty torus can be safely ignored. Thus it is assumed that the BLR and NLR emission line contribution in the observed wavebands, as compared to the observational errors, is sufficiently small as to be non-consequential, as well as any host galactic light pollution will be uniform across wavelengths, or sufficiently small as to be safely ignored (for discussion on this minimization see section ??). These two base assumptions, despite their obvious issues, allows for the simplification of the previously described system, of impossible complexity. In the simplified model it is assumed that the accretion disk and the torus is both governed by a single emission function and both have a single transfer function to describe the response delay to the driving function variations in each filter. This new system could theoretically be resolved through analytical means, given sufficiently high observational density and sufficiently powerful computational resources. In this project neither is available, thus

¹This section relies heavily on Paul J. Atzberger *The Monte-Carlo Method*, Andrieu, Freitas, Doucet & Jordan 2003 *An Introduction to MCMC for Machine Learning* and Ravenzwaaij, Cassey & Brown *A simple introduction to Markov Chain Monte-Carlo sampling*

the use of an MCMC.

The next simplification is in the acceptance of the impossibility of the perfect analytical solution. This is the reason for the implementation of a Markov Chain Monte Carlo approach to problem solving. The MCMC approach to problem solving attempts to "guess" the solution to the problem, and by gradually changing the "guess" to improve the "*goodness of fit*" of the proposed solution the algorithm will attempt to replicate the results. As such the MCMC approach is ideal for solving integration and optimisation, as is relevant for this paper, problems in large dimensional spaces.

In this project the MCMC was used for optimising the proposed solution in such a fashion that the chi-squared (*equation 5.1*) is minimised.

$$\chi^2 = \sum_i \frac{(Observation_i - Calculation_i)^2}{\sigma_i^2} \quad (5.1)$$

5.1.1. Markov Chain Monte Carlo Principle

The MCMC algorithm builds upon two different ideas. The *Monte-Carlo* is the idea of determining statistical properties by randomly sampling points in a given distribution, as opposed to analytically analysing the equations. *Monte-Carlo* relies on the assumption that given a sufficiently large random sampling from a statistical distribution then the relevant distribution parameters can be approximated with a high degree of accuracy, like the probability of getting ten consecutive "heads" in a game of "heads and tails". The *Markov Chain* property inherent in the MCMC, conversely, alters changeable parameters by the generation of random samples through a sequential process. In essence each random sample is investigated for the *goodness of fit* and the best sample is utilised as a stepping stone for the following randomly generated sample. Thus each new sample is dependent only on the previous sample, not samples prior to the last accepted step. A MCMC algorithm then becomes a method of generating a set of progressively better samples x_i using a *Monte Carlo* approach based upon a *Markov Chain* mechanism.

5.1.2. Fixed Transfer Function MCMC

Artificially creating the driving function, to be used as a base component of a reverberation mapping analysis, is a non-trivial task, that necessitates a strong understanding of the various components involved in defining an AGN light curve (see sections 3.1, 3.2 & 3.3). Generating a light curve, that follows the general empirically determined properties of AGN light curves itself, is a well documented possibility in AGN literature. It is however noteworthy that much literature, older than a few years, assumes a PSD α value of -2 rather than the -1.7 to -3.4 documented by Smith et al. 2018 [34]. The difficulty arises in the attempt to generate a reliable driving function based around several unknown transfer functions and unevenly sampled response functions. This difficulty is the cause for the initial experimentation in generating a driving function

based solely on observed light curves generated in the accretion disk and Dust Torus with a non-changing transfer function. Thus initially a simple fixed transfer function following *equation 4.7* was assumed.

The initial attempt relied upon the use of a "crawler" to alter the driving function. This "crawler" would at each successive iteration of the MCMC algorithm alter one point in the driving function by a small amount. Regardless of the acceptance or rejection of the alteration the crawler would move to the next resolved point on the driving function and repeat the process. This method had several severe drawbacks in its implementation.

1. Each point on the driving function became entirely independent of its neighbors. Due to the infinite number of possible solutions to a driving function to provide a fit for the observed light curves based on a fixed transfer function, this caused severe variations on timescales of a few days, much more severe than anything observed in the AGN.
2. Given the significant observational breaks in the data (see *figure 3.1*) the driving function became almost unbound in these gaps. This almost unbound state allowed the driving function to create un-physical peaks.
3. The driving function did not follow the observed physical properties of AGN light curves discussed in *sections 3.1, 3.2 & 3.3*.
4. Individually altering all points in the light curve, and running *goodness of fit* estimations was a computationally heavy and in-efficient process.

Issues 1 through 3 can be addressed by upgrading the acceptance criteria for the MCMC algorithm. Traditionally an MCMC algorithm will decide upon the acceptance of the proposed change based upon a *goodness of fit* analysis. This however did not appear to be sufficient to successfully produce a physically believable light curve. As such additional factors were introduced, so the acceptance was judged based on the following parameters;

1. Determining the chi-squared of the $F_l(t, \lambda)$ and the suggested light curve, so an indication of the *goodness of fit*.
2. Determining the double derivative of the driving function, thus determining the speed at which the variations in the light curve changes. In observed light curves this is a gradual process, and "spiking" is rarely if ever observed.
3. Determining the PSD slope of the driving function, and implementing the Smith et al. 2018 [34] values into it.
4. Producing a Kelly fitting for the driving function, allowing a degree of "*smoothing*" of the driving function.

5. Checking if any proposed light curve points is negative, as that is an un-physical state for flux emission.

The code then randomly alters the point of the "crawler" on the driving function, and re-estimates item 1 through 4. In the case of a favorable comparison between the "*before*" and "*after*" state the alteration is saved and the code moves onwards to the following point. The favorability of an outcome is evaluated by a series of parameters.

1. ***Chi-Squared***: In all cases the sum of the residuals squared must be less than the previous alteration.
2. ***Double Derivative***: The double derivative is compared to the maximum rate of change of the observed light curve and is accepted if it is no more than 40 percent larger than the originally observed. This is done to prevent rapid changes to the driving function that would ultimately make for a more stable, but ultimately unphysical solution to the driving function. 40 percent has been chosen as it is felt that despite the observed light curve becoming somewhat more smooth as a result of the Transfer Function, it would be unlikely to be that prominent. The alternative is the sum of the change in the rate of change of both adjacent points as well as the altered points decreases overall. This would be accepted as well, pending other factors.
3. ***PSD slopes***: Assuming 1 and 2 holds true, the change can be accepted if the PSD slope is moving closer to the accepted slope, or inside 0.05 of the accepted (so as to allow some freedom of movement of the driving function).
4. ***Kelly***: In the case of 1 holding true, and 2 follows the path of the set of double derivatives overall decreasing there will be a statistical possibility of 5 percent of a change being accepted IF the Kelly function provides an overall better fit and the PSD slope is no more than 0.3 out. This is done primarily to utilise the Kelly function as a method of approximating LC's and hence allowing for the use of this additional resource in providing a more physical fitting, as well as counterbalancing the possibility of the driving function becoming stable in an unstable equilibrium position due to the other limitations.

The main issue using the single crawler is the slowness of the convergence of the driving function. Thus it becomes necessary to investigate possibilities of generate entire, physically reliable light curves, so as to modify the entire function simultaneously, and thus attempt a faster convergence. It has been known for decades that the AGN light curves follow a Power Spectral Density function, with the slope being the issue of contention (*section 3.2*). Due to the Smith et al. 2018 paper, analysing the Kepler Light Curves, it becomes possible to provide a reliable physical basis for the simulated light curves in the plain assumption that the AGN light curves can be completely explained by the use of PSD functions. The issue of generating randomised functions of with the required PSD slopes was outside the scope of this project. Rather than inventing a separate algorithm a python module called "*colorednoise*"² was utilised.

²<https://github.com/felixpatzelt/colorednoise>

The program operates using a series of changeable parameters as part of the MCMC algorithm. The input functions are the observed light curves in the various bands. The light curves has been generated as discussed previously and is represented by a date, flux and error on the flux. The best results has been obtained by the use of data from the AGN NGC3783, due to the density of observations and the strength of the observed flux. Due to the developmental nature of the attempt to generate a reliable driving function for the use in reverberation mapping, the main analysis has been focused on this AGN in the attempt to reduce the error associated with poor sampling and low observational density. The MCMC defined changeable parameters are:

5.1.2.0.1 Temperature of the Dust Torus (T):

The Temperature in the dust torus is represented by a single, changeable value and given by the Planck Radiation law. It is assumed that only energy previously absorbed from the AGN, by the Torus, contributes to the Torus energy emission. The Planck Radiation law is used to identify the fraction of light re-emitted by the Torus that are being emitted at a given wavelength (*figure ??*).

This is not physically accurate, as the dust torus is non-uniform, rather being best represented by a series of concentric rings of varying temperature and composition. This additional complexity was experimented upon briefly, so as to more accurately mimic the dust torus, by implementing a simple model whereby the Dust Torys Black Body emission was composed of several individual Black Body emission function of varying, equally spaced temperatures of equal weight. It was however discarded for two primary reasons. The main issue was that the increased complexity, caused by the necessary addition of further changeable parameters, as well as the computational cost of evaluating multiple sets of the Planck Radiation law, significantly slowed the algorithm. The secondary reason for the exclusion of such a model is demonstrated in *figure ??*. It is clearly shown that the more complex combined Black Body spectrum of 10 varying temperatures can be approximated reasonably well by a single temperature. Thus the overall gain of implementing such a model, at this early stage, does not justify the computational cost. In the case of a working MCMC algorithm it would be more reasonable to attempt a more accurate Torus emission model, which should be well beyond the simple example just utilised. Such an additional undertaking was, however, outside the scope of this project.

5.1.2.0.2 The natural log of the thermal lag ($\mu_{thermal}$):

This value is the representation of the lag time of the thermal part of the AGN light curve as defined in *equation 4.8*. It is the natural logarithm of the mean value of the delay in the thermal transfer function. Thus it is an exemplary indication of the radius of the Torus.

5.1.2.0.3 The natural log of the width of the thermal lag ($\sigma_{thermal}$):

This value designates the natural log of the width of the thermal lag. As such this value

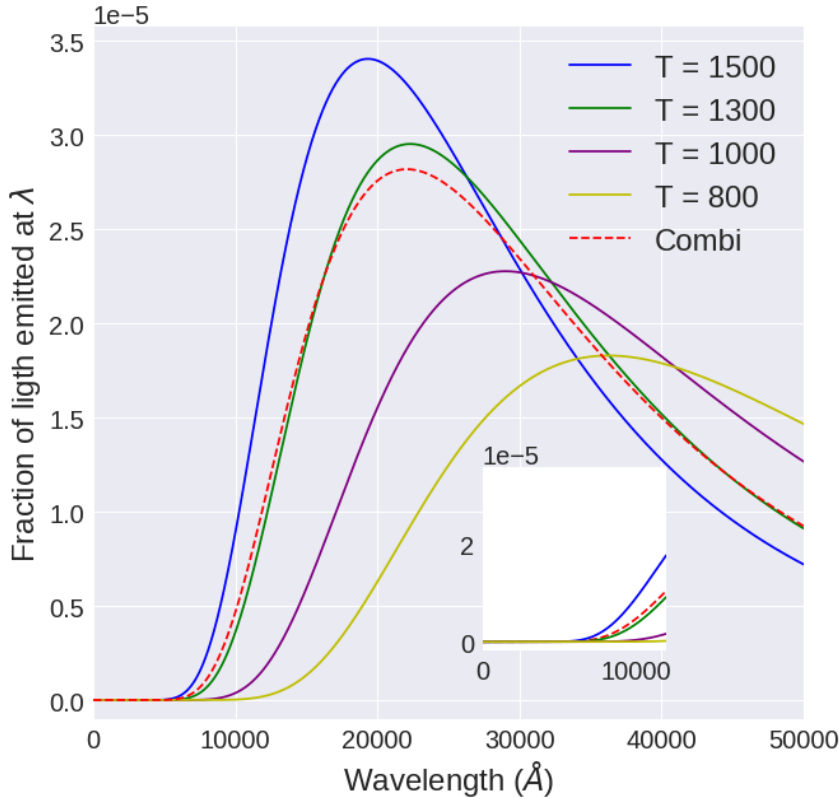


Figure 5.1: The fraction of Black Body emission being emitted at various wavelengths. The dotted red line is the simple temperature varying Dust Torus Black Body emission model, composed of 10, equally spaced temperatures of equal weight between $T = 800\text{K}$ and $T = 1500\text{K}$. The $T = 1300\text{K}$ Black Body emission aptly demonstrates the small gains at an increased computational cost by not simplifying the Torus model.

can be utilized to gain a relative understanding of the size of the thermally radiating medium. A thin, optically thick shell in the Torus would represent itself as a delta function, whereas the more physical case of a thick, optically thick Torus has a wider contribution function.

5.1.2.0.4 The thermal fraction of the observed flux (A_T):

A measure of the relationship between the fraction of observed light originating in the accretion disk, and the Dust Torus. For an accurate understanding of the fraction of light originating in the dust torus it must be considered in conjunction with the individual normalisations of the Accretion Disk flux in the differing bands (N_S).

5.1.2.0.5 The BLR transfer function normalisation (N_{AD}):

This is a 7 value array representing the normalisation of the Accretion Disk flux compared to the driving function in the different bands. This value represents the fraction of the driving function energy that becomes re-emitted by the Accretion Disk in the relevant wavelength band.

5.1.2.0.6 The natural log of the Accretion Disk lag (μ_{AD}):

This value is the representation of the lag time of the Accretion Disk part of the observed AGN light curve as defined in *equation 4.8*. It is represented by a 7 part array, for the different observed wavelength bands.

5.1.2.0.7 The natural log of the width of the Accretion Disk lag (σ_{AD}):

This value designates the width of the Accretion Disk lag. As such this value can be utilized to gain a relative understanding of the size of the Accretion Disk, as it provides a measure of the temporal width inside which the AGN undergoes emission at a given observed wavelength. It is represented by a 7 part array, for the different observed wavelength bands.

The N_{AD} array in conjunction with the A_T -value is re-evaluated every 10.000 iterations through the use of minimization, of the reduced χ^2 from *equation 5.1*. The re-evaluation utilises the known *power law* dependence of the Accretion Disk SED, combined with the Planck Law distribution of the thermal component to fit the N_{AD} array and A_T -value simultaneously. This approach, to the optimization of the values in the N_{AD} array and A_T -value, originated in the attempt to both constrain the mean flux of the driving function, as well as reduce the number of free parameters in the MCMC, and thus provide a faster algorithm. Early in the development it was determined, that a free moving normalization, of the AD transfer function, removed the constraints on the mean flux of the driving function. The arbitrary movements of the driving functions is not a problem, in the case of a fully working algorithm, as such would allow the MCMC to actually determine the relevant values. It was however early realised that in an algorithm undergoing development it became difficult to determine the origin for non-convergence, and the semi-constrain of the mean-flux value would reduce the number of unknown quantities, as well as decrease the probability of changes to the driving function originating in the re-alignment of the mean-flux of the driving function, as opposed to increased accuracy of the structure of the driving function. As the aim of this project, and indeed reverberation mapping in general, was not to worry about the absolute flux values, rather the lags between the bands, it became an acceptable sacrifice. That is not necessarily to conclude that the increased freedom of the driving function and the increased free parameters would, in a fully working algorithm, lead to non-convergence, it would however significantly slow the algorithm. It has thus been down-prioritized to re-introduce the increased freedom of movement of the driving function mean-flux, as this is not strictly the short-term aim of this project. That is not necessarily the same as this value is non-changing, as the re-evaluation of the N_{AD} array and A_T -value happens every 10.000 iterations, thus allowing slow convergence. This re-evaluation could occur with increased frequency, at the cost of increased computational cost.

The *Kelly model* parameters (τ_{Kelly} , σ_{Kelly} and b) is re-evaluated once very 500 iterations. In an ideal model it would necessarily be assumed that these values must be re-evaluated constantly, so as to fit the ever changing driving function. This however

proved at an early stage to become unfeasible, due to the computational cost associated with the minimization process utilised in obtaining these *Kelly parameters*. One of the main difficulties in the creation of this algorithm is the attempt to reduce the running time to a reasonable time-frame. As such it was concluded that due to the small impact of individual alterations to the overall driving function, and thus the almost negligible short term changes in the *Kelly parameters*, it would be a reasonable approximation to assume the parameters would only change every 500 iterations. Additionally the *Kelly model* relies on a certain degree of randomization based around the light curve variance given by $\tau_{\text{Kelly}}\sigma_{\text{Kelly}}^2/2$, as demonstrated through *equation 3.4*. This randomization is in the original *Kelly model* utilised to demonstrate a confidence interval for regions of low observational sampling (*figure ??*). In this algorithm however the sampling number of *equation 3.4* is not sufficiently high as to smooth the *Kelly model* on each iteration it is utilised, and thus the short term inaccuracies in the parameters will be overshadowed by the randomization inherent in the model. This deviation from the original use of the model occurs for two reasons. The first is the computational cost incurred in the full run of the algorithm governing the *Kelly model*, this however could be resolved by the reduction in the frequency of the model being run, that would follow by a more thorough utilisation of the model. The second and main reason lies in the difficulty in the evolution of the driving function. The use of the colorednoise generator allows the generation of possible light curves without any connection to the existing light curves in an efficient manner. This however leads to decreased probability of changes to the driving functionm being accepted, as the scatter from the un-correlated light curves increases. Thus it becomes necessary to counteract this scatter, this is done through the automatic smoothening that naturally occurs from the *kelly model*. The danger arises in the quickness at with the Kelly smoothening occurs. Due to the general slowness of the algorithm it becomes a significant risk that the immediate smoothening of a *kelly model* cold "lock" the driving function such that the remaining parameters changes to fit the smoothed function at an early stage. In this program however each individual instance of the *kelly model* is heavily randomized due to the low number of samples obtained, however over the course of the iterations the *Kelly model* will have a probability of 0.01 to run for every discarded change, and as many successive times as the change is accepted. Thus a gradual smoothening is observed that does not unduly prevent the program from developing the driving function, but allows gradual reduction of scatter caused by un-correlated colorednoise functions and thus allows continuous development.

The convolution theorem

$$f(x) \circledast g(x) = \mathfrak{F}^{-1} [\mathfrak{F}(f(x)) \times \mathfrak{F}(g(x))] \quad (5.2)$$

is used to preserve the structure of the PSD function. The new addition to the existing function, whether it is a colorednoise generated addition or a *Kelly model* addition, is assigned a weight varying from 0.5 to 2.5×10^{-5} and *equation 5.2* becomes

$$f(x) \circledast g(x) = \mathfrak{F}^{-1} \left[\exp \left[(1 - \text{weight}) \times \log(\mathfrak{F}(f(x))) + \text{weight} \times \log(\mathfrak{F}(g(x))) \right] \right]. \quad (5.3)$$

The large variability in the weight assigned to the changes to the driving function is to allow a dynamic process to occur, where significant changes can be made in the earlier stages and smaller alterability in the latter stages. A possible further development would be to make this process dynamic and "intelligent" to optimize the changes at each state.

The alterations to the driving function and free parameters of the AGN were defined somewhat by the fate of the previous alteration. There are three possible combinations of alterations to the driving function and the free parameters;

1. *Alterations based on the Kelly model:* In this instance alterations occurred solely in the driving function. This became a combination of alterations occurring through the use of the *Kelly model* and the *colorednoise generator* (sections 3.1 & 3.2). These alterations both included the generation of an entirely new light curve being combined with the existing light curve through the use of *equation 5.3*. This double alteration of the driving function was an attempt to increase the computational speed at which the algorithm converged. The *Kelly alteration* generally, despite the previously discussed randomized nature of it, had an increased likelihood of acceptance due to its generally smoothening nature. The *colorednoise generated* light curve alteration was assigned lesser weight than the *Kelly alterations* and was used to add otherwise rejected change to the driving function to reduce the risk of stagnation due to the low probability that any random curve will provide an overall reduced χ^2 by itself.
2. *Random free parameter changes:* This would change the driving function through the *colorednoise* method, as well as chose a direction of exploration for the remaining parameters discussed earlier. All parameters would the be altered in the direction chosen for that individual parameter, with a randomized step size.
3. *Directed free parameter changes:* Much like the previous change, but utilised in the event of §2 being accepted. In this event all free parameters continuously moves in the predetermined direction until the fit is not continuously improved.

§1 happens with a probability of 0.01 in the case of either §2 or §3 is rejected and endures as long as it provides improved fitting. Despite the low chance of §1 being initialised, due to its enduring nature in the face of improved fitting it still represents of the order 5 – 20 % of the accepted changes, depending on the number of iterations having run. In the early stages of the algorithm (inside the first 20.000 iterations) it is in the lower end of the spectrum, and then gradually increase. §2 happens in the case of rejection of §1 or with a probability of 0.99 in the case of rejection of §2. §3 happens in the situation of §2 being accepted, or with $p = 0.99$ when §3 is rejected. The algorithm is a very basic MCMC, the computational cost could possibly be reduced through the implementation of more advanced sampling algorithms. The time constraints inherent in the project however did not allow for additional exploration in this direction.

The weight of any individual changes made to the driving function is as discussed

previously varying from 0.5 to 2.5×10^{-5} . They are additionally "hidden" behind changes to the remaining parameters. That is not to say that the driving functions does not undergo significant alterations over the course of the program being run, as the probability over the course of the program of changes being accepted ranges somewhere between $p \sim 0.1$ and $P \sim 0.05$ depending on the number of iterations already having run. The driving function changes are coupled with changes to the free parameters due to the low likelihood of any one random noise function can increase the fit of the model. As such it necessitates allowing the driving function alterations to be coupled with the changes happening in the free parameters, thus light curve alterations causing significantly worsening of the *goodness-of-fit* will still be rejected, but alterations causing the status-quo or only slight worsening might still become accepted.

Chapter 6

Discussion

6.1. FLUX CALIBRATIONS

This project has shown the possibility of measuring the change in the AGN luminosities, as a function of time through the use of local reference stars in the image frames. The majority of the observed AGNs, in this sample, has demonstrated a clear time dependence on the observed luminosities. It is noteworthy that the structure functions for the observed, variable, AGNs while in agreement about the variability time-scale between the different bands, vastly disagrees in the "turnoff point". The "turnoff point" becomes, in the course of this project, a noteworthy indicator for the sampling quality of the light curves. While it has been proven that AGN in the local universe does experience a general turnoff (Vries et al. 2005 [13]) it is not observed in AGN more distant than $z = 0.6$, while the turnoff observed in local samples doesn't appear until after more than a decade of sampling. Additionally the NGC3783, that is extensively sampled and searched in this project, appears in the Favre et al. 2005 [15] paper, with a two decade sampling, and a structure function in good agreement with the K band sampling from this project, experiencing no turnoff. Thus it appears a good estimator of the quality of the data, across the various observational bands. This estimator clearly indicates the JHK bands as providing a superior sampling of the observed AGNs.

The flux calibrations, of the observed AGNs, has been subject to significant errors. While it has proven difficult to determine the origin of the scattered griz-band observations, in particularly in the z- and i-bands, it is apparent that the magnitude determinations of the reference stars is a source of large systemic errors on the data. The uncertainty in the star magnitude calibrations, done as part of this project, is likely governed by three main errors. The obvious source of magnitude uncertainty is the time difference between the standard star observations, and those of the AGN image plate, and thus the reference stars. Despite the attempt at countering this error though careful selection of nights for the calibration, it is still a significant error that cannot be discounted. The best example of this error is the exclusion of the P525-E z-band imaging at 10/11-17. Despite the simultaneously sampled gri-bands being in good agreement with P525-E observations from 21/10-17, as exemplified by the calibration of

the F9 reference stars, done exclusively by these two observations with low estimated errors, the estimated magnitude error, as done though the use of both nights, in the z-band approached 0.6. Similarly large, inexplicable, errors arose from the z-band calibration of the H0557 frame reference stars, also relying partly on the on 10/11-17 sampled P525-E, prompting the general removal of the z-band observations of P525-E from this night. Additional errors arises, presumably, from the same processes that causes the massive optical scatter. This error could be from the atmospheric conditions, although it appears unlikely given the general quality of the data arising from the La Silla Observatory Site. The final source of error on the flux calibrations arises from the errors in the 2MASS and PanSTARRS surveys. This error would normally be negligible in the comparisons with the errors inherent in this project, and this is indeed the case for the 2MASS errors. It is however difficult to say anything definite about the PanSTARRS errors, as they are widely varying, and in several cases are not reported.

The systemic error in the flux calibrations, arising from the magnitude calibration of the reference stars, may be improved upon through planned observations of standard stars measured in PanSTARRS in close proximity time wise to the observations of the AGN frames below -30° declination. It would, additionally, be a sensible future approach to further investigate the origin of the large scatter in the optical bands, in particularly in the z-band.

Observationally the investigation into the AGN light curves has been of sufficient length that it is possible for the more active AGNs to determine their variability timescale, and it is possible to get an indication of the amplitude changes from the AGNs. The norm for the changing AGNs appears to be amplitudes of 20 – 30% of the mean. It is however early in the observations to draw meaningful conclusions from such, as it is really only NGC3783, F51 and MARK1239 that demonstrates a full descent or rise in the amplitude, from end to end. Likewise conclusions regarding the lag times of the observed AGNs becomes difficult without extensive modeling. It is nominally possible to see the indications of a thermal time-lag in the MARK1239 of about 60-100 days between the optical and IR bands, and in ESO323 towards the end of the observations, between in particularly the r and K bands. The best possibilities of observing good quality time-lags without extensive modeling would have been the NGC3783 and NGC7213, due to the superior sampling density, and lower magnitudes. This has however proven difficult in the latter, due to the slow variations on NGC7213, combined with large uncertainties and scatter. While NGC3783 does show clear variations, and with generally good quality data, it is unfortunate that both instances, where the luminosity change reverses, is in the vicinity of an observational gap.

6.2. THE MCMC MODELING

The ultimate aim of this project was the design of an algorithm capable of utilising the generated AGN light curves for reverberation mapping. For this purpose the creation of a reverberation mapping algorithm using MCMC methods were attempted.

The initial concern centered around the creation of an artificial driving function that would satisfy the physical conditions normally surrounding an AGN light curve.

Chapter 7

Conclusion

It would be the general recommendation from this project for future investigations to schedule two months worth of observation, aligning the observations of the PanSTARRS included standard stars temporally close to the AGN observed at below -30° declination so as to improve upon the magnitude calibration by reducing the influence of atmospheric changes. The project has succeeded in generating AGN light curves of varying quality, should the source of the unreasonable scatter in the optical bands be identified, the quality may be sufficient to determine the individual lags through a light curve modeling.

Throughout the cause of this project the main task has remained the determination of accurate AGN fluxes. This task has been subject to numerous difficulties and setbacks. Due to the significant variations in the observed flux from any astronomical object over time, due to atmospheric changes, the initial stage was to identify relevant reference stars, due to the non-changing stellar luminosity, in the observed image frames, and determine their magnitudes. This was complicated by the non-existence of stars in the PanSTARRS survey below a declination of -30° , necessitating the design an additional program for *stellar magnitude calibrations*. Despite the apparent simplicity of the task from a theoretical standpoint it was complicated by the practical and observational challenges. Despite *The REM Team* completing regular Standard Star observations throughout the nights, it is important to note that many of these are taken below a declination of -30° , thus negating their usefulness, when compared with PanSTARRS data. Thus reference star calibrations done in the course of this project often necessitates the comparisons of stars observed several hours apart. As demonstrated in *figures 2.5 & 2.6* the atmospheric conditions undergoes significant changes over the course of the night. Thus any single night calibrations of reference

stars, despite the apparent low error, must be treated with some caution, and they are thus identified in *table 4.2*. Further in the cause of the calibrations it becomes obvious

Appendices

Appendix A

Individual Light Curve Plots

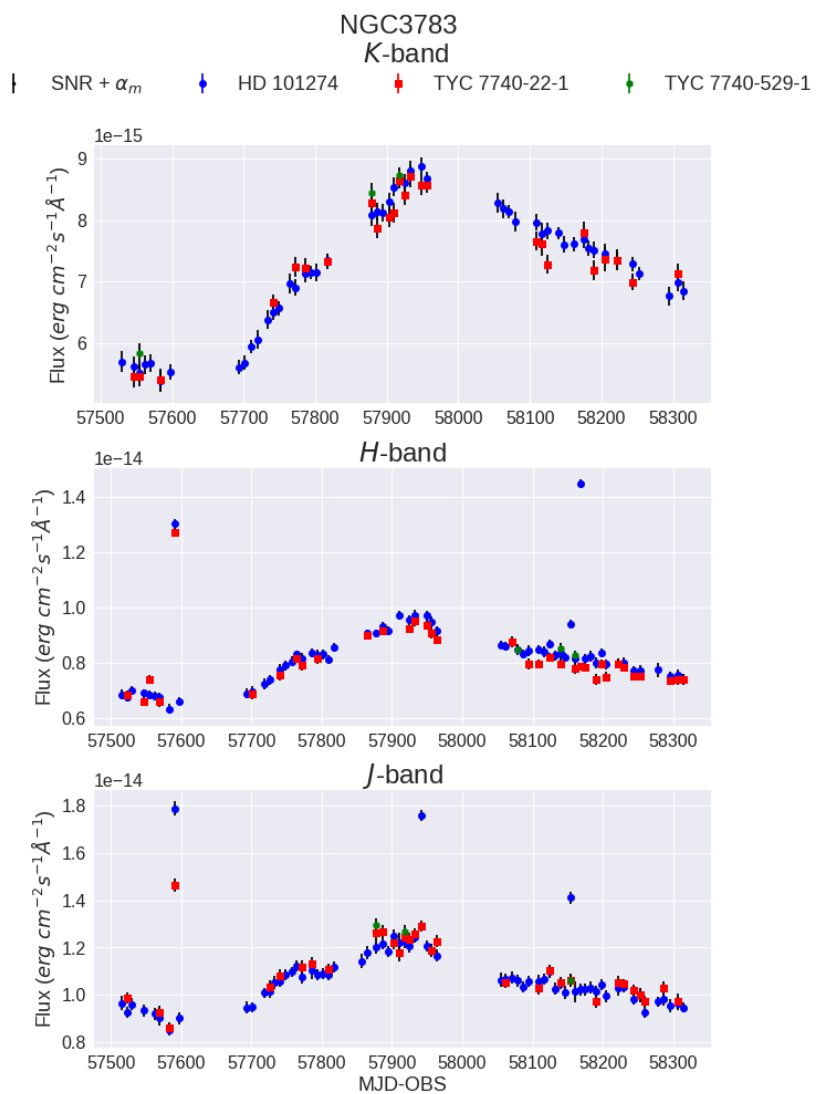
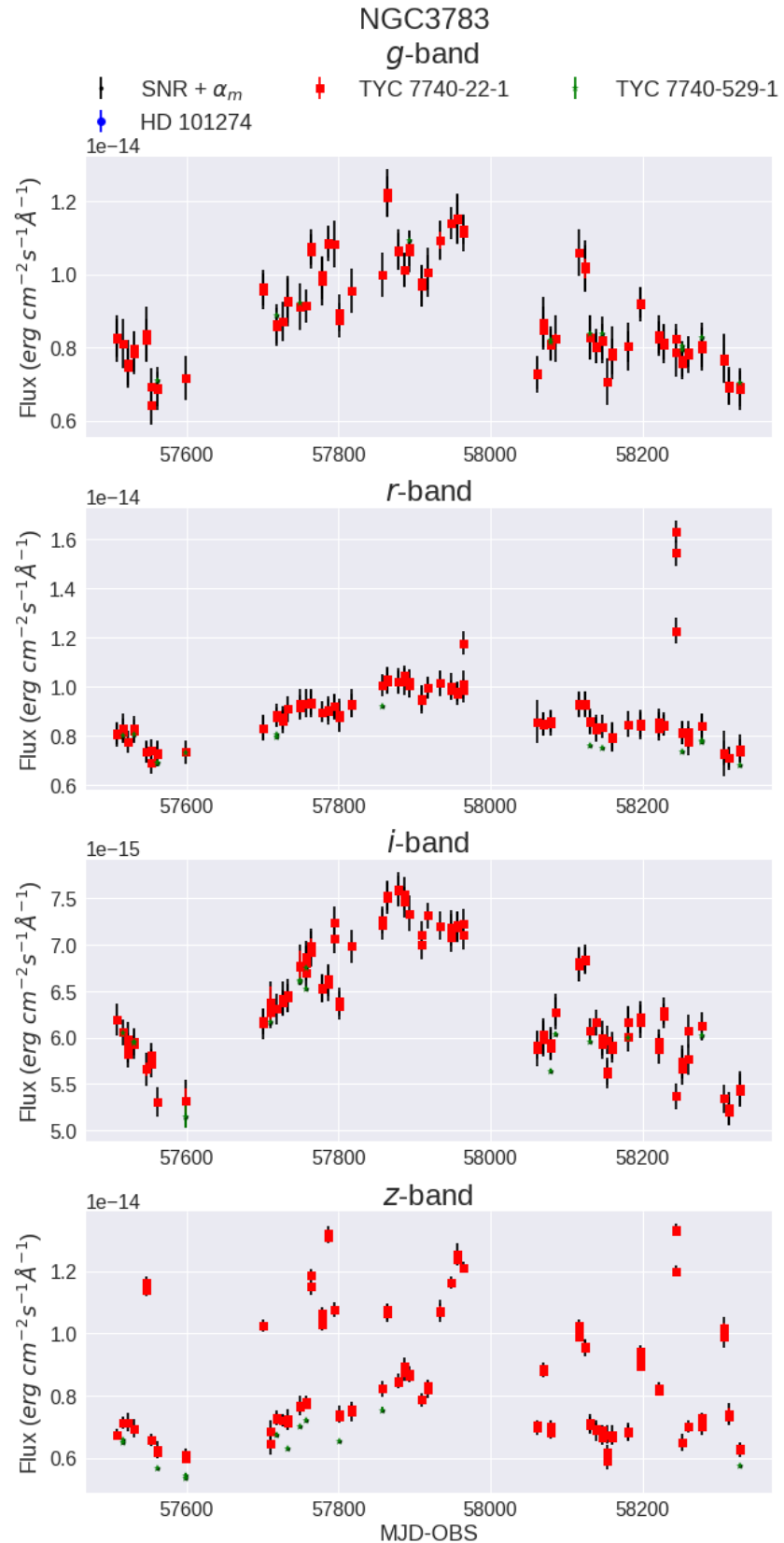


Figure A.1: The NGC3783 JHK band fluxes.

**Figure A.2:** The NGC3783 *griz* fluxes.

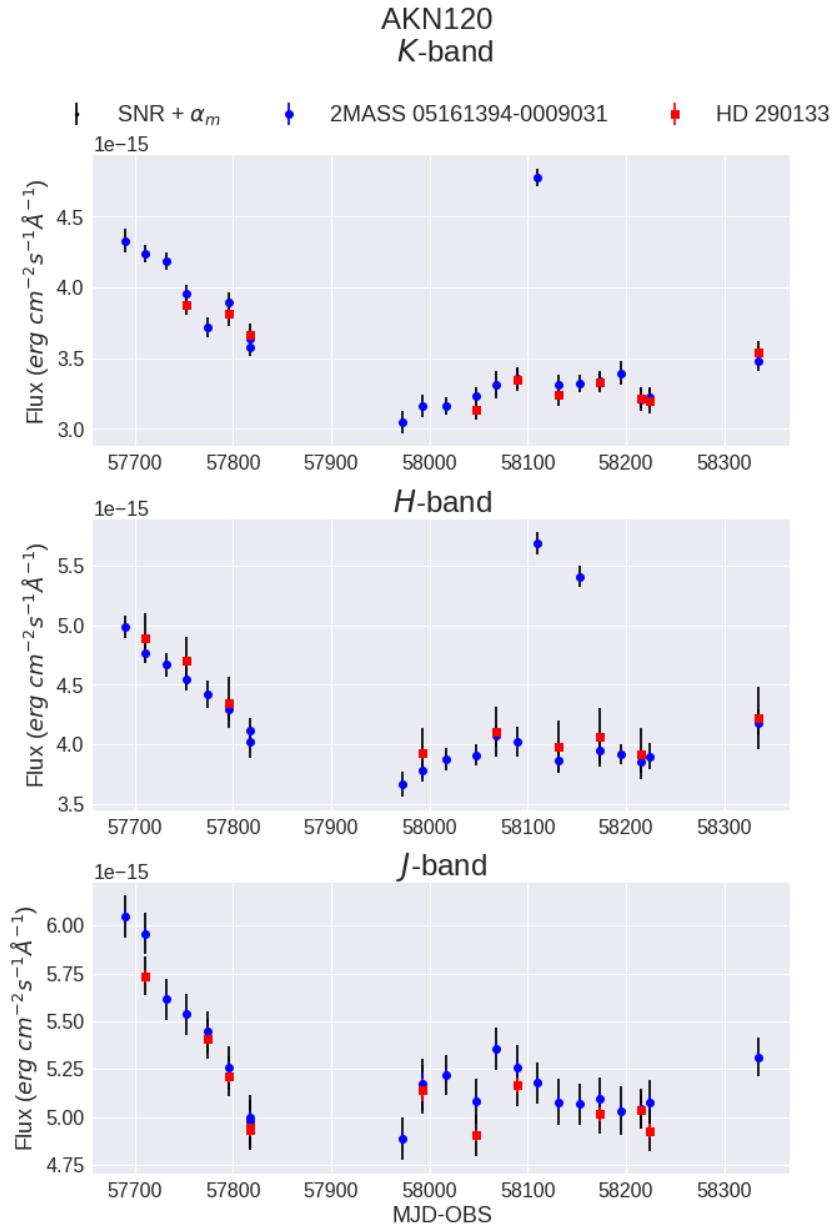


Figure A.3: The AKN120 *JHK* band fluxes.

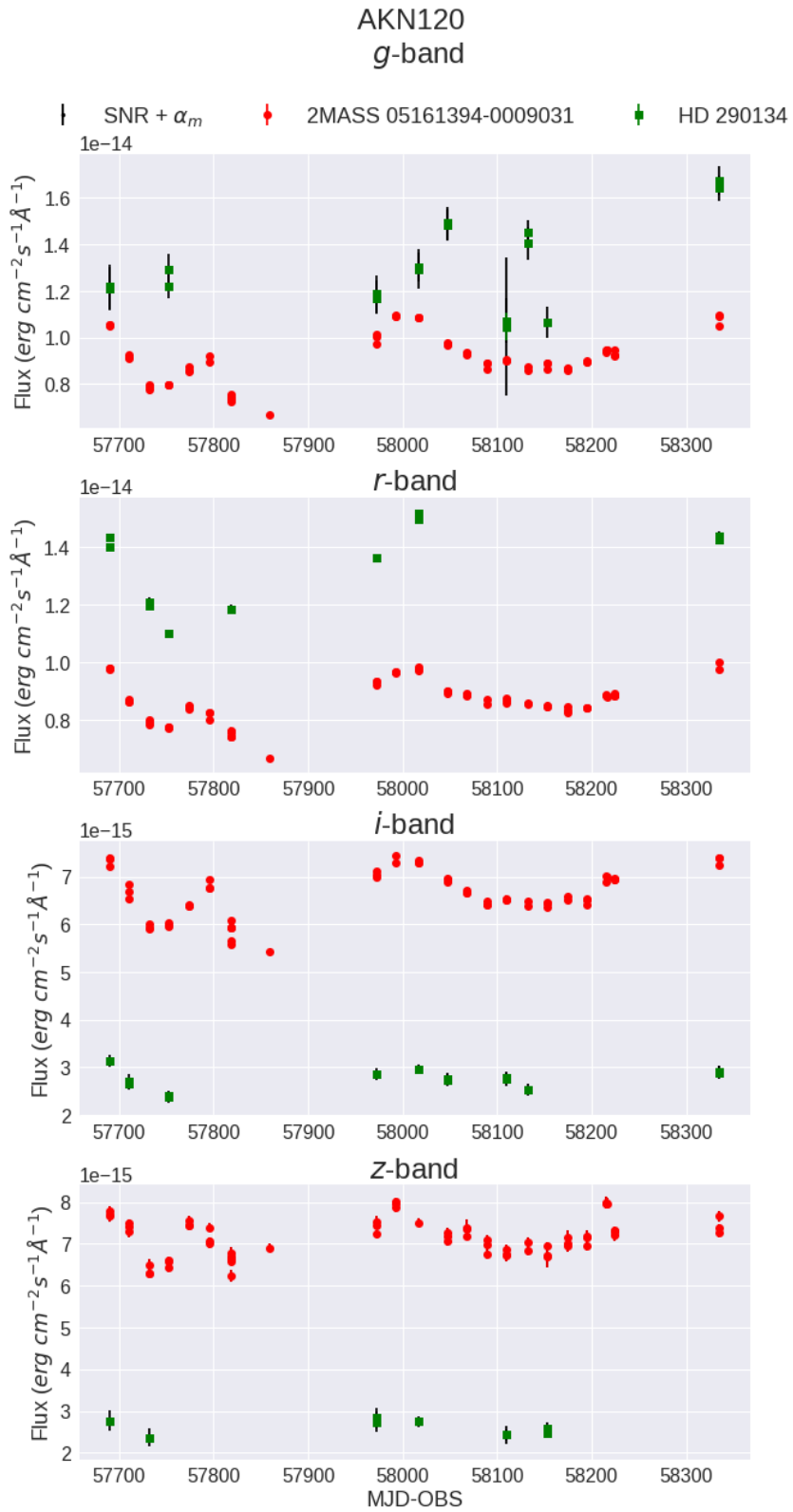


Figure A.4: The AKN120 *griz* fluxes.

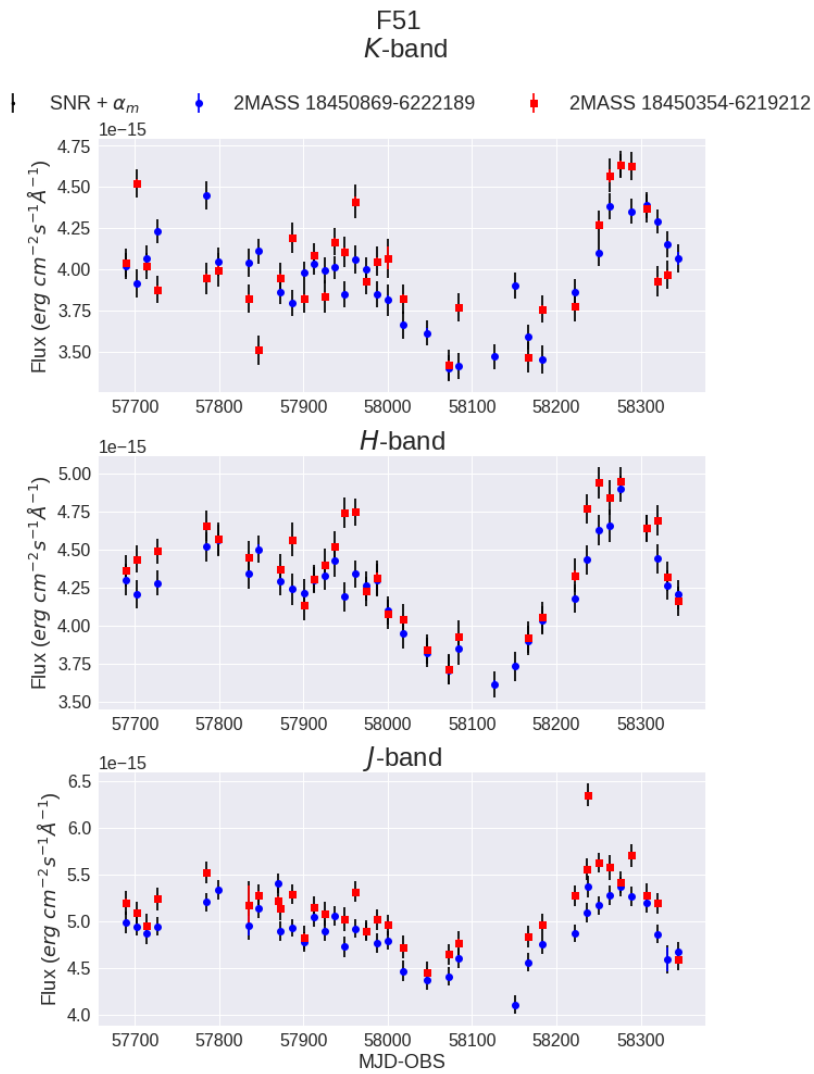


Figure A.5: The $F51$ JHK band fluxes.

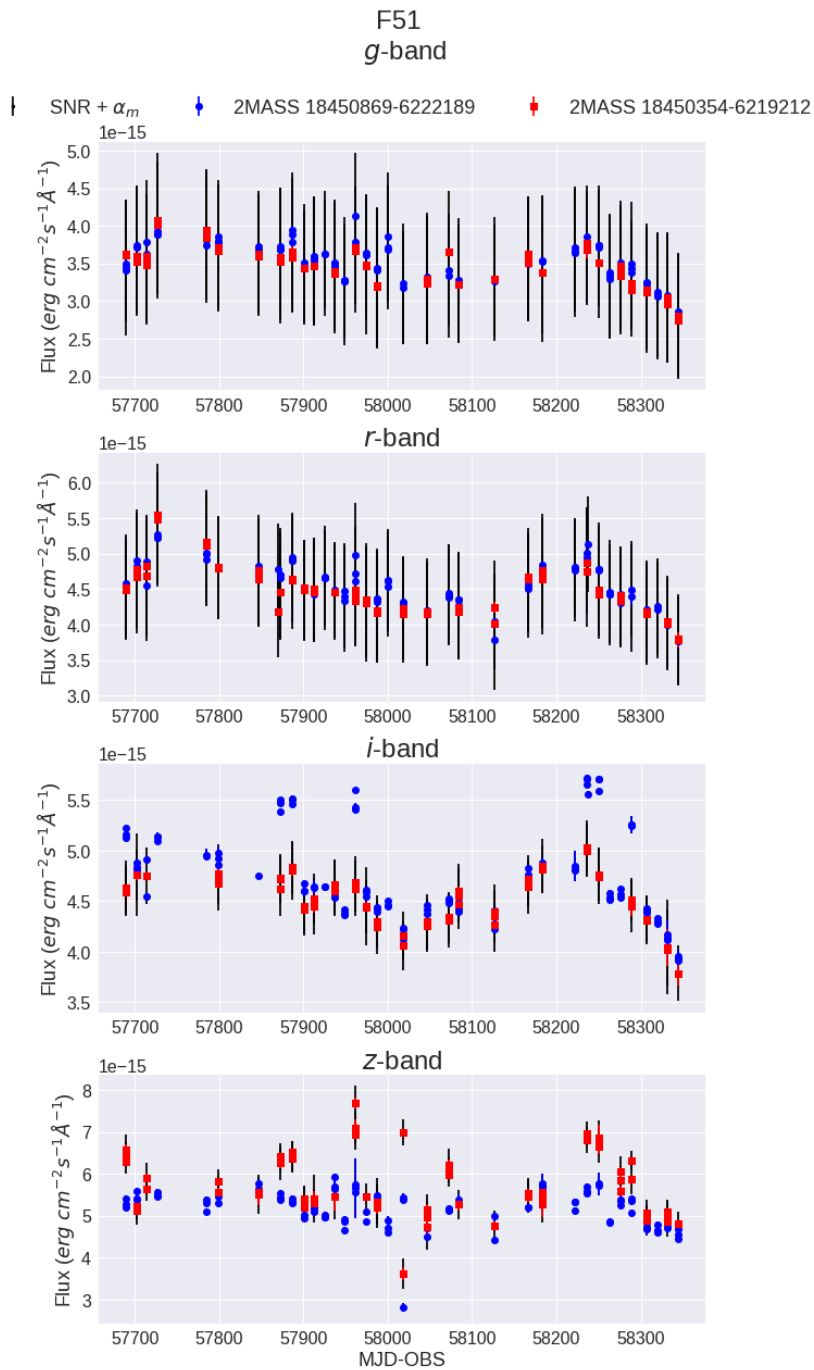


Figure A.6: The F51 *griz* fluxes.

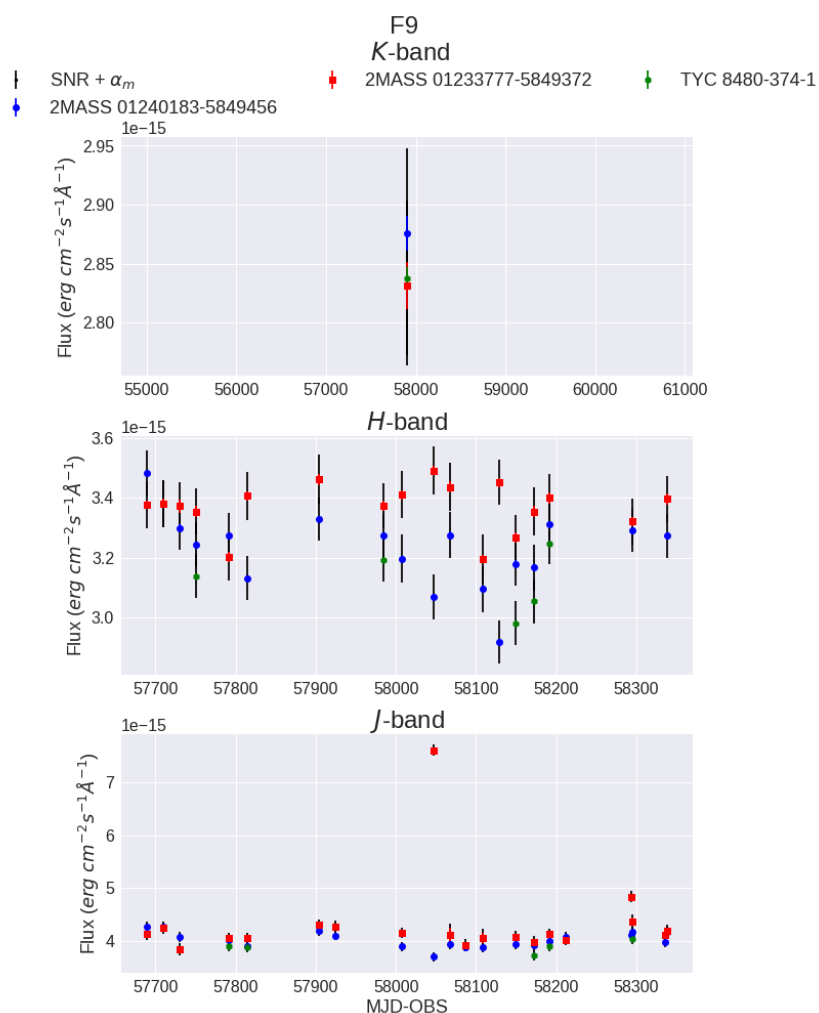


Figure A.7: The F9 JHK band fluxes.

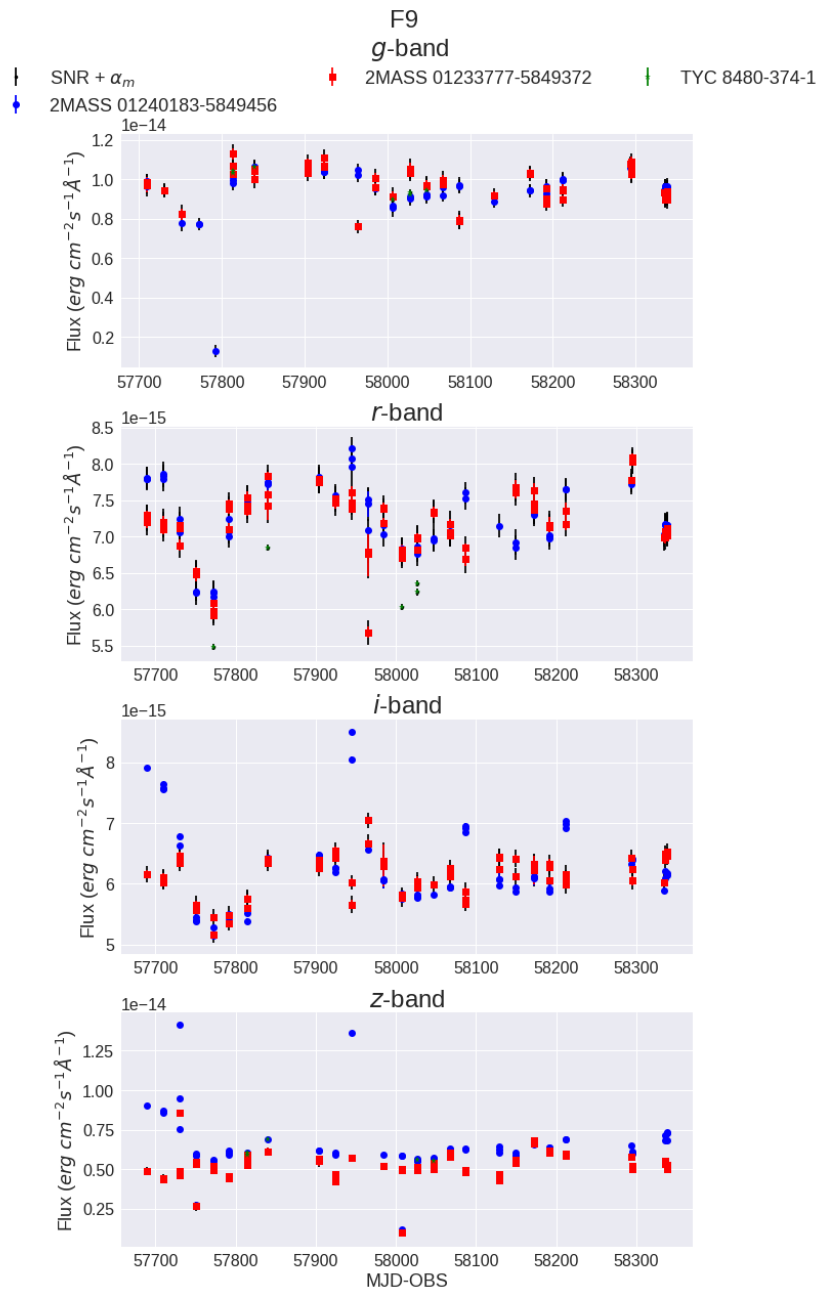


Figure A.8: The F9 griz fluxes.

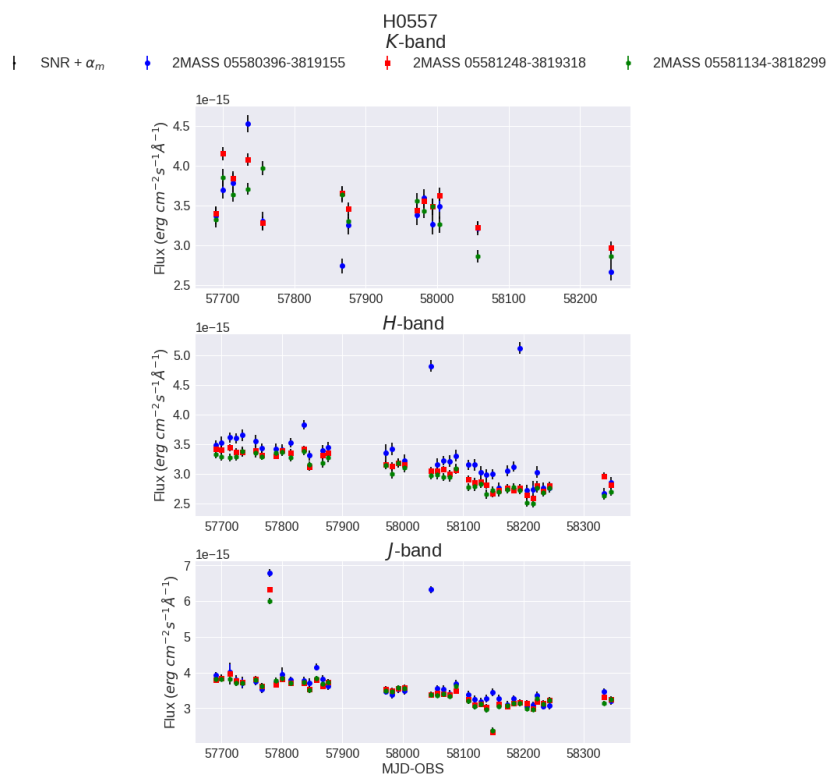


Figure A.9: The H0557 JHK band fluxes.

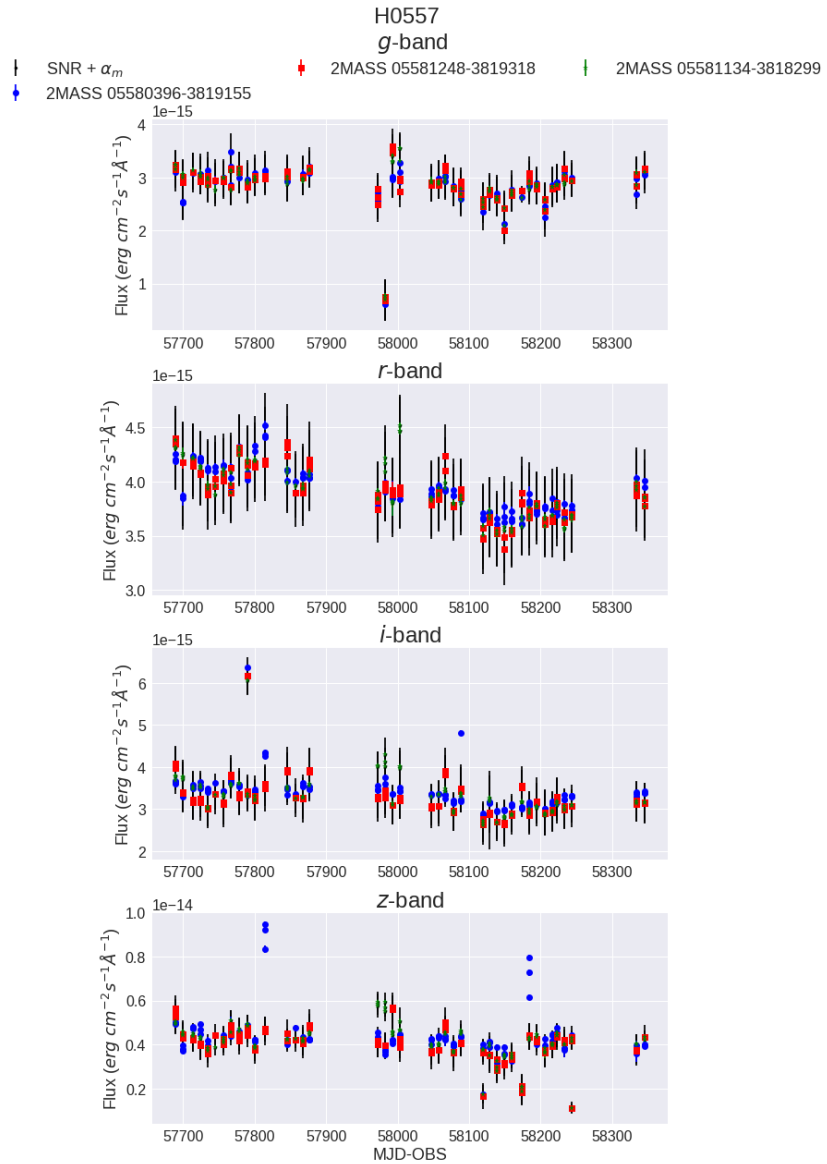


Figure A.10: The H0557 *griz* fluxes.

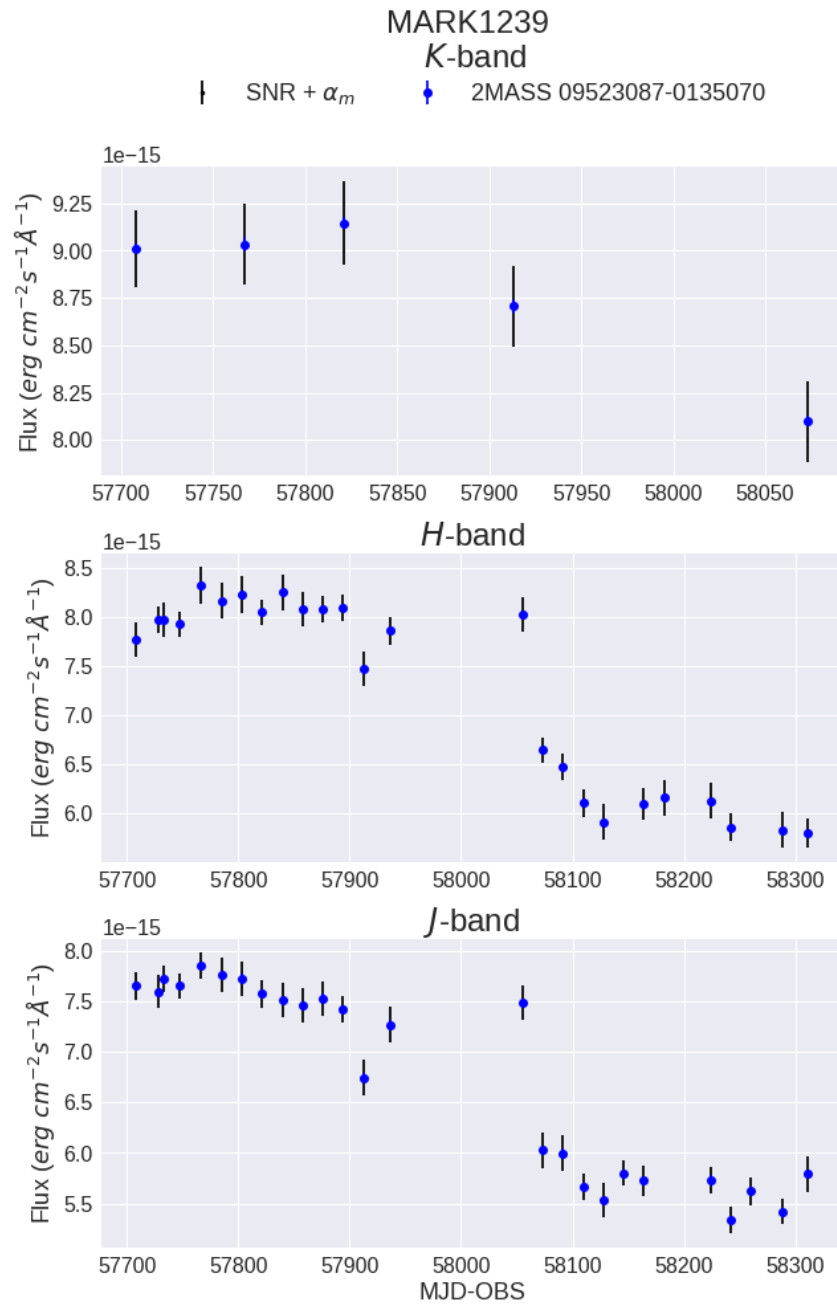
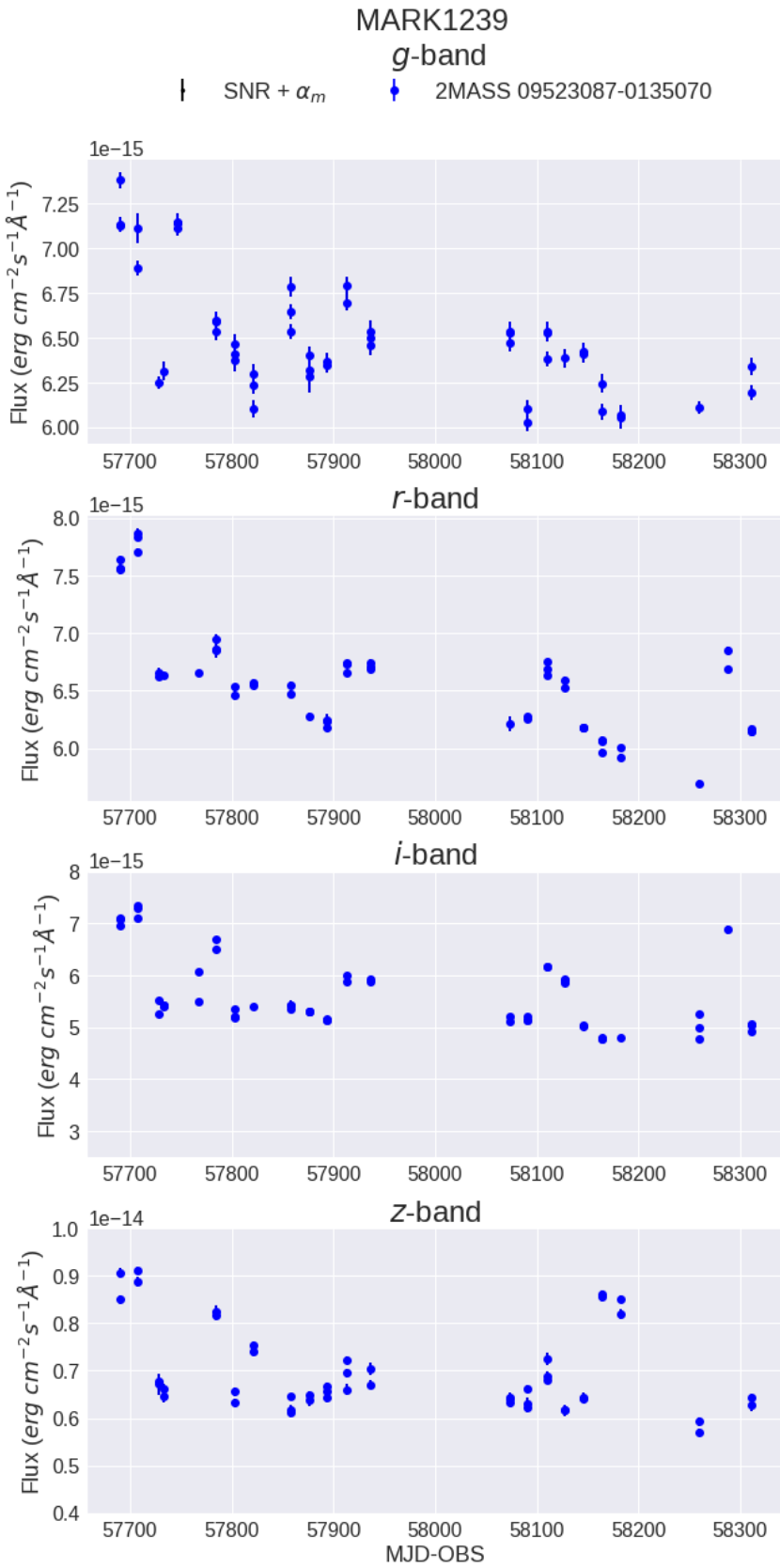


Figure A.11: The MARK1239 JHK band fluxes.

**Figure A.12:** The MARK1239 *griz* fluxes.

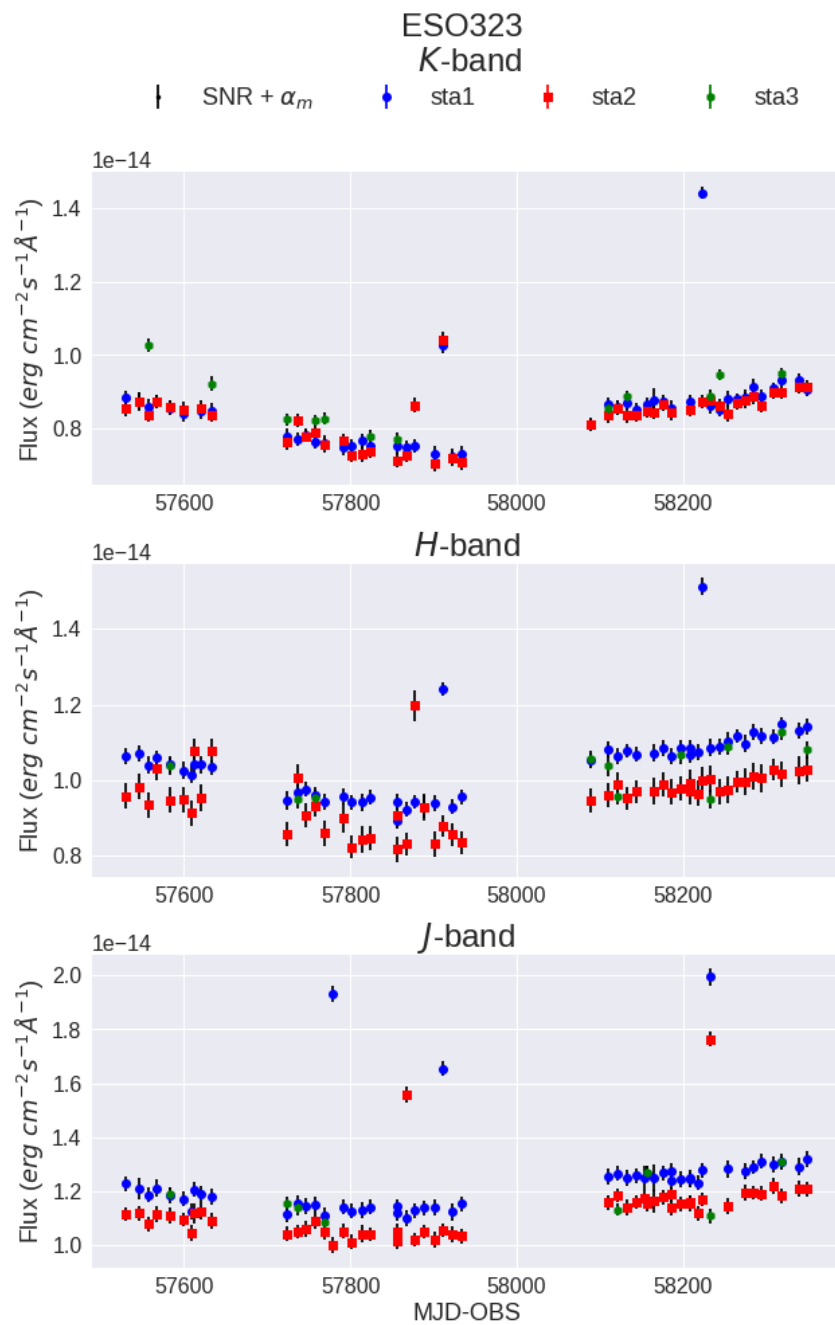
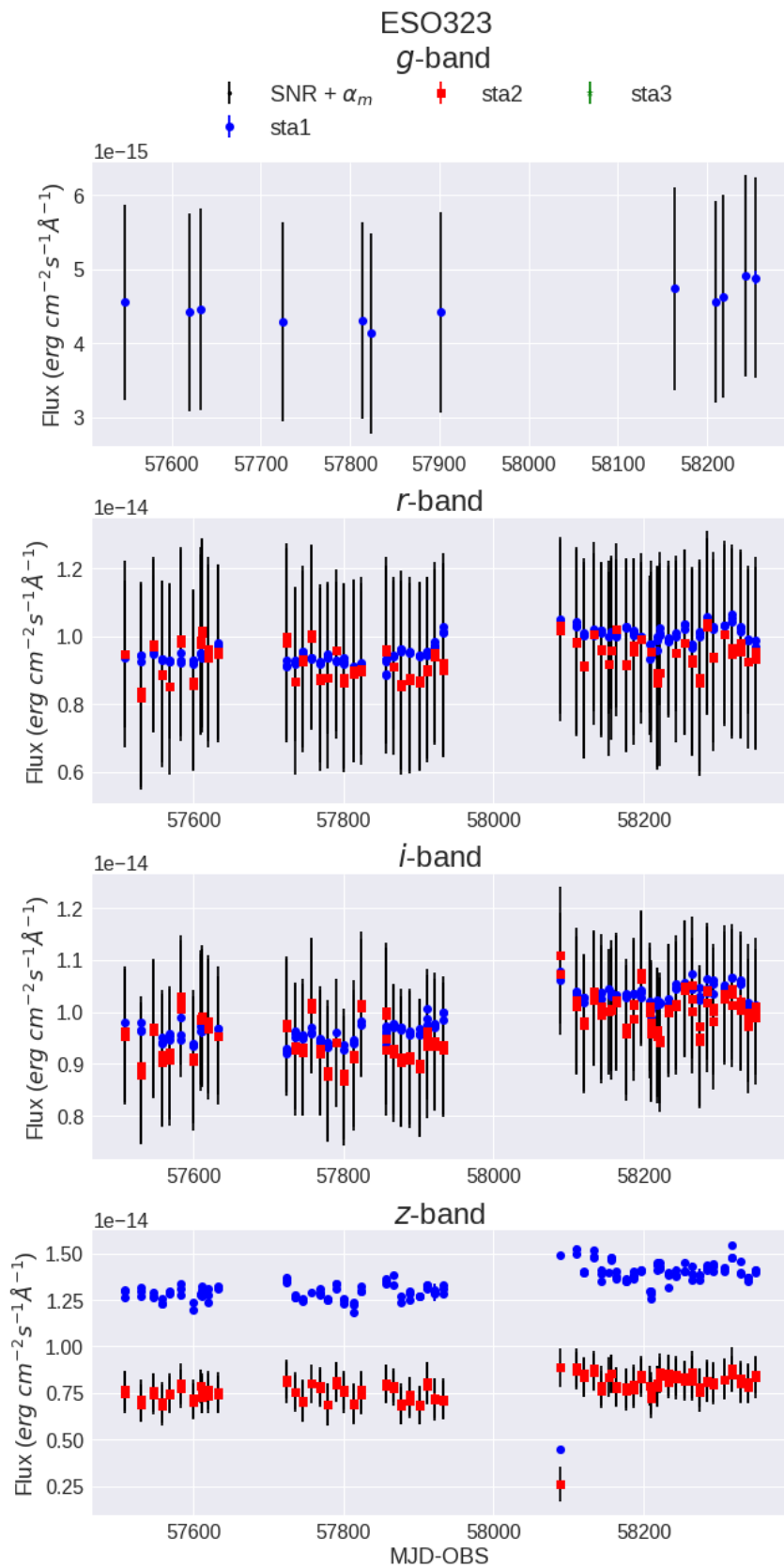


Figure A.13: The ESO323 JHK band fluxes.

**Figure A.14:** The ESO323 *griz* fluxes.

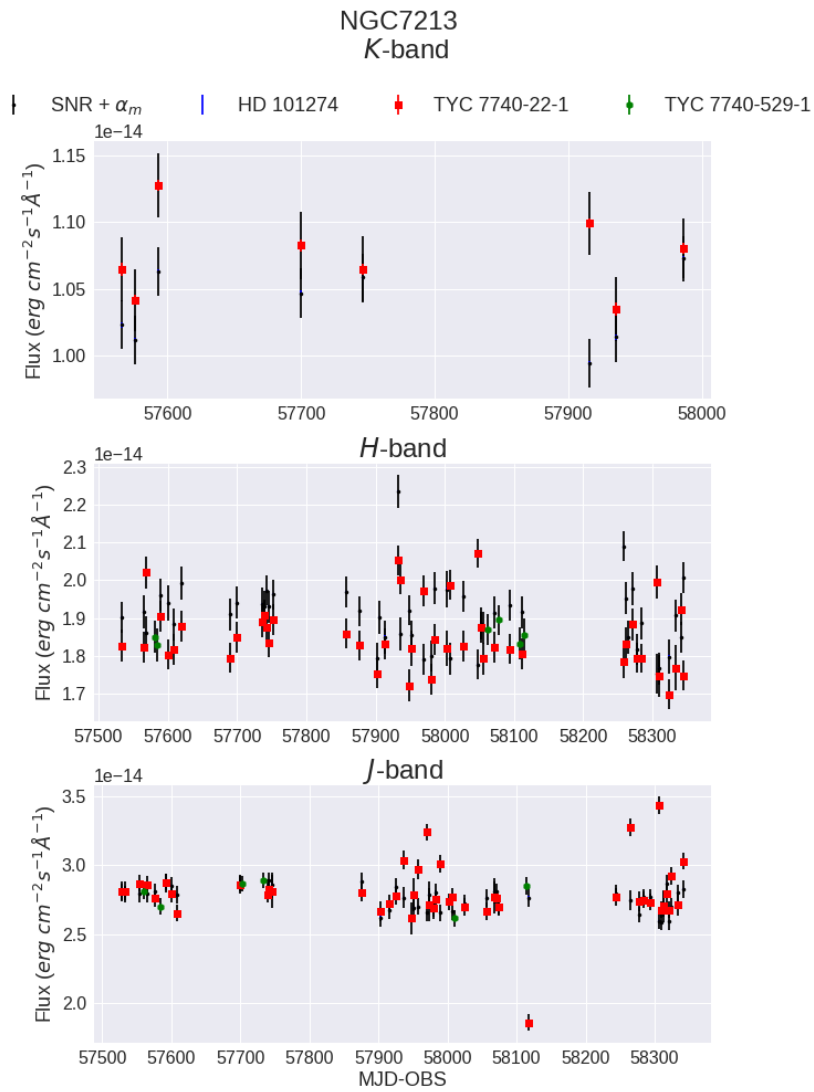
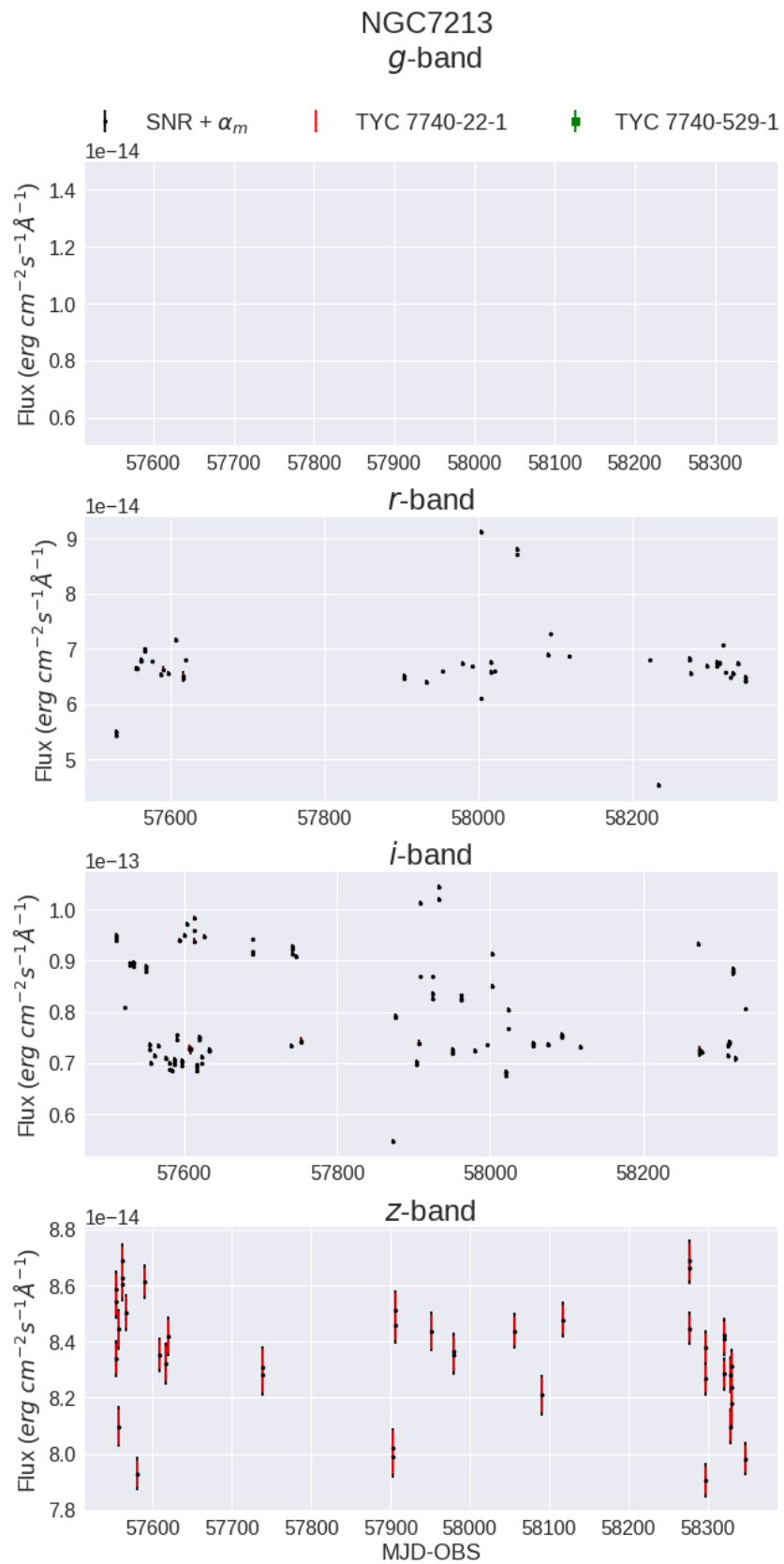


Figure A.15: The NGC7213 JHK band fluxes.

Figure A.16: The NGC7213 *griz* fluxes.

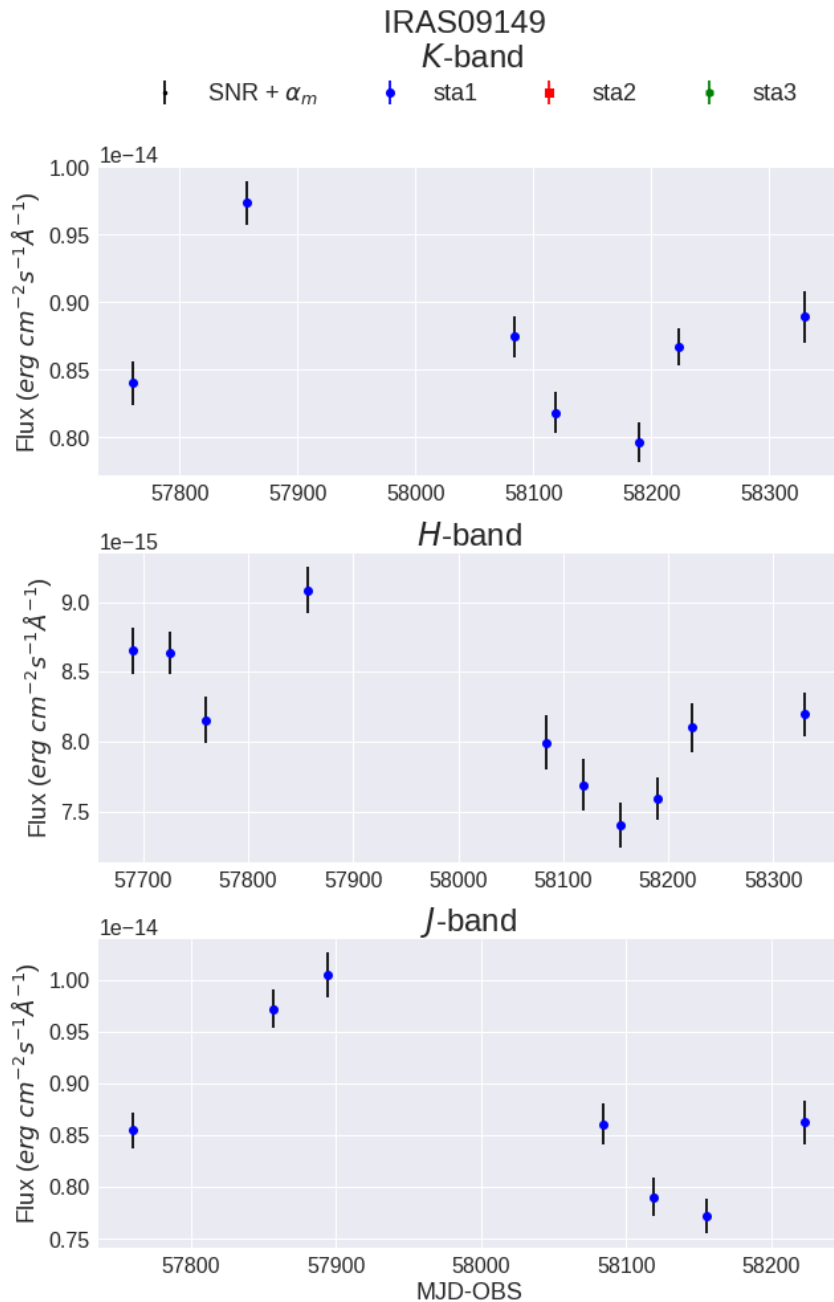
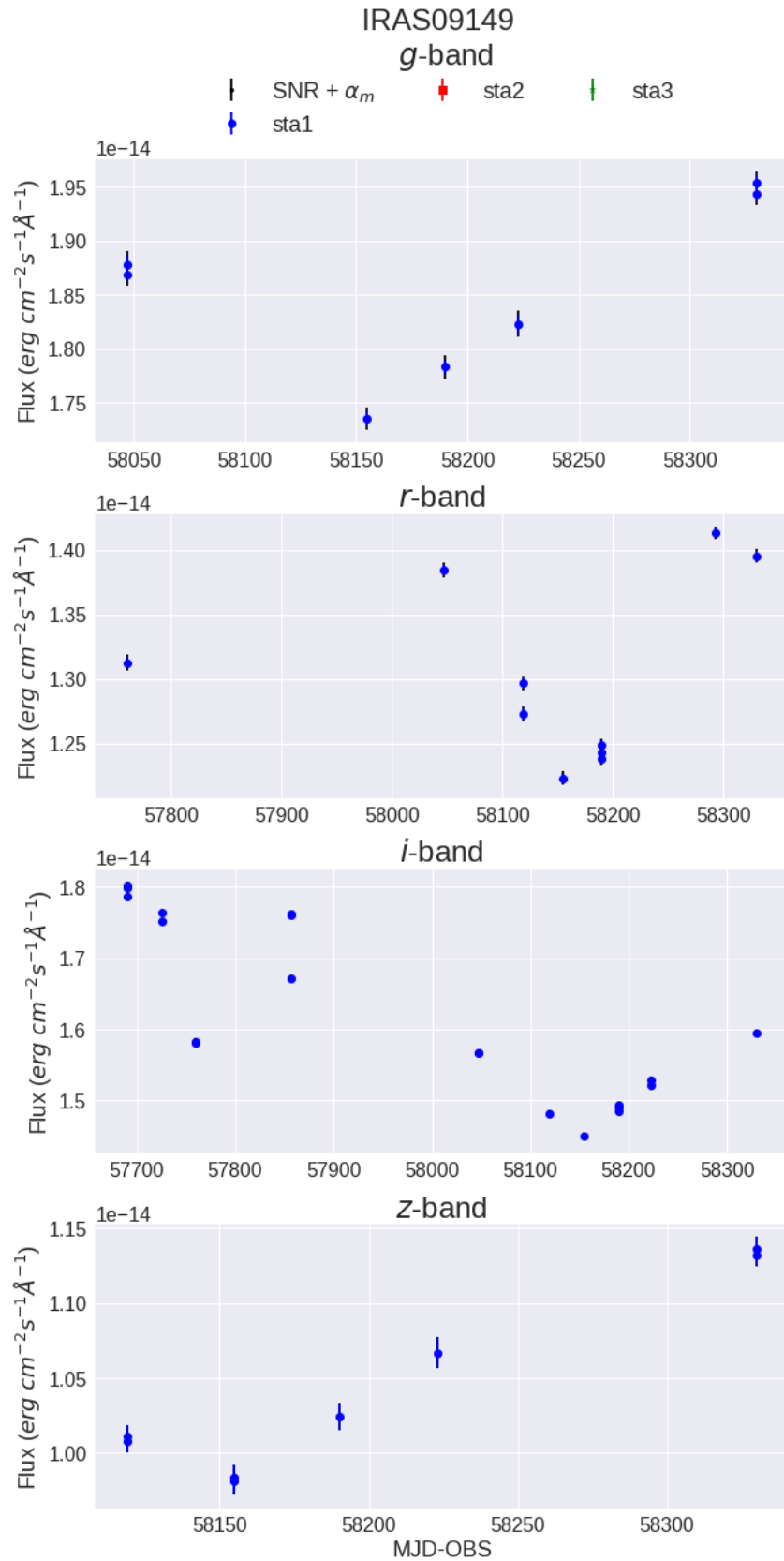


Figure A.17: The IRAS09149 JHK band fluxes.

Figure A.18: The IRAS09149 *griz* fluxes.

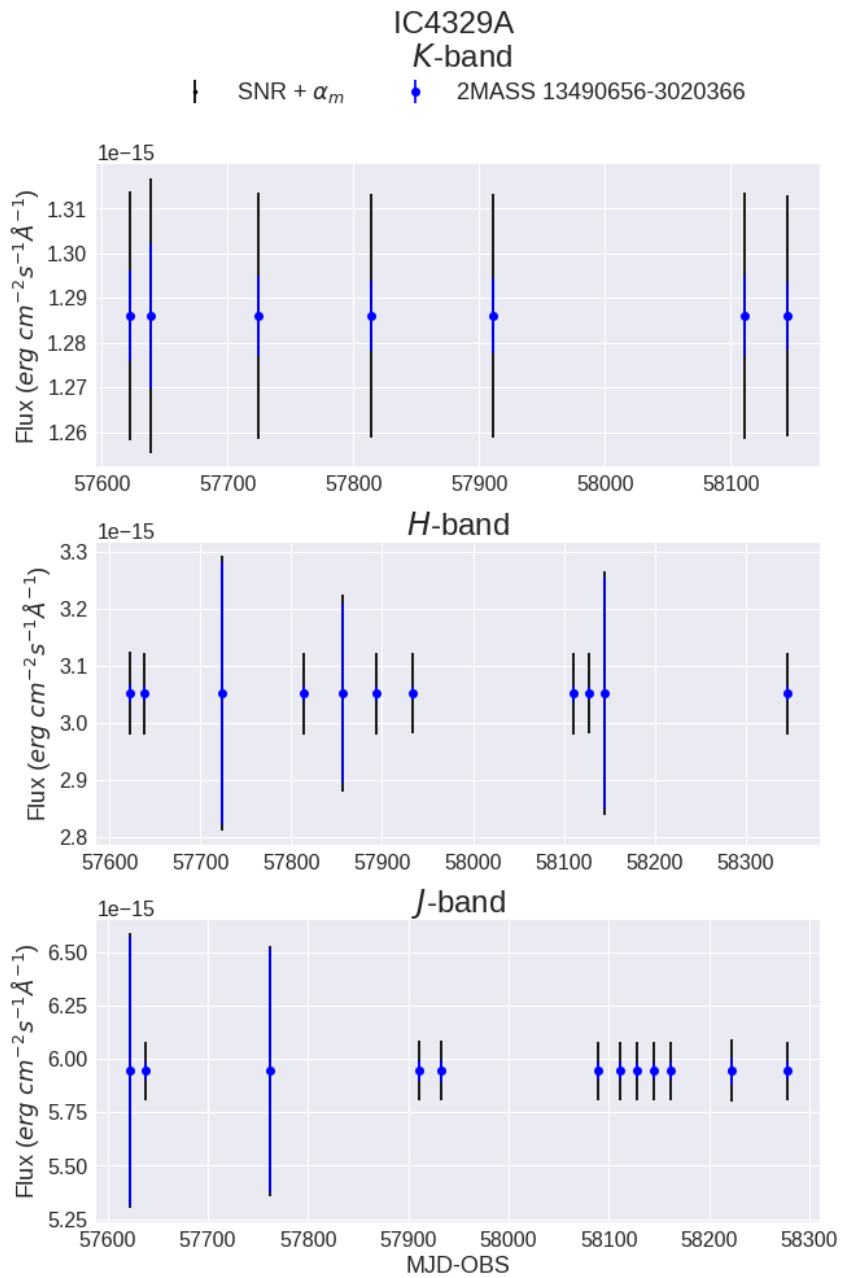


Figure A.19: The IC4329A JHK band fluxes.

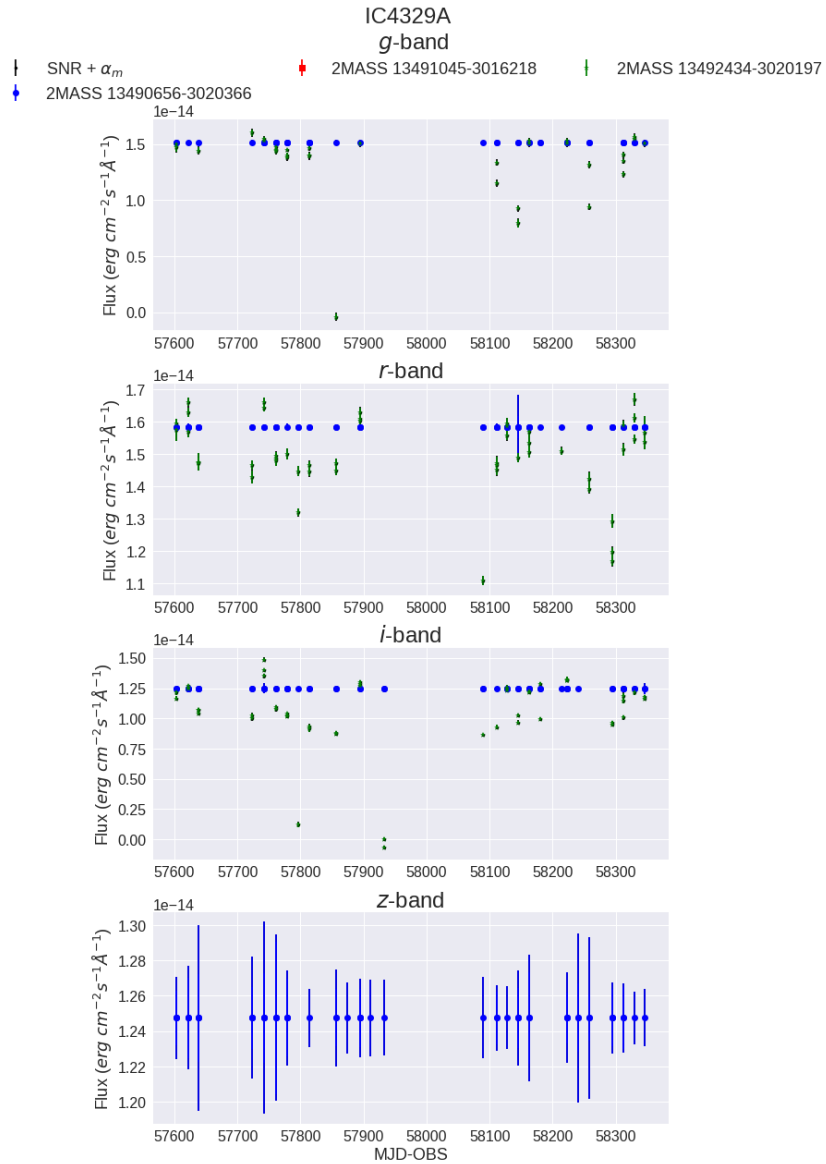


Figure A.20: The IC4329A *griz* fluxes.

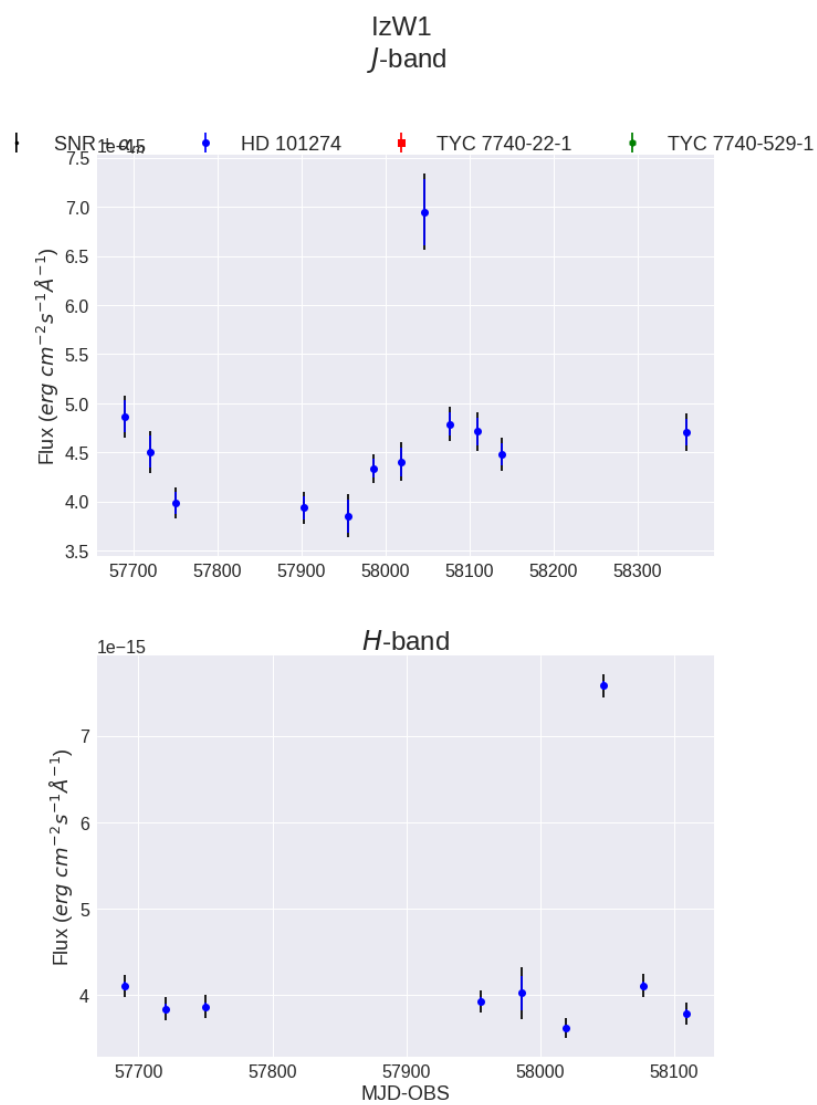


Figure A.21: The IzW1 JHK band fluxes.

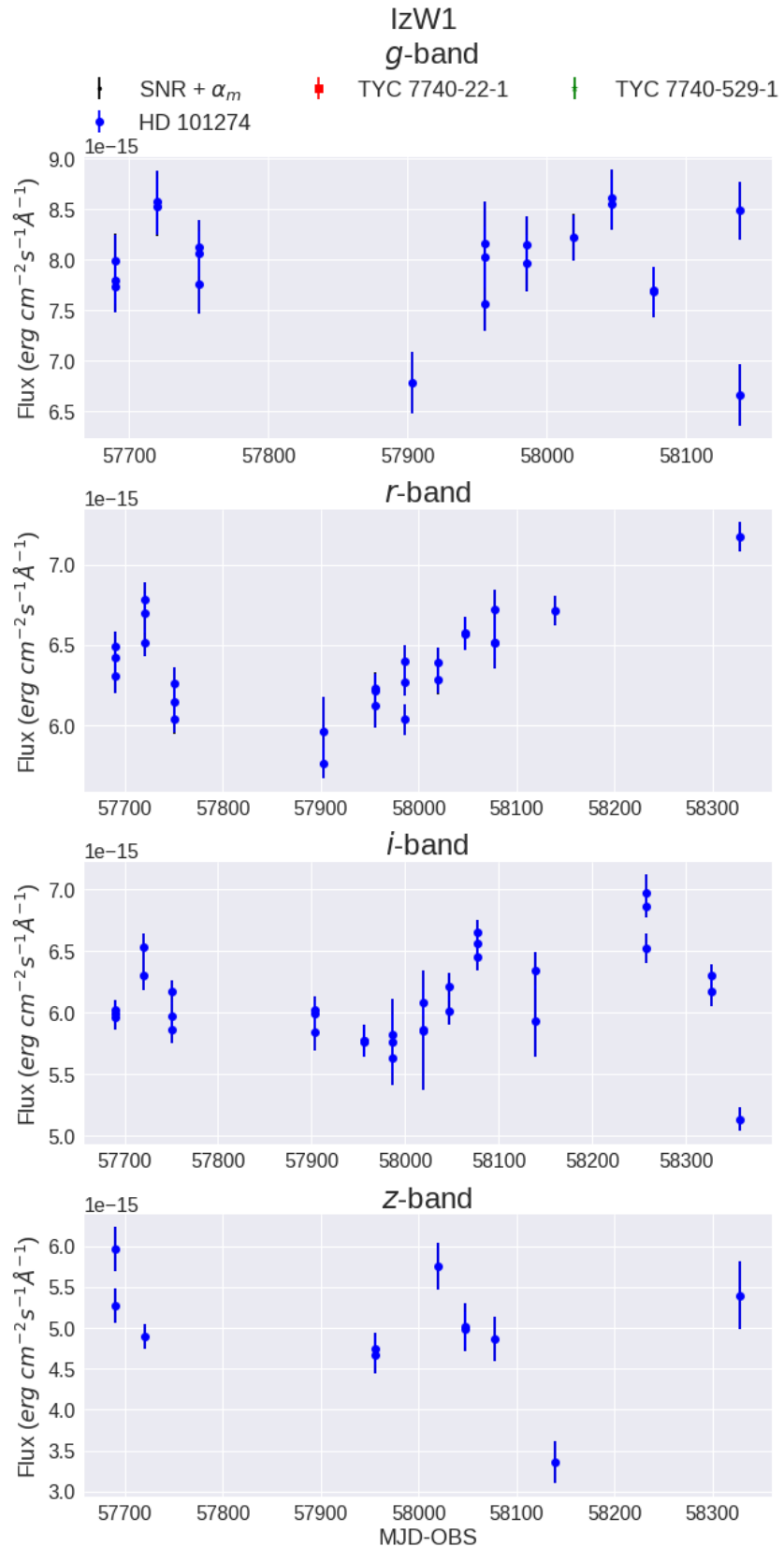


Figure A.22: The IzW1 *griz* fluxes.

Appendix B

AGN Signal-to-Noise Ratio Plots

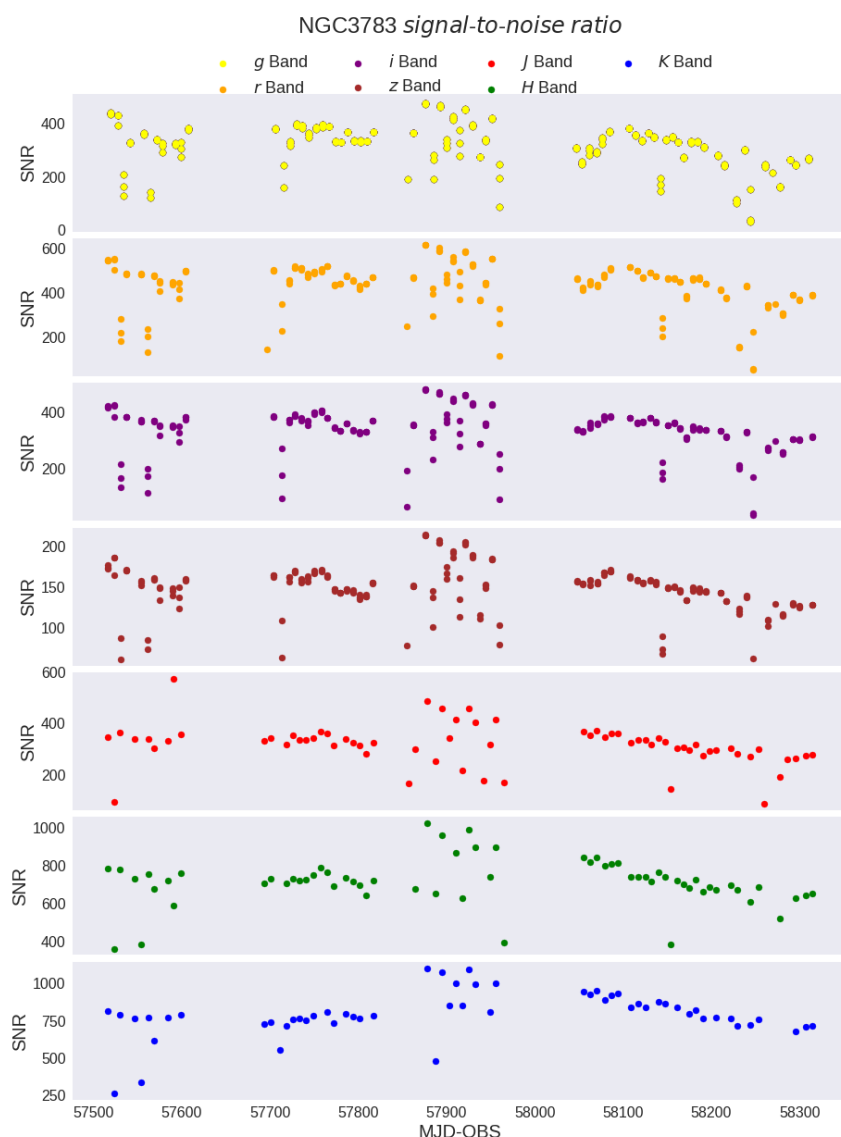


Figure B.1: The NGC3783 signal-to-noise ratios.

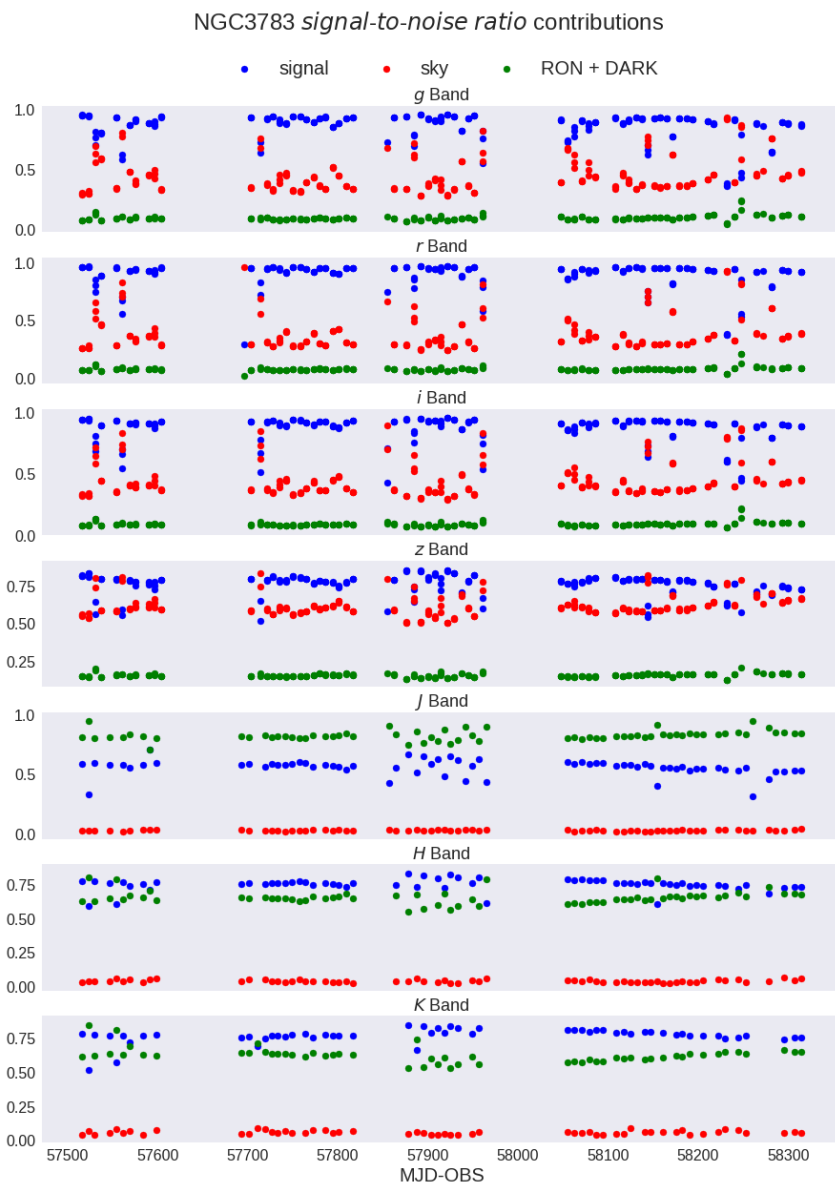


Figure B.2: The individual shot noises divided by the entire shot noise.

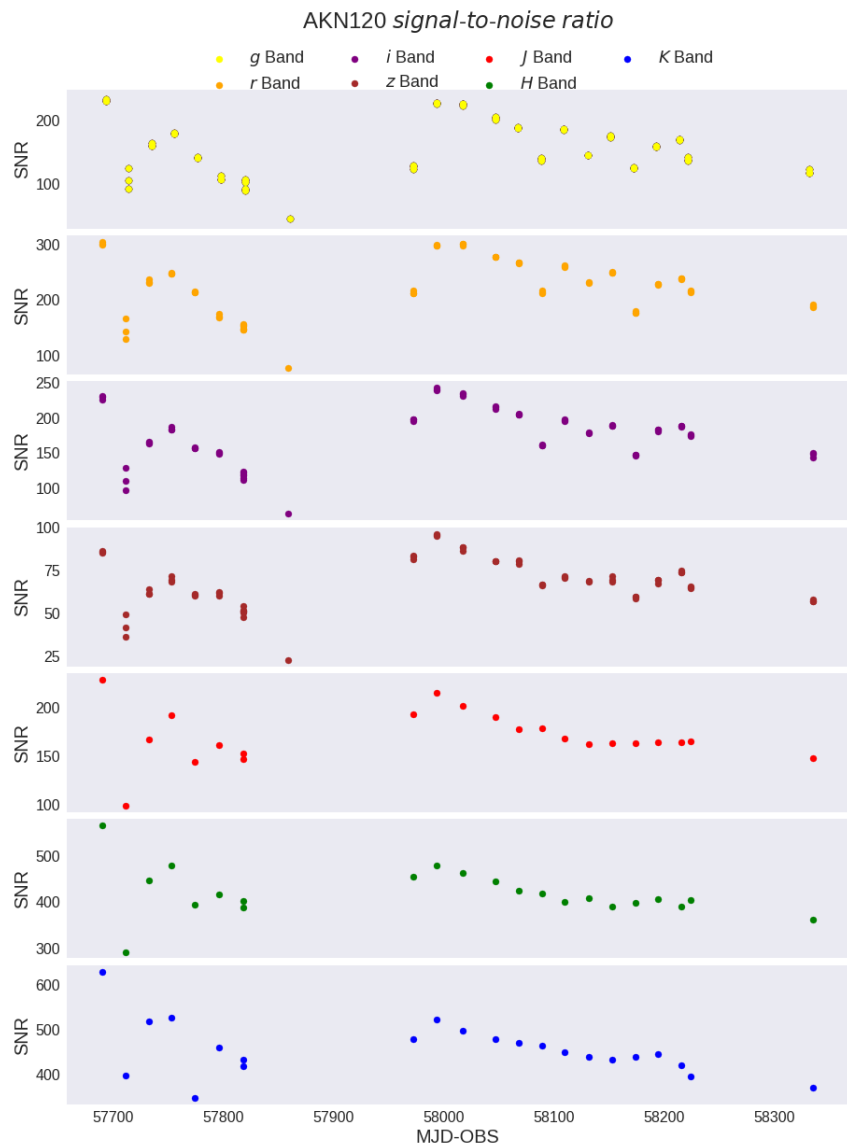


Figure B.3: The AKN120 signal-to-noise ratios.

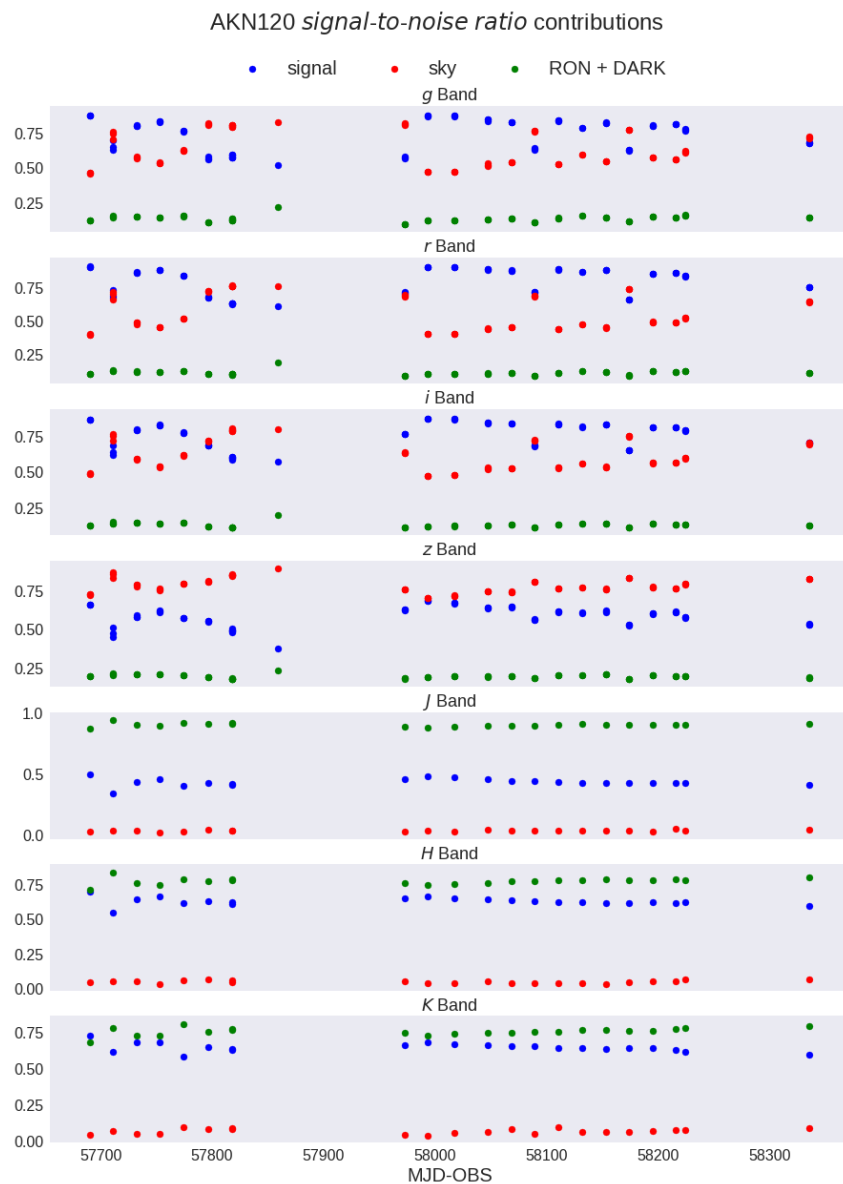


Figure B.4: The individual shot noises divided by the entire shot noise.

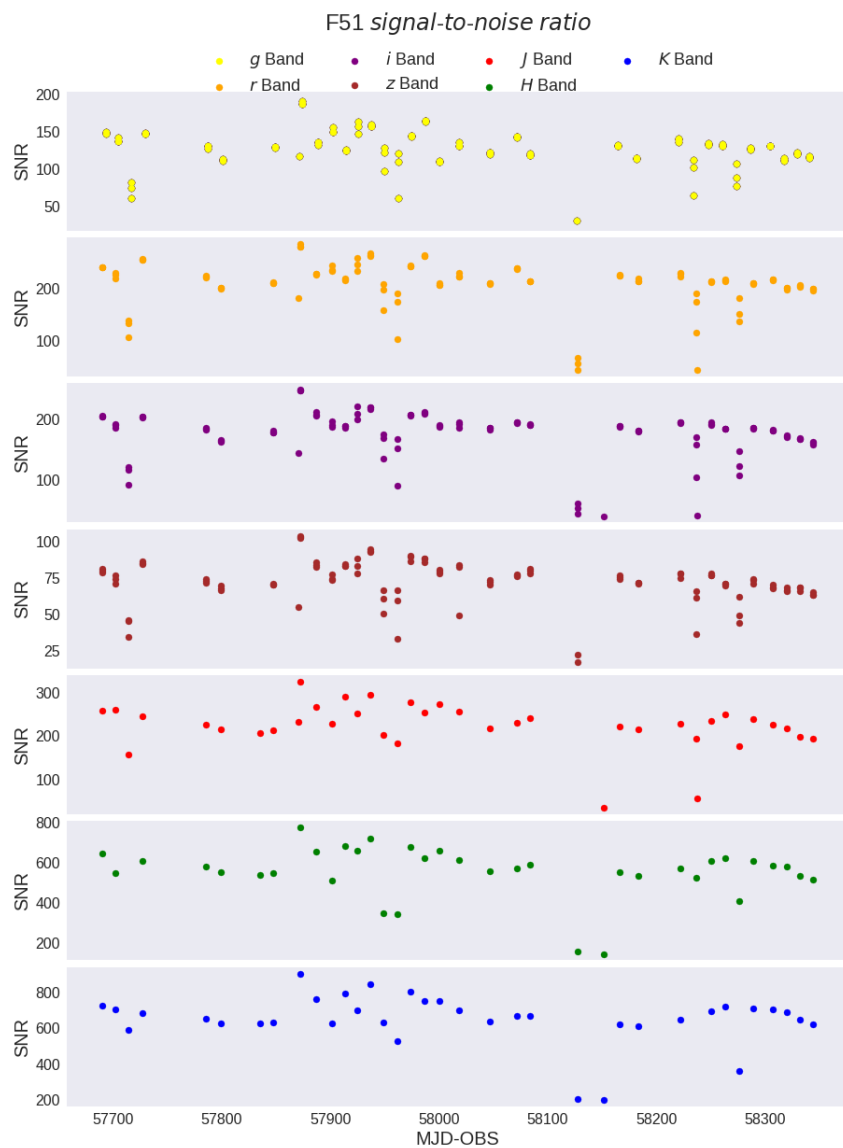


Figure B.5: The F51 signal-to-noise ratios.

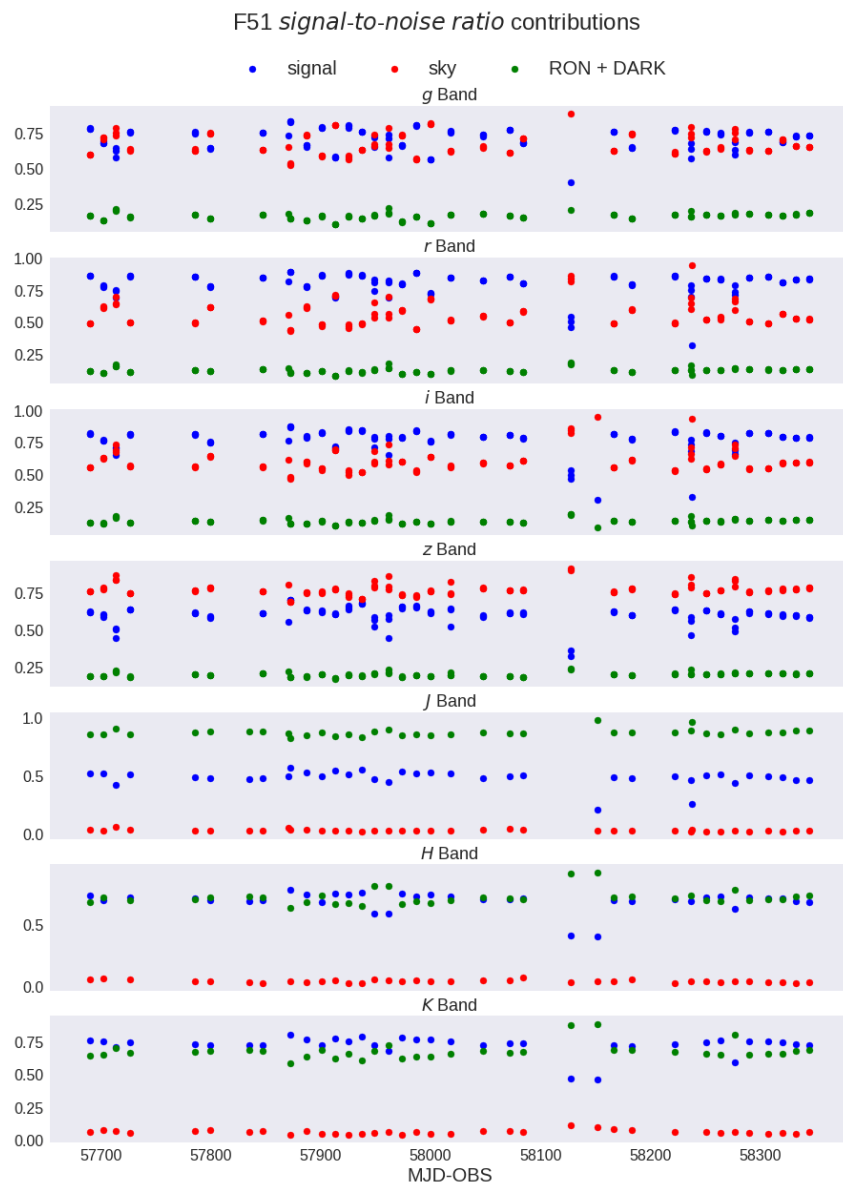


Figure B.6: The individual shot noises divided by the entire shot noise.

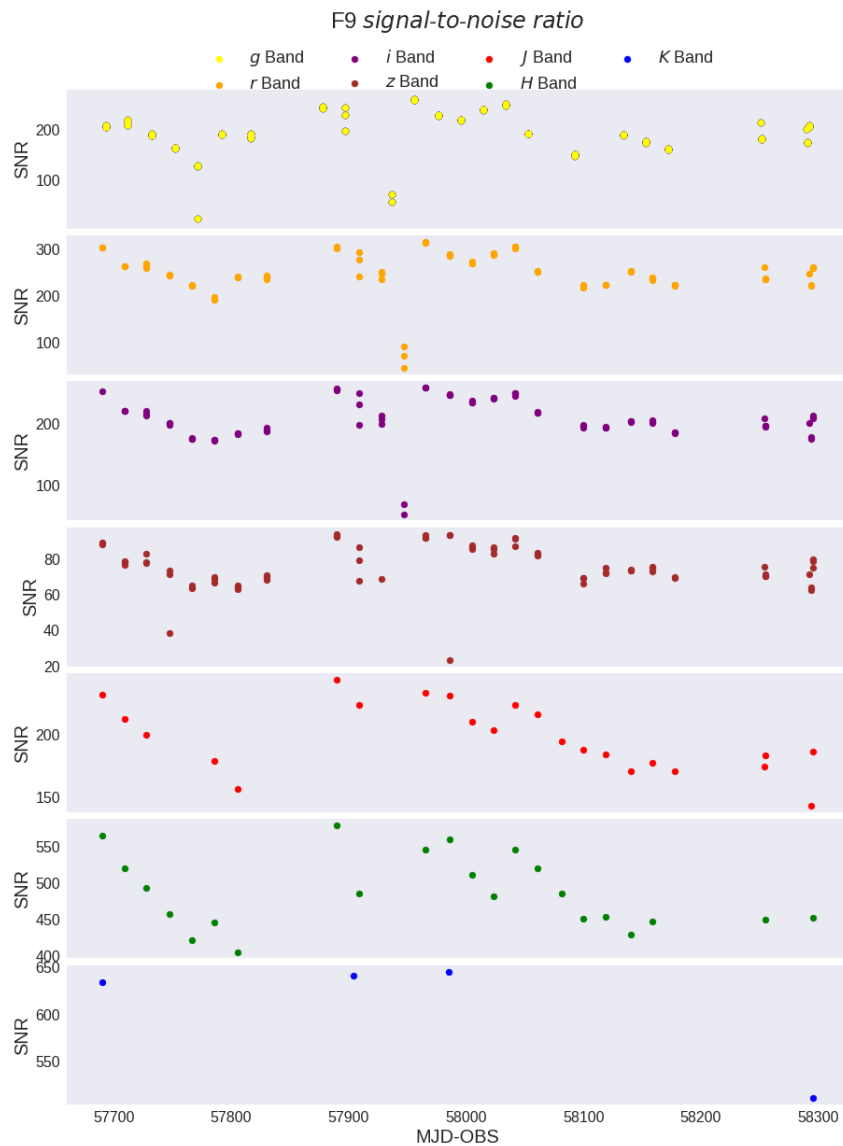


Figure B.7: The F9 signal-to-noise ratios.

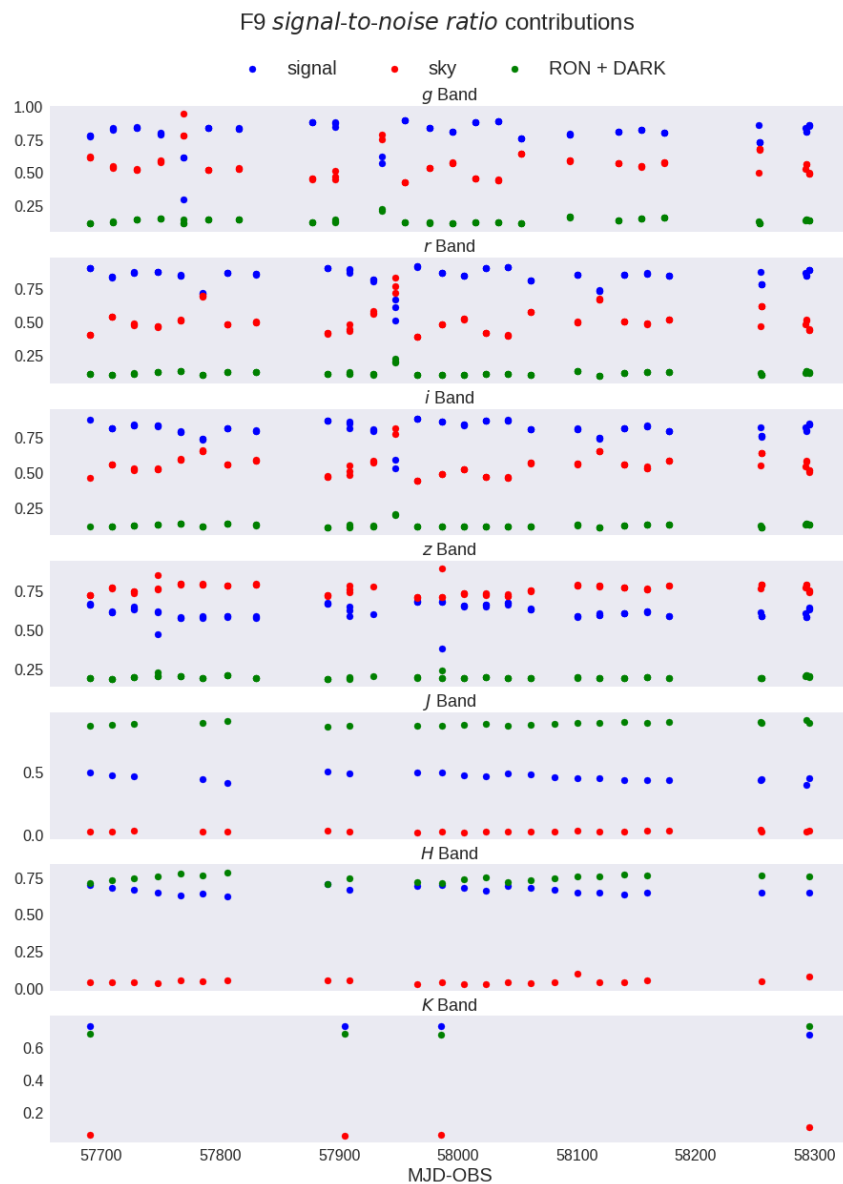


Figure B.8: The individual shot noises divided by the entire shot noise.

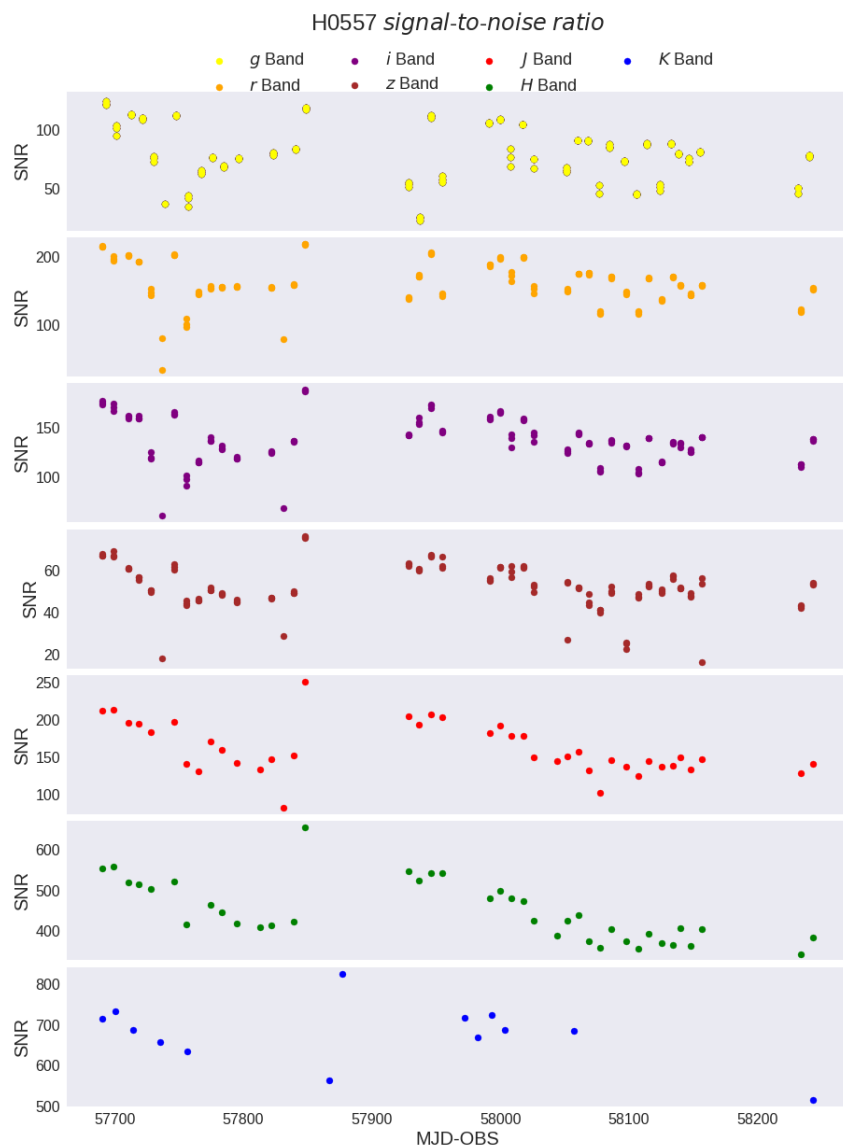


Figure B.9: The H0557 signal-to-noise ratios.

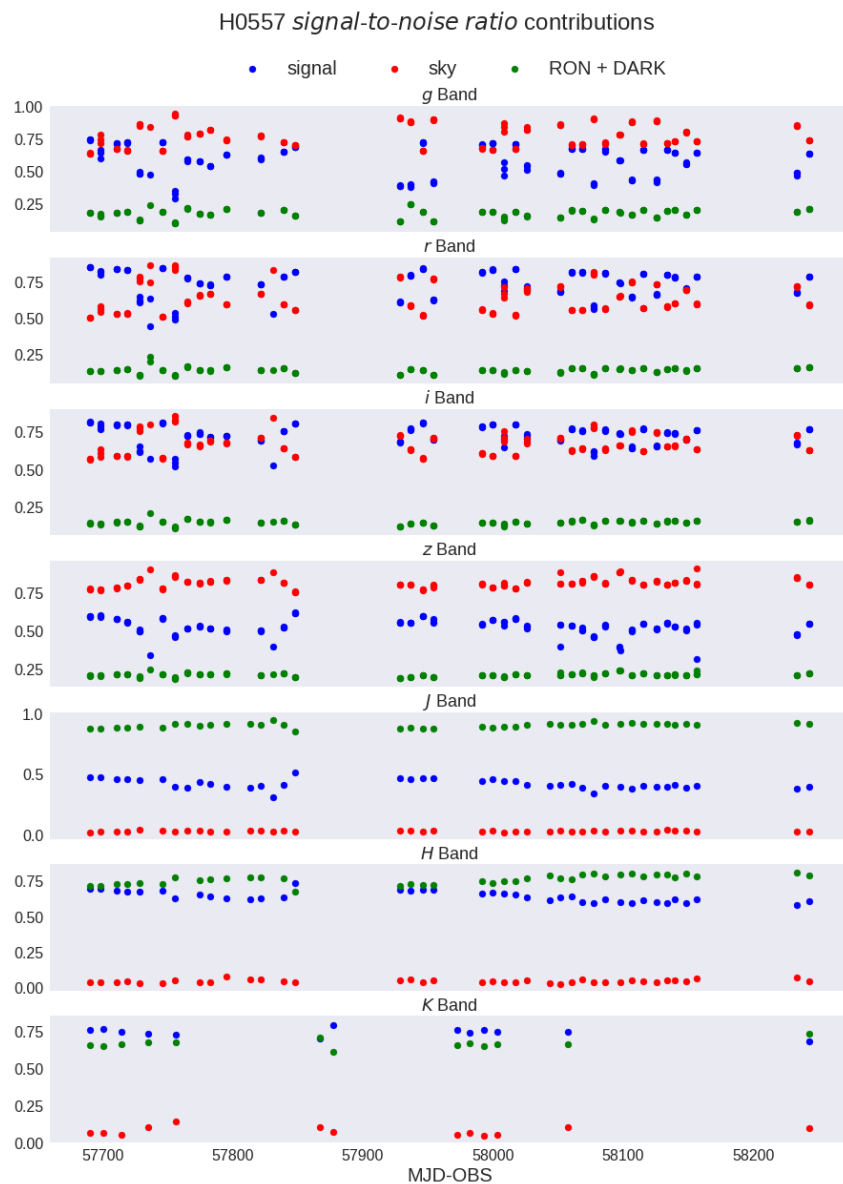


Figure B.10: The individual shot noises divided by the entire shot noise.

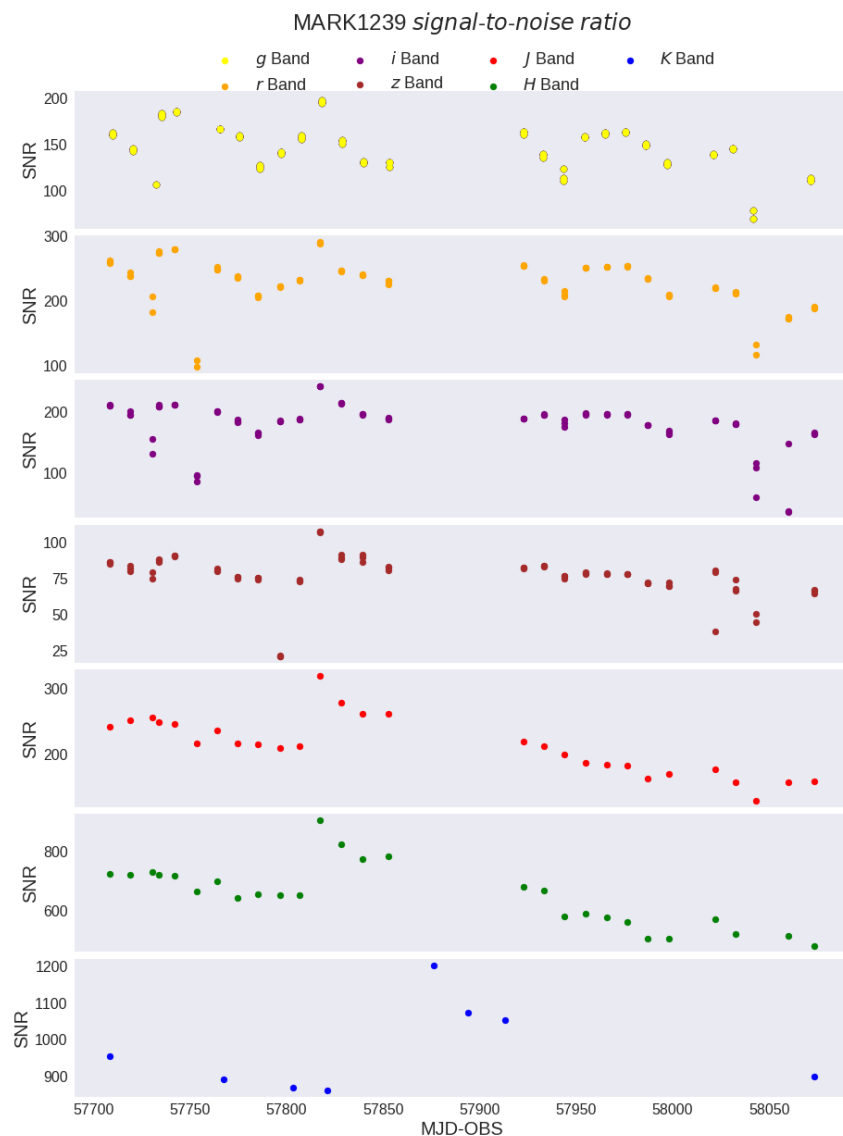


Figure B.11: The MARK1239 signal-to-noise ratios.

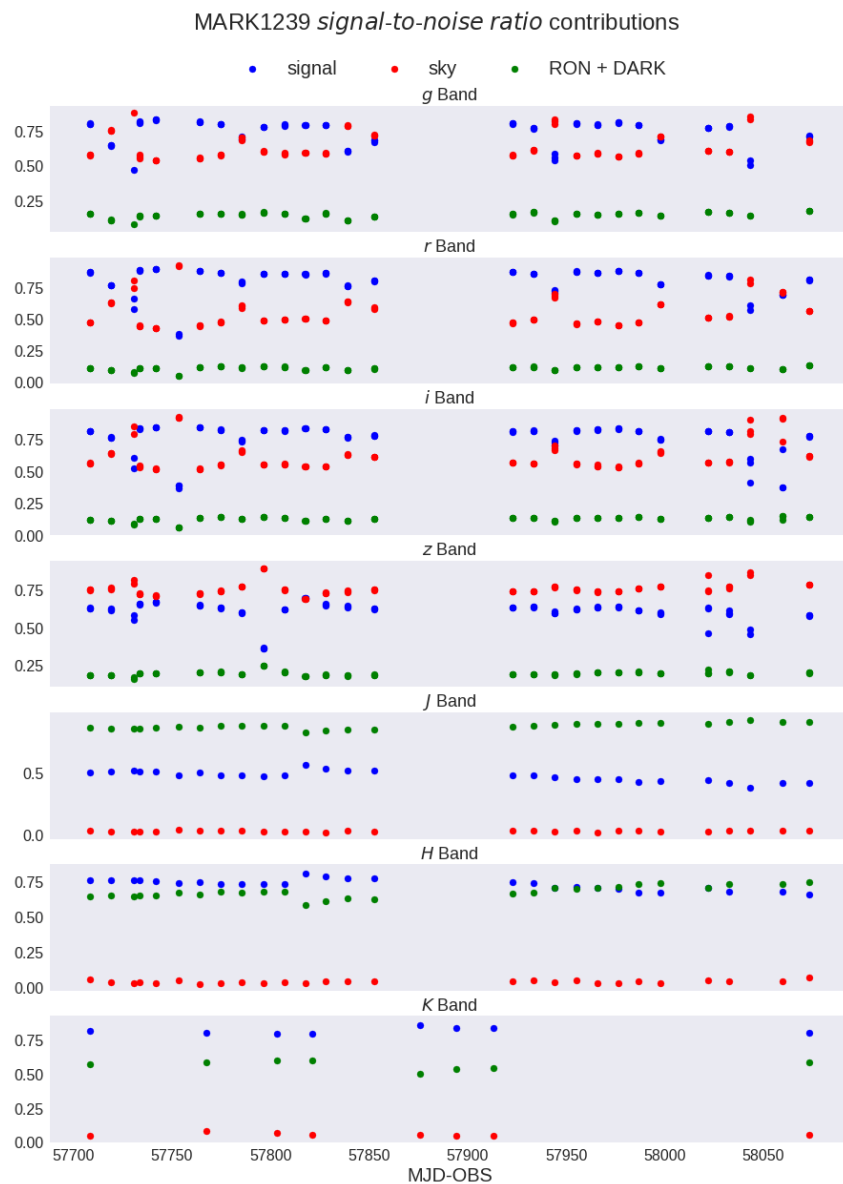


Figure B.12: The individual shot noises divided by the entire shot noise.

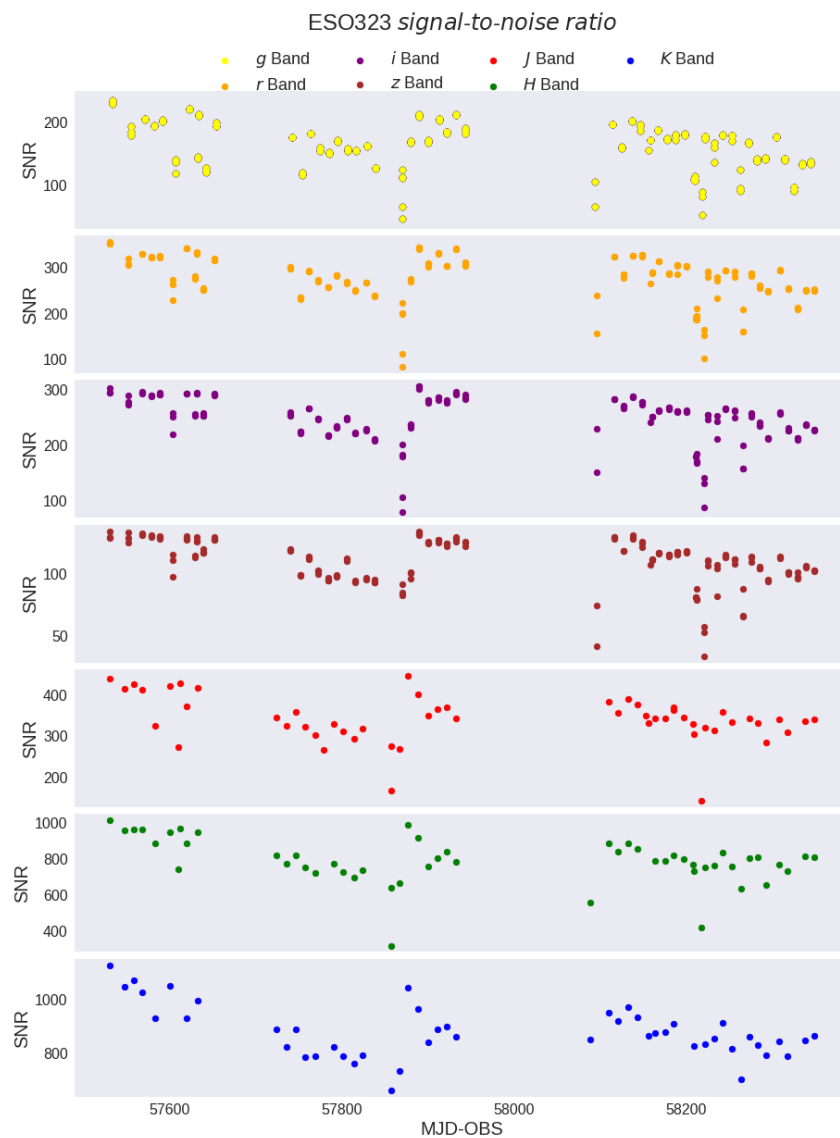


Figure B.13: The ESO323 signal-to-noise ratios.

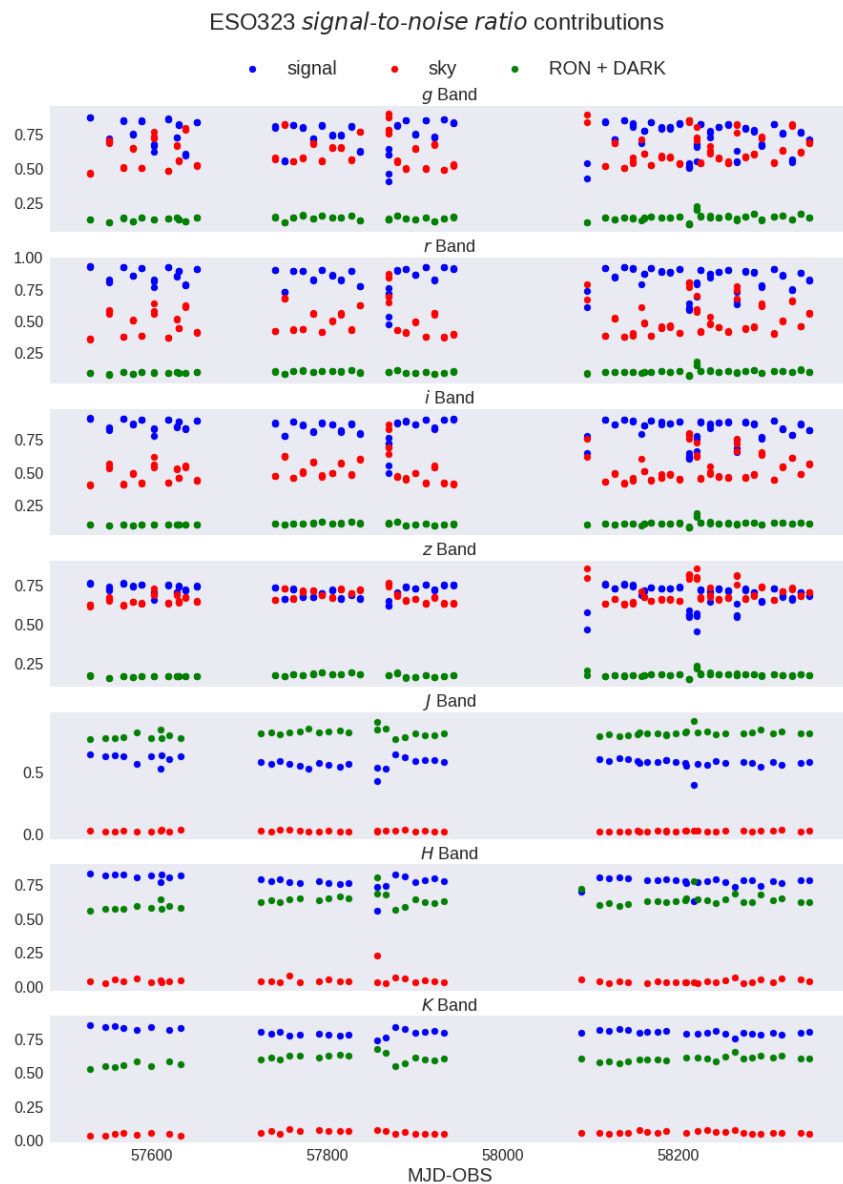


Figure B.14: The individual shot noises divided by the entire shot noise.

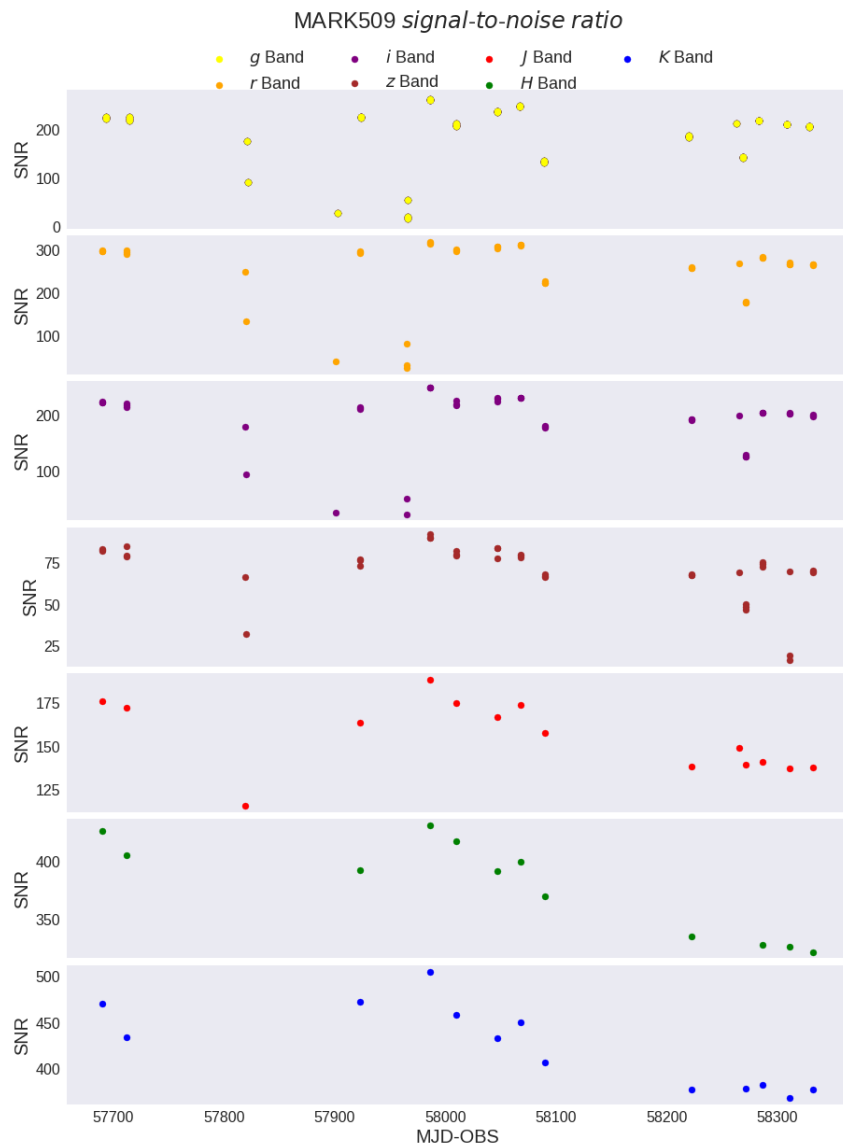


Figure B.15: The MARK509 signal-to-noise ratios.

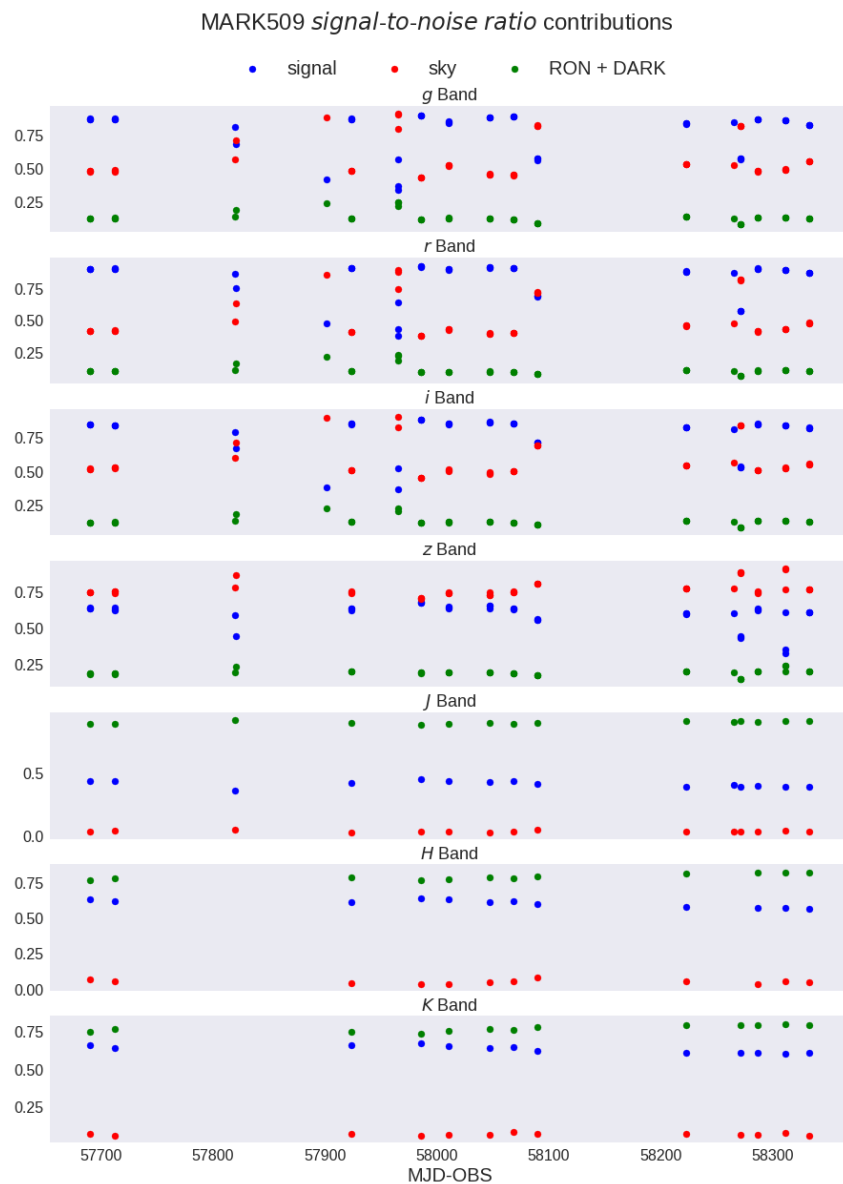


Figure B.16: The individual shot noises divided by the entire shot noise.

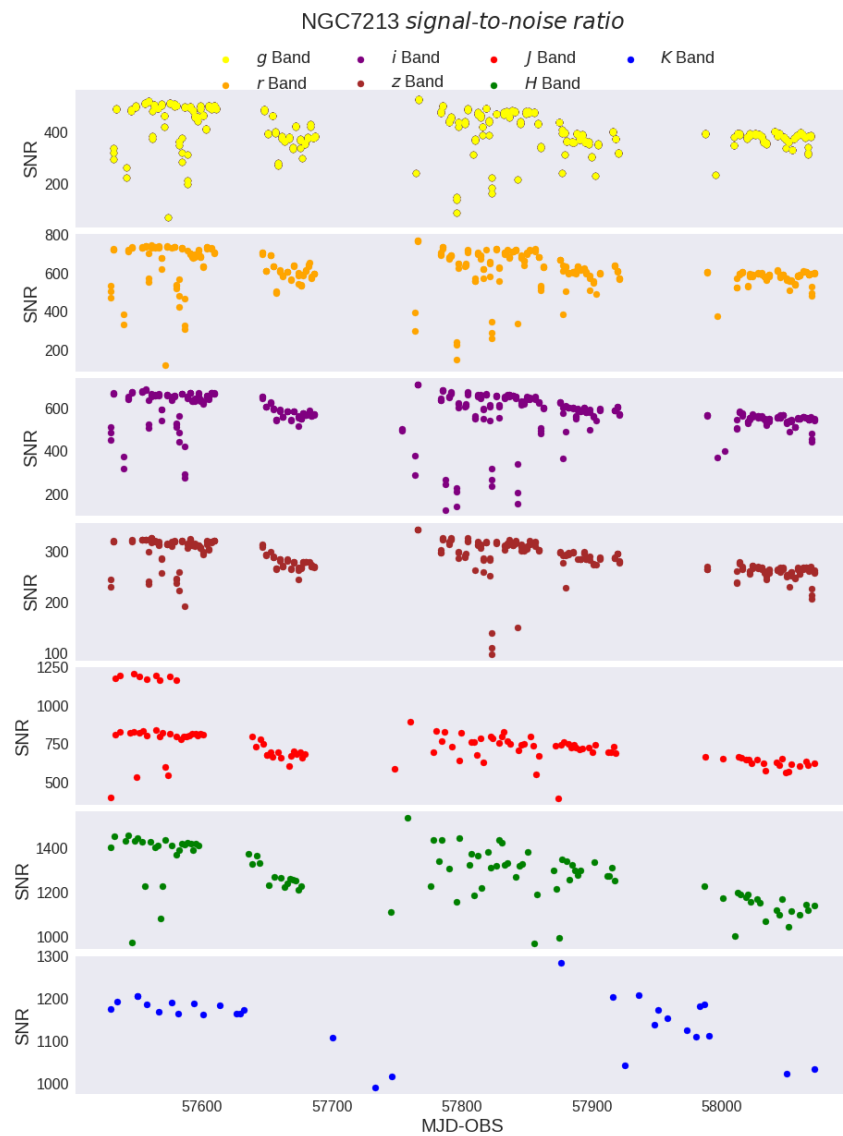


Figure B.17: The NGC7213 signal-to-noise ratios.

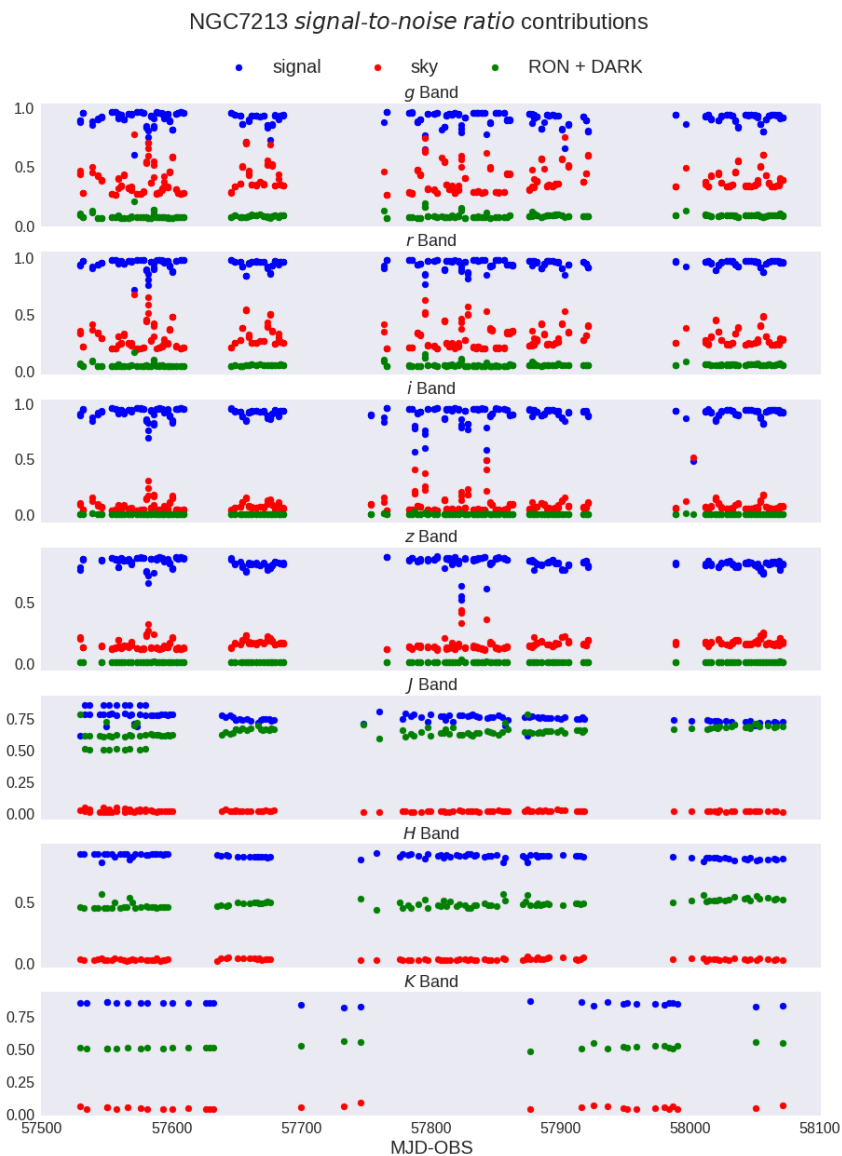


Figure B.18: The individual shot noises divided by the entire shot noise.

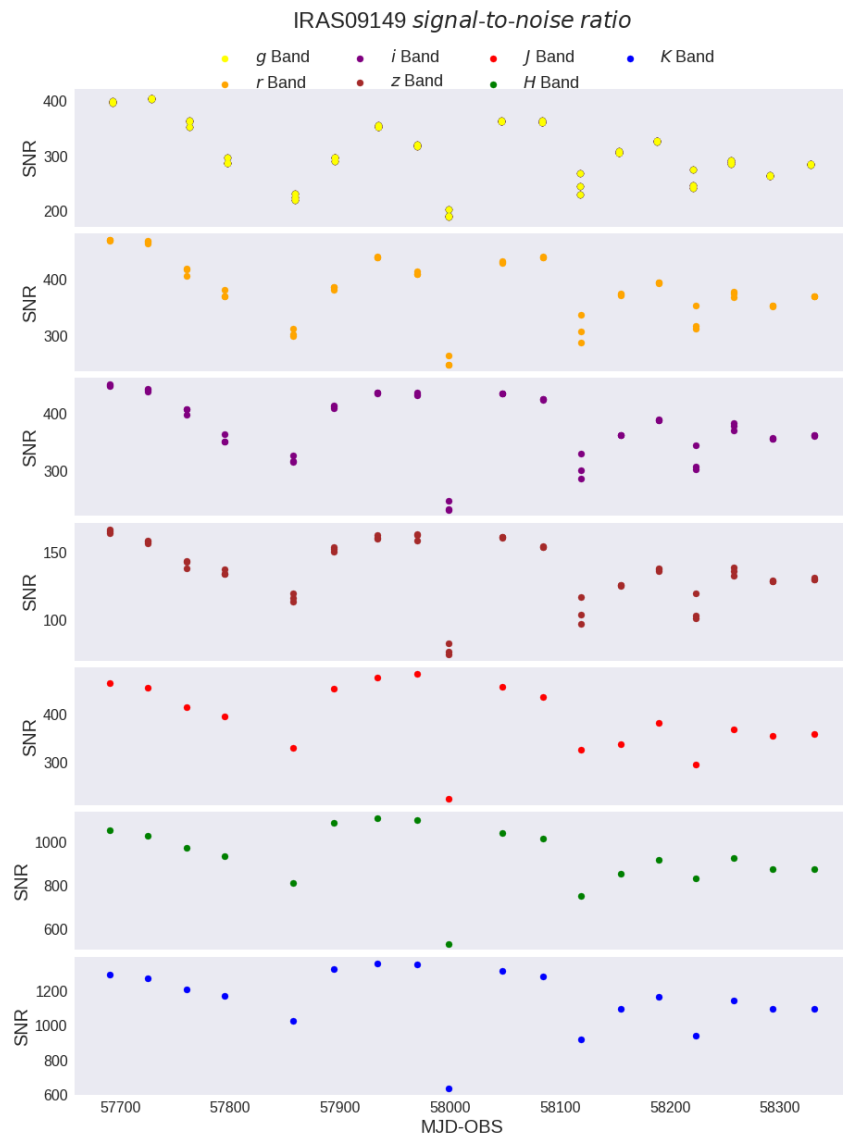


Figure B.19: The IRAS09149 signal-to-noise ratios.

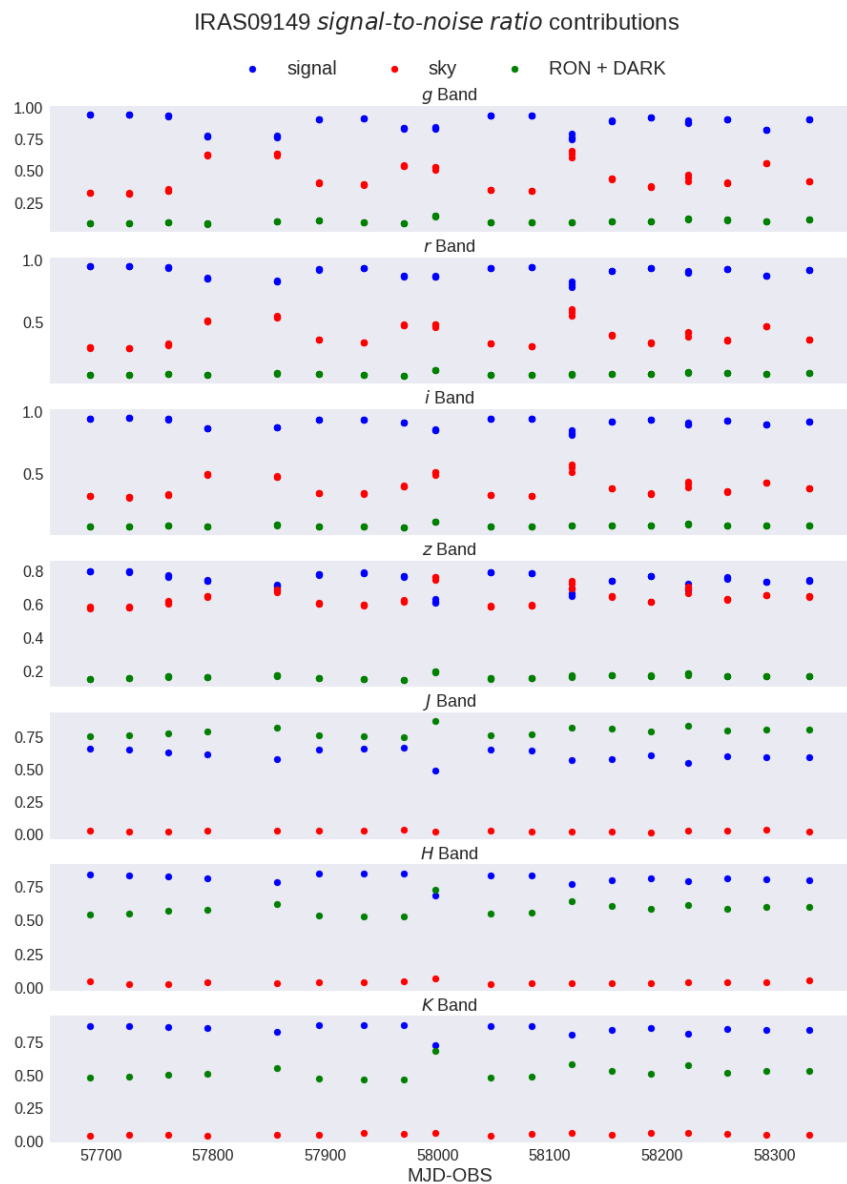


Figure B.20: The individual shot noises divided by the entire shot noise.

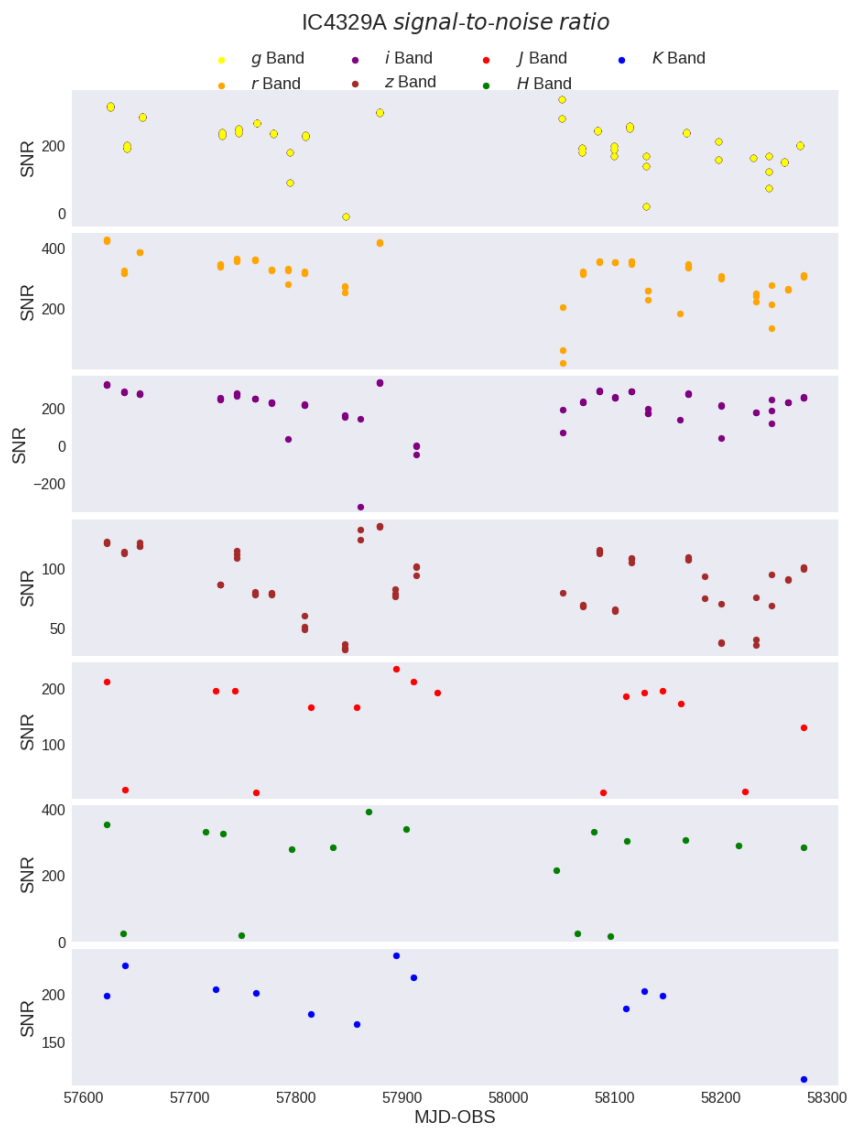


Figure B.21: The IC4329A signal-to-noise ratios.

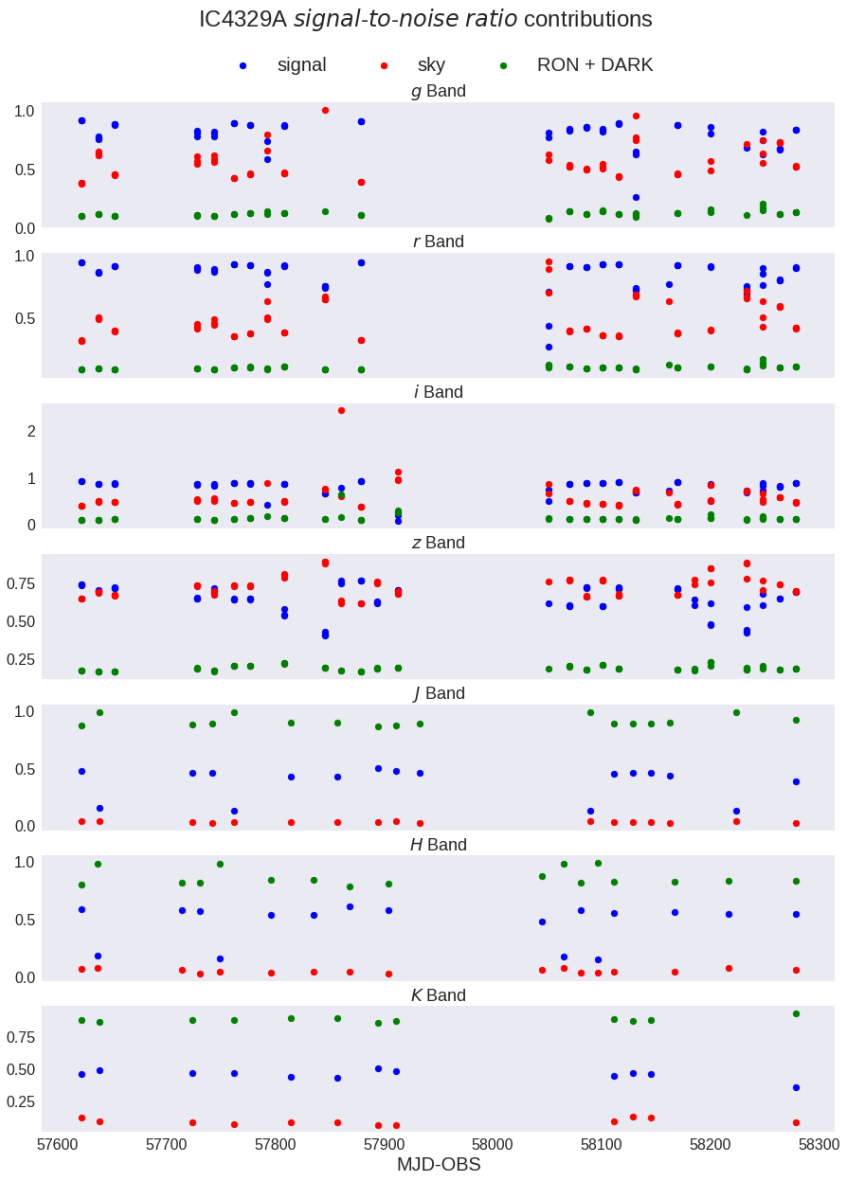


Figure B.22: The individual shot noises divided by the entire shot noise.

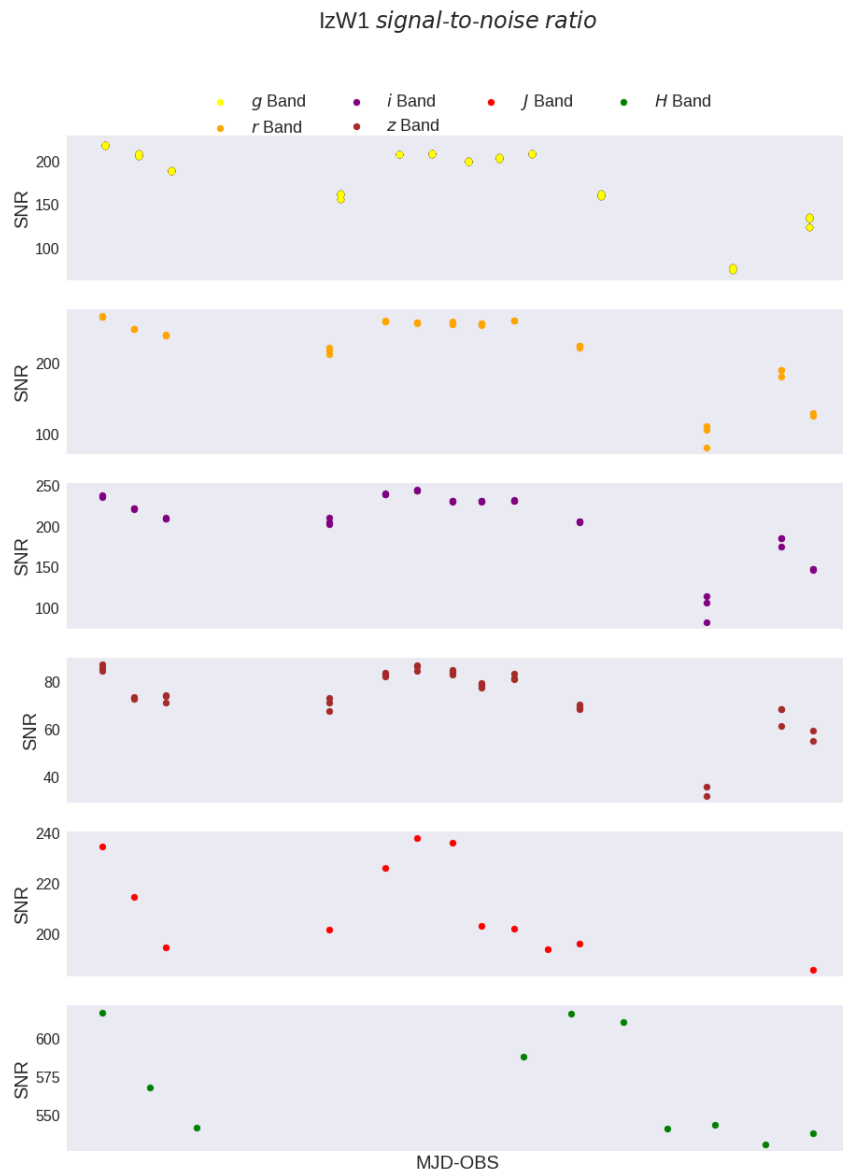


Figure B.23: The IzW1 signal-to-noise ratios.

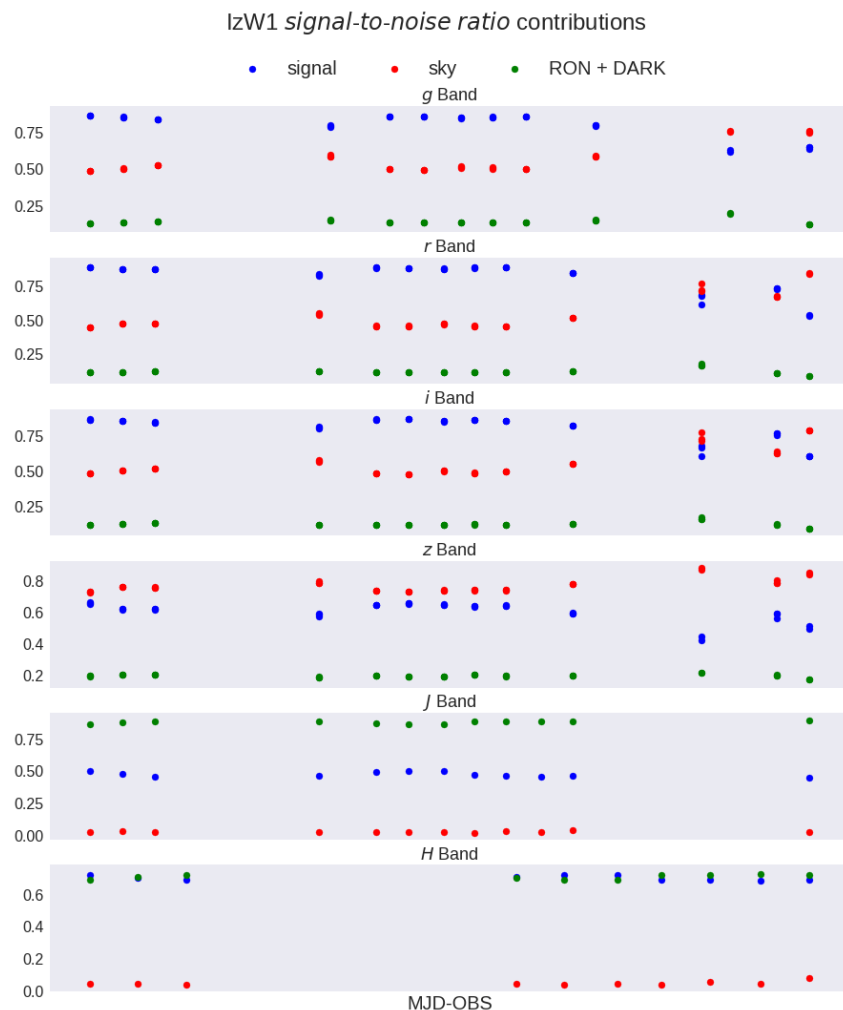


Figure B.24: The individual shot noises divided by the entire shot noise.

Appendix C

Structure Function Plots

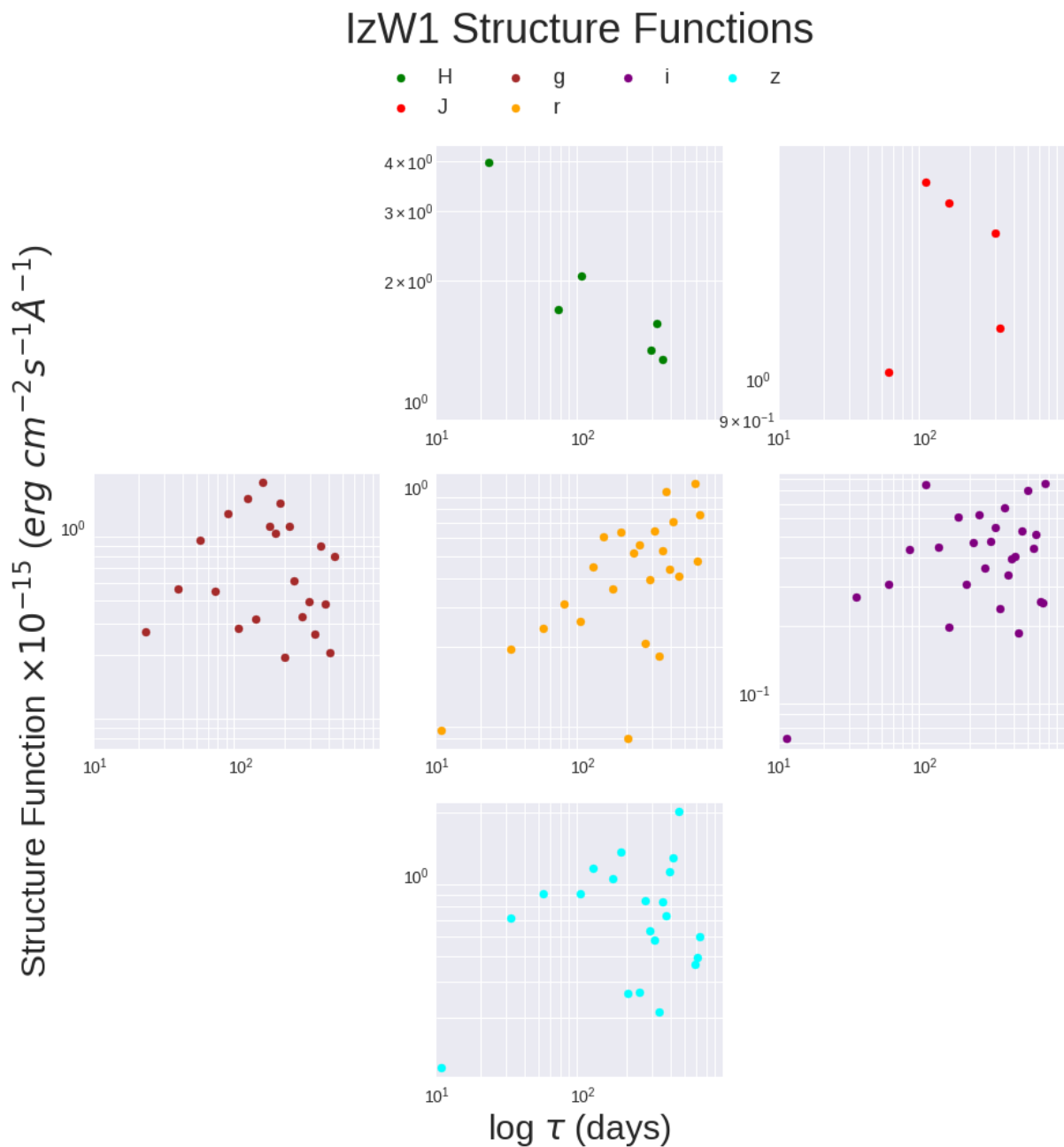


Figure C.1: The NGC3783 structure functions.

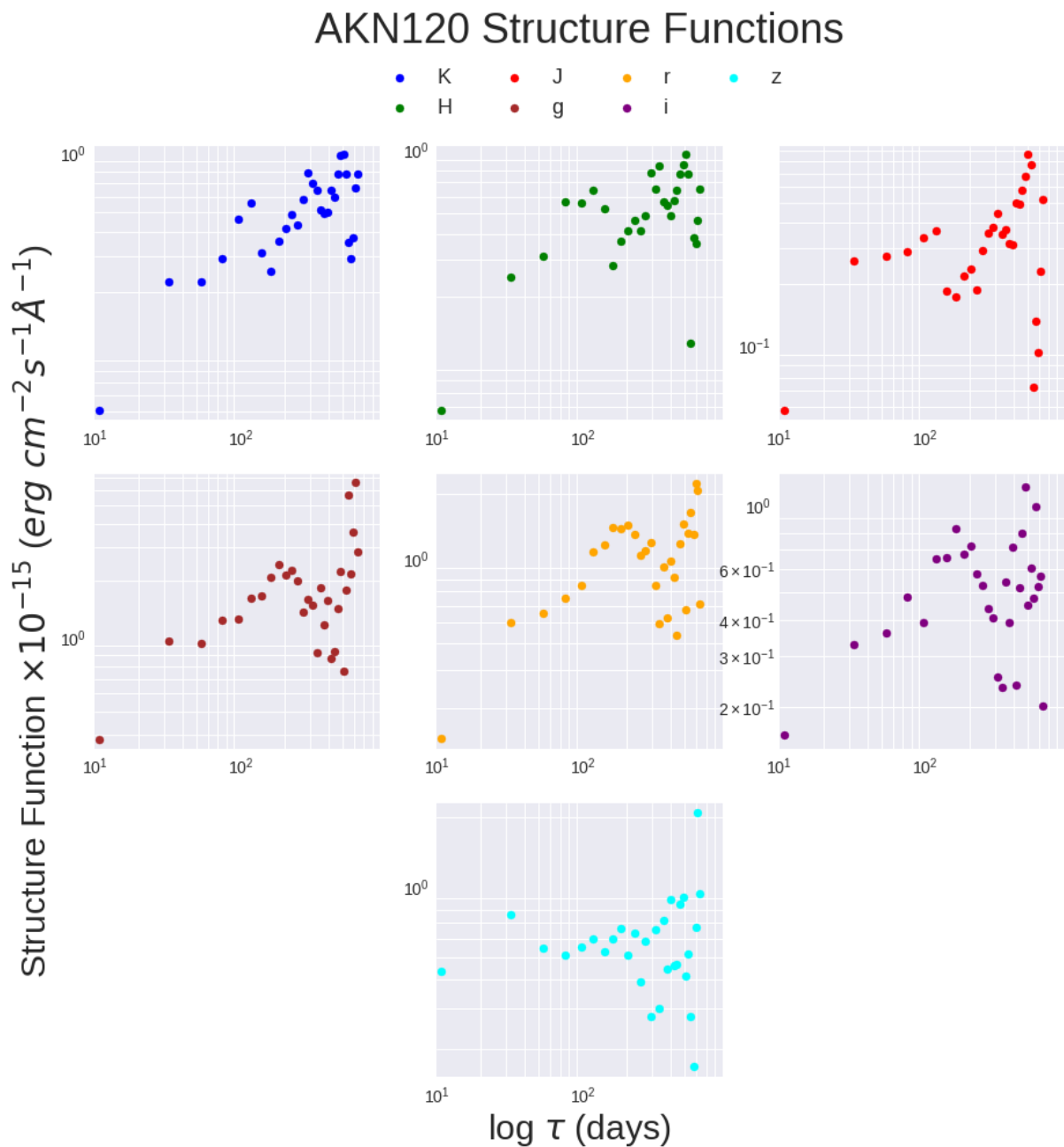


Figure C.2: The AKN120 structure functions.

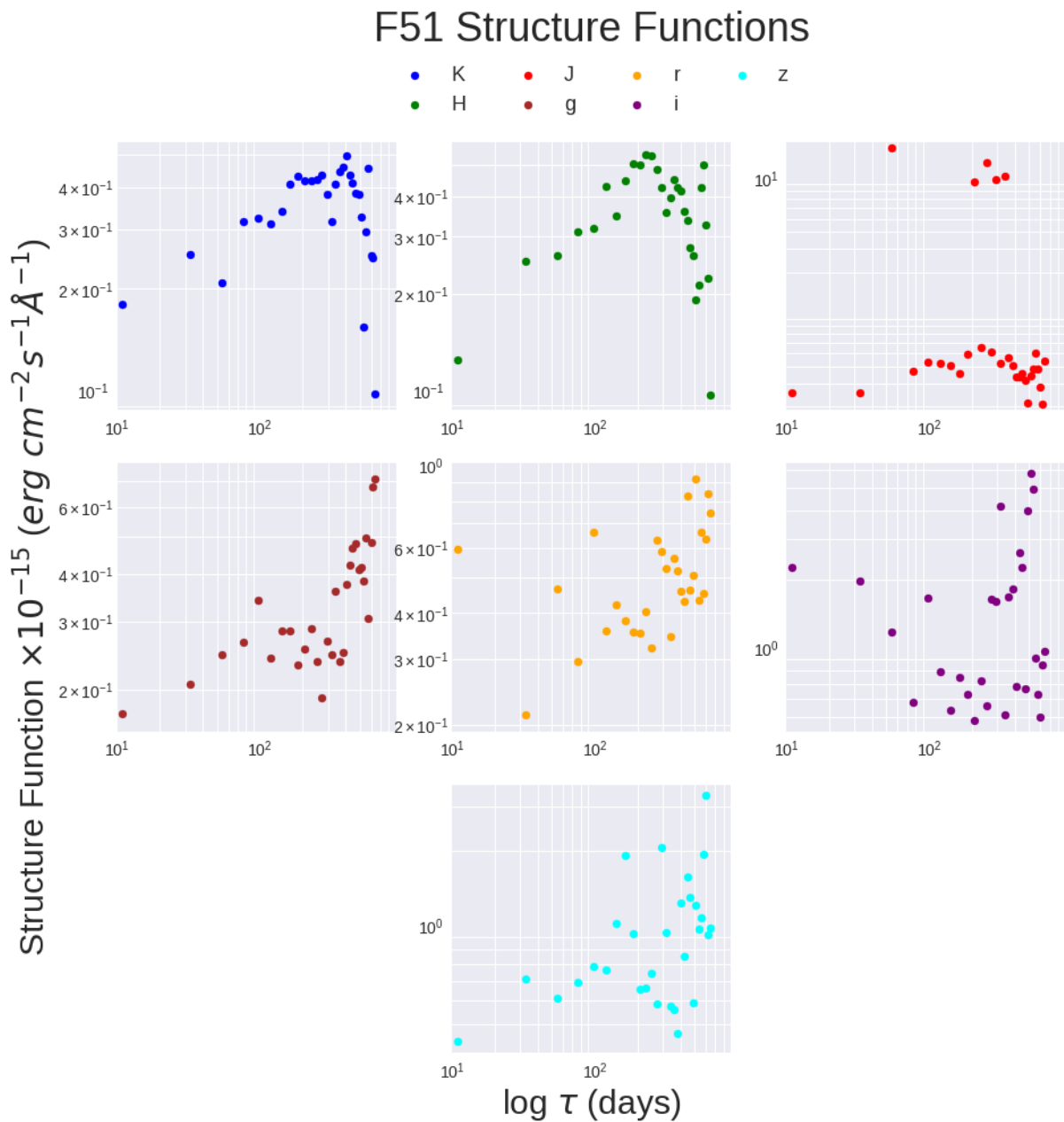


Figure C.3: The F51 structure functions.

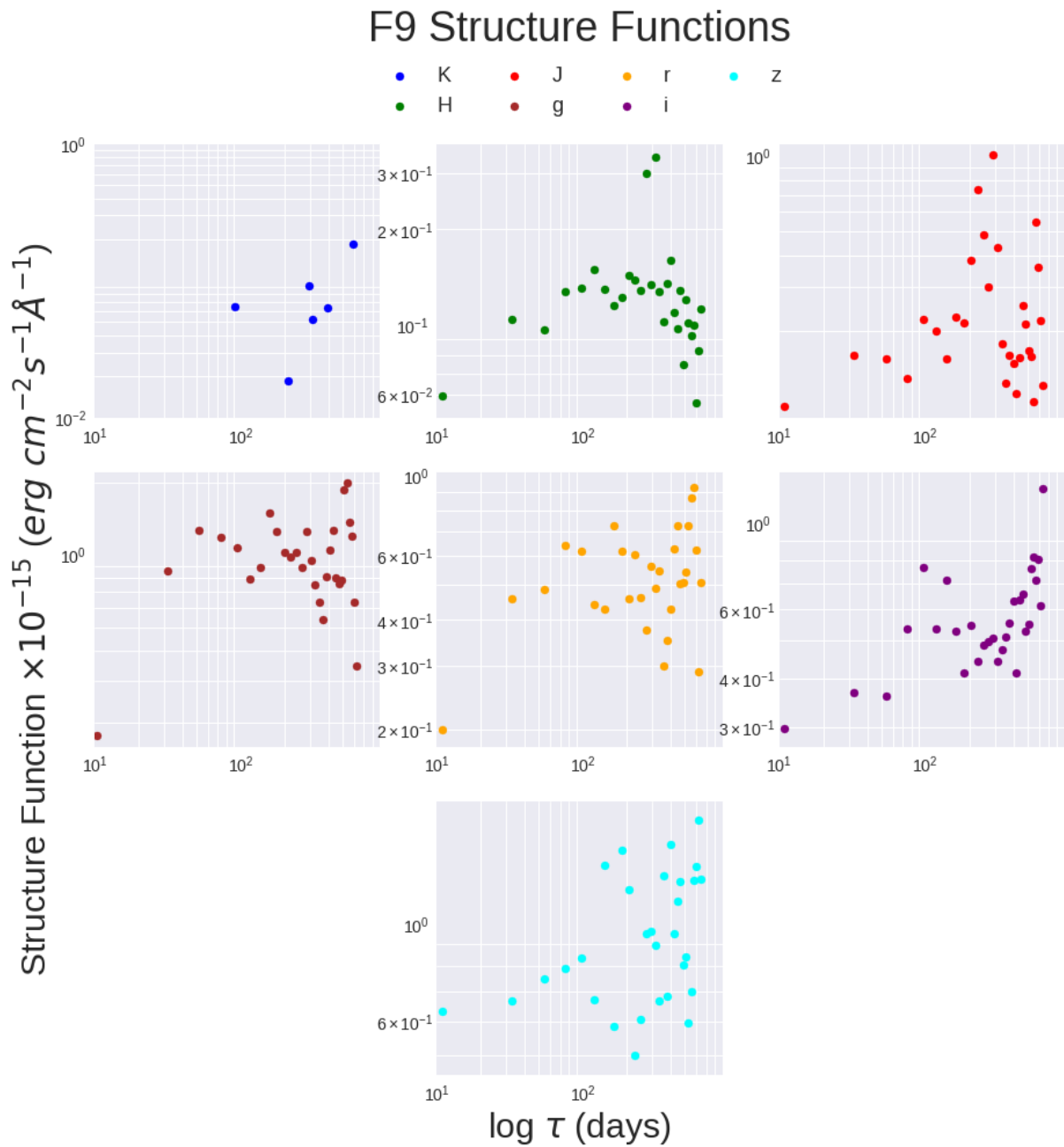


Figure C.4: The F9 structure functions.

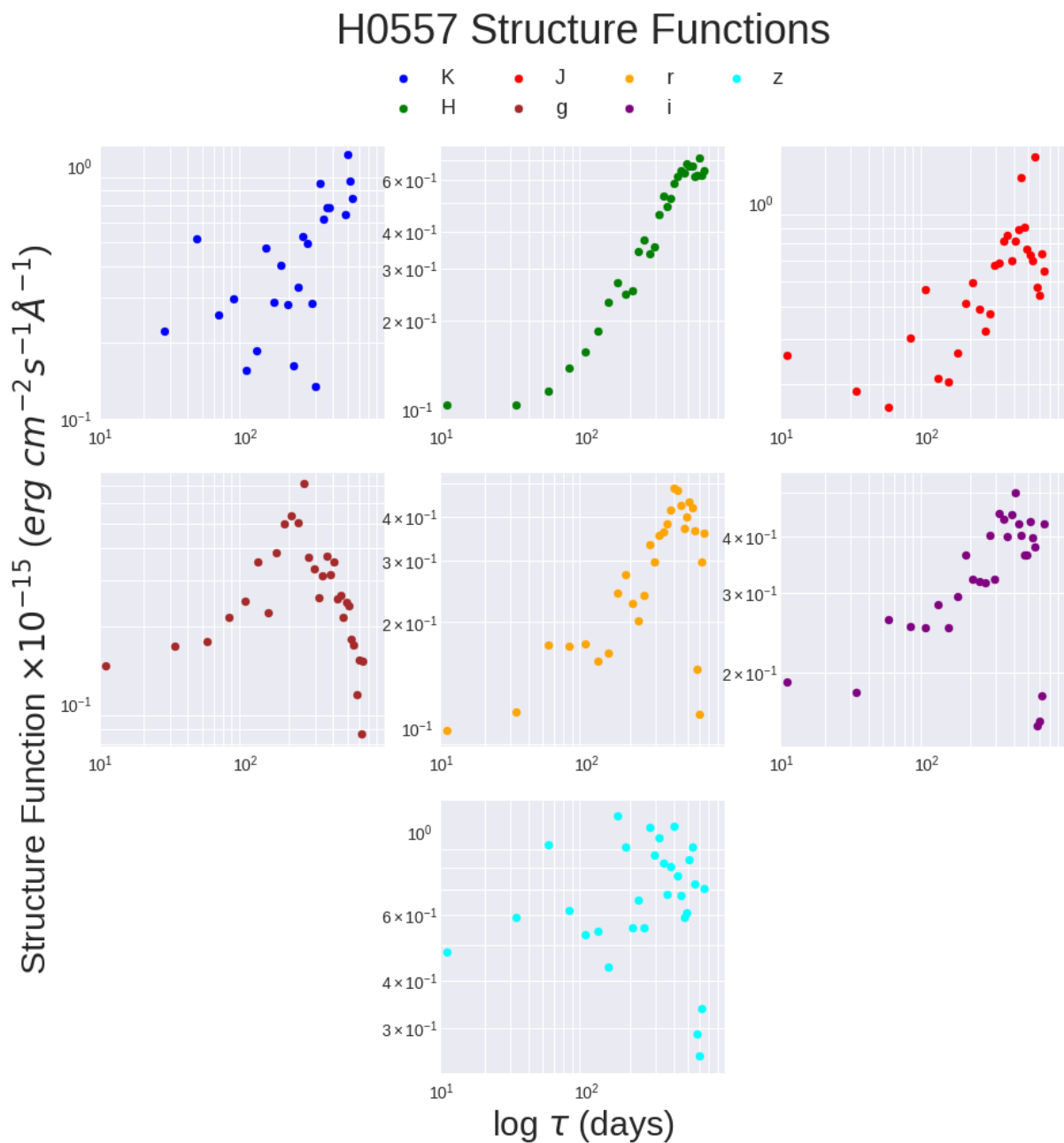


Figure C.5: The H0557 structure functions.

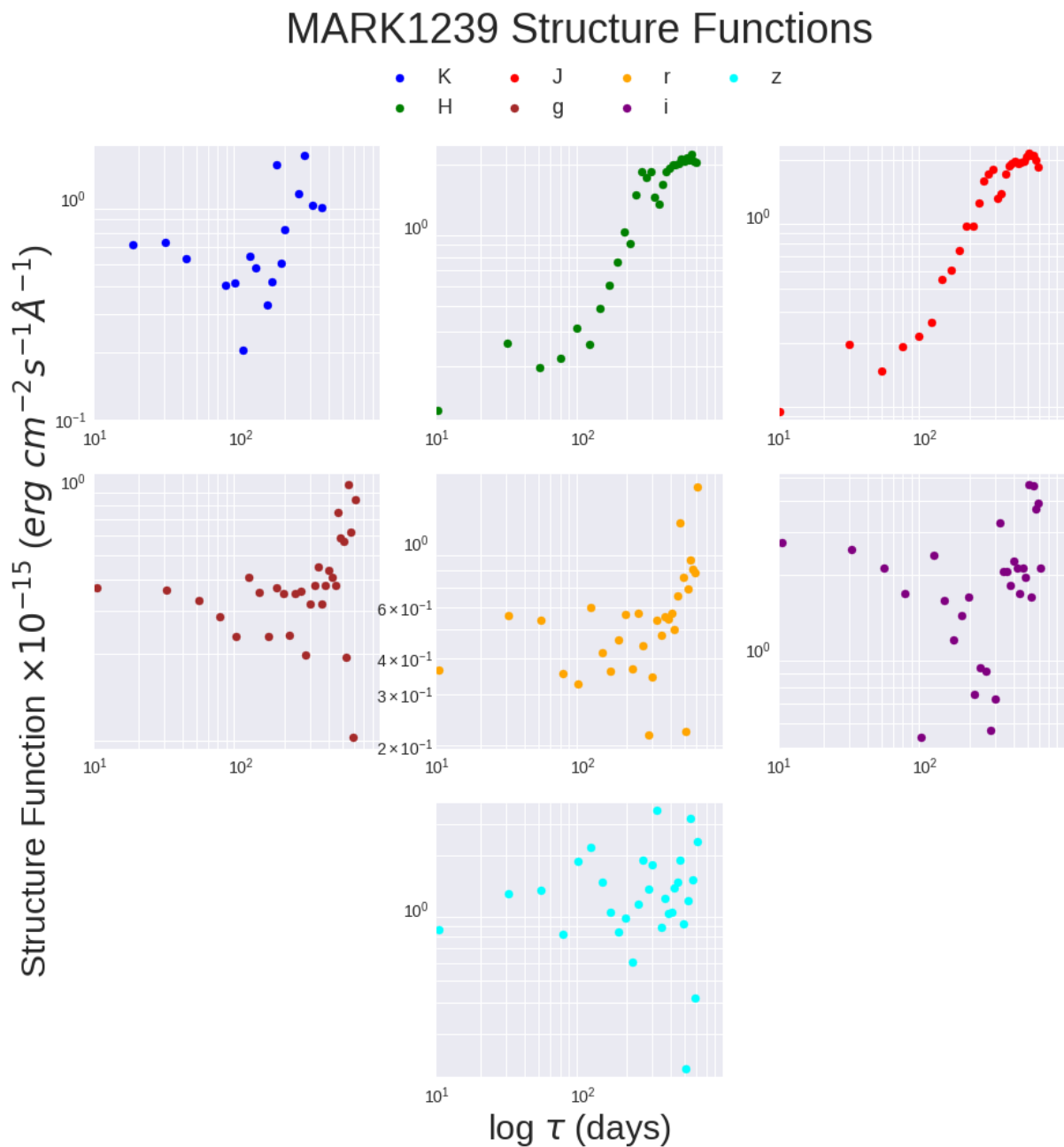


Figure C.6: The MARK1239 structure functions.

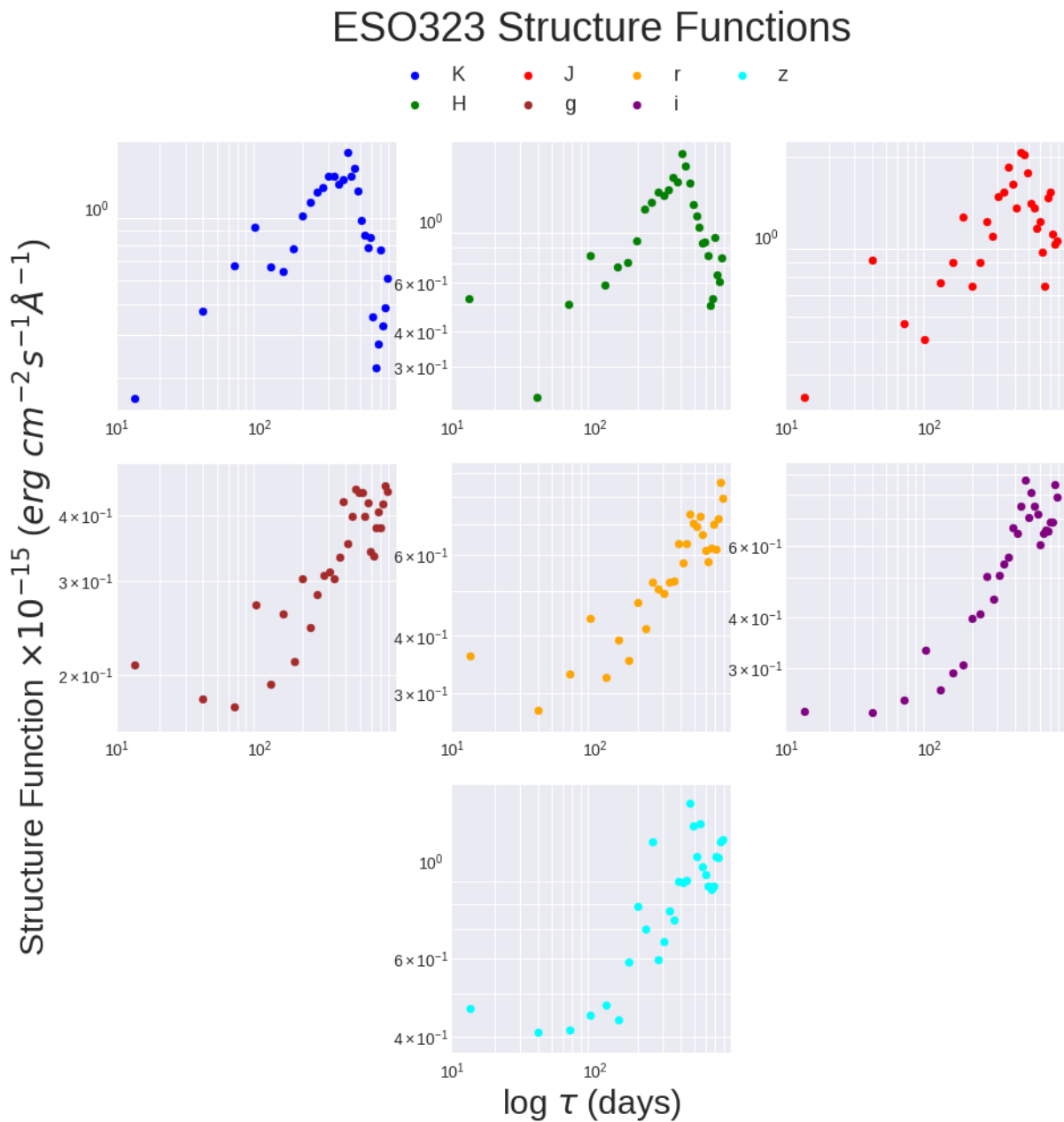


Figure C.7: The ESO323 structure functions.

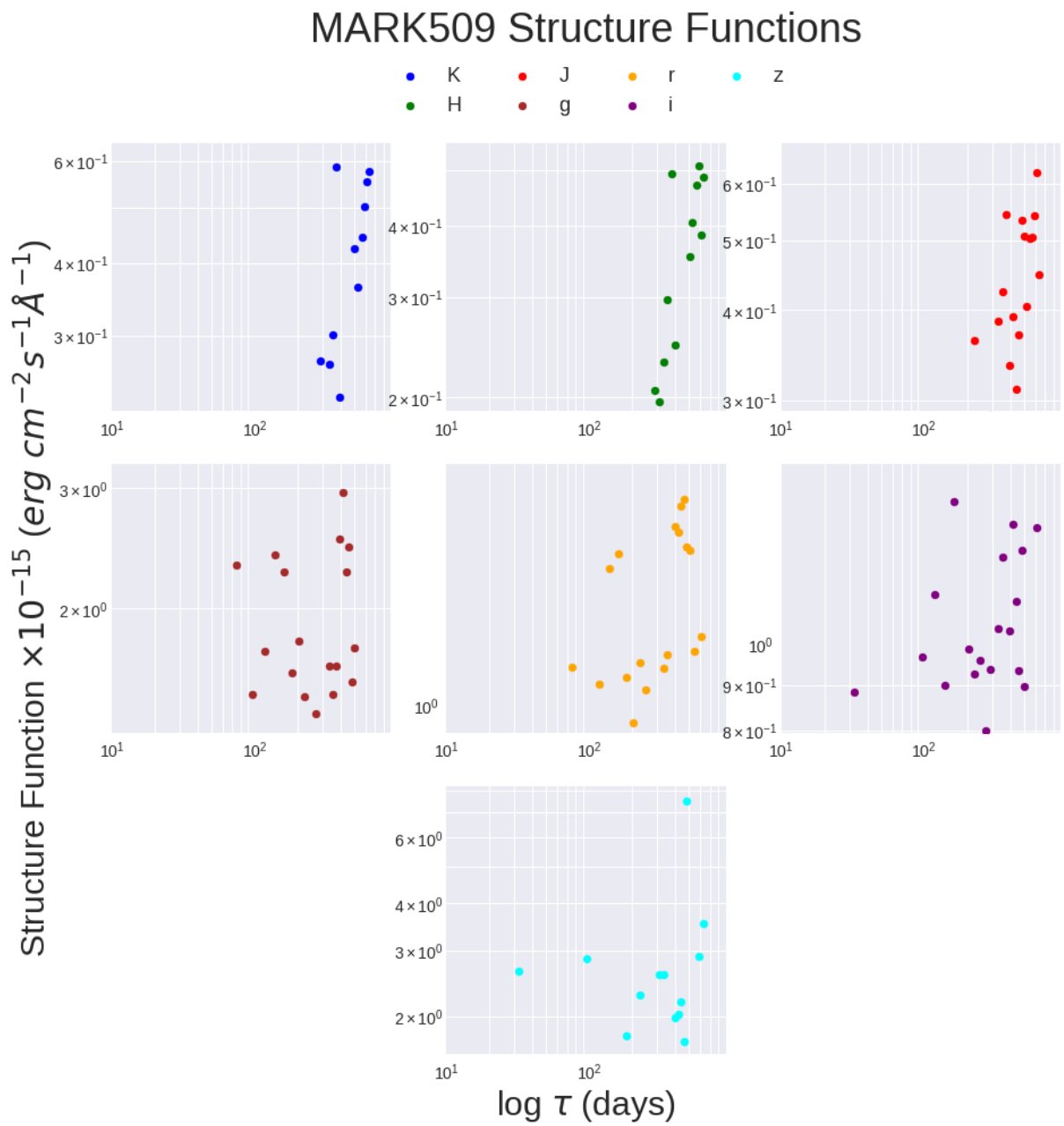


Figure C.8: The MARK509 structure functions.

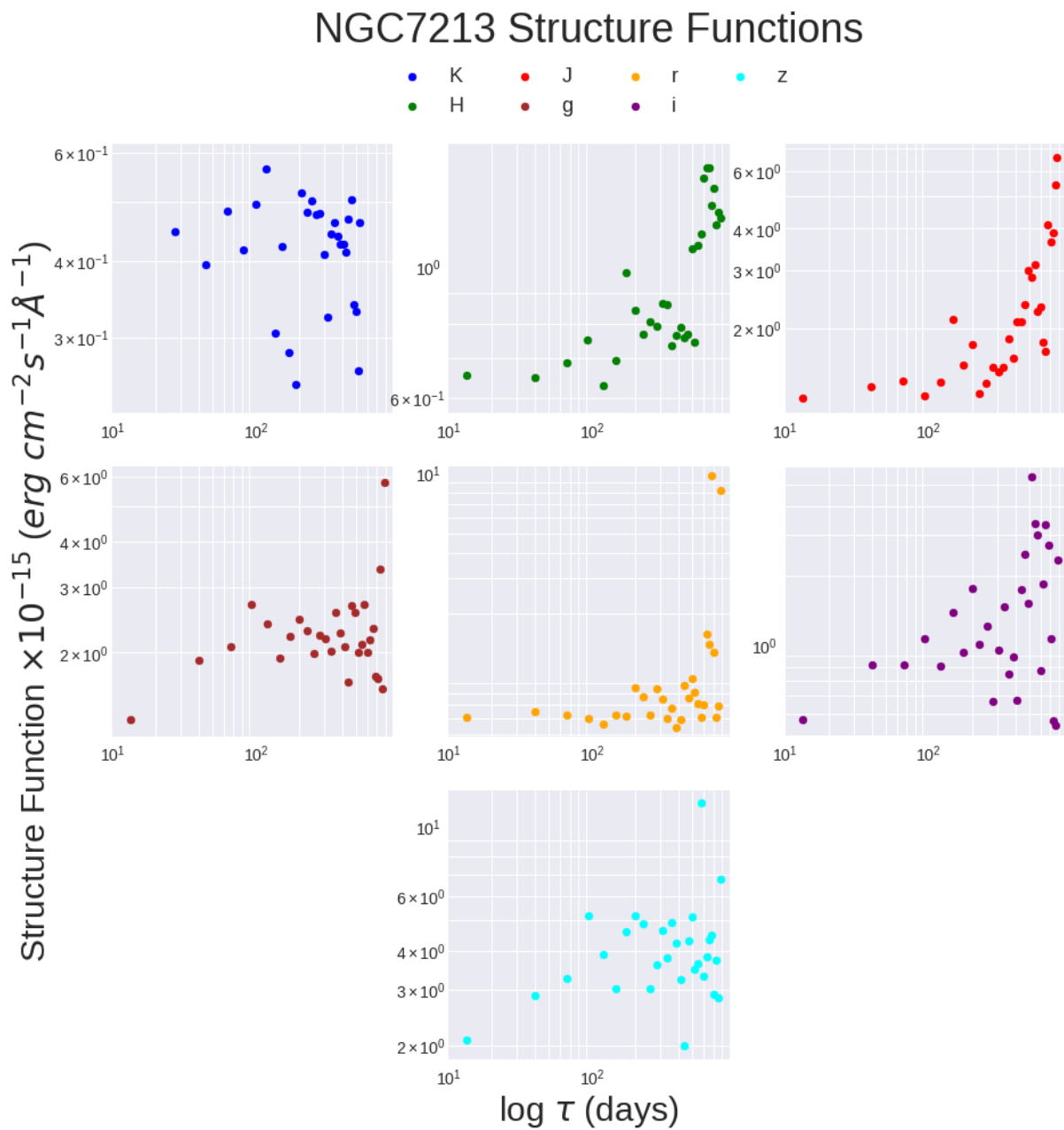


Figure C.9: The NGC7213 structure functions.

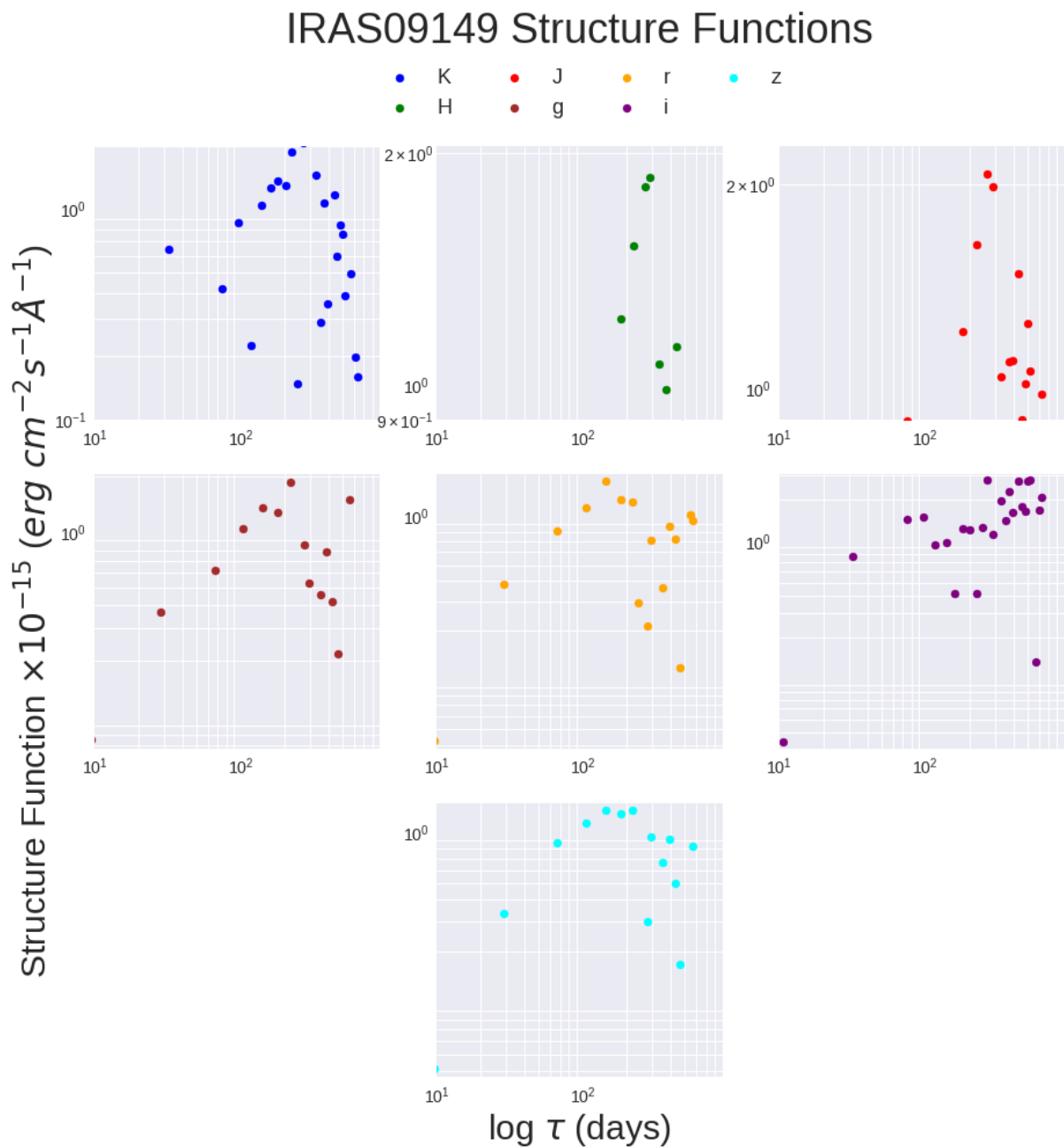
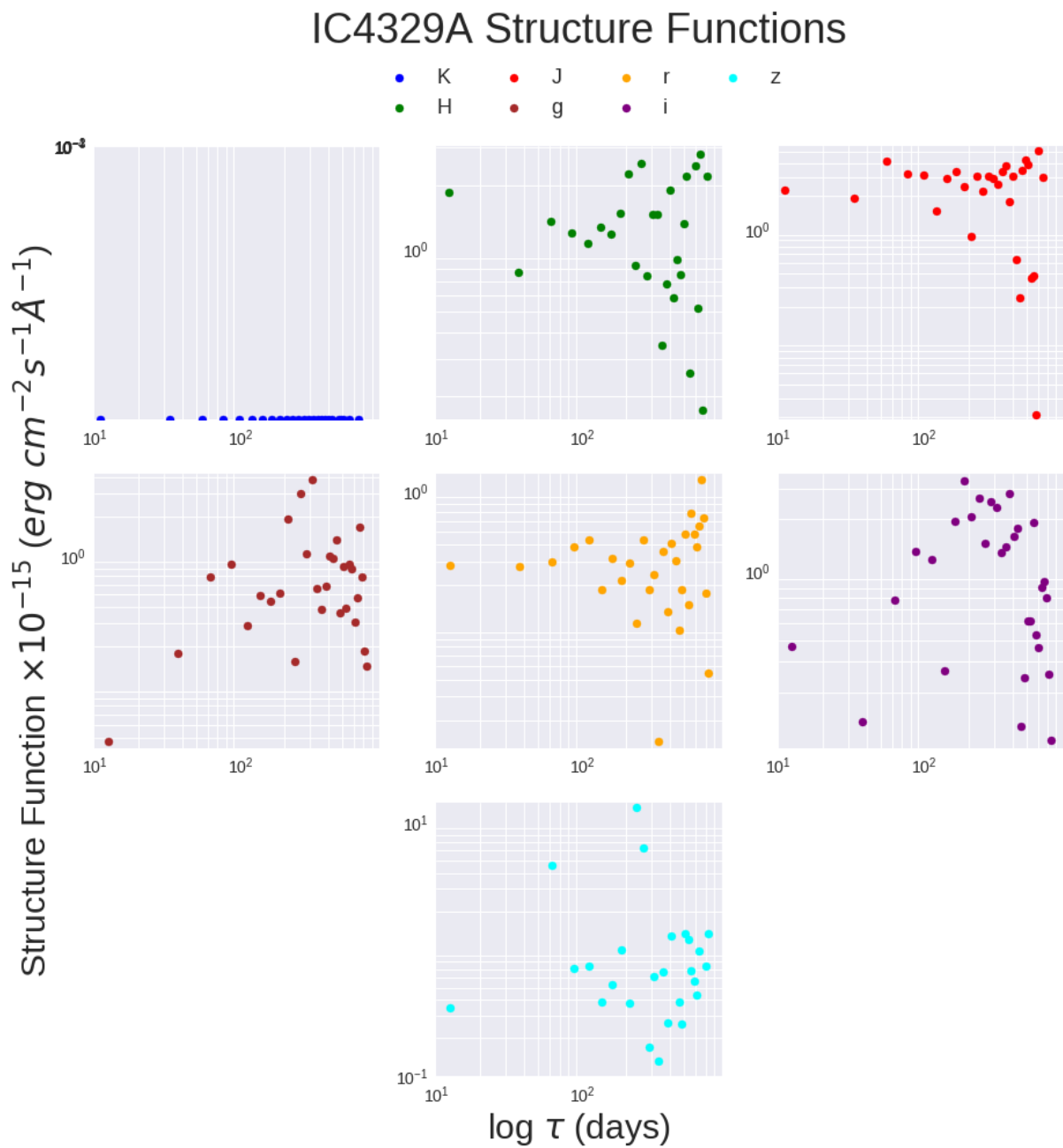


Figure C.10: The IRAS09149 structure functions.

**Figure C.11:** The IC4329A structure functions.

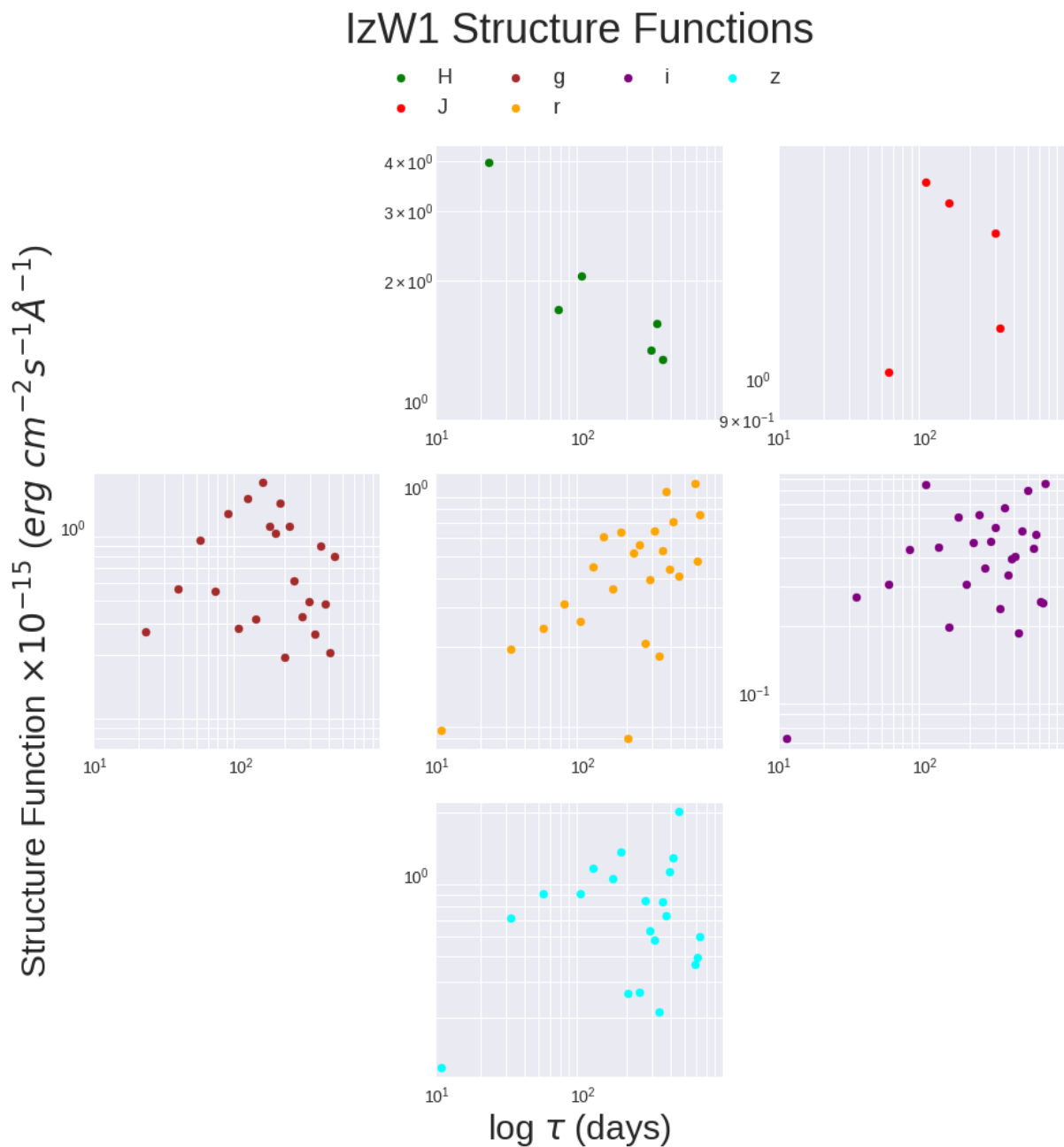


Figure C.12: The IzW1 structure functions.

7.1. READING LIST

Bibliography

- [1] https://www.ipac.caltech.edu/2mass/releases/allsky/doc/sec6_4a.html.
- [2] <http://www.astronomy.ohio-state.edu/~martini/usefuldata.html>.
- [3] <http://simbad.u-strasbg.fr/>.
- [4] SEXtractor Computer Software.
- [5] <http://archive.stsci.edu/panstarrs/search.php>.
- [6] The two micron all sky survey at ipac.
- [7] ALMEIDA, C. R., AND RICCI, C. Nuclear obscuration in active galactic nuclei. *arXiv:1709.00019 [astro-ph.GA]* (2017).
- [8] BERTIN, DURRET, AND MAMON. SExtractor v2.13 user's guide, 2012. https://www.astromatic.net/wsvn/public/filedetails.php?repname=public+documents.sextractor_doc&path=%2Fsextractor.pdf&rev=24.
- [9] BIANCHI, S., MAIOLINO, R., AND RISALITI, G. Agn obscuration and the unified model. *Advances in Astronomy vol. 2012, id. 782030* (2012).
- [10] BONVIN, V., COURBIN, F., SUYU, S. H., MARSHALL, P. J., RUSU, C. E., SLUSE, D., TEWES, M., WONG, K. C., COLLETT, T., FASSNACHT, C. D., TREU, T., AUGER, M. W., HILBERT, S., KOOPMANS, L. V. E., MEYLAN, G., RUMBAUGH, N., SONNENFELD, A., AND SPINIELLO, C. H0licow – v. new cosmograil time delays of he 0435–1223: H0 to 3.8 per cent precision from strong lensing in a flat λ cdm model. *Monthly Notices of the Royal Astronomical Society Volume 465, Issue 4* (2017).
- [11] BRUNETTI, M., AND PRODI, F. The climate system. *The European Physical Journal Conferences January 2015* (2015).
- [12] COLLABORATION, P., AGHANIM, N., ASHDOWN, M., AUMONT, J., BACCIGALUPI, C., BALLARDINI, M., BANDAY, A. J., BARREIRO, R. B., BARTOLO, N., BASAK, S., BATTYE, R., BENABED, K., BERNARD, J.-P., BERSANELLI, M., BIELEWICZ, P., BOCK, J. J., BONALDI, A., BONAVERA, L., BOND, J. R., BORRILL, J., BOUCHET, F. R., BOULANGER, F., BUCHER, M., BURIGANA, C., BUTLER, R. C., CALABRESE, E., CARDOSO, J.-F., CARRON, J., CHALLINOR, A., CHIANG, H. C., COLOMBO, L. P. L., COMBET, C., COMIS, B., COULAIIS, A., CRILL, B. P., CURTO, A., CUTTAIA, F., DAVIS, R. J., DE BERNARDIS,

- P., DE ROSA, A., DE ZOTTI, G., DELABROUILLE, J., DELOUIS, J.-M., DI VALENTINO, E., DICKINSON, C., DIEGO, J. M., DORÉ, O., DOUSPIS, M., DUCOUT, A., DUPAC, X., EFSTATHIOU, G., ELSNER, F., ENSSLIN, T. A., ERIKSEN, H. K., FALGARONE, E., FANTAYE, Y., FINELLI, F., FORASTIERI, F., FRALIS, M., FRAISSE, A. A., FRANCESCHI, E., FROLOV, A., GALEOTTA, S., GALLI, S., GANGA, K., GÉNOVA-SANTOS, R. T., GERBINO, M., GHOSH, T., GONZÁLEZ-NUEVO, J., GÓRSKI, K. M., GRATTON, S., GRUPPUSO, A., GUDMUNDSSON, J. E., HANSEN, F. K., HELOU, G., HENROT-VERSILLÉ, S., HERRANZ, D., HIVON, E., HUANG, Z., ILIĆ, S., JAFFE, A. H., JONES, W. C., KEIHÄNEN, E., KESKITALO, R., KISNER, T. S., KNOX, L., KRACHMALNICOFF, N., KUNZ, M., KURKI-SUONIO, H., LAGACHE, G., LAMARRE, J.-M., LANGER, M., LASENBY, A., LATTANZI, M., LAWRENCE, C. R., LE JEUNE, M., LEAHY, J. P., LEVRIER, F., LIQUORI, M., LILJE, P. B., LÓPEZ-CANIEGO, M., MA, Y.-Z., MACÍAS-PÉREZ, J. F., MAGGIO, G., MANGILLI, A., MARIS, M., MARTIN, P. G., MARTÍNEZ-GONZÁLEZ, E., MATARRESE, S., MAURI, N., McEWEN, J. D., MEINHOLD, P. R., MELCHIORRI, A., MENNELLA, A., MIGLIACCIO, M., MIVILLE-DESCHÈNES, M.-A., MOLINARI, D., MONETI, A., MONTIER, L., MORGANTE, G., MOSS, A., MOTTET, S., NASELSKY, P., NATOLI, P., OXBORROW, C. A., PAGANO, L., PAOLETTI, D., PARTRIDGE, B., PATANCHON, G., PATRIZII, L., PERDEREAU, O., PEROTTO, L., PETTORINO, V., PIACENTINI, F., PLASZCZYNSKI, S., POLASTRI, L., POLENTE, G., PUGET, J.-L., RACHEN, J. P., RACINE, B., REINECKE, M., REMAZEILLES, M., RENZI, A., ROCHA, G., ROSSETTI, M., ROUDIER, G., RUBIÑO-MARTÍN, J. A., RUIZ-GRANADOS, B., SALVATI, L., SANDRI, M., SAVELAINEN, M., SCOTT, D., SIRRI, G., SUNYAEV, R., SUUR-USKI, A.-S., TAUBER, J. A., TENTI, M., TOFFOLATTI, L., TOMASI, M., TRISTRAM, M., TROMBETTI, T., VALIVIITA, J., VAN TENT, F., VIBERT, L., VIELVA, P., VILLA, F., VITTORIO, N., WANDELT, B. D., WATSON, R., WEHUS, I. K., WHITE, M., ZACCHEI, A., AND ZONCA, A. Planck intermediate results xlvi. reduction of large-scale systematic effects in hfi polarization maps and estimation of the reionization optical depth. *Astronomy & Astrophysics Volume 596, id.A107* (2016).
- [13] DE VRIES, W. H., BECKER, R. H., WHITE, R. L., AND LOOMIS, C. Structure function analysis of long term quasar variability. *arXiv:astro-ph/0411348v1* (2004).
- [14] ET AL, C. Starlink gaia version 4.4.1, 2014.
- [15] FAVRE, P., COURVOISIER, T. J.-L., AND PALTANI, S. Agn variability time scales and the discrete-event model. *arXiv:astro-ph/0508620* (2005).
- [16] FERNÁNDEZ ARENAS, D., TERLEVICH, E., TERLEVICH, R., MELNICK, J., CHÁVEZ, R., BRESOLIN, F., TELLES, E., PLIONIS, M., AND BASILAKOS, S. An independent determination of the local hubble constant. *Monthly Notices of the Royal Astronomical Society Volume 474, Issue 1* (2017).
- [17] HONIG, S. F., AND KISHIMOTO, M. The dusty heart of nearby active galaxies. ii. from clumpy torus models to physical properties of dust around agn. *Astronomy and Astrophysics Volume 523* (2010).
- [18] HUGHES, I. G., AND HASE, T. P. A. *Measurements and their Uncertainties A practical guide to modern error analysis*. Oxford University Press, 2010.

- [19] INAF. <http://www.rem.inaf.it/>.
- [20] KELLY, B. C., BECHTOLD, J., AND SIEMIGINOWSKA, A. Are the variations in quasar optical flux driven by thermal fluctuations? *The Astrophysical Journal Volume 698, Number 1* (2009).
- [21] MO, H., VAN DE BOSCH, F., AND WHITE, S. *Galaxy Formation and Evolution*. Cambridge University Press, 2010/2016 (3rd edition).
- [22] NENKOVA, M., IVEZIC, Z., AND ELITZUR, M. Dust emission from active galactic nuclei. *The Astrophysical Journal Letters Volume 570, Number 1* (2002).
- [23] O.HAINAUT, 2005. <https://www.eso.org/~ohainaut/ccd/sn.html>.
- [24] PALMER, J., AND DAVENHALL, A., 2001. <http://star-www.rl.ac.uk/docs/sc6.htm#toc>.
- [25] PETERSON, B. M. Reverberation mapping of active galactic nuclei1. *Publications of the Astronomical Society of the Pacific Volume 105, Number 685* (1993).
- [26] PETERSON, B. M. *An Introduction to Active Galactic Nuclei*. Cambridge University press, 1997/2001/2003.
- [27] POZO NUNEZ, F., CHELOUCHE, D., AND KASPI, S. Accretion disk reverberation mapping of active galactic nuclei at wise observatory. *arXiv:1807.02724* (2018).
- [28] RIESS, A. G., CASERTANO, S., YUAN, W., MACRI, L., ANDERSON, J., MACKENTY, J. W., BOWERS, J. B., CLUBB, K. I., FILIPPENKO, A. V., JONES, D. O., AND TUCKER, B. E. New parallaxes of galactic cepheids from spatially scanning the hubble space telescope: Implications for the hubble constant. *arXiv:1801.01120* (2018).
- [29] RIESS, A. G., MACRI, L. M., HOFFMANN, S. L., SCOLNIK, D., CASERTANO, S., FILIPPENKO, A. V., TUCKER, B. E., REID, M. J., JONES, D. O., SILVERMAN, J. M., CHORNOCK, R., CHALLIS, P., YUAN, W., BROWN, P. J., AND FOLEY, R. J. A 2.4 *arXiv:1604.01424* (2016).
- [30] RISALITI, G., AND LUSSO, E. A hubble diagram for quasars. *The Astrophysical Journal Volume 815, Number 1* (2015).
- [31] SCHNEIDER, P. *Extragalactic Astronomy and Cosmology - An Introduction*. Springer Berlin Heidelberg New York, 2006.
- [32] SEXTRACTOR. sextractor.readthedocs.io.
- [33] SKIELBOE, A. *Colossal creations of gravity From clusters of galaxies to active galactic nuclei*. PhD thesis, Dark Cosmology Centre, Niels Bohr Institute University of Copenhagen, 2016.

- [34] SMITH, K. L., MUSHOTZKY, R. F., BOYD, P. T., MALKAN, M., HOWELL, S. B., AND GELINO, D. M. The kepler light curves of agn: A detailed analysis. *The Astrophysical Journal Volume 857, Number 2* (2018).
- [35] UTTLEY, P., AND McHARDY, I. M. The flux-dependent amplitude of broadband noise variability in x-ray binaries and active galaxies. *Monthly Notices of the Royal Astronomical Society Volume 323, Issue 2* (2001).
- [36] VAUGHAN, S., EDELSON, R., WARWICK, R. S., AND UTTLEY, P. On characterizing the variability properties of x-ray light curves from active galaxies. *Monthly Notices of the Royal Astronomical Society Volume 345, Issue 4* (2003).
- [37] WEIDNER, C., AND KROUPA, P. Evidence for a fundamental stellar upper mass limit from clustered star formation. *Monthly Notices of the Royal Astronomical Society Volume 348, Issue 1* (2004).
- [38] WOLTJER, L. Emission nuclei in galaxies. *Astrophysical Journal Vol. 130*, (1959), 38.